

# Superthermal Electron Dynamics in the HSX Stellarator

by

Ali Elsayed Ali Ibrahim Abdou

A dissertation submitted in partial fulfillment of  
the requirements for the degree of

Doctor of Philosophy  
(Nuclear Engineering and Engineering Physics)

at the  
University of Wisconsin-Madison

2005

UMI Number: 3200160

## INFORMATION TO USERS

The quality of this reproduction is dependent upon the quality of the copy submitted. Broken or indistinct print, colored or poor quality illustrations and photographs, print bleed-through, substandard margins, and improper alignment can adversely affect reproduction.

In the unlikely event that the author did not send a complete manuscript and there are missing pages, these will be noted. Also, if unauthorized copyright material had to be removed, a note will indicate the deletion.

**UMI<sup>®</sup>**

---

UMI Microform 3200160

Copyright 2006 by ProQuest Information and Learning Company.

All rights reserved. This microform edition is protected against unauthorized copying under Title 17, United States Code.

ProQuest Information and Learning Company  
300 North Zeeb Road  
P.O. Box 1346  
Ann Arbor, MI 48106-1346

# A dissertation entitled

Superthermal Electron Dynamics  
in the HSX Stellarator

submitted to the Graduate School of the  
University of Wisconsin-Madison  
in partial fulfillment of the requirements for the  
degree of Doctor of Philosophy

by

Ali Elsayed Ali Ibrahim Abdou

Date of Final Oral Examination: September 21, 2005

Month & Year Degree to be awarded: December 2005 May August

\*\*\*\*\*  
Approval Signatures of Dissertation Committee

Raymond J. Fink

Daniel

Chris Heggen

Josh Horowitz

Stef C. R.

Signature, Dean of Graduate School

Martin Calvalleri /zh

### Abstract:

The Helically Symmetric eXperiment (HSX) is a novel machine with quasi-helical symmetry in mod  $\bar{B}$  which promises improved single particle confinement. Superthermal electrons are generated in HSX during two different processes, (1) runaway electron formation in loop voltages developed during magnetic field ramp-up and ramp-down phases and (2) during 2<sup>nd</sup> harmonic X-mode ECRH using 28 GHz 50 kW Gyrotron. The normal magnetic configuration is Quasi-Helically Symmetric (QHS), with dominant  $n=4$ ,  $m=1$  components in the magnetic field spectrum. With a set of auxiliary coils, the quasihelical symmetry can be broken (Mirror and AntiMirror configurations). In this work the resolved hard x-ray emission in the HSX is analyzed using a CdZnTe detector. The detector is housed in a lead box adjacent to the vacuum vessel, with a 4 mm pinhole and 200  $\mu\text{m}$  stainless steel filter placed in front of the detector. Superthermal electrons generated during field ramp-up were suppressed using two different techniques, (1) controlled neutral gas puff and (2) using pulsed UV Xe flash lamp. The hard x-ray spectra were accumulated in a series of similar ECRH discharges. The behavior of the superthermal electrons during the microwave discharge has been studied for densities in the range of  $0.1$  to  $1.0 \times 10^{12} \text{ cm}^{-3}$ . The magnetic configuration has also been altered between QHS, Mirror and AntiMirror configurations in order to determine the effect of magnetic ripples on characteristic energies and densities of superthermal electrons. Pulse height analysis of the hard x-ray emission shows the presence of x-ray photons with energies as high as 1 MeV during the microwave discharge. The Hard x-ray emission shows inverse nonlinear density dependence, where at low density ( $0.2 \times 10^{12} \text{ cm}^{-3}$ ) the

intensity is 14 times higher than at higher density ( $1.0 \times 10^{12} \text{ cm}^{-3}$ ). The spectra also show higher x-ray intensities and photon energies in QHS compared to the MIRROR configuration while no signal was detected in the AntiMirror configuration. The time evolution of the hard x-ray signal shows that QHS has longer superthermal electron confinement time in the order of 8 msec (estimated from the decay time of the hard x-ray signal after the microwave power is turned off) compared to 1 msec in the Mirror configuration. Calculations of single particle heating in the microwave electric field using a relativistic Lorentz model and single particle orbits using guiding center equations in magnetic co-ordinates indicated that the improved confinement in the quasisymmetric configuration is responsible for the more efficient heating of superthermal electrons.

For my Parents, wife, brothers and kids who supported me during this  
work.

### Acknowledgements

The major driving force behind the completion of this thesis is Professor David Anderson, my thesis research advisor at the Department of Electrical and Computer Engineering. He gave me useful advice, suggesting new ideas and was always willing to discuss question I might have in spite of his busy schedule. It is pleasure to take the opportunity to recognize his support and guidance. I thank him for not only his academic guidance, but also for his perspective on the social aspect of academia.

I am very thankful to my academic advisor Professor Raymond Fonck at the Engineering Physics Department who academically guided me through my graduate work. I'm gratefully acknowledging the significant contribution to this work made by Dr. Abdulgader Almagri who acted as my scientific advisor; I benefited a lot from his experience. Much of the conceptual framework for this work is due to him. He helped me in bringing up the hard x-ray detection system to work, collecting the data, analyzing and explaining it. Sincere thanks goes to Dr. Konstantin Likin for his expert advice in microwave heating. He helped me significantly in ECR heating model. He taught me many valuable things about microwaves and ECH.

I would like to extend my gratitude to those individuals who have offered their assistance in the completion of this thesis. Dr. Joe Talmadge and Dr. Simon Anderson for reviewing the work and valuable discussions. Dr. Rob O'Connell of the MST group at the physics department of UW Madison for using his pulse height analysis code and his valuable discussions. Almost every member of the group has assisted me at one time on another, their support is gratefully acknowledged. Dr. Paul Probert for his professional

electronic design assistance, Mike Frankowski for manufacturing the collimators, radiation shields detector boxes and support structures for my experiment, Evan Jolitz for his professional operation of the HSX for taken the data during this research work, and Tony Piccione for his generous help in electronics.

I would also like to thank my colleagues at the HSX for their sincere help and support. I wish to thank specially John Canik and Walter Guttenfelder for raising many insightful questions and suggestions during the course of this work. Their support and encouragement during this work was invaluable. Jerahmie Radder with Canik and Walter did a wonderful job in proofreading and checking the grammar and punctuation of the English language of this manuscript. I also wish to thank the rest of the HSX group for their support and collaboration, this group includes: Dr. Chuanbao Deng, Dr. Kan Zhai, Dr. Carsten Lechte, Seunghun Oh, John Schmitt, Victor Sakaguci, Jane Lu, Jeremy Loree, Alexis Briesemeister, Andrew Herr. Working together with those colleagues has not only been a good learning experience, but also a great pleasure.

I also wish to thank Professors Chris Hegna, Noah Hershkowitz and Stewart Prager for their membership on my defense committee.

I wish to acknowledge the lifelong encouragement and support of my parents and family and to thank my wife and kids for their patience, support and companionship. Finally, I want to express my gratitude to God whose blessings made this effort fruitful.

## Table of Contents

Abstract .....	i
Acknowledgements .....	iv
List of Tables .....	xii
List of Figures .....	xiii

## Chapter 1: Introduction.

1.0: Introduction.....	1
1.1: Motivation.....	1
1.2: The HSX Stellarator.....	2
1.2.1: Variation of the Magnetic Field Structure in HSX .....	9
1.2.2: Plasma Production and Heating in HSX.....	14
1.2.3: HSX Diagnostics.....	16
1.3: Superthermal Electrons in Fusion Plasmas.....	18
1.3.1: Superthermal Electrons in Non-Helical Devices .....	19
1.3.2: Superthermal Electrons in Helical Devices .....	20
1.3.2.1: Suppression of Electron Runaways during Magnetic Field Ramping.....	20
1.3.2.2: Confinement of ECR Generated Superthermal Electrons in Helical Devices .....	22
1.3.3: Single Particle ECRH Theory.....	25
1.4: Thesis Outline.....	26

## **Chapter 2: Diagnostics and Hardware.**

2.0: Introduction.....	33
2.1: X-ray Spectroscopic System.....	33
2.1.1: Stainless Steel Filter.....	36
2.1.2: Lead Shield and Collimator .....	38
2.1.3: The CdZnTe Detector .....	40
2.1.4: Electronics .....	45
2.1.5: The Pulse Height Analysis Software. ....	46
2.2: Complimentary HSX Diagnostics used in this Work .....	52
2.2.1: Soft X-ray Detectors .....	52
2.2.2: Diamagnetic Loop.....	53
2.2.3: Loop Voltage .....	55
2.2.4: Microwave Interferometer .....	55
2.2.5: Thomson Scattering .....	56

## **Chapter 3: Superthermal Electron Sources in HSX.**

3.0: Introduction.....	59
3.1: Electron Runaway during Field Ramping .....	60
3.1.1: Electron Runaway Theory .....	62
3.2: Techniques of Decoupling Superthermal Electron Sources .....	66
3.2.1: Base Pressure method .....	67
3.2.2: Ultraviolet Xenon Flash Lamp Method. ....	73
3.3: Modeling of Electron Runaways during Field Ramping .....	78

	viii
3.4: Electron Runaway during ECRH Discharges .....	82
3.5: Summary .....	90

## **Chapter 4: Hard X-ray Measurements in HSX.**

4.0: Introduction.....	92
4.1: Evidence of Superthermal Electron Generation in HSX .....	93
4.2: Spectrum Difference between Configurations.....	100
4.3: Hard X-ray Time Evolution.....	103
4.4: Hard X-ray Plasma Density Dependence .....	107
4.5: Hard X-ray Microwave Power Dependence.....	120
4.6: Hard X-ray Resonance Location Dependence.....	122
4.7: Summary.....	128

## **Chapter 5: Single Particle Heating Model**

5.0: Introduction.....	131
5.1: Model Description .....	132
5.1.1 Microwave Electric Field Model. ....	133
5.1.2: Magnetic Field Model.....	135
5.1.3: Model Assumption.....	137
5.1.4: Code Description .....	139
5.1.5: Energy Gain Dependence on Initial Phase .....	144
5.2: Analytical Solution .....	145
5.3: Energy Gain Parametric Dependence .....	147
5.3.1: Microwave Power Dependence .....	147

5.3.2: Perpendicular Index of Refraction.....	148
5.3.3: Perpendicular Velocity Dependence.....	150
5.3.4: Parallel Velocity Dependence.....	151
5.4: Summary.....	153

## **Chapter 6: Single Particle Confinement in HSX.**

6.0: Introduction.....	156
6.1: Electron Guiding Center Equations .....	157
6.2: The HSX Magnetic Spectrum .....	161
6.3 The Microwave Heating Operator .....	167
6.4: The Numerical Solution.....	172
6.5: Confinement Differences between Configurations during ECRH .....	176
6.6: Confinement Differences between Configurations after ECRH is Turned off.....	196
6.6.1: Neutral Gas Densities in the HSX Stellarator.....	197
6.6.2: Estimation of Superthermal Electron Confinement Times.....	201
6.7: Summary.....	204

## **Chapter 7: Conclusions and Future Work.**

7.1: Conclusion .....	208
7.2: Future Work .....	211

## **Appendix 1: Plasma X-ray Generation Theory**

A1.0: Introduction.....	214
A1.1: Sources of X-ray in Plasma.....	216

A1.1.1: Continuum Spectrum Source. ....	216
A1.1.1.1: Free-Free Bremsstrahlung. ....	217
A1.1.1.2: Free-Bound Recombination. ....	219
A1.1.2: Line Emission Sources. ....	220

## **Appendix 2: Pulse Height Analysis Program**

A2.0: Introduction. ....	224
A2.1: The Pulse Height Analysis Program. ....	225
A2.1.1: How the Program Works?.....	225
A2.2: Program Input and Output. ....	230
A2.2.1: Program Input. ....	230
A2.2.2: Program Output.....	232
A2.2.2.1: Simple Output. ....	232
A2.2.2.2: Detailed Output.....	236
A2.3: Program Listing. ....	241
A2.3.1: The Main PHA Program. ....	241
A2.3.2: Auxiliary Programs.....	261

## **Appendix 3: Electron Collision Frequencies**

A3.0: Introduction. ....	267
A3.1: Electron Coulomb Collisions.....	268
A3.2: Electron Neutral Collisions.....	275

## **Appendix 4: Single Particle Heating Program**

A4.0: Introduction.....	280
A4.1: The Single Particle Heating Model .....	280
A4.2: Program Input .....	281
A4.3: Program Output.....	283
A4.4: Program Listing .....	285

## **Appendix 5: Single Particle Drift Orbit Program**

A5.0: Introduction.....	295
A5.1: The Single Particle Drift Orbit Model .....	295
A5.2: Program Input .....	296
A5.3: Program Output.....	297
A5.4: Program Listing .....	300

## **Appendix 6: Variation of mod B along Field Line**

A6.0: Introduction.....	314
A6.1: Mod B Variation along Magnetic Field Line.....	317

## List of Tables

### **Chapter 1:**

<b>Table 1.1:</b> HSX Machine Parameters.....	8
<b>Table 1.2:</b> Properties of the Various HSX Magnetic Configurations. ....	10
<b>Table 1.3:</b> Parameters of the HSX Plasma. ....	15

### **Chapter 2:**

<b>Table 2.1:</b> CdZnTe physical characteristics.....	42
<b>Table 2.2:</b> CdZnTe detection characteristics.....	42
<b>Table 2.3:</b> EG&G Ortec 671 amplifier settings .....	46

### **Chapter 3:**

<b>Table 3.1:</b> Xenon flash lamp specifications .....	75
---	----

### **Chapter 6:**

<b>Table 6.1:</b> Fraction of Resonance Crossing Time.....	189
<b>Table 6.2:</b> Resonance Zone Crossing Probability.....	189
<b>Table 6.3:</b> Electron Final Energy .....	190
<b>Table 6.4:</b> Electron Drift Orbit Relative Width .....	190

## List of Figures

### Chapter 1:

<b>Figure 1.1:</b> General view of the HSX device.....	3
<b>Figure 1.2:</b> Variation of the magnitude of B along field line in QHS .....	6
<b>Figure 1.3:</b> Radial variation of $b_{mn}$ for QHS configuration .....	7
<b>Figure 1.4:</b> Flux surfaces for QHS configuration .....	7
<b>Figure 1.5:</b> HSX main and auxiliary coils mounted on the supporting rig.....	9
<b>Figure 1.6:</b> Direction of currents in auxiliary coils.....	10
<b>Figure 1.7:</b> Radial variation of $b_{mn}$ for magnetic configurations. ....	11
<b>Figure 1.8:</b> Flux surfaces for magnetic configuration.....	11
<b>Figure 1.9:</b> Variation of the magnitude of B along field line in Mirror.....	12
<b>Figure 1.10:</b> Variation of the magnitude of B along field line in AntiMirror.....	13
<b>Figure 1.11:</b> Rotational transform radial variation for magnetic configurations .....	14
<b>Figure 1.12:</b> Vertical view of box port C .....	15
<b>Figure 1.13:</b> HSX diagnostics approximate layout .....	16
<b>Figure 1.14:</b> HSX status plot .....	17

### Chapter 2:

<b>Figure 2.1:</b> X-ray absorption coefficient for CdZnTe.....	34
<b>Figure 2.2:</b> CdZnTe pulse height analysis system mounted on HSX .....	35
<b>Figure 2.3:</b> Hard x-ray spectroscopic system signal chain .....	36
<b>Figure 2.4:</b> X-ray transmission for stainless steel 304 from 0.001 to 2 MeV.....	37
<b>Figure 2.5:</b> X-ray transmissions for lead from 0.001 to 10 MeV .....	39

<b>Figure 2.6:</b> Collimator geometry .....	40
<b>Figure 2.7:</b> EV-280 CdZnTe detector and its built-in pre-amplifier.....	41
<b>Figure 2.8:</b> Gamma ray spectrum for Am <sup>241</sup> .....	43
<b>Figure 2.9:</b> Calibration curves for CdZnTe at different amplifier gains.....	45
<b>Figure 2.10:</b> Raw hard x-ray signal during the plasma.....	47
<b>Figure 2.11:</b> Raw hard x-ray single pulse with Gaussian shape .....	48
<b>Figure 2.12:</b> Hard x-ray signal and noise level.....	50
<b>Figure 2.13:</b> Fitting the individual pulses to Gaussian .....	50
<b>Figure 2.14:</b> Hard x-ray histogram and spectrum .....	51
<b>Figure 2.15:</b> Curve fitting to calculate the electron temperature .....	51
<b>Figure 2.16:</b> SXR signal from 5-chord-array, chord # 3.....	53
<b>Figure 2.17:</b> Plasma stored energy, W in joules during ECRH discharge.....	54
<b>Figure 2.18:</b> Loop voltage signals in QHS .....	55
<b>Figure 2.19:</b> Plasma line average density in QHS. ....	56
<b>Figure 2.20:</b> Electron density profile in QHS. $\langle n_e \rangle \sim 10^{12} \text{ cm}^{-3}$ .....	57
<b>Figure 2.21:</b> Electron temperature profile in QHS. $\langle n_e \rangle \sim 10^{12} \text{ cm}^{-3}$ .....	57
<b><u>Chapter 3:</u></b>	
<b>Figure 3.1:</b> Main coils current and toroidal loop voltage. ....	61
<b>Figure 3.2:</b> Hard x-ray emitted during current ramp-up and ramp-down.....	64
<b>Figure 3.3:</b> Hard x-ray signal in QHS and Mirror during field ramping. ....	65
<b>Figure 3.4:</b> Hard x-ray signal at $P_{\text{base}} = 7.5 \times 10^{-8}$ torr during the ECRH discharge. ....	68
<b>Figure 3.5:</b> Hard x-ray signal at $P_{\text{base}} = 5.6 \times 10^{-7}$ torr during the ECRH discharge. ....	68

<b>Figure 3.6:</b> Hard x-ray signal at $P_{\text{base}} = 6.5 \times 10^{-7}$ torr during the ECRH discharge. ....	69
<b>Figure 3.7:</b> Hard x-ray signal at $P_{\text{base}} = 4.4 \times 10^{-6}$ torr during the ECRH discharge. ....	69
<b>Figure 3.8:</b> Hard x-ray signal at current ramping, No gas puff. ....	71
<b>Figure 3.9:</b> Hard x-ray signal during current ramping. ....	72
<b>Figure 3.10:</b> Hard x-ray signal during current ramping. ....	72
<b>Figure 3.11:</b> Hard x-ray signal during current ramping. ....	73
<b>Figure 3.12:</b> Xenon flash lamp. ....	74
<b>Figure 3.13:</b> Xenon flash lamp output light spectrum. ....	75
<b>Figure 3.14:</b> Loop voltage during field ramping. ....	76
<b>Figure 3.15:</b> Plasma electron density time evolution. ....	78
<b>Figure 3.16:</b> Hard x-ray signal for two different lamp firing times. ....	78
<b>Figure 3.17:</b> Hard x-ray generated when flash lamp was fired at 290 msec. ....	80
<b>Figure 3.18:</b> Hard x-ray generated when flash lamp was fired at 900 msec. ....	80
<b>Figure 3.19:</b> Hard x-ray generated when flash was lamp fired at 1000 msec. ....	81
<b>Figure 3.20:</b> Hard x-ray generated when flash lamp was fired at 1500 msec. ....	81
<b>Figure 3.21:</b> Second harmonic ECRH from wave particle interaction perspective. ....	84
<b>Figure 3.22:</b> Second harmonic ECRH from wave particle interaction perspective. ....	85
<b>Figure 3.23:</b> Maximum energy gained during second harmonic ECRH. ....	88
<b>Figure 3.24:</b> Raw hard x-ray signal during second harmonic ECRH. ....	89
<b><u>Chapter 4:</u></b>	
<b>Figure 4.1:</b> HSX discharge signals in QHS at low and high plasma densities ....	94
<b>Figure 4.2:</b> Different HSX diagnostics detect superthermal electrons. ....	96

<b>Figure 4.3:</b> Plasma line-averaged electron density and soft x-ray time evolution.....	98
<b>Figure 4.4:</b> Radiated Power Measured using Bolometer in HSX.....	101
<b>Figure 4.5:</b> Hard x-ray spectrum during on-axis ECRH for QHS and Mirror.....	102
<b>Figure 4.6:</b> HXR counts time evolution for QHS and Mirror at low density. ....	104
<b>Figure 4.7:</b> HXR average photon energy time evolution for QHS and Mirror.....	106
<b>Figure 4.8:</b> HXR maximum photon energy time evolution for QHS and Mirror.....	106
<b>Figure 4.9:</b> The variation of the HXR counts with plasma.....	107
<b>Figure 4.10:</b> Comparison between different collision processes .....	109
<b>Figure 4.11:</b> The variation of the HXR average photon energy with density.....	112
<b>Figure 4.12:</b> The variation of the HXR maximum photon energy with density.....	112
<b>Figure 4.13:</b> HSX spectrum at three different plasma densities for QHS.....	114
<b>Figure 4.14:</b> HSX spectrum at three different plasma densities for Mirror.....	114
<b>Figure 4.15:</b> HSX counts time evolution at three different densities for QHS.....	115
<b>Figure 4.16:</b> HSX counts time evolution at three different densities for. Mirror. ....	115
<b>Figure 4.17:</b> Plasma density time evolution for fixed and ramp-up densities. ....	118
<b>Figure 4.18:</b> HXR counts time evolution for fixed density and density ramp-up. ....	118
<b>Figure 4.19:</b> HXR $\langle E \rangle$ time evolution for fixed density and density ramp-up.....	119
<b>Figure 4.20:</b> HXR $E_{\text{maximum}}$ time evolution for fixed density and density ramp-up. ...	119
<b>Figure 4.21:</b> HXR spectrum for three different microwave powers. ....	121
<b>Figure 4.22:</b> HXR average photon energy microwave power dependence. ....	121
<b>Figure 4.23:</b> Plasma stored energy heating location dependence .....	124

<b>Figure 4.24:</b> HXR intensity heating location dependence .....	124
<b>Figure 4.25:</b> Plasma stored energy density scan for QHS configuration.....	126
<b>Figure 4.26:</b> Plasma stored energy density scan for Mirror configuration. ....	126
<b>Figure 4.27:</b> HXR counts density scan for QHS configuration. ....	127
<b>Figure 4.28:</b> HXR counts density scan for Mirror configuration. ....	127
<b><u>Chapter 5:</u></b>	
<b>Figure 5.1:</b> Vertical view of Box Port C showing the microwave beam. ....	133
<b>Figure 5.2:</b> Top view of HSX showing beam location and resonance point .....	134
<b>Figure 5.3:</b> Toroidal variation of $ B $ on axis for QHS, Mirror and AntiMirror. ....	137
<b>Figure 5.4:</b> $ B $ on axis in the heating zone for QHS, Mirror and AntiMirror. ....	138
<b>Figure 5.5:</b> Electron orbit in lab coordinates following magnetic-axis in the .....	140
<b>Figure 5.6:</b> Magnetic field followed by the electron on-axis in the heating zone. ....	141
<b>Figure 5.7:</b> Electron total energy time evolution through the resonance zone .....	141
<b>Figure 5.8:</b> Electron total energy time evolution through the resonance zone .....	142
<b>Figure 5.9:</b> Electron total energy time evolution through the resonance.....	143
<b>Figure 5.10:</b> Electron energy gain $\Delta W$ as a function of initial phase $\phi$ .....	145
<b>Figure 5.11:</b> Net Electron-energy gain $\langle \Delta W \rangle$ as a function of microwave power.. ...	148
<b>Figure 5.12:</b> Net Electron-energy gain $\langle \Delta W \rangle$ as a function of $N_{\text{perpendicular}}$ .....	149
<b>Figure 5.13:</b> Net Electron-energy gain $\langle \Delta W \rangle$ as a function of $W_{\perp}$ .....	151
<b>Figure 5.14:</b> Net Electron-energy gain $\langle \Delta W \rangle$ as a function of $W_{\text{initial}}$ .....	152
<b>Figure 5.15:</b> Net Electron-energy gain $\langle \Delta W \rangle$ as a function of pitch angle .....	153

**Chapter 6:**

<b>Figure 6.1:</b> The variation of QHS spectral components with minor radius.....	163
<b>Figure 6.2:</b> The variation of Mirror spectral components with minor radius .....	164
<b>Figure 6.3:</b> Magnetic field variation along field line at $r/a = 0$ .....	165
<b>Figure 6.4:</b> Magnetic field variation along field line at $r/a = -0.5$ .....	166
<b>Figure 6.5:</b> Magnetic field variation along field line at $r/a = 0.5$ .....	166
<b>Figure 6.6:</b> Plasma cross section at box port C showing resonance zone.....	168
<b>Figure 6.7:</b> Electron Net Energy Gain .....	170
<b>Figure 6.8:</b> Net Electron Power Gain.....	170
<b>Figure 6.9:</b> $r$ - $\theta$ plot of electron drift orbit for $\varepsilon = 5$ keV, $r/a = 0.5$ .....	174
<b>Figure 6.10:</b> $r$ - $\phi$ plot of electron drift orbit for $\varepsilon = 5$ keV, $r/a = 0.5$ .....	174
<b>Figure 6.11:</b> $r$ - $\theta$ plot of electron drift orbit for $\varepsilon = 100$ eV, $r/a = 0.05$ .....	175
<b>Figure 6.12:</b> The time evolution for the magnetic moment .....	176
<b>Figure 6.13:</b> Plasma cross section at $\phi = 0$ .....	178
<b>Figure 6.14:</b> $r$ - $\theta$ plot of electron drift orbit for $\varepsilon = 100$ keV, $r/a = 0.5$ .....	178
<b>Figure 6.15:</b> The variation of the resonance crossing probability .....	180
<b>Figure 6.16:</b> The variation of the electron final energy .....	182
<b>Figure 6.17:</b> The variation of the resonance crossing time.....	183
<b>Figure 6.18:</b> The variation of the electron drift orbit width.....	185
<b>Figure 6.19:</b> $r$ - $\theta$ plot of electron drift orbit for $\varepsilon = 100$ keV .....	186
<b>Figure 6.20:</b> The time evolution of magnetic moment .....	187
<b>Figure 6.21:</b> The variation of the magnetic field amplitude .....	191

<b>Figure 6.22:</b> The fraction of particles on direct loss orbits in AntiMirror .....	192
<b>Figure 6.23:</b> The fraction of particles on direct loss orbits in AntiMirror .....	193
<b>Figure 6.24:</b> Floating potential on collector plates as a function $n_e$ in QHS .....	195
<b>Figure 6.25:</b> Floating potential on collector plates as a function $n_e$ in AntiMirror .....	195
<b>Figure 6.26:</b> The profiles of neutral densities for atomic and molecular hydrogen.....	198
<b>Figure 6.27:</b> The neutral base pressure measured using the micro-ion gauge .....	199
<b>Figure 6.28:</b> The energy variation of the electron collision frequencies .....	200
<b>Figure 6.29:</b> The hard x-ray variation with probe insertion distance.....	202
<b>Figure 6.30:</b> The time evolution of neutral gas density .....	203
<b>Figure 6.31:</b> The time evolution of the hard x-ray counts .....	204
<b><u>Appendix 1:</u></b>	
<b>Figure A1.1:</b> Schematic drawing of the Bremsstrahlung process.....	214
<b>Figure A1.2:</b> Dependence of the Bremsstrahlung $d\sigma$ on photon energy .....	218
<b>Figure A1.3:</b> Anisotropy of the Hard X-ray emission .....	219
<b><u>Appendix 2:</u></b>	
<b>Figure A2.1:</b> The Pulse Height Analysis Code running in plot mode 4 .....	224
<b>Figure A2.2:</b> Raw hard x-ray signal during the plasma.....	225
<b>Figure A2.3:</b> The Pulse Height Analysis (PHA) Program flow chart .....	226
<b>Figure A2.4:</b> Raw hard x-ray single pulse with Gaussian shape .....	228
<b>Figure A2.5:</b> Hard x-ray signal and noise level.....	228
<b>Figure A2.6:</b> Fitting the individual pulses to a single Gaussian .....	229
<b>Figure A2.7:</b> Hard X-ray histogram and spectrum. ....	229

<b>Figure A2.8:</b> Curve fitting to calculate the electron temperature. ....	230
---	-----

### **Appendix 3:**

<b>Figure A3.1:</b> Maxwell Integral $\psi$ and related functions. ....	270
<b>Figure A3.2:</b> Electron-electron collision frequencies .....	272
<b>Figure A3.3:</b> Electron-electron collision times.....	273
<b>Figure A3.4:</b> Electron-ion collision frequencies.....	273
<b>Figure A3.5:</b> Electron-ion collision times.....	274
<b>Figure A3.6:</b> Electron-electron, $\nu_s^{e/e}$ . ....	274
<b>Figure A3.7:</b> Electron-ion, $\nu_s^{e/i}$ . ....	275
<b>Figure A3.8:</b> $\sigma^{e/n}$ ionization cross section energy variation. ....	276
<b>Figure A3.9:</b> Electron-neutral, $\nu^{e/n}$ , collision frequency energy variation .....	277
<b>Figure A3.10:</b> Electron-neutral, $\tau^{e/n}$ , collision time energy variation .....	277
<b>Figure A3.11:</b> Comparison between various collision processes .....	278

### **Appendix 4:**

<b>Figure A4.1:</b> Electron orbit in lab coordinates following magnetic-axis .....	283
<b>Figure A4.2:</b> Magnetic field followed by the electron on-axis.....	284
<b>Figure A4.3:</b> Electron total energy time evolution through the resonance zone .....	284

### **Appendix 5:**

<b>Figure A5.1:</b> r- $\theta$ plot of electron drift orbit for $\varepsilon = 5$ keV, $r/a = 0.5$ .....	298
<b>Figure A5.2:</b> r- $\phi$ plot of electron drift orbit for $\varepsilon = 5$ keV, $r/a = 0.5$ .....	298
<b>Figure A5.3:</b> r- $\theta$ plot of electron drift orbit for $\varepsilon = 100$ eV, $r/a = 0.05$ .....	299

<b>Figure A5.4:</b> The time evolution for the magnetic moment .....	299
--	-----

## **Appendix 6**

<b>Figure A6.1:</b> The variation of QHS spectral components with minor radius .....	315
<b>Figure A6.2:</b> The variation of Mirror spectral components with minor radius .....	316
<b>Figure A6.3:</b> Variation of $ B $ along field line, $r/a = 0$ .....	318
<b>Figure A6.4:</b> Variation of $ B $ along field line, $r/a = 0.05$ .....	318
<b>Figure A6.5:</b> Variation of $ B $ along field line, $r/a = -0.05$ .....	319
<b>Figure A6.6:</b> Variation of $ B $ along field line, $r/a = 0.1$ .....	319
<b>Figure A6.7:</b> Variation of $ B $ along field line, $r/a = -0.1$ .....	320
<b>Figure A6.8:</b> Variation of $ B $ along field line, $r/a = 0.2$ .....	320
<b>Figure A6.9:</b> Variation of $ B $ along field line, $r/a = -0.2$ .....	321
<b>Figure A6.10:</b> Variation of $ B $ along field line, $r/a = 0.3$ .....	321
<b>Figure A6.11:</b> Variation of $ B $ along field line, $r/a = -0.3$ .....	322
<b>Figure A6.12:</b> Variation of $ B $ along field line, $r/a = 0.4$ .....	322
<b>Figure A6.13:</b> Variation of $ B $ along field line, $r/a = -0.4$ .....	323
<b>Figure A6.14:</b> Variation of $ B $ along field line, $r/a = 0.5$ .....	323
<b>Figure A6.15:</b> Variation of $ B $ along field line, $r/a = -0.5$ .....	324
<b>Figure A6.16:</b> Variation of $ B $ along field line, $r/a = 0.6$ .....	324
<b>Figure A6.17:</b> Variation of $ B $ along field line, $r/a = -0.6$ .....	325
<b>Figure A6.18:</b> Variation of $ B $ along field line, $r/a = 0.7$ .....	325
<b>Figure A6.19:</b> Variation of $ B $ along field line, $r/a = -0.7$ .....	326
<b>Figure A6.20:</b> Variation of $ B $ along field line, $r/a = 0.8$ .....	326

<b>Figure A6.21:</b> Variation of $ B $ along field line, $r/a = -0.8$ .....	327
<b>Figure A6.22:</b> Variation of $ B $ along field line, $r/a = 0.9$ .....	327
<b>Figure A6.23:</b> Variation of $ B $ along field line, $r/a = -0.9$ .....	328
<b>Figure A6.24:</b> Variation of $ B $ along field line, $r/a = 1.0$ .....	328
<b>Figure A6.25:</b> Variation of $ B $ along field line, $r/a = -1.0$ .....	329

# Chapter 1

## Introduction

### 1.0: Introduction

This thesis research is focused on studying superthermal electron dynamics, i.e. their production mechanisms and confinement in different magnetic configurations in the Helically Symmetric eXperiment (HSX) stellarator, through studying their hard x-ray emission.

Section 1.1 describes the motivation behind this work. Section 1.2 provides technical details about HSX. A literature survey of the dynamics of superthermal electrons in fusion plasmas is given in Section 1.3, and an outline of the thesis is given in Section 1.4.

### 1.1: Motivation

Tokamaks and stellarators play a major role in the development of fusion plasma physics, and they both are potential candidates as future fusion power plants. Stellarators avoid some of the fundamental problems of tokamak power plants: current drive, disruptions and positional stability. They have attractive features such as inherently steady-state, disruption free operation, and low recirculating power. Because of this, stellarators are a large part of the world fusion program with large experimental investment and substantial performance<sup>1</sup>. However, stellarators have other features that

can limit there chance of being a future power plant: complicated coil systems, and having bad particle orbits at very low collisionality.

Collisionless  $\alpha$ -particle confinement is an important aspect of toroidal magnetic fusion confinement systems<sup>2</sup>. In this respect, stellarators behave quite differently from tokamaks. While tokamaks completely confine collisionless orbits, stellarators generally suffer from collisionless  $\alpha$  particle loss. Trapped  $\alpha$ -particles are lost in a time orders of magnitude smaller than the slowing down time (typical  $\alpha$  particle slowing down time for present day fusion devices  $\sim 0.1$  sec). One solution to overcome this problem is given by quasi-helically symmetric stellarators<sup>3</sup>, in which the helical symmetry of  $\vec{B}$  leads to complete confinement of collisionless particles.

The HSX experiment is a novel machine with quasi-helical symmetry in mod  $\vec{B}$ , which promises improved single particle confinement<sup>4</sup>. Superthermal electrons are produced in HSX during ramp-up of the modular coil current, and during the 2<sup>nd</sup> harmonic X-mode, Electron Cyclotron Resonance Heating (ECRH) discharges. The motivation of this work is to look at the characteristics of superthermal electrons through study of their hard x-ray emission to better understand how quasi-symmetry improves confinement in HSX.

## 1.2: The HSX Stellarator

The HSX stellarator<sup>5</sup>, shown in Figure 1.1, is the first operating stellarator based upon the principles of quasi-symmetry; this symmetry ensures good confinement of trapped particles in the long mean free path (LMFP) regime.

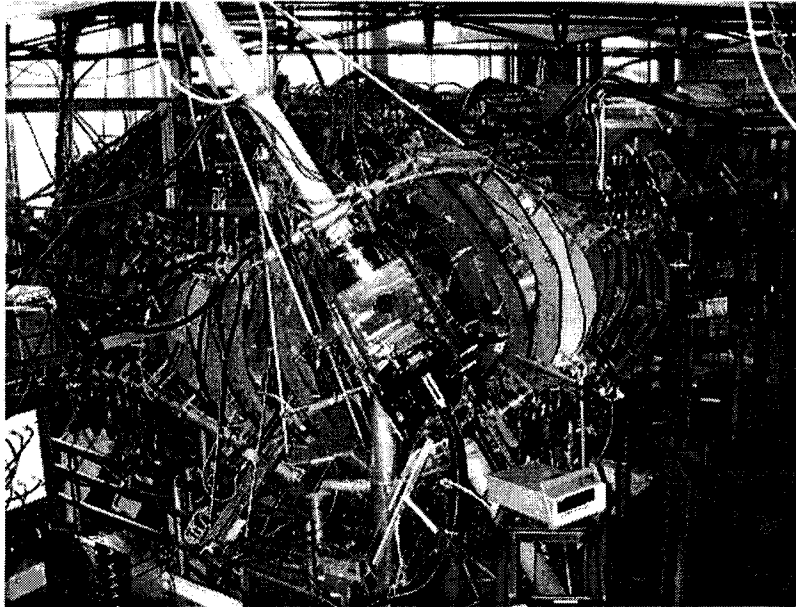


**Figure 1.1: General view of the HSX device.**

A quasi-helically symmetric (QHS) stellarator is a toroidal magnetic confinement system that, to a good approximation, has no toroidal curvature and a helical direction of symmetry in  $|\vec{B}|$ . By restoring a direction of symmetry to a toroidal stellarator, the quasi-helical stellarator solves one of the fundamental disadvantages of conventional stellarators; poor neoclassical transport in the low collisionality or long mean free path regime. This poor transport arises due to the combination of toroidal and helical modulation of the magnitude of  $\vec{B}$  along a field line. The asymmetry in the magnetic ripple results in a large deviation of a trapped particle orbit from a magnetic surface. Poor neoclassical transport of conventional stellarators in the low collisionality regime can limit their performance as fusion reactors.

Deviations of trapped particle orbits from magnetic surfaces are determined by the variation of the magnitude of  $\vec{B}$  along a field line. Quasi-helically symmetric

stellarators can actually have lower neoclassical transport than an equivalent tokamak. The fundamental transport properties of the QHS configuration compared to tokamak can be understood by examining the magnetic field spectrum. The magnetic field magnitude along a line of force in an ideal conventional stellarator can be written as:

$$B = B_o [1 - \varepsilon_t \cos \vartheta - \varepsilon_h \cos (N\varphi - m\vartheta)] \quad (1.1)$$

Where  $\theta$  and  $\varphi$ : are the poloidal and toroidal angles respectively,  $\varepsilon_t$  and  $\varepsilon_h$  : are the magnitudes of field modulation due to toroidicity, and the helical spectral component respectively, and  $m$  and  $N$ : are the poloidal and toroidal mode numbers. In a straight-field-line-coordinate system, such as Boozer or Hamada coordinates<sup>6</sup>, the equation for a magnetic field line is determined by the rotational transform  $\iota$ :

$$\vartheta = \iota\varphi \quad (1.2)$$

The magnetic field strength along a field line for a conventional stellarator can then be written solely in terms of the toroidal angle as:

$$B = B_o [1 - \varepsilon_t \cos \iota\varphi - \varepsilon_h \cos (N - m\iota)\varphi] \quad (1.3)$$

For a stellarator there are  $\iota$  periods in the variation of the magnitude of  $\bar{B}$  along a magnetic field line due to toroidal curvature in one toroidal transit. There is an additional modulation resulting from the helical ripple. For the helical ripple, however, there are  $|N - m\iota|$  periods for one toroidal transit of the magnetic field line.

In a quasi-helically symmetric stellarator, the toroidal curvature component of the spectrum (but not the actual inverse aspect ratio itself) has been designed to be negligible. The variation of the magnetic field along a field line can then be given approximately by:

$$B = B_o [1 - \varepsilon_h \cos(N - m\iota)\varphi] \quad (1.4)$$

This expression is analogous to that of tokamak, except that  $\varepsilon_t$  has been replaced by  $\varepsilon_h$  and  $\iota$  is replaced by  $|N - m\iota|$ , the effective transform. The effective transform is larger than a comparable tokamak by the factor  $|N - m\iota| \sim 3$  in HSX compared to the actual transform  $\iota \sim 1$ . Consequently, the displacement of the drift surfaces for passing particles is smaller for quasihelical stellarator than for tokamak. Similarly, the widths of banana orbits are smaller, neoclassical transport is less than in a comparable tokamak. The magnitude of the bootstrap and Pfirsch-Schluter currents are smaller in the quasihelical stellarator than a comparable tokamak by the same factor  $|N - m\iota|$ . The magnetic field spectrum for HSX based on a representation of the finite-size coil model that includes the turn-to-turn transition, the pancake-to-pancake cross-over and the coil feeds, specified in straight-line Boozer coordinate is given by:

$$B = B_o \sum_{n,m} b_{n,m} \cos(n\varphi - m\vartheta), \quad (1.5)$$

where  $b_{mn}$  is the magnitude of the spectral components, and  $[n, m]$  are the toroidal and poloidal mode numbers respectively. The variation of the magnitude of  $\bar{B}$  along a field line at an effective plasma radius of 0.5 is shown in Figure 1.2. An example of drift orbit for an energetic (50 keV) electron with pitch angle,  $\alpha = 85^\circ$  in the QHS magnetic configuration as calculated using a guiding center drift code (will be describe in Chapter 6) is also shown in Figure 1.2. The electron starts from the outside of the torus ( $\vartheta = 0^\circ$ ,  $\varphi = 0^\circ$ ,  $r/a = 0.5$ ) in the low field side at the bottom of the magnetic well in front of the

microwave antenna. Because of the symmetry in the magnetic field ripples in the QHS configuration, the particle drift off the home flux surface is minimal and the electron is well confined as shown in the figure.

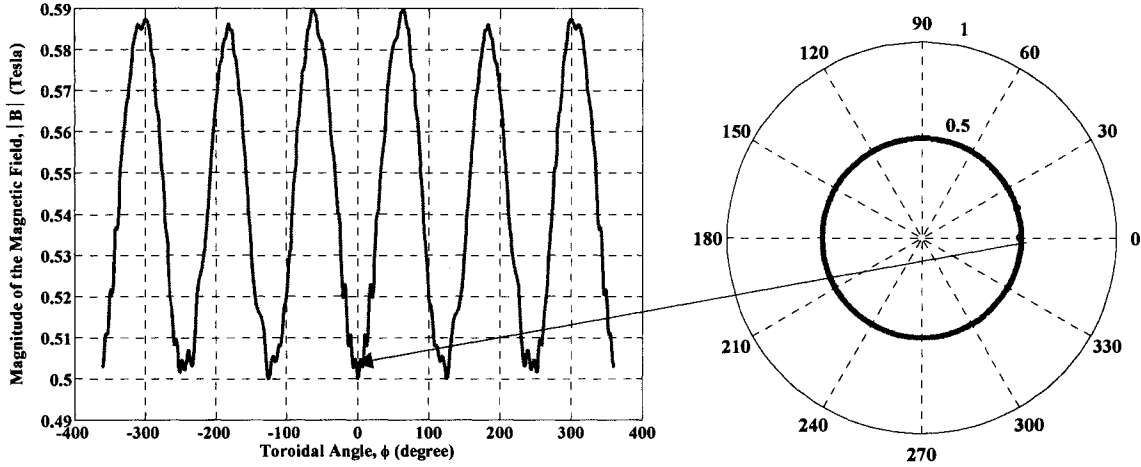


**Figure 1.2: Variation of the magnitude of  $\bar{B}$  along a field line for the QHS configuration at  $r/a = 0.5$  (left). Example of orbits in  $r$ - $\theta$  coordinates for 50 keV electrons in the QHS configuration for ( $\theta = 0^\circ$ ,  $\phi = 0^\circ$ ,  $r/a = 0.5$ ) and pitch angle =  $85^\circ$  (right).**

The radial variation of  $b_{mn}$  for the QHS configuration in HSX is shown in Figure 1.3. The respective flux surfaces are shown in Figure 1.4. The ( $n=0$ ,  $m=0$ ) mode (the average value of the field on surface) is not shown in Figure 1.3, as its inclusion would have necessitated too large a vertical axis; excluding this mode is unimportant, as it does not contribute to neoclassical transport (D.C. component of the field). The ( $n=4$ ,  $m=1$ ) mode is the largest mode for QHS mode. The right hand frame of Figure 1.3 illustrates the magnitude of the nine largest symmetry breaking components. The principle symmetry breaking terms are the (4,2) and (48,0) modes, the (48,0) term represents the ripple due to the finite number of coils in HSX.

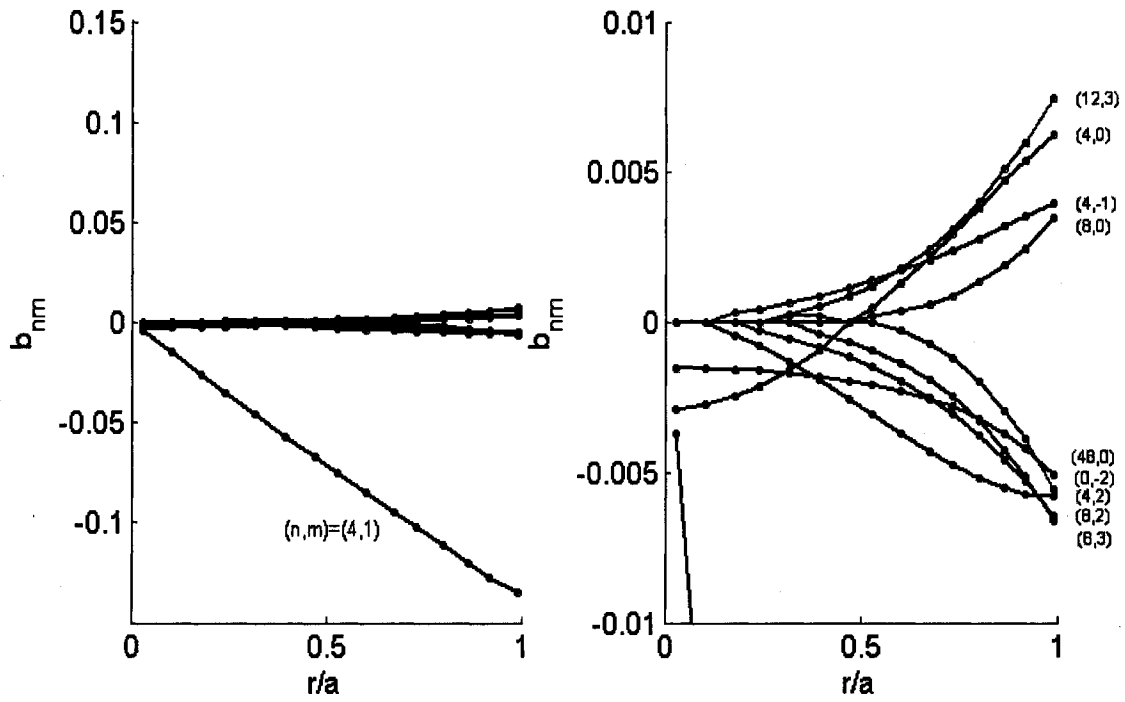


**Figure 1.3: Radial variation of  $b_{nm}$  for QHS configuration (left), and the details of the small symmetry breaking components present in the spectrum (right). Note the different scales. Figure courtesy of S. Gerhardt.**

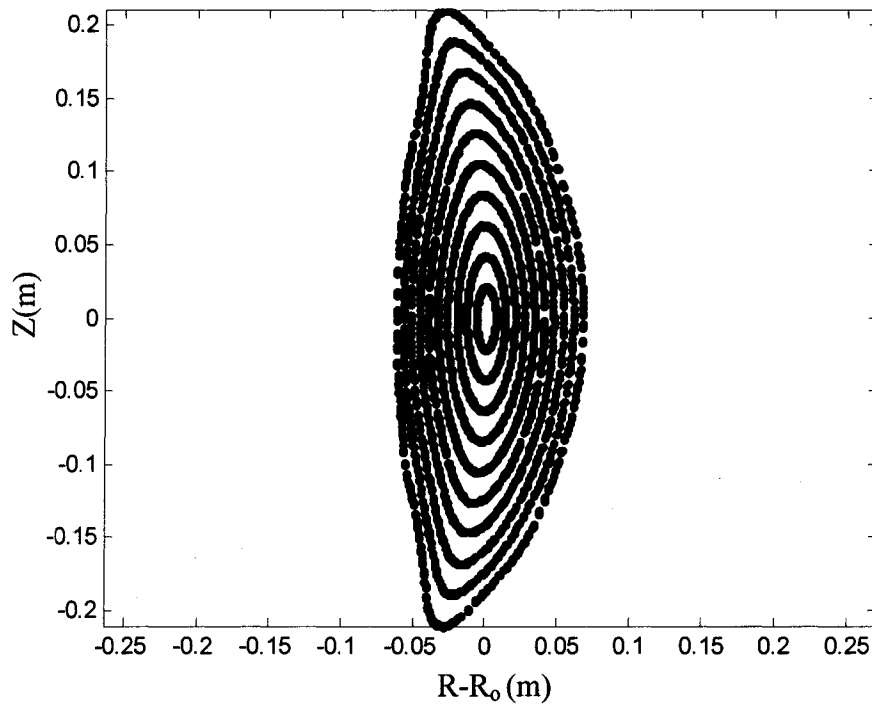


**Figure 1.4: Flux surfaces for the QHS configuration. Figure courtesy of S. Gerhardt**

Some of the terms (12,3) and (8,2) have the same helicity as the main (4,1) spectral component. All of these symmetry-breaking terms are beneath the 1% level at the edge.

The leading terms of the magnetic field spectrum for the HSX Experiment at low magnetic field have been determined experimentally by analyzing the orbits of passing particles<sup>7</sup>. The images produced by the intersection of electron orbits with a fluorescent mesh are recorded with a charge coupled device and transformed into magnetic coordinates using a neural network. To obtain the spectral components, the transformed orbits are then fit to an analytic expression that models the drift orbits of the electrons. The results confirm for the first time that quasihelical stellarators have a large effective transform that results in small excursions of particles from a magnetic surface. The drift orbits are also consistent with a very small toroidal curvature component in the spectrum.

The main parameters of HSX stellarator are given in Table 1.1.

Property	Value
Major Radius	1.2 m
Average Plasma Minor Radius	0.12 m
Plasma Volume	$\sim 0.37 \text{ m}^3$
Number of field periods	4
Number of Modular Coils/Field Period	12
Number of Auxiliary Coils/Field Period	12
Rotational Transform: Axis	1.05
Edge	1.12
Coil Current (at 1 Tesla)	10.7 kA
Magnetic field strength	Currently 0.5 T, Max 1.25 T
Magnetic Pulse Length (Flat Top)	$\leq 0.2 \text{ sec}$
ECR Heating Max Power (Source)	200 kW
ECR Pulse Length	Up to 50 msec
Density (cut-off) at fundamental	$1 \times 10^{13} \text{ cm}^{-3}$

**Table 1.1: The HSX machine parameters.**

### 1.2.1: Variation of the Magnetic field structure in HSX

In addition to the coils that produce the quasi-helical magnetic field, HSX has a set of auxiliary coils that allow the magnetic field topology to be altered. There are 48 auxiliary coils, 12 per field period, mounted on the main modular coil support rings.

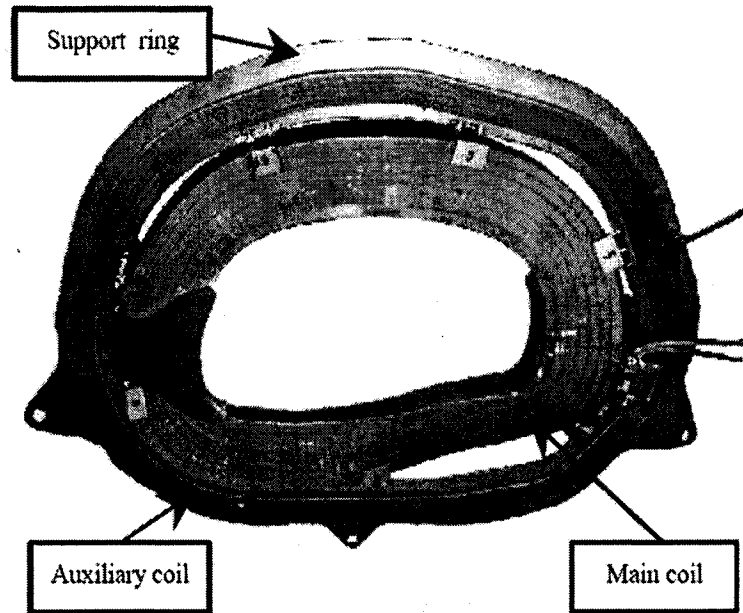


**Figure 1.5: HSX main and auxiliary coils mounted on the support ring.**

A picture of one of the main modular coils and an auxiliary coil mounted on the coil supporting ring is shown in Figure 1.5. Each of the auxiliary coils is planar, although non-circular. Figure 1.6 shows three possible modifications to the HSX quasi-helical configuration that can be formed with the auxiliary coils. The plus and minuses at the top of the figure indicate the direction of the current for each particular auxiliary coil with respect to the modular coils. The magnitude of the current is the same for all coils in the auxiliary set. General properties of the three configurations are summarized in Table 1.2<sup>8</sup>. The magnitude of the Mirror term can be varied by adjusting the ratio of the current in

the auxiliary set to the main modular coil current. The standard Mirror configuration has 10% of the total ampere-turns of the main coil set.

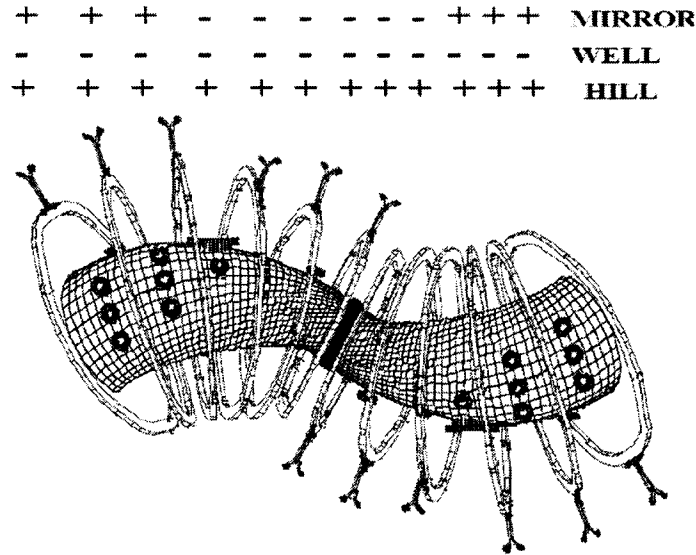


**Figure 1.6: Direction of current in auxiliary coils with respect to modular coils for one field period (plus (+) is current in the same direction as modular coils; minus (-) indicates the opposite direction.**

Configuration	Auxiliary Coil	Dominant Feature
<b>QHS</b>	None	Best transport
<b>Mirror</b>	3 coils on the end add to main; center 6 opposite	Transport similar to conventional stellarator
<b>Anti-Mirror</b>	Opposite phasing to Mirror	Deep ripple on low-field side at ECH launcher
<b>Well</b>	All currents opposite to main coil currents	Well depth, $\iota$ , and stability increase
<b>Hill</b>	Opposite to Well mode	Opposite to Well mode

**Table 1.2: Properties of the various HSX magnetic configurations.**

The radial variation of  $b_{mn}$  for the QHS, Mirror and AntiMirror configurations in HSX are shown in Figure 1.7. The flux surfaces for the 3 configurations are shown in Figure 1.8.

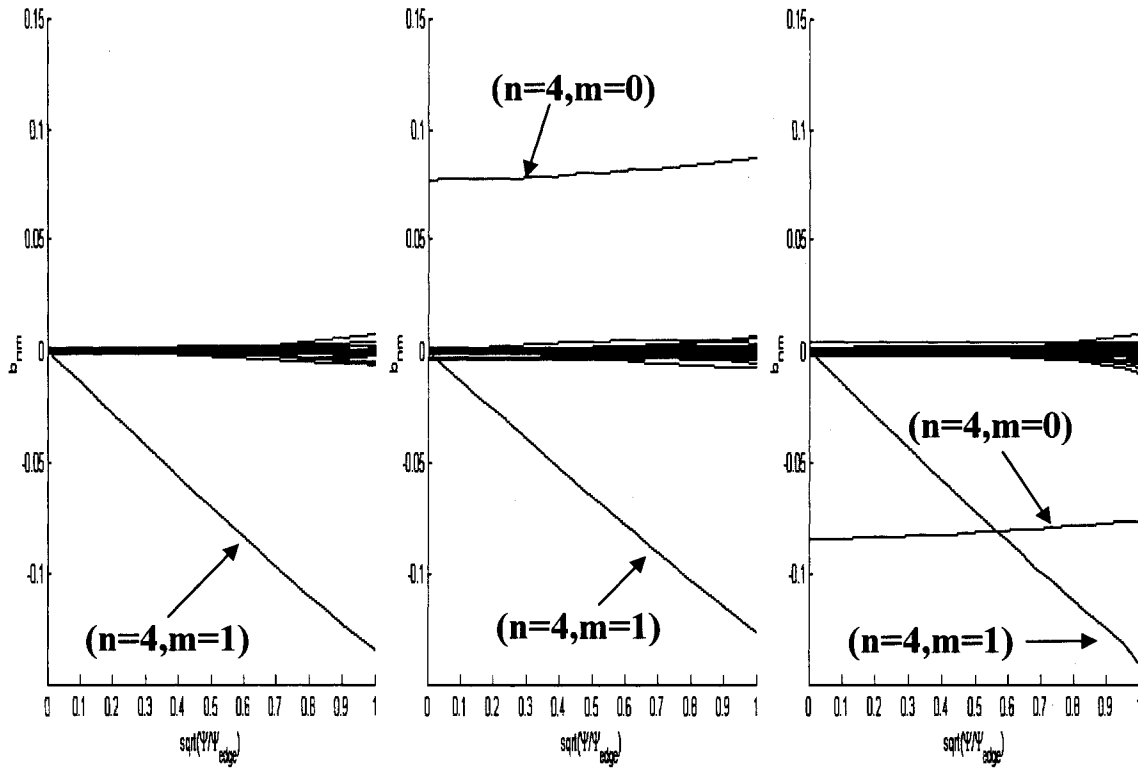


**Figure 1.7: Radial variation of  $b_{nm}$  for QHS, Mirror and AntiMirror configurations.**  
Figure courtesy of S. Gerhardt

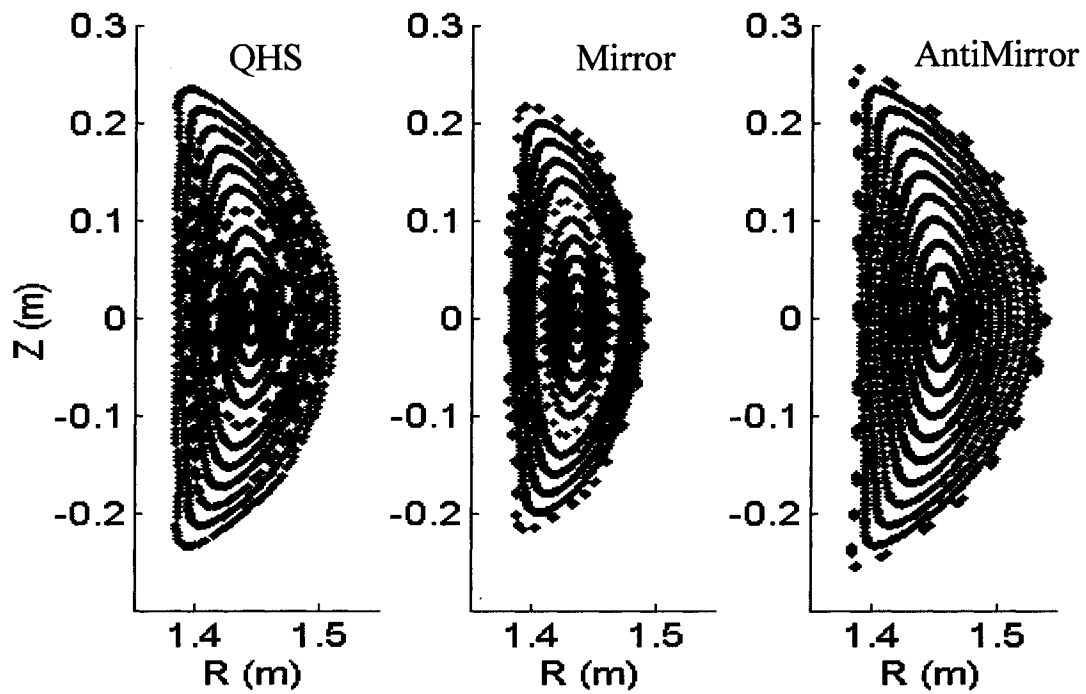


**Figure 1.8: Flux surfaces for the QHS, Mirror and AntiMirror configuration.**

It is seen that the main spectral difference between the QHS and the Mirror configuration is the large  $n=4$ ,  $m=0$  toroidal mirror term which goes all the way to the magnetic axis. In the Mirror configuration the largest helical  $(4,1)$  mode is augmented by an equally large toroidal mirror mode. As with the QHS case, all other modes are less than 1% level, including the small amount of toroidal curvature introduced by the planar auxiliary coils. The variation of the magnitude of  $\bar{B}$  along a field line at an effective plasma radius of 0.5 for the Mirror and AntiMirror configurations are shown in Figures 1.9 and 1.10. Examples of drift orbits for energetic (50 keV) electrons with pitch angles  $\alpha = 85^\circ$  in the Mirror and AntiMirror magnetic configurations are also shown in Figures 1.9 and 1.10.

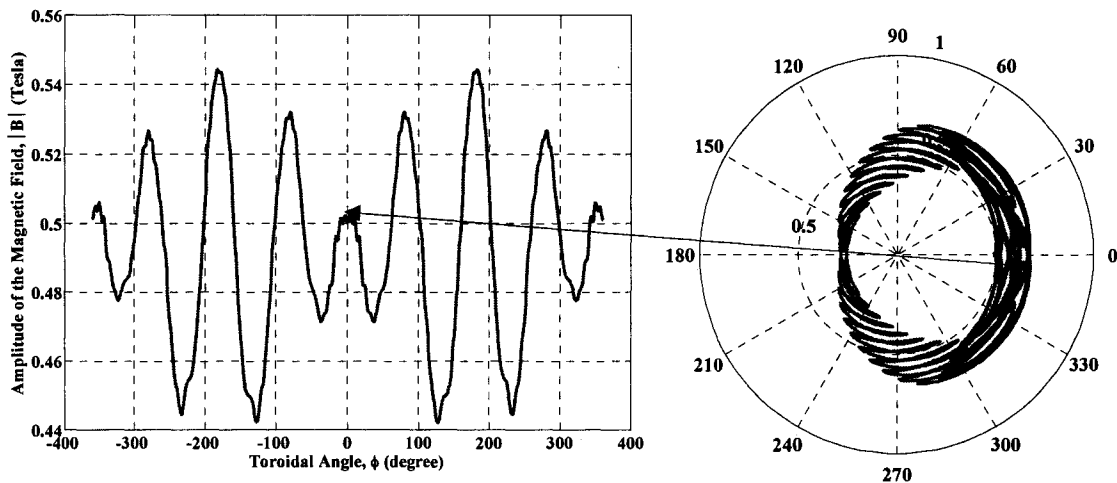


**Figure 1.9: Variation of the magnitude of  $\bar{B}$  along a field line for the Mirror configuration at  $r/a = 0.5$  (left). Example of orbits in  $r$ - $\theta$  coordinates for 50 keV electrons in the Mirror configuration for ( $\theta = 0^\circ$ ,  $\phi = 0^\circ$ ,  $r/a = 0.5$ ) and pitch angle =  $85^\circ$  (right).**

In the Mirror case shown in Figure 1.9, the electron starts from the outside of the torus ( $\theta = 0^\circ$ ,  $\phi = 0^\circ$ ,  $r/a = 0.5$ ) in the low field side at the local minimum of the magnetic field in front of the microwave antenna. Because of the asymmetry in the magnetic field ripples in the Mirror configuration, the particle drift off the home flux surface is large

compared to the QHS configuration, but the electron is still confined in the plasma region as shown in the figure. The situation is completely different in the AntiMirror configuration where electrons launched at the low field side ( $\vartheta = 0^\circ$ ,  $\phi = 0^\circ$ ,  $r/a = 0.5$ ) in the outboard of the machine are on direct loss orbits, and leave the machine quickly as shown in Figure 1.10.

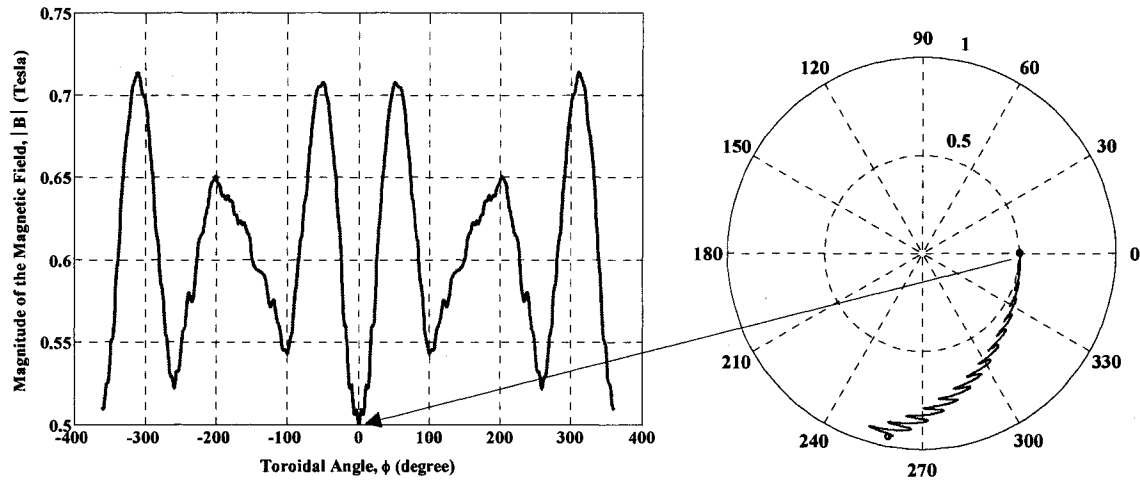


**Figure 1.10: Variation of the magnitude of  $\bar{B}$  along a field line for the AntiMirror configuration at  $r/a = 0.5$  (left). Example of orbits in  $r$ - $\vartheta$  coordinates for 50 keV electrons in the AntiMirror configuration for ( $\vartheta = 0^\circ$ ,  $\phi = 0^\circ$ ,  $r/a = 0.5$ ) and pitch angle =  $85^\circ$  (right).**

Figure 1.11 shows the rotational transform profile for the QHS and Mirror configuration. Note that the Mirror configuration has a slightly larger transform and slightly reduced volume. The major difference in neoclassical transport between the two modes is determined by the large transport degradation introduced by the inclusion of the Mirror term. The small difference in transform has only a minor effect on the transport coefficients. Because of anomalous transport, no large differences are expected between QHS and Mirror under present operating conditions<sup>9</sup>. It is expected that collisionless high

energy electrons are not affected by turbulent transport as bulk electrons are, and their confinement will be governed solely by the magnetic field topology.

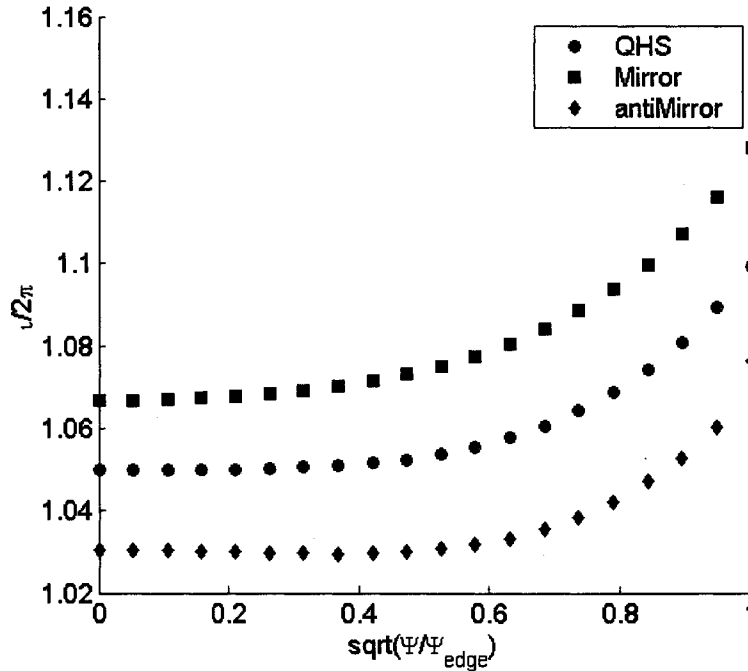


**Figure 1.11: Rotational transform variation with  $r$  for QHS, Mirror and AntiMirror modes. Figure courtesy of S. Gerhardt.**

### 1.2.2: Plasma Production and Heating in HSX

Plasma for this work is produced and heated in HSX using 2<sup>nd</sup> harmonic, X-mode electron cyclotron resonance heating. The ECRH source consists of a 200 kW gyrotron operating at a frequency of 28 GHz, with a maximum pulse length of 50 msec. A system of waveguides and mode converters is used to transport the microwave radiation from the gyrotron to the machine<sup>10</sup>. The microwave radiation penetrates the machine through a quartz window, and the power is reflected off of an ellipsoidal focusing mirror into the plasma from the low field side of the machine. A set of microwave diodes spaced toroidally around the machine is used to measure the microwave absorbed power<sup>11</sup>

through attenuation measurements coupled with ray tracing calculations. The microwave beam is focused on the magnetic axis for central power deposition and has a spot size of  $\sim 4$  cm.

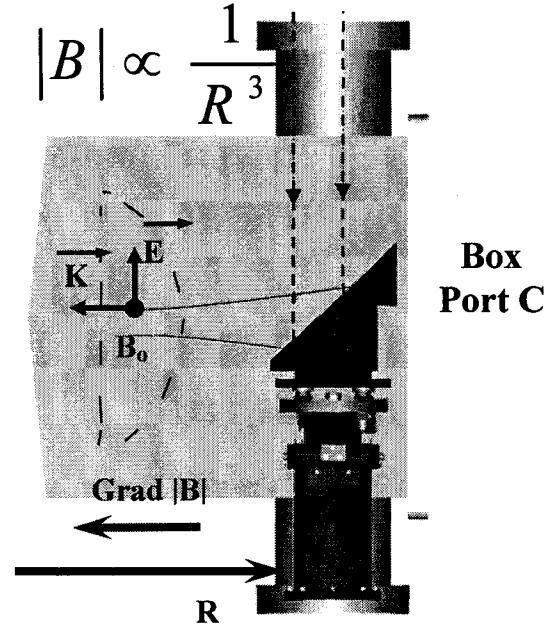
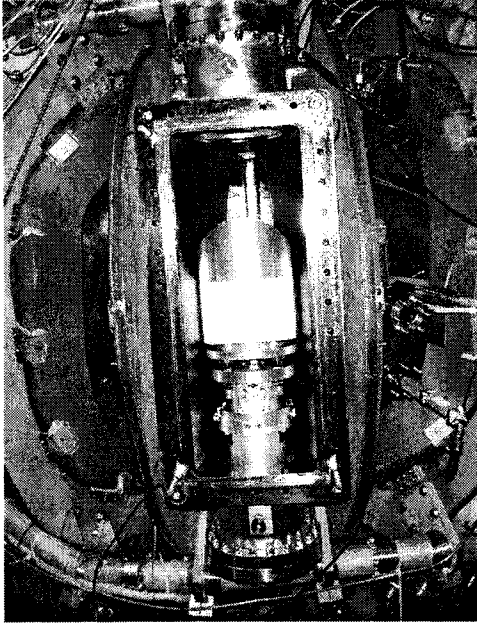


**Figure 1.12: Vertical view of Box Port C showing the microwave launching system.**  
Figure courtesy of K. Likin.

Figure 1.12 shows a schematic of the microwave launching system at box port C. Typical HSX plasma parameters are illustrated in Table 1.3.

Property	Value
B	0.5 T
$n_e$	$1 \times 10^{18} \text{ m}^{-3}$
$T_e, T_i$	200 eV, 20 eV
$\omega_{ce}, \omega_{ci}$	14 GHz, 7.6 MHz
$\omega_{pe}, \omega_{pi}$	9 GHz, 210 MHz
$v_{te}, v_{ti}$	$6 \times 10^6 \text{ m/s}$ , $4.4 \times 10^4 \text{ m/s}$
$r_{Le}, r_{Li}$	$7 \times 10^{-5} \text{ m}$ , $1 \times 10^{-3} \text{ m}$

**Table 1.3: Parameters of the HSX plasma.**

The parameters are typical of discharges with line average density  $\bar{n}_e \sim 1 \times 10^{12} \text{ cm}^{-3}$  at a location  $r/a \sim 0.6$ .

### 1.2.3: HSX Diagnostics

Figure 1.13 illustrates the HSX diagnostic approximate layout, the modular coils and the box ports.

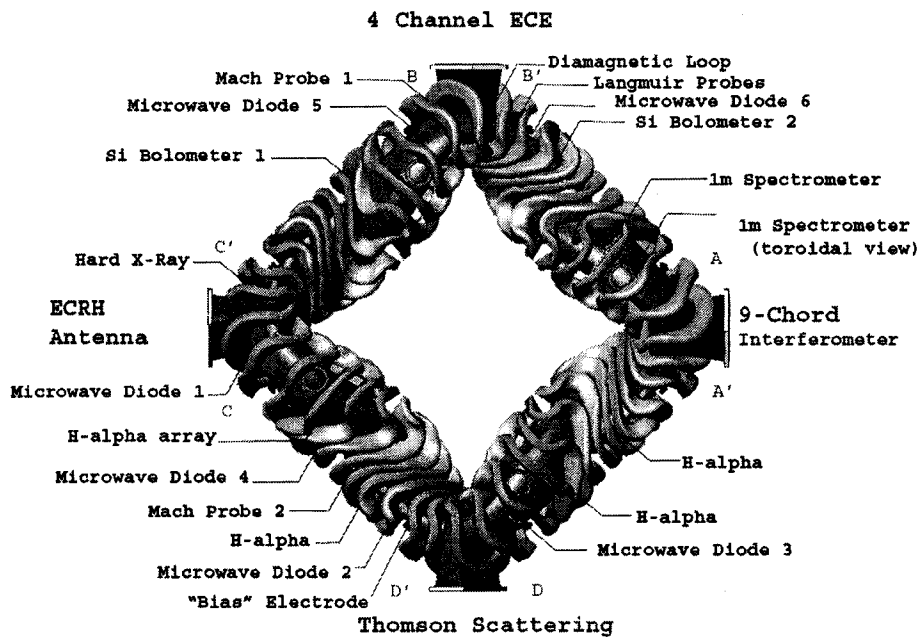


**Figure 1.13: HSX diagnostics approximate layout. Figure courtesy of J. Radder and K. Likin.**

The diagnostic systems include a 9 chord 280 GHz microwave interferometer for measuring the plasma line-averaged electron density and density fluctuations<sup>12</sup> operated in collaboration with UCLA, a diamagnetic loop for measuring plasma stored energy, a 10 channel Thomson scattering system for measuring both electron density and temperature<sup>13</sup>, a soft x-ray (SXR) triplet for measuring central electron temperature, a 5-channel SXR, and single chord hard x-ray (HXR) pulse height analysis (PHA) systems to

study the superthermal electrons in different magnetic configurations. A set of  $H_\alpha$  monitors is used to infer neutral density. A set of microwave diodes to is used to measure microwave absorbed power, multi-channel Electron Cyclotron Emission ECE radiometer to measure electron temperature, magnetic probes for measuring magnetic fluctuations, a set of electrostatic probes for studying edge plasma turbulence, fast spectrometer system for monitoring plasma impurity level, and a UV-enhanced photo-diode for measuring plasma radiated power, and a toroidal flux loop for measuring plasma loop voltage during field ramping. More details of the hard x-ray diagnostic will be presented in Chapter 2.

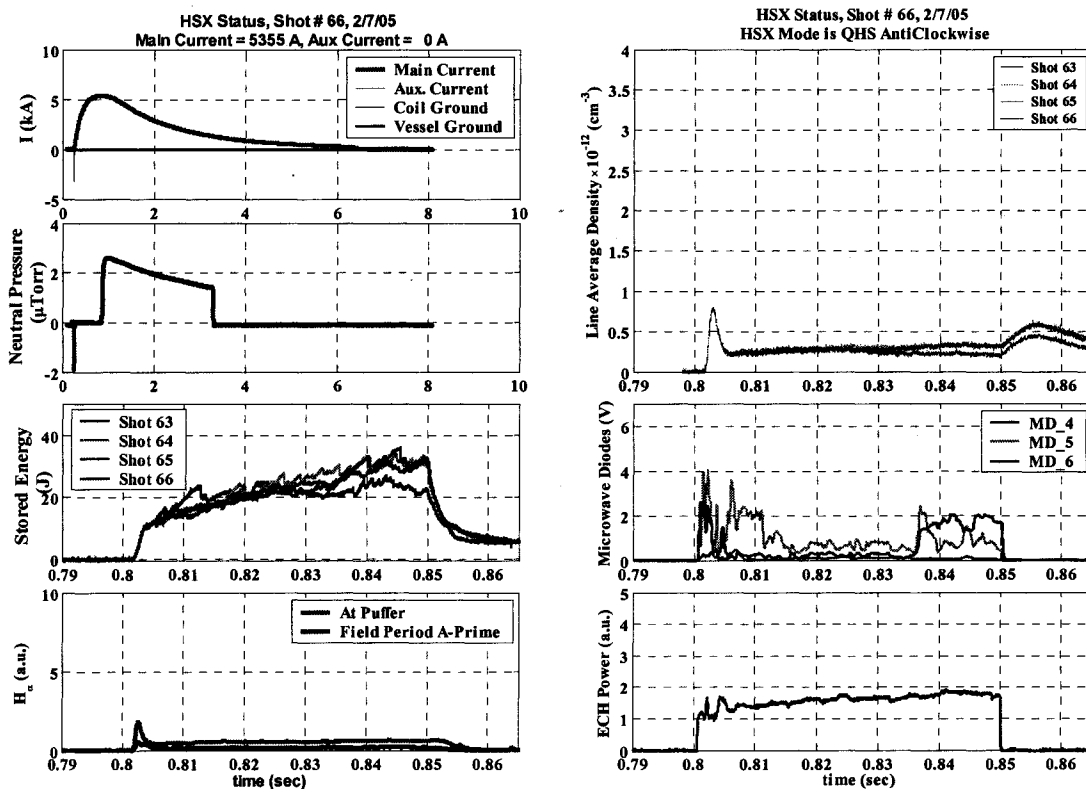


**Figure 1.14: HSX status plot shows common operational diagnostic signals during the discharge.**

Common operational diagnostic signals during a plasma discharge are shown in Figure 1.14. The main and auxiliary coil currents, the neutral pressure, the stored energy

and the  $H_\alpha$  signals are shown from top to bottom in the left hand frame, while the line-average plasma density, non-absorbed power measured by a set of microwave diodes, and the electron cyclotron input power signals are shown from top to bottom in the right hand frame.

### 1.3: Superthermal Electrons in Fusion Plasmas

Electron cyclotron resonance heating is a well established and widely used technique for plasma production and heating in toroidal fusion devices<sup>14,15,16</sup>. During Electron Cyclotron Resonance (ECR) discharges electrons are heated by electron cyclotron resonance in the resonance zone. In this zone the frequency of the microwave driving the discharge is an integral multiple of the local electron cyclotron frequency<sup>17</sup>. In order to achieve currentless operation in stellarators, ECRH is often used to produce and heat the plasma because of its capability of starting up the plasma from a neutral gas state<sup>18</sup>. ECRH has been applied successfully in stellarator/heliotron devices to produce and heat currentless plasmas<sup>19,20,21,22,23,24</sup>.

A characteristic feature of ECRH across a wide range of magnetic configurations is the generation of a superthermal electron tail with high perpendicular velocities, especially at low density and high microwave power<sup>25,26</sup>. Superthermal electrons can also be generated during magnetic field ramping in stellarators and heliotrons through the process of runaway formation in electric fields, as will be discussed in Chapter 3. The superthermal electron tail emits a continuum bremsstrahlung radiation due to collisions between the tail electrons and the bulk electrons and ions (the electron-ion

bremsstrahlung is dominant<sup>27</sup>, electron-electron bremsstrahlung can be neglected at electron energies below 1 MeV<sup>28</sup>). Important information about the superthermal electron dynamics and the physical mechanism of their production can be obtained from studying their hard x-ray emission.

A review of the previous experimental and theoretical work obtained so far on diagnosing and studying the dynamics of superthermal electrons will be presented. In Section 1.3.1, a brief listing of previous superthermal electron studies and experimental hard x-ray measurements in non-helical devices is given. Section 1.3.2 lists the previous results for helical devices. Theoretical work regarding single particle ECRH theory is presented in Section 1.3.3.

### **1.3.1: Superthermal Electrons in Non-Helical Devices**

In a number of experiments in magnetic fusion, a tail of superthermal electrons plays an essential role, such as the formation of electron rings in mirror machines, formation of thermal barriers, suppressing MHD instabilities, carrying plasma currents in lower hybrid, and ECR current drives, etc. Plasma hard x-ray emission has been used to diagnose these electrons and to study their characteristics and dynamics. The first investigations were performed on magnetic mirrors, where electron cyclotron resonance heating produced hot electron rings. Dandi<sup>29,30</sup>, Shohet<sup>31</sup>, England and Haste<sup>32</sup> have pioneered the x-ray diagnosis of these rings. Ikegami et al.<sup>33</sup> found an increase of the x-ray emission when the second and third harmonics of the electron cyclotron frequency on axis of a magnetic mirror matches the microwave frequency. In tandem mirror

experiments<sup>34,35</sup>, superthermal electrons are necessary to form a thermal barrier. In toroidal devices, superthermal electrons are created at low densities through electron runaway in toroidal loop voltages, and plasma bremsstrahlung has been used to study runaway rates<sup>36</sup>. In current drive experiments<sup>37,38,39,40,41</sup>, superthermal electrons are formed by Landau damping of the lower hybrid waves.

### **1.3.2: Superthermal Electrons in Helical Devices**

Among several methods of superthermal electron production in helical devices, we are interested in two of them, as they are similar to our current research: superthermal electrons produced during (1) magnetic field ramping and (2) 2<sup>nd</sup> harmonic X-mode ECRH discharges. The current section is divided into two subsections. A survey of the work done in two helical devices, the ATF and TJ-II torsatrons, for suppressing superthermal electrons generated during magnetic field ramping is given in Section 1.3.2.1. The effect of magnetic ripples on superthermal electron confinement and their hard x-ray emission during ECRH in helical devices is given in Section 1.3.2.2.

#### **1.3.2.1 Suppression of Electron Runaways during Magnetic Field Ramping**

Runaway electron formation and confinement occur frequently in pulsed heliotrons, torsatrons, and stellarators because of the high loop voltages generated during magnetic field ramping and the confinement of electrons on the vacuum flux surfaces of those machines<sup>42,43</sup>. Runaway electrons constitute a serious concern as the final runaway energy can become sufficiently large to cause serious damage to the confining structures. Besides the structural damage, when runaway electrons hit the material walls they generate high doses of x-rays that are harmful to occupational personnel working near the

devices. Furthermore, if runaway electrons are not suppressed, they will be present during the flat top region of the magnetic field where the ECRH discharge takes place and affect the plasma generation and characteristics due to the high microwave absorption efficiency of superthermal electrons. Measurements of hard x-rays from the Advanced Toroidal Facility (ATF) torsatron<sup>44</sup> ( $l=2$ ,  $m=12$ ,  $R=2.1\text{m}$ ,  $\langle a \rangle=0.27\text{m}$ ,  $B_{\text{max}}=2\text{T}$ ,  $t_{\text{axis}} \approx 0.3$ ,  $t_{\text{edge}} \approx 0.1$ ,  $P_{\text{ECRH}}=200\text{ kW}$ ,  $53.2\text{ GHz}$  gyrotron @  $2^{\text{nd}}$  harmonic ECRH), show that runaway electrons were produced during the field ramping, but there was usually also a steady state runaway electron component during the flat top portion of the fields. For a 1T final field, the loop voltage was typically  $\sim 10\text{ V}$  in both the ramp up and the ramp down. The duration of the ramp-up was typically shorter, lasting 0.1-0.4 sec, while the ramp-down duration was longer with somewhat lower amplitude. The high loop voltage produced during the ramp-down of the field often produce the more serious problem because, if plasma was present, it provides free electrons that can be accelerated by the loop voltage. Relativistic electron orbits were studied in the ATF geometry; the orbits at higher energies were shifted inward more than the orbits at the lower energies. The study showed that runaway electron orbits tend to fill the vacuum vessel and are not localized. A runaway suppression system consisting of a rotating paddle in combination with programmed field ramping proved to be very effective at reducing the runaway electron population. The paddle remains normally in the center of the vacuum vessel and is only removed to allow plasma production and is reinserted during field ramp-down to suppress runaway production. The paddle was the major source of bremsstrahlung, although other objects in the vacuum chamber also serve as targets. Massive gas injection

due to the neutral beams and an auxiliary gas puff also very efficiently suppresses the ramp-down x-rays. There was evidence that some of the runaway electrons are confined to islands and that because of this the paddle was not 100% effective. The maximum x-ray energy was determined to be  $\sim 12\text{-}15$  MeV from the pulse height analysis. The mean energy was a few MeV.

During magnetic field ramp-up and ramp-down phases, runaway electrons are generated and hard x-ray emission has been detected in the TJ-II<sup>45</sup> torsatron ( $m=4$ ,  $R=1.5\text{m}$ ,  $\langle a \rangle=0.1\text{-}0.25\text{m}$ ,  $B=1\text{T}$ ,  $P_{\text{ECRH}}=250\text{ kW}$  @  $53.2\text{ GHz}$ ,  $2^{\text{nd}}$  harmonic). Hard x-ray energies up to  $1.5\text{ MeV}$  and  $200\text{ keV}$  were measured during the field ramping and the ECRH discharges respectively. Typical loop voltages of  $\sim 1\text{V}$  and  $\sim 3\text{V}$  were measured during current ramp-up and ramp-down, respectively. To prevent high x-ray doses and damage to the wall of the device, a mechanical paddle was installed inside the vacuum chamber as in ATF that cuts the magnetic surfaces a few milliseconds both before and after the flat top.

### 1.3.2.2 Confinement of ECR Generated Superthermal Electrons in Helical Devices

Measurements of hard x-rays have also been reported in electron cyclotron resonance heated plasmas for many helical devices. In HELIOTRON DR<sup>46</sup> ( $R=0.9\text{m}$ ,  $\langle a \rangle=0.07\text{ m}$ ,  $B=0.5\text{T}$ ), the plasma was produced by second harmonic X-mode using  $28\text{ GHz}$ ,  $200\text{ kW}$  gyrotron as in HSX. An energy spectrum in the range  $100\text{ to }500\text{ keV}$  was measured with a NaI scintillator located outside the vacuum vessel. It was found that hard x-rays have a nonlinear inverse scaling with plasma electron density; i.e. intense hard x-ray emission at low line average density  $\bar{n}_e < 0.3 \times 10^{13}\text{ cm}^{-3}$  and damped emission at high

density  $\bar{n}_e > 0.3 \times 10^{13} \text{ cm}^{-3}$  (over dense plasma is produced using O-X-B mode conversion in HELIOTRON DR). At low density the equivalent superthermal tail temperature was  $\sim 80 \text{ keV}$ . The orbits of superthermal electrons with high pitch angles are greatly affected by strong helical field ripples. It was found that the orbits of accelerated electrons and their confinement vary greatly depending on whether the electrons are accelerated at the inside or outside of the torus.

Hard x-rays have also been studied in the TJ-IU torsatron<sup>47</sup>, ( $l=1$ ,  $m=6$ ,  $R=0.6\text{m}$ ,  $\langle a \rangle = 0.1\text{m}$ ,  $B=0.5\text{-}0.7 \text{ T}$ ). In this device, the magnetic field configurations are characterized by rotational transform on axis,  $\iota(0)$ , ranging from 0.15 to 0.32 with almost negligible shear, and magnetic well depths of the order 6%. Plasmas were produced by electron cyclotron resonance heating (X-mode 2<sup>nd</sup> harmonic,  $P_{\text{ECRH}}=90\text{-}250\text{kW}$ , pulse duration  $\sim 25 \text{ ms}$ , @  $37.5 \text{ GHz}$ ). Ray tracing calculations predicted single pass power absorption of the order 20%, and therefore absorption by resonant superthermal electrons at high magnetic field was expected (due to the relativistic shift). Together with the hard x-ray fluxes related to runaway electrons generated during magnetic field ramping, x-ray energies in the range 1–1000 keV were also detected during the ECRH phase.

Superthermal electron populations have been identified from their soft x-ray and hard x-ray spectra recorded using Si(Li) (1–30 keV) and NaI(Tl) (over 20 keV) detectors respectively. The behavior of superthermal electrons were studied in plasmas with line average densities,  $\bar{n}_e \sim 0.2\text{-}0.6 \times 10^{13} \text{ cm}^{-3}$  and electron temperature,  $T_e \sim 100\text{-}200 \text{ eV}$ , for ECRH input power (100–200 kW) and magnetic field configuration scans ( $0.15 \leq \iota(0) \leq$

0.3, with magnetic field ripple from 5.6% to 25%). It has been found that there exists a clear relationship between the characteristic energy of superthermal electrons and the radial profile of the magnetic ripple. Evaluation of the energy carried by the superthermal electron tail indicates that in plasmas with lowest  $\epsilon$  (corresponding to the lowest magnetic ripple) on the axis, superthermal electrons absorb the input power much more efficiently. Also, pronounced non-isotropic velocity distributions and toroidal asymmetries were observed. The interpretation of these observations has been based in terms of the parallel diffusion under off axis absorption.

In the Large Helical Device (LHD)<sup>48</sup> stellarator ( $R=3.9\text{m}$ ,  $\langle a \rangle=0.6\text{m}$ ,  $B=3\text{ T}$ ) a hard x-ray spectrum up to 200 keV has been observed from ECRH plasmas. Because LHD uses superconducting magnets (i.e. D.C. field), no hard x-ray from electron runaways before the plasma were detected. Hard and soft x-rays were measured simultaneously in the same port. A Si(Li) detector was used to measure soft x-rays in the range 4–10 keV, while a Ge detector was used to measure the hard x-rays below 250 keV. The hard x-rays increase faster than the soft x-rays. The delay time of the soft x-ray emission indicated impurity build up following the bulk temperature increase. After switching off the ECRH pulse, the soft x-ray signal decays exponentially with a time constant  $\tau = 150\text{ msec}$ . On the contrary, hard x-rays rapidly disappear within 10 msec. The soft x-ray decay time matches the energy confinement time for ECR heated plasma in LHD. Superthermal electron decay times were found to be a competition between collisional slowing down and particle loss due to helical ripple processes. The effective electron temperature was obtained from the hard x-ray distribution in the energy range

60-200 keV under the assumption of a Maxwellian distribution. The density of the high-energy electrons was obtained with the analysis of both spectra of thermal and non-thermal emission measured simultaneously with the Ge detector.

### 1.3.3: Single Particle ECRH Theory

During electron cyclotron resonance heating electrons cross the resonance zone differently, i.e. their acceleration is strongly dependent on the phase difference between the microwave electric field and the electron cyclotron gyro orbit. The electron will be accelerated for zero phase difference and decelerated for  $180^\circ$  phase difference. For this reason, it is difficult to obtain a quantitative description of the behavior of superthermal electron groups during ECRH given long times (in gyromotion) between resonance crossings. In order to calculate the superthermal electron time evolution during heating, one has to follow the electron during multiple resonance zone crossings and for long times, and average over many electrons.

The single particle electron cyclotron resonance heating theory has been carried out extensively both analytically and numerically by several authors to study stochastic motion of charged particles, especially those trapped in magnetic mirror configurations. Roberts and Buchsbaum<sup>49</sup> examined the motion of charged particles under the influence of plane electromagnetic waves propagating along a constant magnetic field. In their analysis they included the magnetic field of the electromagnetic wave in the force equation and solved the relativistic equation of motion. Fredricks<sup>50</sup> added a random phase shift, periodic in time to calculate the energy gained during cyclotron acceleration. Single

particle heating calculations for mirror machines were studied in the late sixties and early seventies by several authors. Grawe<sup>51</sup> hypothesized that electrons lose coherence with the applied microwave electric field in a time equal to the mirror bounce time and obtained theoretical estimates of the ECR heating rates. Kawamura et al<sup>52</sup> calculated harmonic resonance heating and Eldridge<sup>53</sup>, in addition, included the relativistic mass shift and Doppler effect. Extensive theoretical and computational calculations were made by Jaeger<sup>54</sup> et al, Lieberman and Lichtenberg,<sup>55,56,57</sup> and Sprott and Edmonds<sup>58</sup>. They showed that an upper energy barrier limits the electron maximum attainable kinetic energy during ECRH in a mirror field. The existence of the barrier is attributed to the relativistic mass increasing the cyclotron frequency so the particle is no longer in resonance with the external electromagnetic wave electric field. Accordingly, the resonance zone is shifted toward the higher magnetic field side of the torus for relativistic electrons. Carter<sup>59</sup> demonstrated that, when particle orbits are trapped in a magnetic well very near to cyclotron harmonic resonance, the quasilinear concept of weakly perturbed, uncorrelated passages through the resonance breaks down and nonlinear effects become important. We will show in Chapter 5 that for on-axis heating electrons are not reflected on a resonance point in the three different configurations. For this reason, the Carter model is not applicable in our case.

## 1.4: Thesis Outline

As stated earlier, the HSX machine has the flexibility to run under multiple magnetic configurations: quasihelical symmetry where neoclassical transport is

comparable to tokamaks and with broken symmetry where neoclassical transport properties are degraded back to the level of a conventional stellarator. The purpose of this research is to study the effects of symmetry in the magnetic field on the dynamics and confinement of superthermal electrons in HSX through studying their hard x-ray emission. In order to study the hard x-ray emission from superthermal electrons, a pulse height analysis spectroscopy system was built for HSX; the details of the system are given in Chapter 2. Beside the hard x-ray detection system, other HSX diagnostics were used during this research work and will also be discussed.

Superthermal electrons are generated in HSX in two different physical processes as will be described in Chapter 3, during magnetic field ramping in the form of runaways and during the ECRH discharges. Electrons generated during magnetic field ramp-up stay confined during the flat top portion of the field when the plasma discharge takes place. Their presence during the discharge has direct impact on the plasma formation and properties because of their higher microwave absorption. They can accelerate the breakdown process, affect the plasma stored energy, and trigger MHD instabilities. Their hard x-ray emission interferes with x-rays emitted during the ECRH discharge. The research goal was focused on primarily studying those electrons generated during the plasma discharge only and it was necessary to decouple both sources and suppress as nearly as possible electron runaways during field ramping. Two techniques were used to control and suppress the generation of electron runaways: UV light flash using Xenon lamp and puffing gas into the vacuum vessel. A detailed study of the properties of

electron runaways generated during magnetic field ramping and the techniques used to control and suppress them will be discussed in Chapter 3.

The evidence of superthermal electrons generation at low plasma density ( $\bar{n}_e < 5 \times 10^{11} \text{ cm}^{-3}$ ) in the HSX stellarator is given in Chapter 4. The hard x-ray dependence on electron density, microwave power and resonance location in different configurations are discussed in this chapter.

In order to explain the experimental results and investigate whether hard x-ray differences between configurations can be attributed to heating differences between configurations or confinement differences, single particle heating was studied in the different configurations. Chapter 5 describes the single particle heating model. The chapter starts with the mathematical model and its assumptions. A comparison between magnetic configurations from a single particle heating point of view will be evaluated in this chapter.

In order to check if the difference in hard x-ray emission between magnetic configurations is caused by a difference in electron confinement, electron guiding center drift orbits in HSX will be studied in different magnetic configurations in Chapter 6. Finally the research conclusions and suggested future research work are described in Chapter 7.

- 
- <sup>1</sup> Quoted from “U.S. Stellarator program plan”, national stellarator planning committee report, published at <http://www.ornl.gov/sci/fed/stelnews/wp.pdf> and references cited therein
- <sup>2</sup> R.B. White, in “Theory of Fusion Plasmas”, 605, Bologna, Editrice Compositori, Bologna, (1990)
- <sup>3</sup> J. Nuhrenberg and R. Zille, Physics Letters A, **129**(2), 113, (1988)
- <sup>4</sup> A.H. Boozer, Plasma Physics and Controlled Fusion, **37**, A103, (1995)
- <sup>5</sup> F. S. B. Anderson et al., Fusion Technology **27**, 273, (1995).
- <sup>6</sup> W.D. D’haeseleer, W.N.G. Hitchon, J.D. Callen and J. L. Shohet, “Flux Coordinates and Magnetic Field Structure”, Springer-Verlag, (1991)
- <sup>7</sup> J. Talmadge et al., Physics of Plasmas, **8**(12), 5165, (2001)
- <sup>8</sup> D.T. Anderson et al., American Physical Society, 41st Annual Meeting of the Division of Plasma Physics, , WA, abstract #FP11.07, November 15-19, (1999) Seattle
- <sup>9</sup> J.N. Talmadge et al., Fusion Science and Technology, **46**, 255, (2004)
- <sup>10</sup> J. Shafi, et al., Proceeding of the 12<sup>th</sup> International Stellarator Workshop, Madison, Wisconsin, September 27-October 1, (1999).
- <sup>11</sup> K.M. Likin et al., Absorption of X-Wave at the Second Harmonic in HSX, 15<sup>th</sup> Topical Conference on Radio Frequency Power in Plasmas, (2003).
- <sup>12</sup> C. Deng, et al., Review of Scientific Instruments **74**, 1625 (2003)
- <sup>13</sup> K. Zhai et al., **75**(10), 3900, (2004)
- <sup>14</sup> V. Erckmann and U. Gasparino, Plasma Physics and Controlled Fusion, **36**, 1869, (1994)
- <sup>15</sup> R. Prater, Physics of Plasmas, **11**(5), 2349, (2004)
- <sup>16</sup> T.H. Stix, Nuclear Fusion, **15**, 737, (1975)
- <sup>17</sup> T.H. Stix, “Waves in Plasmas”, 2nd edition, Springer-Verlag, (1992)
- <sup>18</sup> K. Ohkubo et al., Nuclear Fusion, **21**(10), 1320, (1981)

- 
- <sup>19</sup> V. Erckman, et al., *ibid*, **2**, 419
- <sup>20</sup> A. Iiyoshi, et al., *Physical Review Letter*, **48**, 745, (1982)
- <sup>21</sup> R. Wilhelm et al., *Plasma Physics and Controlled Fusion*, **26**, 259, (1984)
- <sup>22</sup> V Tribaldos et al., *Plasma Physics and Controlled Fusion*, **40**, 2113, (1998)
- <sup>23</sup> S Kubo et al., *Plasma Physics and Controlled Fusion*, **47**, A81, (2005)
- <sup>24</sup> S. Morimoto et al., *Nuclear Fusion*, **29**(10), 1697, (1989)
- <sup>25</sup> M.R. O'brien et al., *Nuclear Fusion*, **26**, 1625, (1986)
- <sup>26</sup> V.V. Alikaev and V.L. Vdovin, *Soviet Journal of Plasma Physics*, **9**, 538, (1983)
- <sup>27</sup> S.V. Goeler et al., *Nuclear Fusion*, **25**, 1515, (1985)
- <sup>28</sup> B. Grant Logan, "Calculations of X-ray Bremsstrahlung Spectra and Scintillator Detector Yields for Relativistic Electron Energies from 10 keV to 10 MeV", NRL Memo Rep. 2861, Naval Research Laboratory, Washington, (1974)
- <sup>29</sup> R. A. Dandl et al., *Nuclear Fusion*, **1**, 345, (1962)
- <sup>30</sup> R. A. Dandl et al., *Nuclear Fusion*, **4**, 344, (1964)
- <sup>31</sup> J. L. Shohet and D. Greene, *Physical Review Letters* **27**, 90, (1971)
- <sup>32</sup> A. England and G. Haste, *Physical Review*, **A7**, 383, (1973), **A8**, 1475, (1973)
- <sup>33</sup> H. Ikegami et al., *Physical Review Letter*, **19**, 778, (1967)
- <sup>34</sup> E. Silver, *Bulletin of American Physical Society*, **30**, 1580, (1985)
- <sup>35</sup> M. Hirata, et al., *Japanese Journal of Applied Physics*, **28**(1), 96, (1985)
- <sup>36</sup> S. Von Goeler, et al., *Proceedings of Course Diagnostics for fusion reactor conditions*, Varenna, Italy, EVR-8351-1 EN1, 87, (1982)
- <sup>37</sup> S. Von Goeler, et al., *Nuclear Fusion*, **25**, 1515, (1985)
- <sup>38</sup> J. Stevens, et al., *Nuclear Fusion*, **25**, 1529, (1985)

- 
- <sup>39</sup> S. Texter, et al., *Nuclear Fusion*, **26**(10), 1279, (1986)
- <sup>40</sup> R. Bartiromo, *Nuclear Fusion*, **33**(10), 1483, (1990)
- <sup>41</sup> S. Yue-Jiang, et al., *Chinese Physical Society*, **10**(2), 134, (2002)
- <sup>42</sup> A. C. England et. al, *Physics of Fluids B***3**(7), 1671, (1991).
- <sup>43</sup> F. Medina et al., *Plasma Physics and Controlled Fusion*, **40**, 1897, (1998).
- <sup>44</sup> A.C. England et al., *Physics of Fluids B*, **3**(7), 1671, (1991)
- <sup>45</sup> L. Rodrigues-Rodrigo et al., 26<sup>th</sup> EPS Conference on Controlled Fusion and Plasma Physics, Maastricht, 14-18 June 1999. Also *ECA*, **23**, 353, (1999)
- <sup>46</sup> S. Morimoto et al., *Nuclear Fusion*, **29**(10), 1697, (1989)
- <sup>47</sup> F. Medina, et al., *Plasma Physics and Controlled Fusion*, **40**, 1879, (1998)
- <sup>48</sup> S. Muto et al., *Review of Scientific Instruments*, **74**(3), 1993, (2003)
- <sup>49</sup> C.S. Roberts and S.J. Buchsbaum, *Physical Review A*, **135**, 381, (1964)
- <sup>50</sup> R.W. Fredricks, *Journal of Plasma Physics*, **1**, 241, (1967)
- <sup>51</sup> H. Grawe, *Plasma Physics*, **11**, 151, (1969)
- <sup>52</sup> T. Kawamura et al., *Nuclear Fusion*, **11**, 339, (1971)
- <sup>53</sup> O. Eldridge, *Bulletin of the American Physical Society*, **17**, 773, (1972)
- <sup>54</sup> F. Jaeger, A.j. Lichtenberg, and M.A. Lieberman, *Plasma Physics*, **14**, 1073, (1972)
- <sup>55</sup> M.A. Lieberman and A.j. Lichtenberg, *Plasma Physics*, **15**, 125, (1973)
- <sup>56</sup> A.j. Lichtenberg and G. Melin, *Physics of Fluids*, **16**, 1660, (1973)
- <sup>57</sup> A.j. Lichtenberg, M.J. Schwartz and M.A. Lieberman, *Plasma Physics*, **13**, 89, (1971)
- <sup>58</sup> J.C. Sprott and P.H. Edmonds, *Physics of Fluids*, **14**, 2703, (1971)

---

<sup>59</sup> M.D. Carter and J.D. Callen, *Physics of Fluids*, **29**(1), 100, (1986)

# Chapter 2

## Diagnostics and Hardware

### 2.0: Introduction

Electron Cyclotron Resonance Heating is considered a successful method of plasma production and heating in stellarators due to its simplicity, high power efficiency and experimental flexibility<sup>1</sup>. During second harmonic X-mode ECRH, superthermal electron tails with energies up to couple of hundred keV are easily generated. Among various methods to diagnose superthermal electrons (such as, non-thermal bremsstrahlung emission, non-thermal Electron Cyclotron Emission (ECE), etc), the non-thermal bremsstrahlung emission is one of the most efficient as it offers a direct insight on the build-up of the tail electron distribution function<sup>2,3</sup>. To study the dynamics of superthermal electrons in HSX, a hard x-ray detection system working in pulse mode is used. The technical details of the x-ray detection system are described in this chapter. The first section gives a description of the x-ray spectroscopic system used in HSX to study superthermal electrons. Subsequent sections describe other complimentary HSX diagnostics used during the course of this study.

### 2.1: X-ray Spectroscopic System

Determining the energy distribution of x-rays emitted in a given radiation field is one of the requirements of the spectroscopic system. To achieve this goal, the detector must be able to fully absorb the total energy of the most energetic photons incident on it.

During the 2<sup>nd</sup> harmonic x-mode ECRH in the HSX stellarator, x-ray photons are emitted with an average energy between 100-200 keV (depending on plasma density; higher average x-ray photon energy at low density and vice-versa). Photoelectric absorption and Compton scattering are the most important energy deposition mechanisms of the x-ray photons for energies less than a few MeV as shown in Figure 2.1. The photoelectric effect is the dominant interaction mechanism up to a few hundred keV, while Compton scattering is more probable for higher energy x-rays from several hundred up to few MeV.

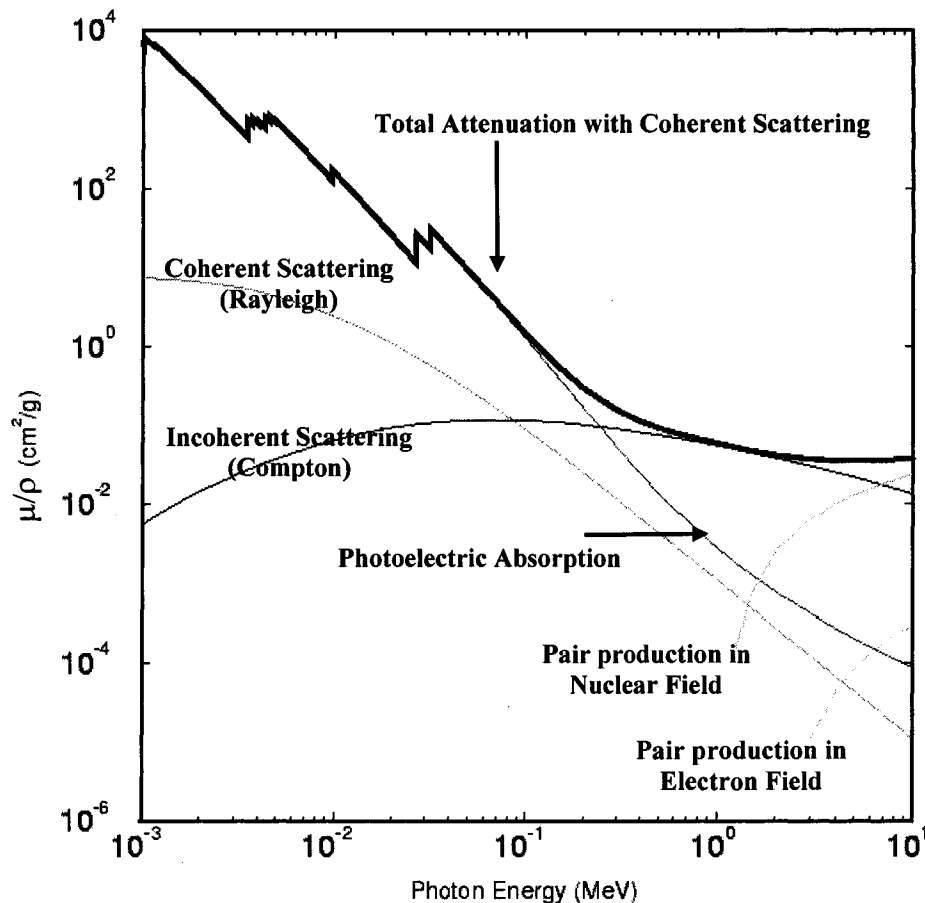
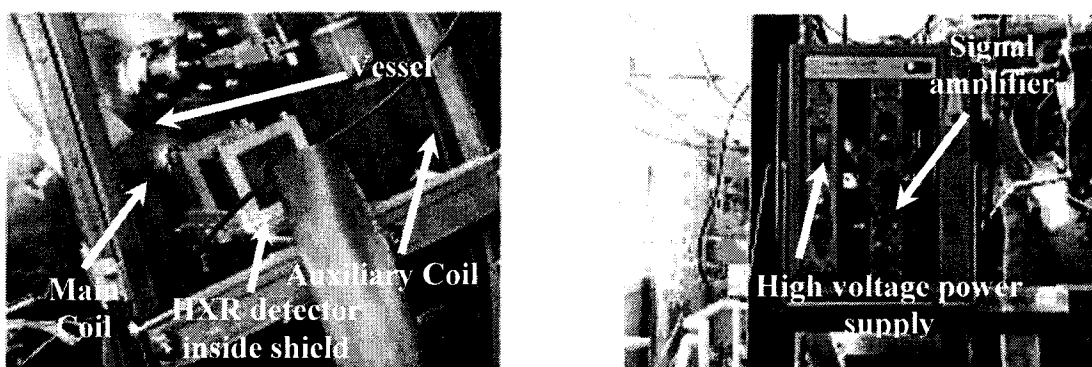


**Figure 2.1: X-ray absorption coefficient for CdZnTe4.**

During photoelectric absorption and Compton scattering interactions in matter, a total (in case of photoelectric absorption) or a fraction (in case of Compton scattering) of the incident photon energy is transferred to the detector electrons in the process of electron-hole-pair formation. The detection process is based on measuring the total collected electronic charge (proportional to the incident photon energy), and the goal of determining the x-ray spectral energy distribution is best met by a detector that maximizes the transfer of energy from the incident x-ray to the detector electrons.



a) Detector

b) Power Supply and Electronics

**Figure 2.2: CdZnTe Pulse Height Analysis System Mounted on HSX**

A Pulse Height Analysis system was built to study the hard x-ray emission during the ECRH discharges. The system is based on CdZnTe detector (the detector and the electronics are on loan from Madison Symmetric Torus MST at the University of Wisconsin Madison). The system is composed of the following components (part of the system is shown in Figure 2.2):

1. High Pass Stainless steel filter ( $E_{\text{photon}} > 20 \text{ keV}$ )
2. Lead shield and Collimator
3. CdZnTe detector

4. Electronics (High Voltage Power Supply, Amplifier, Digitizer, etc)
5. Computer-Based Pulse Height Analysis (PHA) System

The technical details and the explanation of operation of each element as it occurs sequentially in the signal chain illustrated in Figure 2.3, from incident x-ray to computer data handling, are given below.

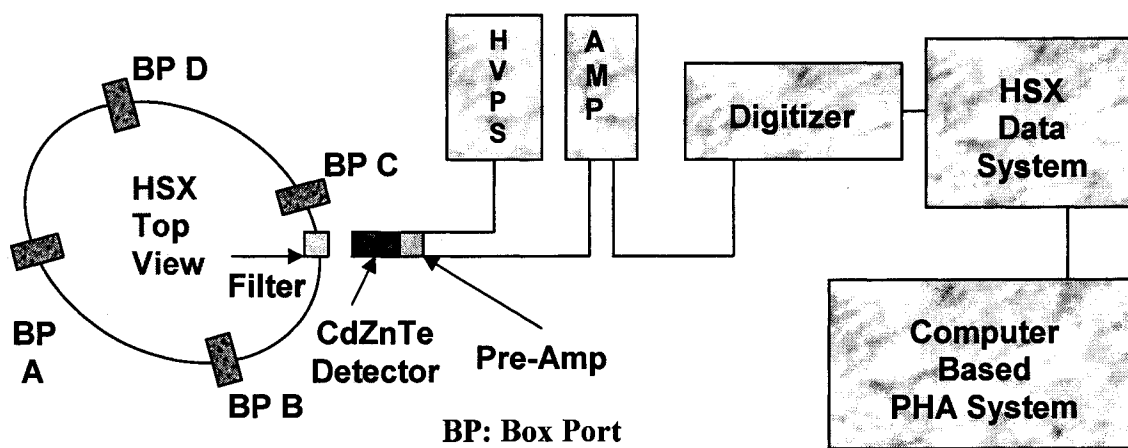
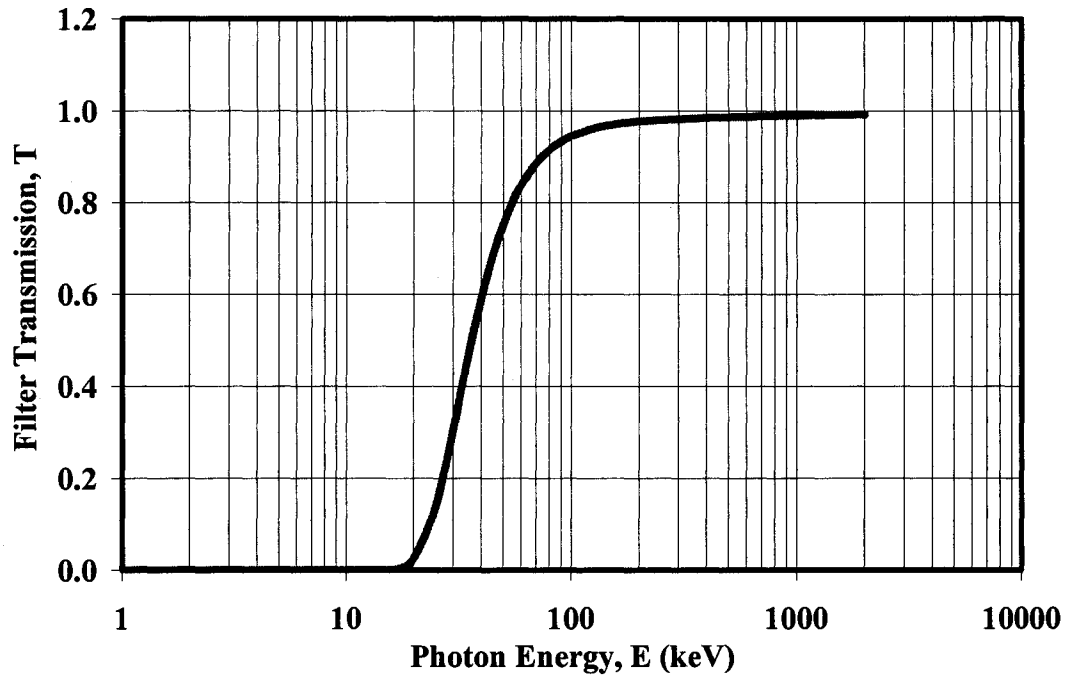


Figure 2.3: Hard x-ray spectroscopic system signal chain

### 2.1.1: Stainless Steel Filter

In order to shield the detector from unwanted radiation (especially low energy soft x-rays) and to avoid unnecessary loading of the detector, the detector is mounted outside the vacuum vessel between coils CP1 and CP2 (C-Prime coils) near box port C as shown in Figure 2.3. The detector is mounted perpendicular to the vacuum vessel in the horizontal mid-plane of the machine. A 200  $\mu\text{m}$  stainless steel filter mounted on a 2 $\frac{3}{4}$ " conflat flange is placed in front of the detector. Figure 2.4 shows the calculated transmission<sup>5</sup> of the stainless steel filter.



**Figure 2.4: X-ray transmission for stainless steel 304 from 0.001 to 2 MeV**

The x-axis represents the photon energy in keV, and the y-axis represents x-ray transmission calculated from:

$$T = \frac{I}{I_o} = e^{-\frac{\mu}{\rho} \rho x} \quad (2.1)$$

$$\mu = N(\sigma_{pe} + \sigma_{cs} + \sigma_{pp}) \quad (2.2)$$

Where,  $I_o$  and  $I$  are x-ray photon intensities before and after the filter,  $\mu$  the total mass absorption coefficient,  $\rho$  and  $N$  are the filter solid state and atomic number densities respectively,  $\sigma_{pe}$ ,  $\sigma_{cs}$ , and  $\sigma_{pp}$  are the photoelectric, Compton scattering and pair production cross sections respectively, and  $x$  the filter thickness. As Figure 2.4 shows, the filter has an energy cut-off below 20 keV (no photons with energies  $< 20$  keV will

penetrate the filter) and photons with energies  $> 200$  keV will penetrate the filter without attenuation.

### **2.1.2: Lead Shield and Collimator**

To make any quantitative x-ray measurement, it is required to have a “clean” geometry of the source-detector arrangement. Well designed, practical collimators and the knowledge of their problems and limits are very important in this respect. Among the well known collimator problems are, (1) insufficient thickness can lead to penetration of radiation and (2) collimated radiation may interact with the collimator material via Compton scattering, positron annihilation and/or fluorescence emission and the resultant x-ray photon can deteriorate the source signal. These problems can be solved by using sufficient thickness to stop radiation penetration and cladding the inner surface with low Z-material (effective in reducing fluorescence emission) or having grooves in the inner part of the collimator (this reduces the surface area seen by the source) to reduce radiation scattering. The x-ray collimator used in HSX was designed to suppress the influence of wall bremsstrahlung by increasing the collimator thickness and adding grooves and Aluminum in the collimator area to eliminate the secondary scattered radiation. This allows us to investigate x-rays sourced only from the plasma. The detector is placed inside a lead box of dimensions 9 cm (width) x 9 (height) cm x 10.2 (length) cm. The wall thickness of the box is 3.84 cm except the front side, which is 5.1 cm thick lead block. The lead box is installed inside an Aluminum box with thickness of 1.5 cm for safe handling and mechanical rigidity. The front side of the detector Aluminum and

lead boxes has a 0.4 cm hole aligned with the detector central line for collimation purposes. Figure 2.5 shows the calculated transmission for lead.

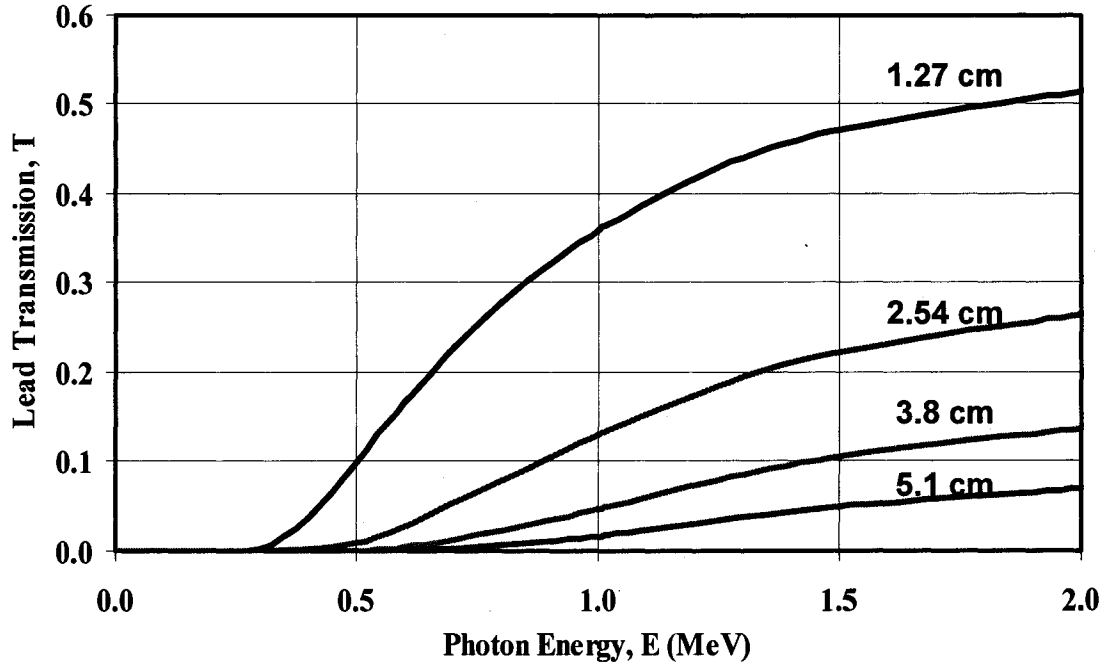


**Figure 2.5: X-ray transmissions for lead from 0.001 to 10 MeV for variable thicknesses**

The figure shows that photons with energies  $< 700$  keV have almost zero transmission.

The detector collimator solid angle is  $2.6 \times 10^{-3}$  steradian.

As Figure 2.6 shows, the volume of the plasma seen by the detector can be represented by a truncated cone:

$$V = \frac{\pi}{3} h (R_1^2 + R_2^2 + R_1 R_2) \quad (2.3)$$

Where  $h$  is the plasma line of sight  $\sim 25$  cm and  $R_1$  and  $R_2$  are the cone small and large bases radii respectively. If the cone bases radii are nearly equal  $R_1 \approx R_2$ , the plasma

volume can be to a good approximation represented by cylinder with volume  $V \approx \pi R^2 h$ . If the plasma volumetric hard x-ray source (isotropic source emission is assumed) is  $I_o$  (photons.cm<sup>-3</sup>.steradian<sup>-1</sup>.sec<sup>-1</sup>), then the intensity directed to the detector in photons/sec will be given by:

$$I = I_o \frac{d\Omega}{4\pi} V \quad (2.4)$$

Where  $d\Omega$  is the detector solid angle in steradian and  $\frac{d\Omega}{4\pi}$  is the fraction of hard x-ray photons directed toward the detector.

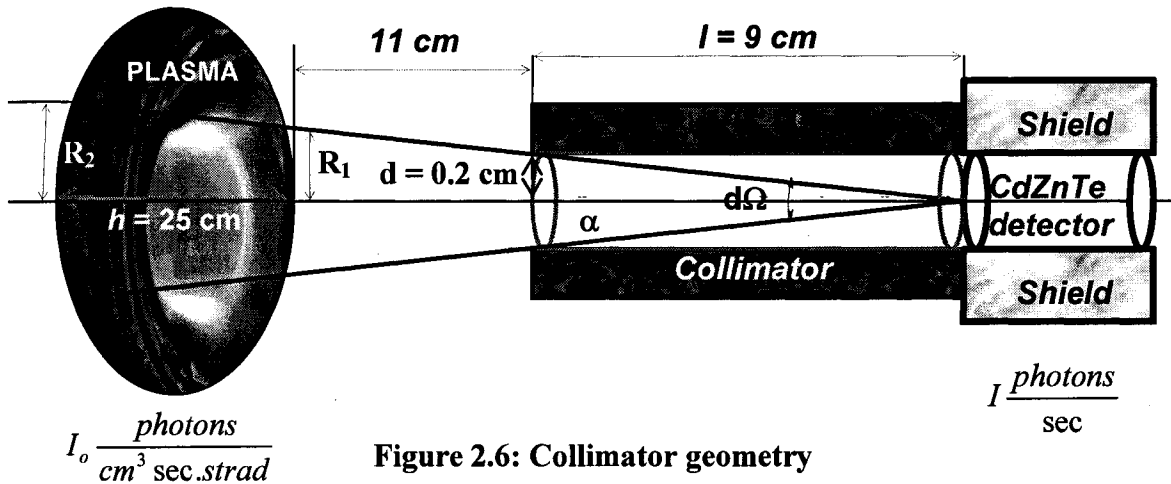
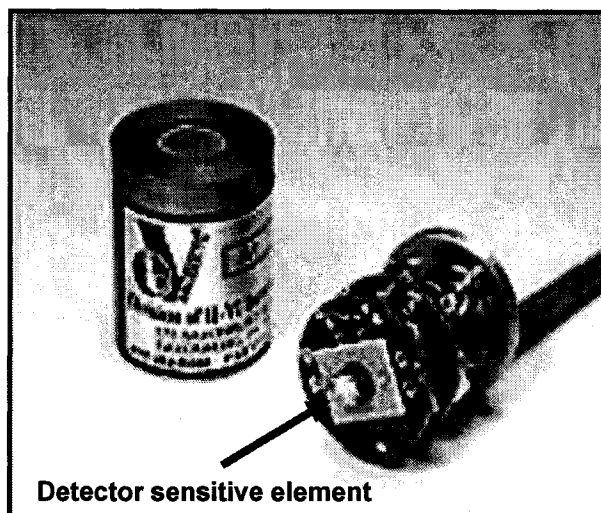


Figure 2.6: Collimator geometry

### 2.1.3: The CdZnTe Detector

CdZnTe is a room temperature semiconductor detector which has undergone rapid development in recent years<sup>6,7</sup>. CdZnTe detectors proved their effectiveness in measuring hard x-ray emission in tokamak and stellarator environments<sup>6</sup>. It has a number of desirable features for X-ray spectroscopy including: room temperature operation, fine spatial resolution, good energy resolution, compact size (due to their high x-ray stopping

efficiency, detectors of small sizes, in the order of few millimeters, can be used), excellent time resolution, and its durability against external magnetic fields (pulsed magnetic fields don't affect detector operation) but sensitive to vibration.



**Figure 2.7: EV-280 CdZnTe detector and its built-in pre-amplifier**

An eV-280 (eV-products) CdZnTe detector<sup>8</sup> shown in Figure 2.7 is used as the detection element for the HSX hard x-ray PHA system. The sensitive element of the detector is 10 mm x 10 mm x 2 mm (L x W x t). It combines relatively high atomic numbers (48 and 52; the higher the atomic number the higher the interaction probability) with a large enough band gap energy (1.572 eV) to permit room temperature operation (band gap is the energy difference between the top of the valence band and the bottom of the conduction band in a semiconductor or an insulator). The detector characteristics are shown in Tables 2.1 and 2.2. The detector is calibrated against a set of radioisotopes, Co<sup>60</sup> (1.17 and 1.33 MeV), Ba<sup>133</sup> (80 and 358 keV), Cs<sup>137</sup> (662 keV), and Am<sup>241</sup> (60 keV). The spectrum is constructed using the software-based PHA program.

Property	Value
Chemical Symbol	Cd <sub>0.9</sub> Zn <sub>0.1</sub> Tl
Atomic Number	48, 30, 52
Average Atomic Number	49.1
Density $\rho$ (gm/cm <sup>3</sup> )	5.78
Band gap $E_p$ (eV)	1.572
Dielectric Constant	10.9
Pair production energy $E_{pair}$ (eV)	4.64
Resistivity $\rho$ ( $\Omega$ cm)	$3 \times 10^{10}$
Electron mobility $\mu_e$ (cm <sup>2</sup> /Vs)	1000
Electron lifetime $\tau_e$ (s)	$3 \times 10^{-6}$
Hole mobility $\mu_h$ (cm <sup>2</sup> /Vs)	50 - 80
Hole lifetime $\tau_h$ (s)	$10^{-6}$
$(\mu\tau)_e$ (cm <sup>2</sup> /V)	$(3-5) \times 10^{-3}$
$(\mu\tau)_h$ (cm <sup>2</sup> /V)	$5 \times 10^{-5}$

**Table 2.1: CdZnTe physical characteristics<sup>4</sup>.**

Property	Value
Dimension	10x10x2 mm
Peak/Valley	> 8:1 @ 59.5 keV
Resolution	< 10% (6 keV)@ 59.5 keV (FWHM)
Peak/Valley	> 3:1 @ 122 keV
Resolution	< 6% (8 keV)@ 122 keV (FWHM)
Peak/Valley	> 1.8:1 @ 622 keV
Resolution	< 3% (20 keV)@ 622 keV (FWHM)

**Table 2.2: CdZnTe detection characteristics<sup>4</sup>.**

Figure 2.8 shows the differential pulse height of the full-energy or photo-peaks (the peaks corresponding to full energy absorption of incident photon energy, as in photoelectric absorption process) for Am<sup>241</sup> at three different amplifier gains. The x-axis represents the pulse height,  $H$ , in volts and the y-axis represents the differential number of pulses per differential pulse height  $\frac{dN}{dH}$ . The figure shows that the highest voltage gain

results in the largest maximum pulse height, but in all cases the area under the differential distribution is constant because same source is used for the three different cases.

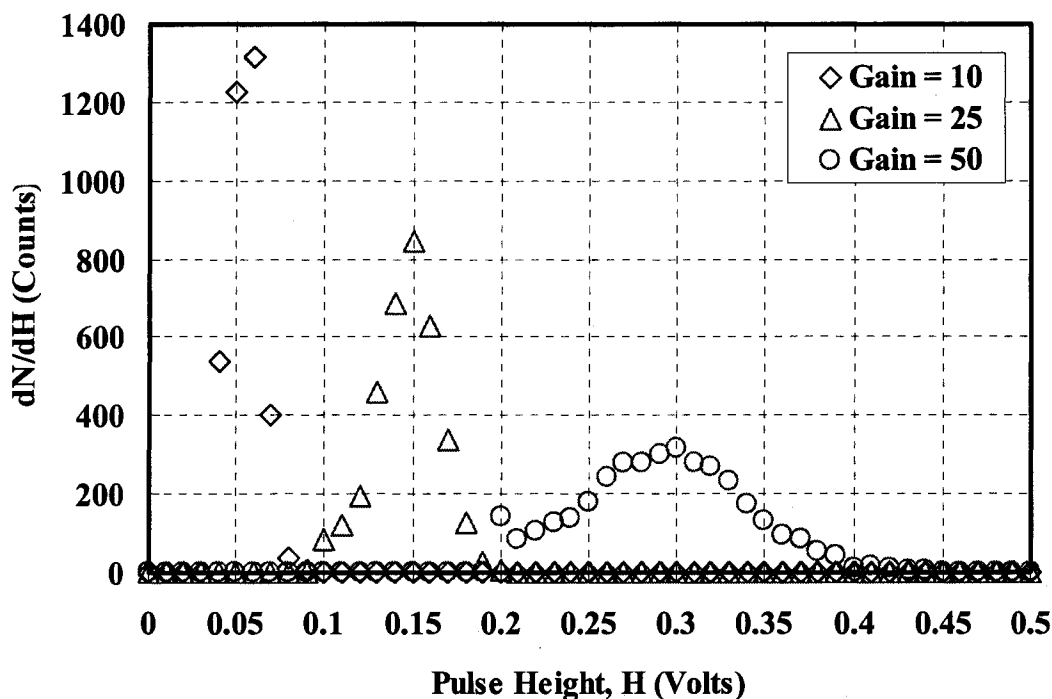


**Figure 2.8: Gamma ray spectrum for  $\text{Am}^{241}$  shows photo-peaks only at three different amplifier gains.**

The PHA program, which will be described later, is used to construct Figure 2.8 as follows:

- 1- The noise level is determined at the specified gain by measuring maximum output signal in volts when the detector is not exposed to any radiation. A noise level of 0.12 volts is measured at a gain = 50.
- 2- Pulses with height above the noise level are recorded, while pulses with height below noise level are rejected.
- 3- The hard x-ray pulse height, H, ranges from the noise level to 10 volts (maximum signal produced by the amplifier).

- 4- The range in step 2 is divided into 1000 intervals of 0.01 Volts each. This sets our energy resolution or bin to 10 mV. Number of channels = 10 volts/  $\Delta H$ .
- 5- Data is collected from a single radioisotope for a long enough time to have good statistics.
- 6- The program searches for pulses with height  $H$  between  $H_n$  and  $H_n + \Delta H$ , where  $H_n$  = the height of channel  $n$ , and  $n$  ranges from 0 to 10.
- 7- The results are plotted as the differential number of pulses per differential pulse height ( $\frac{dN}{dH}$ ) versus pulse height ( $H$ ) in volts as shown in Figure 2.8
- 8- Experiment is repeated for different gains.

To calibrate the detector, i.e. determine the relation between pulse height in volts and incident photon energy in keV, the following procedures have been performed:

- 1- From the spectrum, the full energy or photo-peak location in volts was determined. For  $\text{Am}^{241}$ , photo-peak locations for gains 10, 25 and 50 are 0.06, 0.15 and 0.3 volts respectively as shown in Figure 2.8.
- 2- Additional radioactive sources with different characteristic energies are used and the corresponding photo-peak locations in volts were determined
- 3- A plot between the radioactive source characteristic gamma ray energy in keV (for example 60 keV  $\text{Am}^{241}$ ) and the pulse height  $H$  in volts is obtained (for  $\text{Am}^{241}$  at gain of 10 the photo-peak location is 0.06 volts).

- 4- A curve fitting of the results will give the calibration formula i.e. the relation between the photon energy in keV and pulse height in volts (for example,  $E = 995.62V + 0.771$  at gain of 10 as shown in Figure 2.9).
- 5- The detector was calibrated in this fashion for three different gain settings.

Figure 2.9 shows the calibration curves for three different amplifier gains for the hard x-ray PHA system in HSX. The x-axis represents the pulse height in volts and the y-axis represents the photon energy in keV. All data are taken at a gain of 50 during this thesis work.

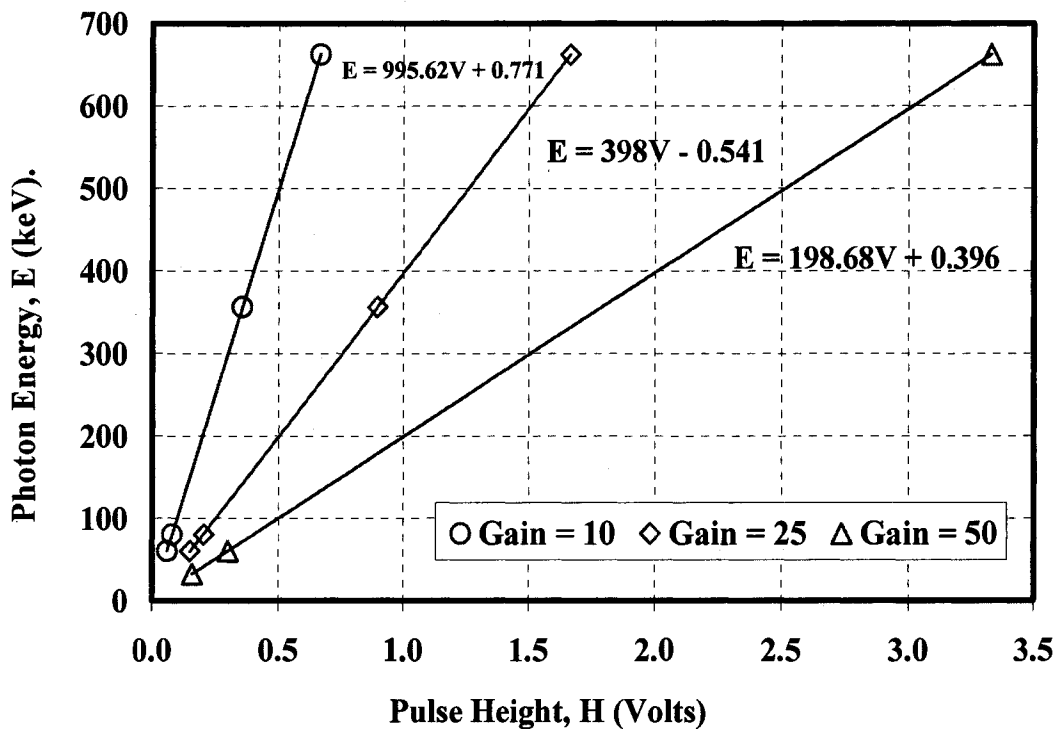


Figure 2.9: Calibration curves for CdZnTe at different amplifier gains.

#### 2.1.4: Electronics

A voltage source is used to bias the detector (the biasing is necessary to collect the total charge produced inside the detector as a result of photon energy deposition)

using a conventional NIM-PIN power supply. The bias voltage is 280 volts. The output signal from the detector preamplifier is fed to an Ortec EG&G 671 amplifier with variable gains and shaping times (related to the time constant of the amplifier shaping circuit, which adjusts the width of the pulse. The longer the shaping time the higher the probability of pulse pile up and vice versa). The amplifier technical properties are described in Table 2.3<sup>9</sup>. The data collected in this study uses an amplifier gain of 50 and a pulse shaping time of 1  $\mu\text{sec}$  (1  $\mu\text{sec}$  amplifier shaping time produces pulses with base width around  $\sim 6 \mu\text{sec}$ , the maximum digitization rate used during this research work was  $1.2 \times 10^6$  Hz which gives  $\sim 7$  digitization points per pulse. The pulse height analysis requires at least 6 data points for Gaussian curve fitting as will be discussed later in this chapter). Then the signal is digitized using a PCI-MIO-16E-1 digitizer with a maximum sampling rate of 1.2 MHz, which is fast enough to define the Gaussian shape pulses.

Property	Value
Gain	Variable 2.5 - 1500
Pulse Shaping Time $\tau$	0.5 – 10 $\mu\text{sec}$
Pulse Shape	Gaussian or triangular
Input Signal Polarity	Positive/negative
Output Signal	Unipolar/bipolar
Input Mode	Normal/differential

**Table 2.3: EG&G Ortec 671 amplifier technical properties<sup>9</sup>.**

### 2.1.5: The Pulse Height Analysis Software

The raw signal shown in Figure 2.10 is processed using a Pulse Height Analysis program. The basic program was written in the IDL language by Dr. R. O'Connell<sup>10</sup> from the MST group at the University of Wisconsin Madison. The program was modified to fit our needs at HSX (the modifications and enhancements include but not limited to, raw

data reading module, peak search module, single and double Gaussian curve fitting modules, also program output functionality was enhanced by adding, electron temperature calculations from x-ray spectrum, total energy flux, and full and simplified output files). The raw signal is sent through a shaping amplifier, which produces Gaussian pulses with amplitude proportional to the x-ray energy as shown in Figure 2.11.

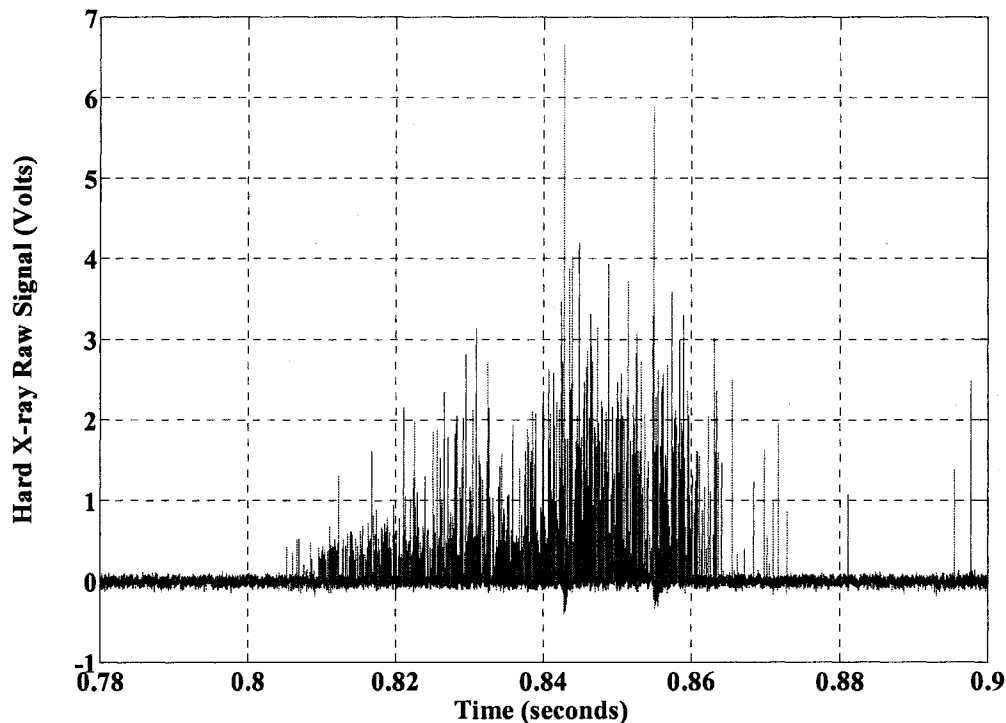


**Figure 2.10: Raw hard x-ray signal during the plasma.**

In conventional hardware-based PHA, the signals at this stage are sent to a pulse height analyzer with predefined energy bins, and the x-ray pulses falling within a given bin are then counted using a scalar counter. The HSX hard x-ray diagnostic uses direct digitization of the signal, which allows for more sophisticated software techniques to analyze the data after the discharge. This gives improved pile-up and noise handling since

more information than just the pulse height is recorded. It also allows more flexible time and energy binning of x-ray events.

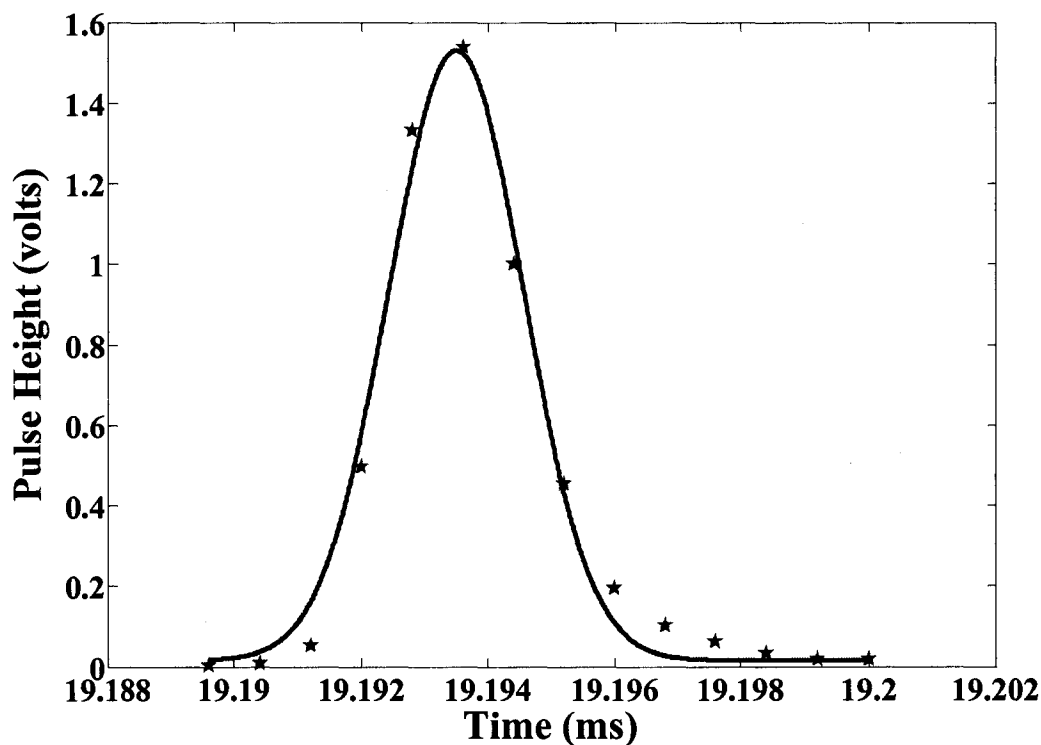


**Figure 2.11: Raw hard x-ray single pulse with Gaussian fitting.**

The Pulse Height Analysis program performs the following tasks:

- 1- Each pulse consists of certain number of data points from the digitizer (depends on the digitization rate and the shaping time). A single pulse is shown in Figure 2.11, the blue stars represent the data points produced by the digitizer and the red line represents the Gaussian curve fitting.
- 2- A pulse is accepted as a real signal if it has a significant number of data points above the noise level. Figure 2.12 shows the noise level in red.

- 3- A collection of data points (at least 6 points are required by the IDL curve fitting subroutine for fitting Gaussian shape pulses) are fitted into a Gaussian shape using the known half width of the pulse as shown in Figure 2.13.
- 4- This leaves three fitting parameters: the time stamp (peak location), the amplitude and the base line shift. The Gaussian function is represented as:

$$f(t) = a_o + a_1 e^{-\left(\frac{t-a_2}{w}\right)^2} \quad (2.5)$$

Where  $a_o$  the base line shift,  $a_1$  the pulse height and  $a_2$  the time stamp (the time of the Gaussian peak).

- 5- Any fits with too high  $\chi^2$  are then attempted to be fitted with a double Gaussian given by:

$$f(t) = a_o + a_1 e^{-\left(\frac{t-a_2}{w}\right)^2} + a_3 e^{-\left(\frac{t-a_4}{w}\right)^2} \quad (2.6)$$

- 6- Events with still too high  $\chi^2$  are disregarded as either unsalvageable pile-up events or random noise.
- 7- The fraction of events flagged as double Gaussian or pile-up is monitored.
- 8- At the end of the fitting procedure the hard x-ray intensity is stored as an array of precisely timed x-ray events.
- 9- The data can be histogrammed as shown in Figure 2.14.
- 10- Finally the hard x-ray spectrum shown in Figure 2.14 is produced and an  $\chi^2$  exponential curve fit is performed to obtain an estimate of the superthermal

electron temperature (shown in Figure 2.15) under the assumption of Maxwellian distribution

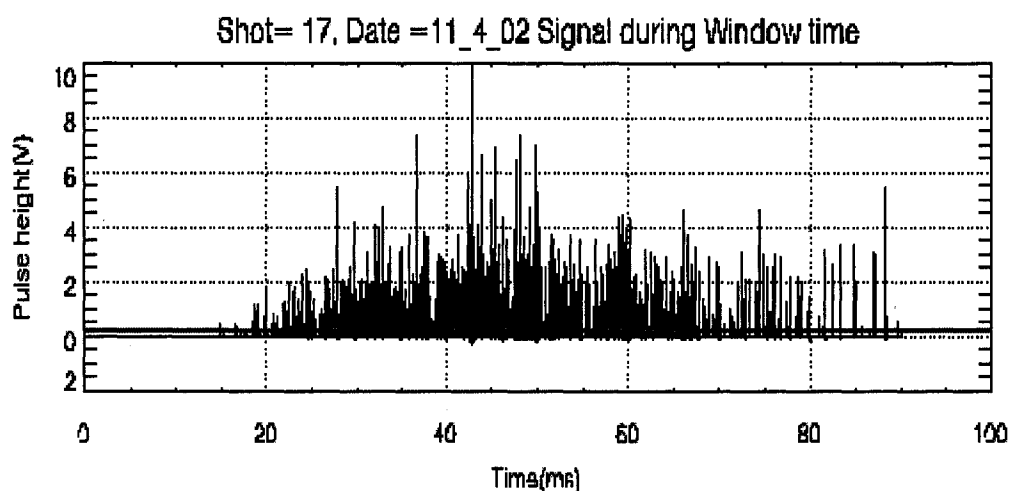


**Figure 2.12: Hard x-ray signal and noise level in red. Time window 0-100 msec corresponds to 800-900 msec.**

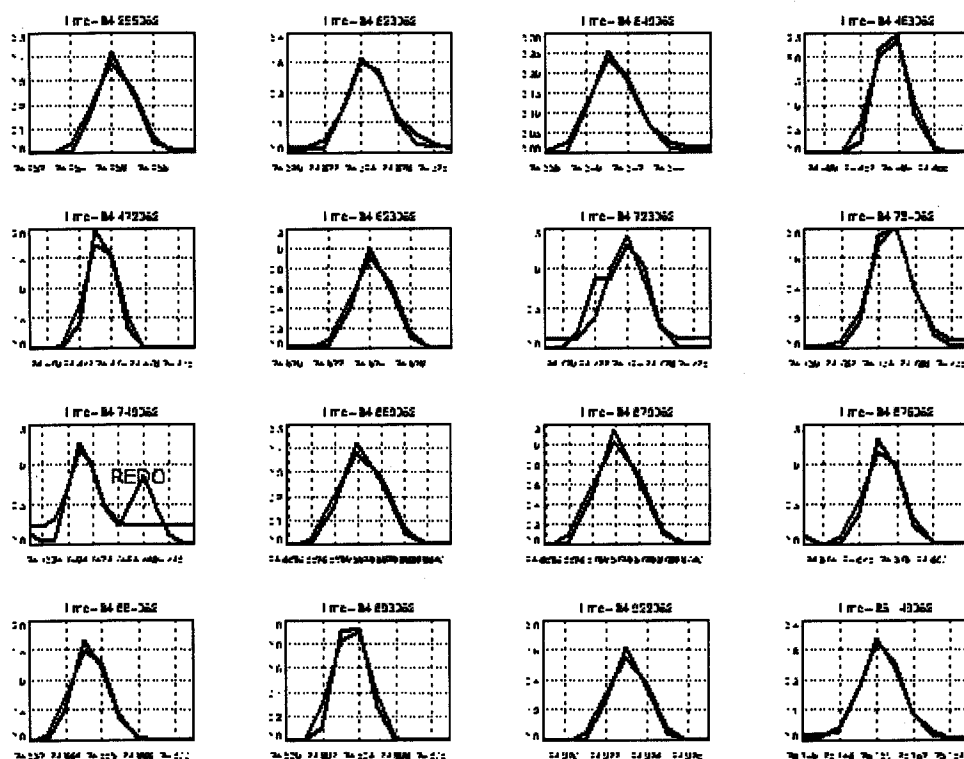


**Figure 2.13: Fitting the individual pulses to a single Gaussian. REDO: fails to fit single Gaussian and double Gaussian will be tried instead.**

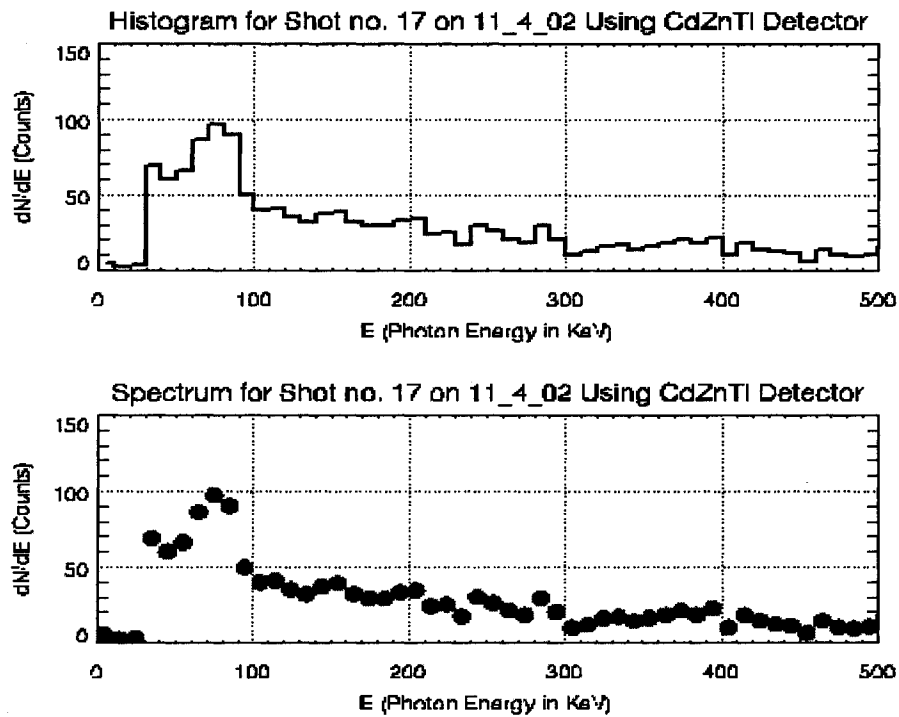


Figure 2.14 Hard X-ray histogram and spectrum.

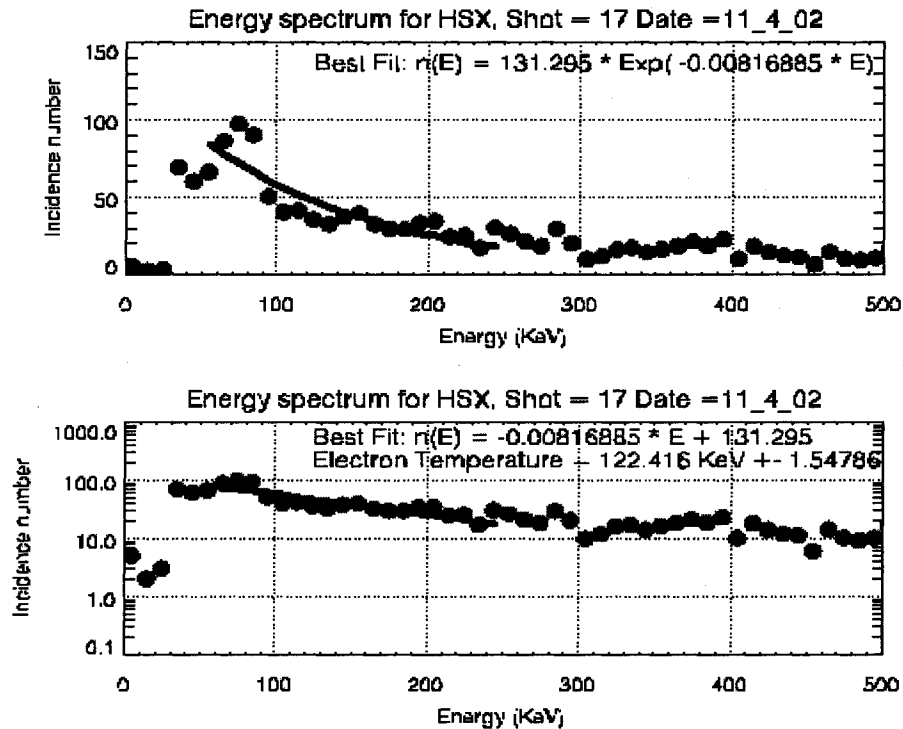


Figure 2.15: Curve fitting to calculate the electron temperature.

## **2.2: Complimentary HSX Diagnostics used in this Work**

During the course of this research, other HSX diagnostics have been used to collect and the data. The following diagnostics were used:

1. Passivated Implanted Planar Silicon (PIPS) for measuring soft x-ray emission constructed by Dr. A. Almagri.
2. Diamagnetic loop for measuring plasma stored energy designed and constructed by Dr. A. Almagri.
3. Flux loop for measuring the loop voltage during main coil current ramp-up and ramp-down designed and operated by Dr. A. Almagri.
4. Interferometer for measuring the plasma electron density constructed by Dr. C. Deng.
5. Thomson scattering for measuring the plasma bulk electron temperature and density constructed and operated by Dr. C. Zeng.

A brief description of each diagnostic used is given below.

### **2.2.1: Soft X-ray Detectors**

Soft x-ray diagnostics on HSX consists of a three-chord and five-Chord PIPS array of detectors. Both systems are installed in the vacuum vessel and are able to measure soft x-ray emission from the plasma. The three-chord and 5-chord use identical PIPS detector and signal amplifier. The three-chord array is used to measure the plasma core electron temperature through a standard filter soft x-ray ratio technique. The

beryllium filters currently used for the three-chord array are 25  $\mu\text{m}$ , 125  $\mu\text{m}$  and 725  $\mu\text{m}$  thick. The five-chord array is used to examine the confinement of the high energy deeply trapped electrons is installed with 7  $\mu\text{m}$  beryllium filters. Figure 2.16 shows the soft x-ray signal from chord number 3 of the 5-chord-array.

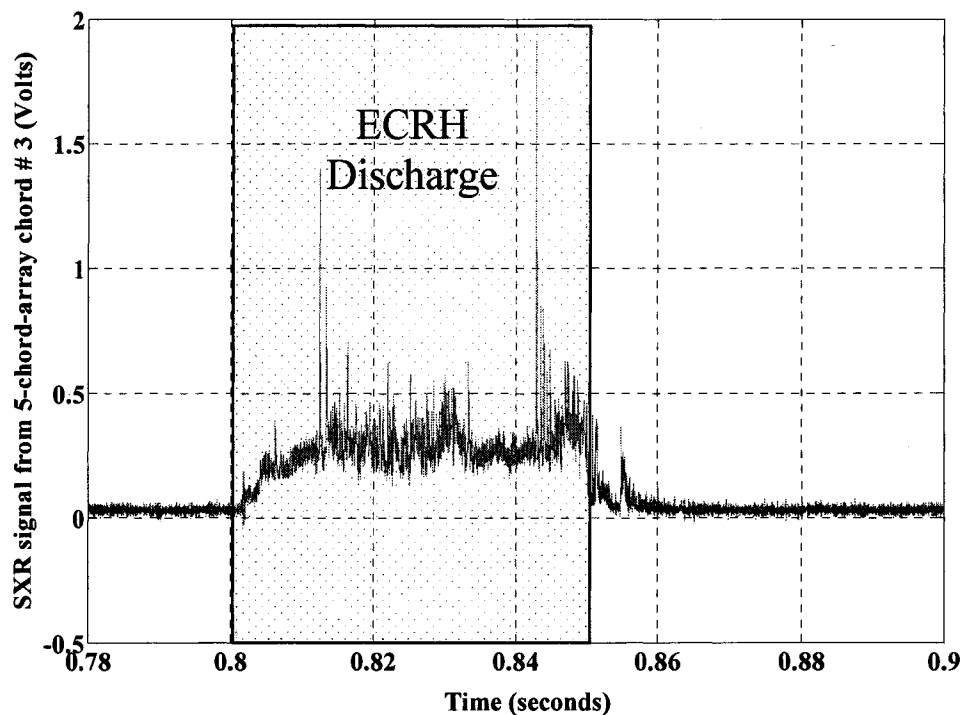


**Figure 2.16: SXR signal from 5-chord-array, chord # 3.**

### 2.2.2: Diamagnetic Loop

The energy content of HSX stellarator plasmas is measured using a diamagnetic loop consisting of a flux coil and locally compensating coil that doesn't link the plasma column. The flux loop has 20 turns and an effective area of 1.827  $\text{m}^2$  and the compensation loop has a 9 turns and an effective area of 0.0527  $\text{m}^2$ .

This set of loops allows measuring the stored energy without modeling the effects of the eddy currents or the redistribution of the main coil currents. The compensating loop is made such that it is only sensitive to  $m=0$  changes in the flux. These two loops are connected to actively remove all the non-plasma contributions to the flux changes. The difference is sent through an active integrator to obtain the flux change  $\delta\phi$  due to the diamagnetic effects. From this differencing technique, the non-plasma noise level is about 2 mv (at gain of 10 and  $RC=10^{-3}$  s). This is equivalent to  $7.2 \times 10^{-6}$  v-s noise in the diamagnetic flux. This gives a resolution in the stored energy of  $\sim 0.8$  J at  $W = 20$  J, corresponding to  $\delta\beta \sim 0.02\%$ .

Figure 2.17 shows the signal from the diamagnetic flux loop for the QHS configuration a at plasma line average density of  $3.2 \times 10^{11} \text{ cm}^{-3}$ .

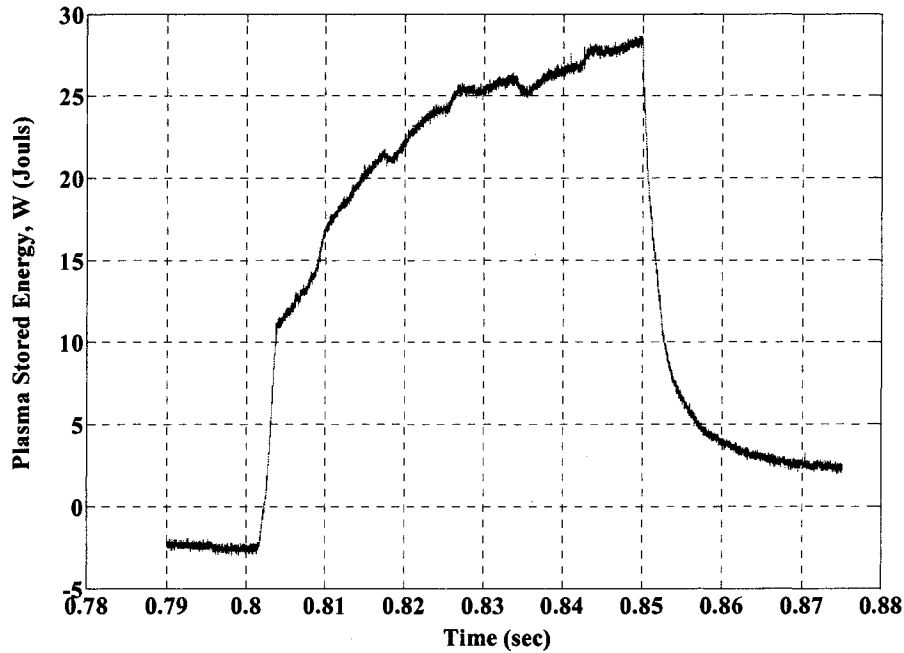


**Figure 2.17: Plasma stored energy, W in joules during ECRH discharge for QHS,  $\langle n_e \rangle 3.5 \times 10^{11} \text{ cm}^{-3}$ .**

### 2.2.3: Loop Voltage

A loop is used to measure the loop voltage induced during coil current ramp-up and ramp-down. It consists of a simple two turn loop toroidally wound around the machine. The loop voltage measured using this loop is 0.5 volts per turn for  $B = 0.5$  Tesla operation. Figure 2.18 shows the loop voltage raw signal.

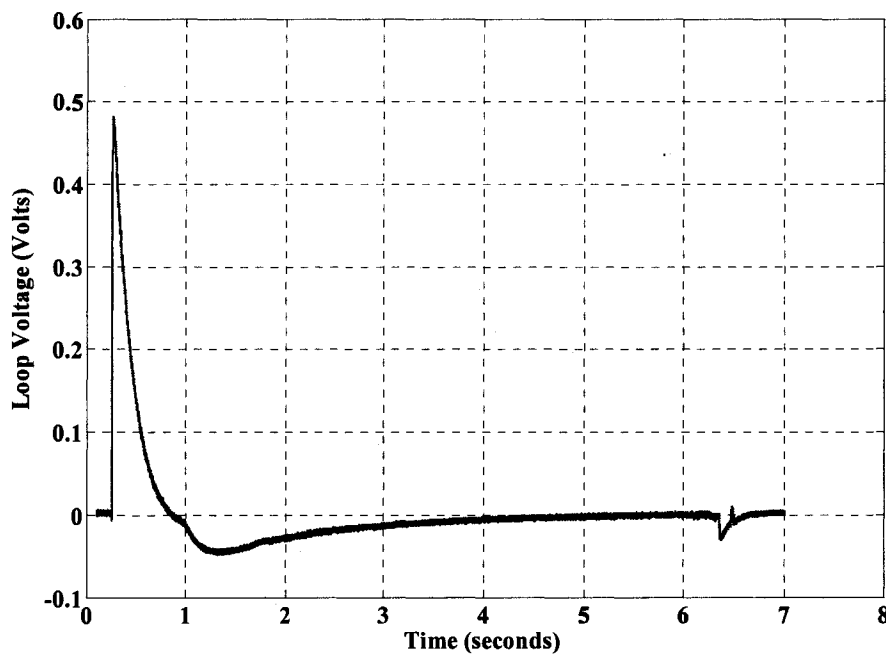
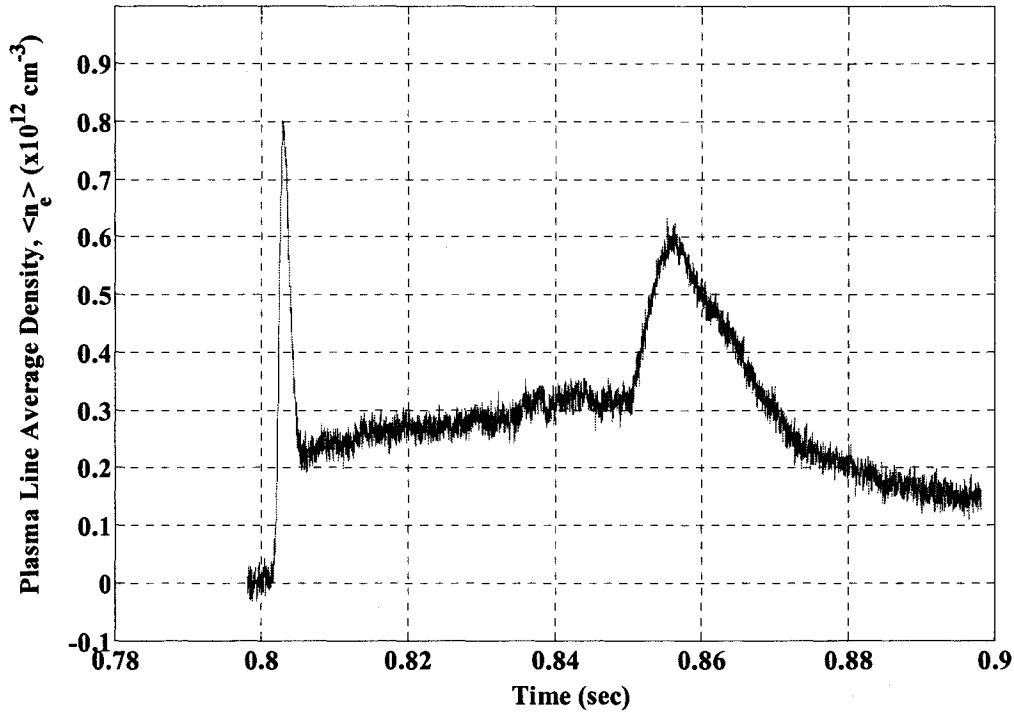


Figure 2.18: Loop voltage signals in QHS.

### 2.2.4: Microwave Interferometer

A multi-channel interferometer system<sup>11,12</sup> is routinely operating in HSX to measure the electron density and equilibrium profile. Figure 2.19 show the line-averaged density during ECRH discharge in QHS mode using the interferometer central chord.



**Figure 2.19: Plasma line average density in QHS.**

The interferometer system has nine viewing chords with 1.5 cm spacing. The source is a bias-tuned Gunn diode at 96 GHz with passive solid-state tripler providing output at 288 GHz (8 mW). The density radial distribution is reconstructed from the measured line-integrated density.

### **2.2.5: Thomson Scattering**

The Thomson scattering system<sup>13</sup> in HSX uses General Atomics built polychromators with a large collection optical system. The system is capable of 10 point profile measurements. Ten identical fiber bundles with a transmission efficiency of 0.6 couple the collected photons to ten polychromators that disperse the collected light. The four wavelength channels in each of the ten polychromators are optimized for the

temperature measurement range from 10 eV–2 keV. A dedicated CAMAC system is used to record the data. The system has been spectrally and absolutely calibrated, which can provide routine profile measurement of the electron temperature and density.

Figures 2.20 and 2.21 shows the plasma electron density and temperature profiles for QHS mode of operation at line average density of  $\langle n_e \rangle \sim 10^{12} \text{ cm}^{-3}$ .

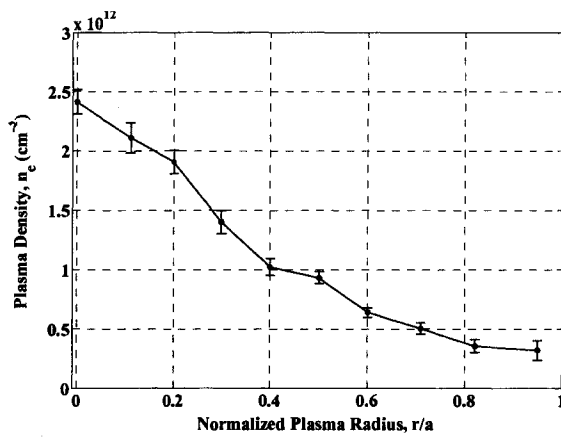


Figure 2.20: Electron density profile in QHS.  $\langle n_e \rangle \sim 10^{12} \text{ cm}^{-3}$ .

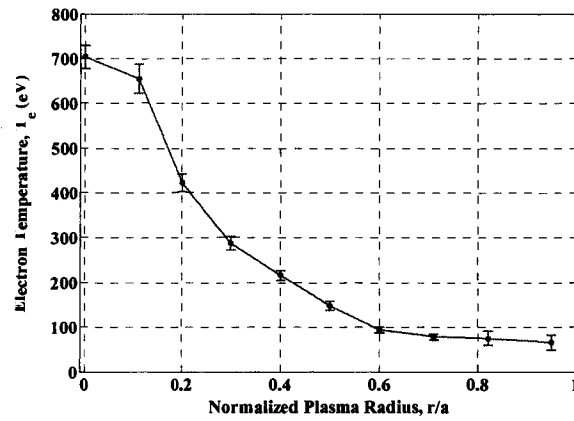


Figure 2.21: Electron temperature profile in QHS.  $\langle n_e \rangle \sim 10^{12} \text{ cm}^{-3}$ .

- 
- <sup>1</sup> V Erckmann et al., *Plasma Physics and Controlled Fusion*, **36**, 1869, (1994).
- <sup>2</sup> H. Knoepfel, "Hard X-Ray Measurements" in "Diagnostics for Fusion Experiments", Pergamon press, (1979).
- <sup>3</sup> I. H. Hutchinson, "Principles of Plasma Diagnostics", 2<sup>nd</sup> edition, Cambridge University Press, (2002).
- <sup>4</sup> XCOM; Photon Cross-Section Online Data Base.  
<http://physics.nist.gov/PhysRefData/Xcom/Text/XCOM.html>".
- <sup>5</sup> XCOM; Photon Cross-Section Online Data Base.  
<http://physics.nist.gov/PhysRefData/Xcom/Text/XCOM.html>".
- <sup>6</sup> Y. Peysson, S. Coda, F. Imbeaux, *Nuclear Instruments and Methods in Physics Research A*, **458**, 269, (2001).
- <sup>7</sup> Y. Peysson, R. Arslanbekov, *Nuclear Instruments and Methods in Physics Research A*, **380**, 423, (1996).
- <sup>8</sup> eV-Products website "<http://www.evproducts.com/>".
- <sup>9</sup> Ortec website at "<http://www.ortec-online.com/electronics/amp/671.htm>".
- <sup>10</sup> R. O'Connell, MST plasma physics group, UW-Madison, private communication.
- <sup>11</sup> D.L. Brower et al., *Review of Scientific Instruments*, **72**(1), 1081, (2001)
- <sup>12</sup> C. Deng et al., *Review of Scientific Instruments*, **74**(3), 1625, (2003).
- <sup>13</sup> K. Zhai et al., *Review of Scientific Instruments*, **75**(10), 3900, (2004)

# Chapter 3

## Superthermal Electron Sources in HSX

### 3.0 Introduction

In the presence of accelerating electric fields in magnetic confinement fusion devices, electrons overcoming the collisional drag force become runaways and can gain energies up to several million electron volts<sup>1,2,3</sup>. Runaway electrons constitute a serious concern as the final runaway energy can become sufficiently large as to cause serious damage to the confining structures. Beside the structural damage, when runaway electrons hit the material walls they generate high doses of x-rays that may be harmful to personnel working near fusion devices.

Runaway electron formation and confinement occur frequently in pulsed heliotrons, torsatrons, and stellarators because of the high loop voltages generated during field ramping and the confinement of electrons on the vacuum flux surfaces of those machines<sup>4,5</sup>. In the HSX stellarator, superthermal electrons are generated by two different processes: (1) electron acceleration in the toroidal electric field developed during the field ramp-up and ramp-down, and (2) acceleration in the microwave electric field during the 2<sup>nd</sup> harmonic X-mode ECRH discharges. A fraction of the superthermal electrons generated during the field ramp-up phase are still confined during the current flat top. They absorb part of the ECRH injected power and speed up the breakdown process as will be shown later in this chapter. These fast electrons emit hard x-rays at the same time

as those generated by ECRH, making it difficult to recognize the origin of the hard x-ray emission during the microwave discharge. The current research interest is focused on studying the dynamics and confinement of superthermal electrons generated by the ECRH discharges. In order to suppress the generation of runaway electrons during the magnetic field ramp-up, it was necessary to understand their generation mechanism, and determine if they have an impact on plasma formation and properties. A detailed description of the generation process and the dynamics of runaway electrons will be presented in this chapter. Section 3.1 is devoted to studying the mechanism of generating superthermal electrons during magnetic field ramping. The techniques of suppressing runaway electrons during field ramping are discussed in Section 3.2. Section 3.3 is devoted to modeling the dynamics of superthermal electrons during field ramping. A brief description of the mechanism of producing superthermal electrons during ECRH discharges will be given in Section 3.4. The chapter will conclude with summary in Section 3.5.

### **3.1 Electron Runaways during Field Ramping**

Unlike tokamaks, in general stellarators are net current-free machines i.e. no current flows in the plasma except bootstrap current. In HSX, magnetic flux surfaces are generated using external currents flowing in modular coils. The current starts to flow in the main coils at ~250 msec from the trigger of the master timer in HSX, reaches a maximum at 800 msec, remains nearly constant for about 100 msec, then ramps down for almost 7 sec. A toroidal loop voltage with a maximum of 0.5 volt per turn is measured

experimentally during the field ramp-up and ramp-down using a two turn flux loop wrapped toroidally around the vacuum vessel. It can also be calculated by solving Faraday's integral law of electromagnetic:

$$\oint_l \vec{E} \cdot d\vec{l} = -\frac{\partial}{\partial t} \int_A \vec{B} \cdot d\vec{s} \quad (3.1)$$

John Canik and John Schmitt of the HSX group calculated the loop voltage by solving the magnetic vector potential equation and predicted a loop voltage of  $\sim 0.6$  volts. Figure 3.1 shows the main coils current and the loop voltage signals for a QHS 0.5 Tesla central heating discharge.

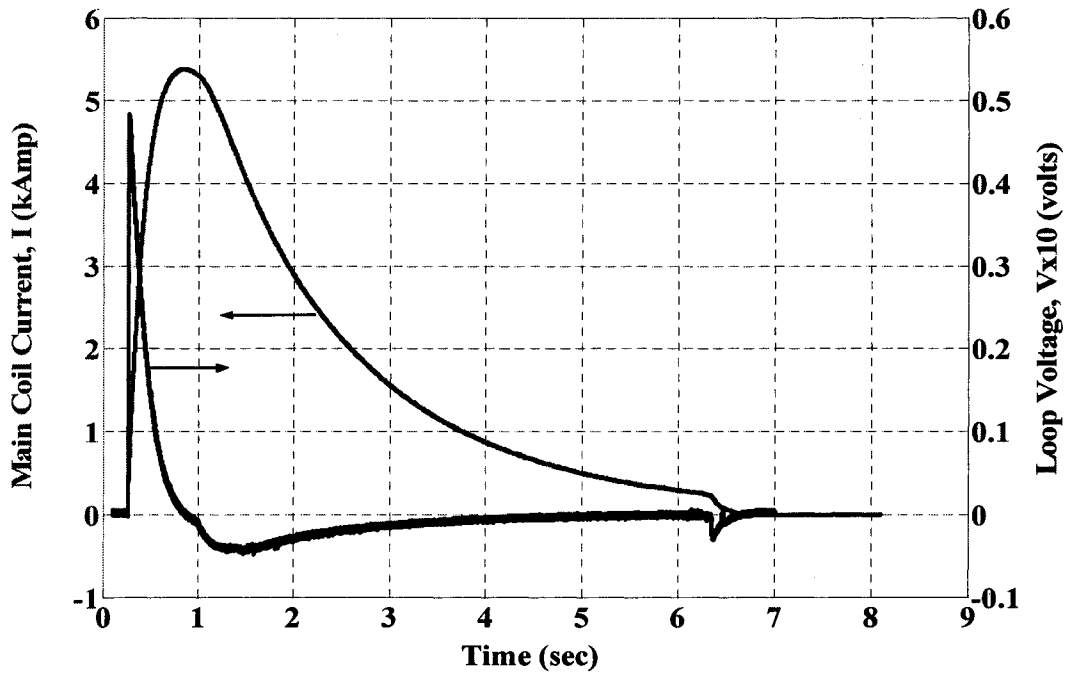


**Figure 3.1: Main coils current and toroidal loop voltage generated during field ramp-up and ramp-down.**

The loop voltage is zero up to the moment the current starts to ramp-up in the main coils, then it jumps to 0.5 volt then decays until it crosses zero at 850 msec. It flips sign during

field ramp-down reaching a minimum of -0.046 volt at 1340 msec, then decays back to zero.

### 3.1.1 Electron Runaway Theory

In order to assist the microwave gas breakdown, seed electrons need to be present during the time the microwave pulse is fired into the machine. At an early HSX operational stage, a thermionic filament working in a continuous mode was used to produce seed electrons. As seed electrons are emitted from the filament, they follow field lines and accelerate in the toroidal electric field during field ramp-up. Electrons emitted from the filament with small kinetic energy in the order of a few electron volts are acted upon by two counteracting forces, the parallel electric field  $E_{\parallel}$  ( $\parallel$  means parallel to the magnetic field line), and the total drag force. The total drag force is composed of, (1) a collisional drag force with the surrounding neutral gas molecules, both elastic and inelastic (i.e. ionization and excitation), (2) a synchrotron drag force, and (3) a bremsstrahlung drag force. The electron velocity is described by Newton's 2<sup>nd</sup> law:

$$\frac{dm_e \gamma \vec{V}}{dt} = q \vec{E} - m_e \vec{V} \nu^{e-n} - F_{sync.} - F_{brem.} \quad (3.2)$$

$$\nu^{e-n} = \sigma_{e-n} n$$

Where,  $\gamma = (1 - \frac{V^2}{C^2})^{-\frac{1}{2}}$ : is the relativistic factor,  $\vec{V}$ : is the electron velocity,  $\vec{E}$ : is the parallel electric field,  $m_e$  and  $q$ : are the electronic mass and charge,  $F_{sync.}$ ,  $F_{brem.}$ : are the synchrotron and bremsstrahlung losses respectively,  $\nu^{e-n}$ : is the electron-neutral total

collision frequency, i.e. summation of elastic ionization and excitation collision frequencies and  $\sigma_{e-n}$ : is the e-n total cross section (the electron-neutral ionization cross

section is given by  $\sigma_{e-n} = \frac{3.123 \times 10^{-15}}{\varepsilon} (\log_{10} \varepsilon + 0.792)^6$ , where  $\varepsilon$  is the electron kinetic

energy in eV). The maximum energy gained during ramp-up and ramp-down depends on many parameters like vessel gas pressure, loop voltage, magnetic configuration, etc. For the QHS configuration and  $10^{-7}$  torr base pressure, the maximum energy is on the order of 1.7-2 MeV. At this energy, synchrotron and bremsstrahlung losses can be neglected<sup>7</sup> with respect to collisional drag losses given by the second term on the left hand side of equation 3.2. If the collisional drag force is larger than the electrostatic force, no runaway electron production will take place. On the other hand, as the electron gains energy in the toroidal electric field, its collision frequency with the surrounding gas molecules will decrease (e-n collision cross section goes like  $\frac{\ln(\nu)}{\nu^2}$ , where  $\nu$  is the electron velocity<sup>6,8</sup>).

If the electric force is larger than the collisional drag force the electron will runaway, and theoretically its energy will increase indefinitely, unless otherwise it leaves the confinement volume. When the electron energy is high enough, it will emit hard x-rays in two different processes; through a close encounter with neutral gas molecules (thin target bremsstrahlung) and when hitting vessel walls or a limiter (thick target bremsstrahlung). Hard x-rays emitted by electron runaways during field ramp-up and ramp-down are shown in Figure 3.2. The x-axis represents the time in seconds and the y-axis represents three different signals; loop voltage in volts, main coil current in kA, and the hard x-ray

raw signal in volts. The figure shows that the loop voltage signals starts at  $\sim 250$  msec and jumps to a maximum of  $\sim 0.5$  volts in very short time (the spike shown is due to the change in slope of the coil current at  $\sim 250$  msec), then starts to decrease and reaches zero at  $\sim 850$ . During the field ramp-down phase the loop voltage reverses polarity.

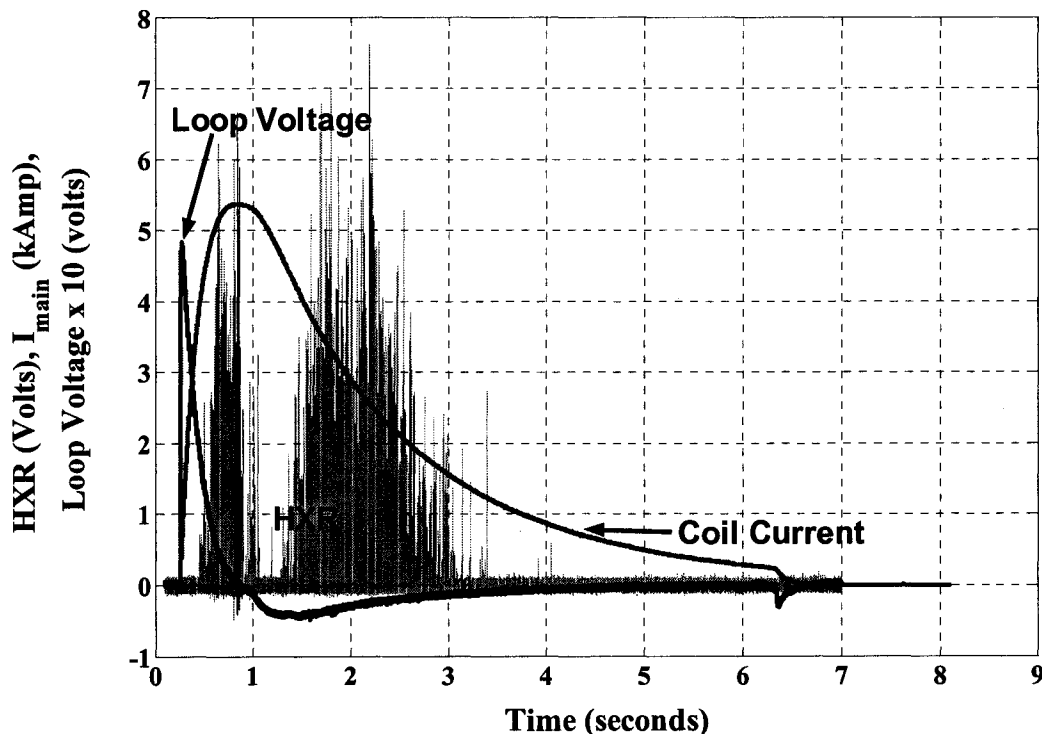


**Figure 3.2: Hard x-ray emitted during field ramp-up and ramp-down.**

The hard x-rays start to appear after  $\sim 100$ - $200$  msec (time taken by seed electrons to overcome electron-neutral collisions and become superthermal) from the inception of the loop voltage. The pulse height (corresponds to electron energy) increases with time to a maximum, then decreases until the signal disappears at 1000. When the loop voltage flips sign during field ramp-down phase, the already accelerated electrons start to decelerate until they reverse their direction. It takes the electrons  $\sim 100$ - $200$  msec to accelerate again in the reversed field and become superthermal. The x-rays start to appear again during the

ramp-down phase after  $\sim 1200$  msec, with higher intensity and pulse height. This can be attributed to the longer acceleration time during the ramp-down phase compared to ramp-up phase.

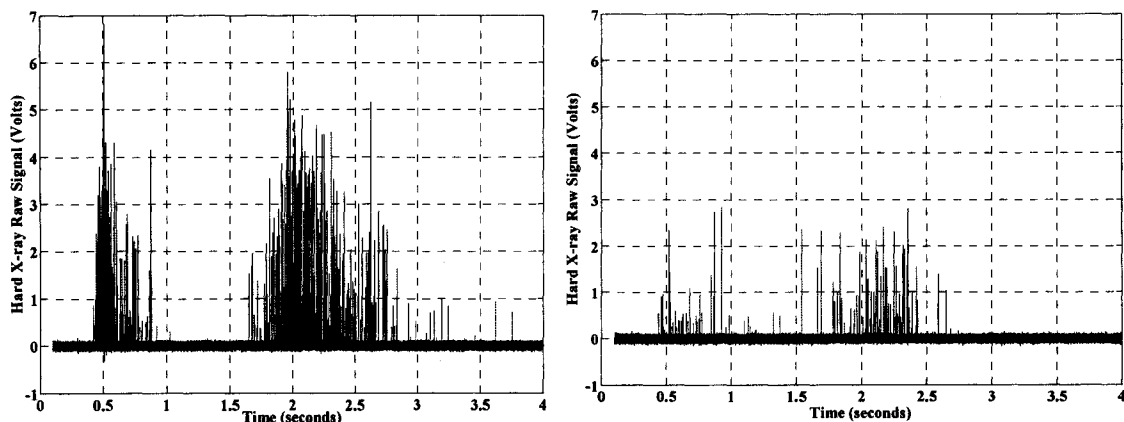


**Figure 3.3: Hard x-ray signal during field ramp-up and ramp-down for QHS (left) and Mirror (right) configurations at base pressure  $P_{\text{base}} \sim 10^{-7}$  torr.**

A large difference in hard x-ray emission during magnetic field ramp-up and ramp-down (magnet shots, no ECRH plasma discharges took place) was noticed between configurations. Figure 3.3 shows the hard x-ray emission from runaway electrons produced during field ramping in QHS and Mirror configurations. There is no signal in case of AntiMirror configuration. The figure shows lower hard x-ray intensity and energies (pulse height) in Mirror compared to QHS configuration. Single particle calculations shows that for passing particles (due to their high parallel velocity, runaway electrons are considered passing particles because the electric field accelerate the particle in the  $\vec{B}$  direction) no difference in confinement between QHS and Mirror configurations is expected. Although the results shown in Figure 3.3 are interesting and show that there is indeed a difference between magnetic configurations, it can't be explained using

passing particle model. A reasonable explanation can be made by assuming that low energy electrons in the Mirror configuration are in direct loss orbits due to their pitch angle scattering resulting from collisions with neutral gas molecules and they leave the machine before they become superthermal. This may be why we see low energy and intensity hard x-rays in Mirror compared to QHS configuration.

### **3.2 Techniques of Decoupling Superthermal Electron Sources.**

As stated earlier in Section 3.0, hard x-rays emitted by superthermal electrons generated during magnetic field ramp-up phase interfere with those emitted during the ECRH discharge. To prevent x-ray interference, it is necessary to suppress the generation of superthermal electrons during field ramp-up phase. Two different mechanisms for suppressing superthermal electrons during field ramp-up were studied: (1) increasing the vacuum base pressure and (2) using ultraviolet flash lamp for preionization. Alternate methods like using a mechanical paddle installed inside the vacuum vessel have been used before on other machines like ATF<sup>9</sup> and TJ-II<sup>10</sup> torsatrons, but were not practical for HSX application. In HSX we noticed that electrostatic probes play an equivalent role as the movable paddle in the ATF and TJ-II machines. When the probes are inserted inside the machine, the hard x-ray signal is reduced and the reduction in the signal is related to the insertion distance of the probe inside the machine. The higher the insertion distance the higher the reduction in the hard x-ray signal. The reduction of the signal can be attributed to the rapid loss of superthermal electrons when they collide with the probe, higher losses are expected when the probe insertion distance increased because of the

higher superthermal electron population generated near the magnetic axis during on-axis ECRH. A detailed discussion of both techniques is given below.

### 3.2.1 Base Pressure Method.

A programmable gas feed system is being used in HSX to control the gas injection into the vacuum vessel. The system consists of a piezoelectric gas flow valve, a plenum, a pulse-width modulated controller, and a Labview interface. The normal base pressure in HSX is about  $10^{-7}$  torr. Increasing the base pressure increases molecular gas density. Equation 3.2 shows that increasing the molecular gas density increases the electron-neutral collision frequency. If the base pressure is increased to a level where the collisional drag force is greater than the accelerating electric force, no electron runaway formation will take place. In order to test this idea experimentally, magnet shots (i.e. no ECRH plasma discharge take place, only field ramping) were taken at different vacuum base pressures. Figures 3.4 through 3.7 show the hard x-ray measurements during magnet shots at four different levels of vacuum base pressure. The x-axis represents the time in seconds and the y-axis represents the hard x-ray raw signal in volts. Every spike or pulse represents a photon counted by the radiation detector. The pulse height corresponds to the x-ray photon energy. (The higher the hard x-ray spike, the more energetic the photon is). The number of spikes per second corresponds to the intensity of the hard x-rays. The higher the hard x-ray intensity, the higher the superthermal electron population and vice versa. The figures show that increasing the gas base pressure from  $7.5 \times 10^{-8}$  to  $4.4 \times 10^{-6}$  torr decreases the hard x-ray intensity and energy.

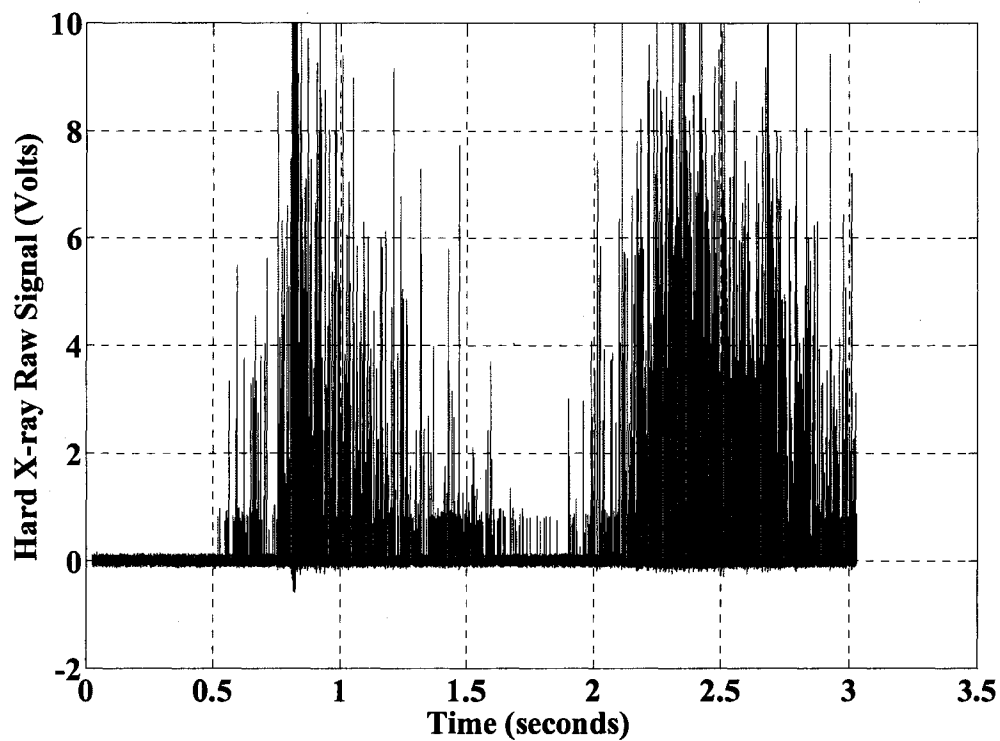


Figure 3.4: Hard x-ray signal during field ramping  $P_{\text{base}} = 7.5 \times 10^{-8}$  torr.

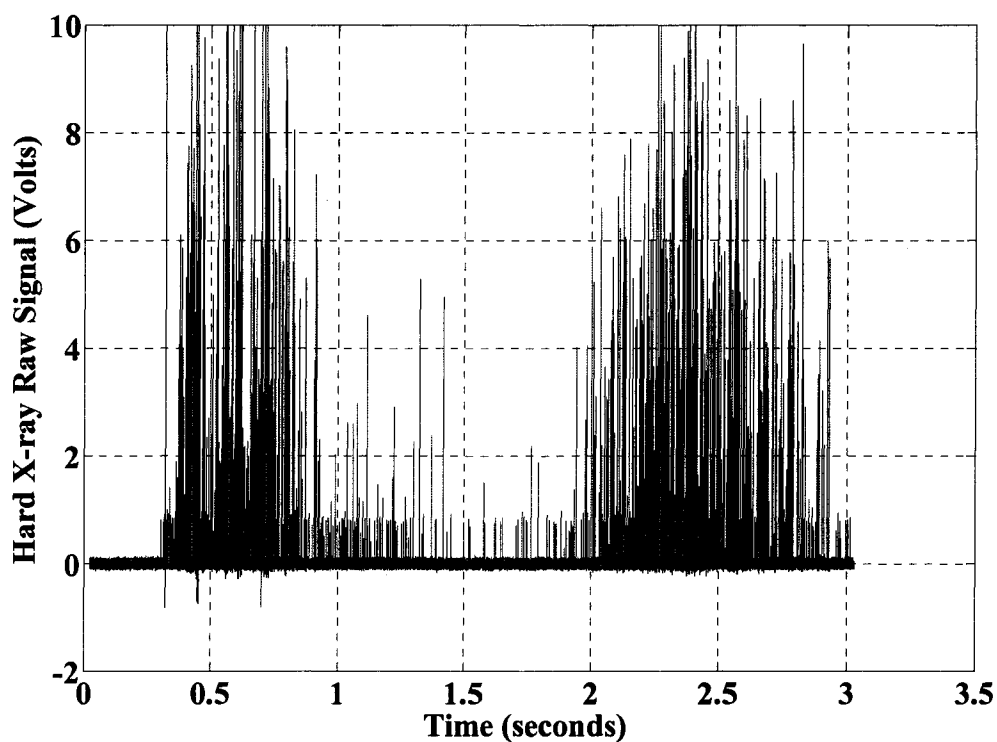


Figure 3.5: Hard x-ray signal during field ramping  $P_{\text{base}} = 5.6 \times 10^{-7}$  torr

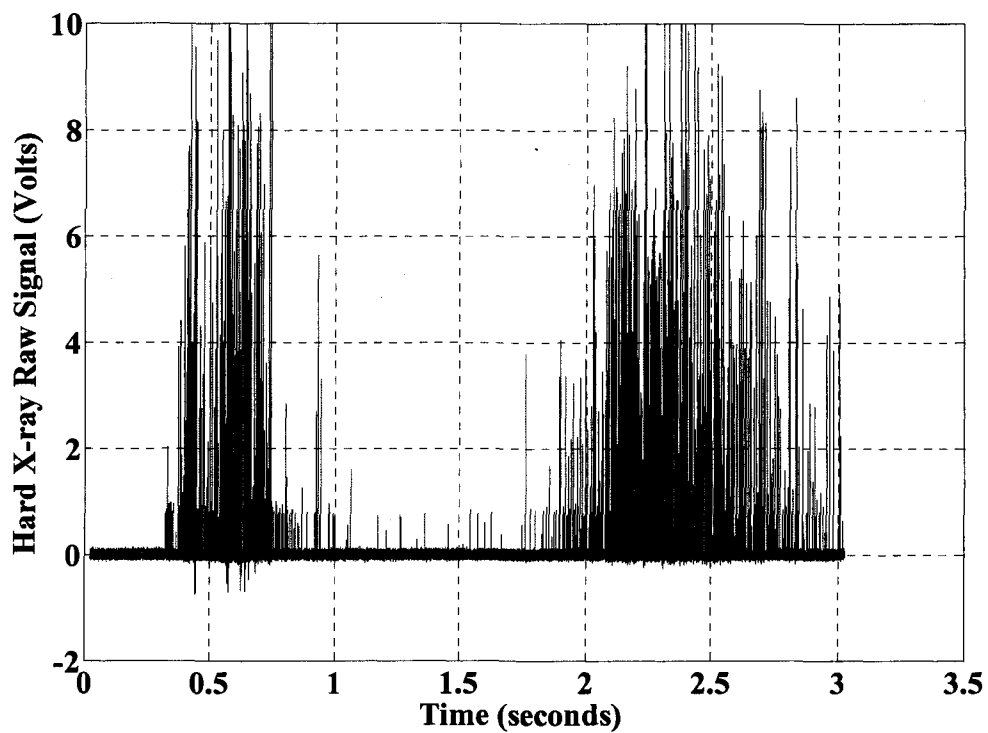


Figure 3.6: Hard x-ray signal during field ramping  $P_{\text{base}} = 6.5 \times 10^{-7}$  torr

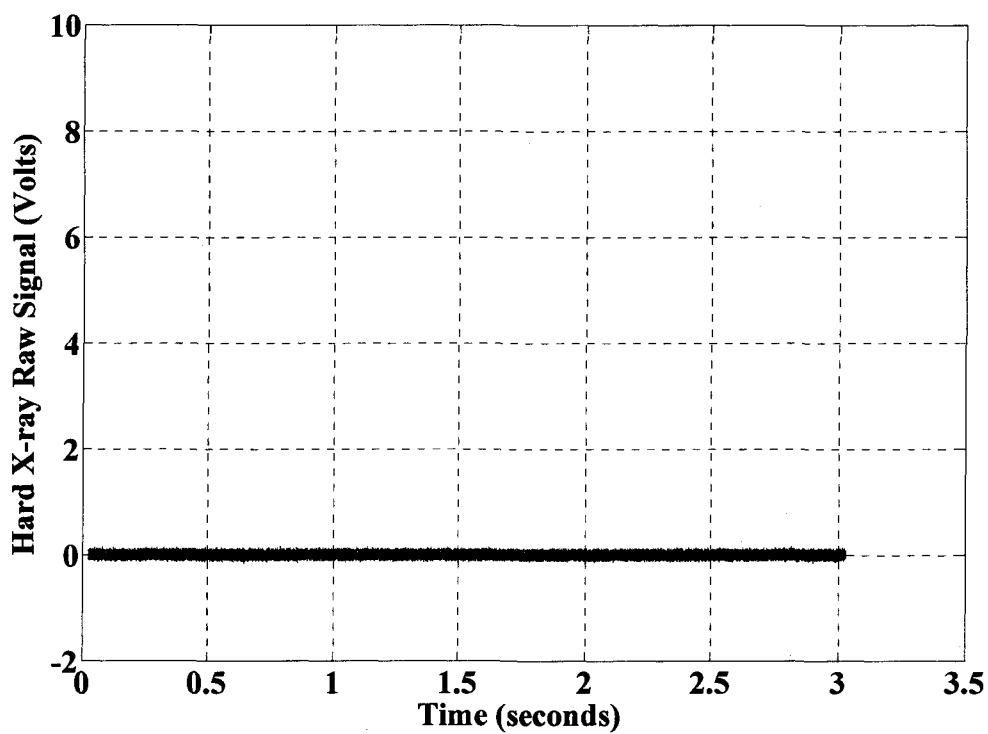


Figure 3.7: Hard x-ray signal during field ramping  $P_{\text{base}} = 4.4 \times 10^{-6}$  torr.

No hard x-rays above the detector threshold energy of 20 keV are detected at a base pressure  $P_{\text{base}} \geq 4.4 \times 10^{-6}$  torr. This indicates that superthermal electrons with energies greater than 20 keV are suppressed during field ramping. At this base pressure, when seed electrons leave the filament and follow local magnetic field lines, they will have sufficient collisions with the surrounding gas molecules to prevent them from accelerating in the toroidal electric field and becoming runaways.

The situation is completely different if superthermal electrons are generated at a normal base pressure, i.e.  $P_{\text{base}} \sim 10^{-7}$  torr, and then a gas puff is used to suppress them. In another set of experiments, the base pressure was kept constant at  $\sim 10^{-7}$  torr at the beginning of the magnet shot so that superthermal electrons are easily generated and an intense hard x-ray signal is produced. At 780 msec from the trigger of the master timer in, a uniform gas puff for duration of 70 msec is injected into the machine. Figures 3.8 through 3.11 show the results of puffing gas after superthermal electrons are already generated during field ramping. The x-axis represents the time in seconds, the left y-axis represents the hard x-rays emitted from superthermal electrons during the magnet shots and the right y-axis represents the neutral base pressure during the experiment as measured by micro ion gauge (the ion gauge has a response time of  $\sim 50$  msec). Figure 3.8 shows a normal magnetic shot without any additional gas puff. The base pressure was  $P_{\text{base}} \sim 2 \times 10^{-7}$ . Figures 3.9 through 3.11 show that, the higher the amount of gas puffed into the machine the lower the hard x-ray intensity and energy generated after the beginning of the puff. Figure 3.11 shows that gas puffs with a maximum pressure of the order of  $\sim 10^{-4}$  torr was sufficient to suppress superthermal electron generation at later

times to the gas puff. This pressure is higher than the pressure needed to suppress the production of superthermal electrons measured in the previous experiment  $\sim 4.4 \times 10^{-6}$  torr. This can be explained in light of superthermal electron collisionality with neutral gas molecules. As described in Appendix 3, the electron-neutral collision cross section goes like  $\sigma_{e-n} \propto \ln(v)v^{-2}$ , where  $v$  is the electron velocity, so smaller electron-neutral collisionality  $\nu_{e-n} = \sigma_{e-n}n$  is expected at higher electron energy as compared to lower energies. In order to increase the collisionality and suppress the already generated superthermal electrons  $n$  should be increased, i.e. more gas is needed. This can be achieved by increasing the amount of gas puffed into the machine after the superthermal electrons are already generated. The dip in the pressure signal shown in Figure 3.8 indicates that the micro ion gauge is sensitive to the magnetic field.

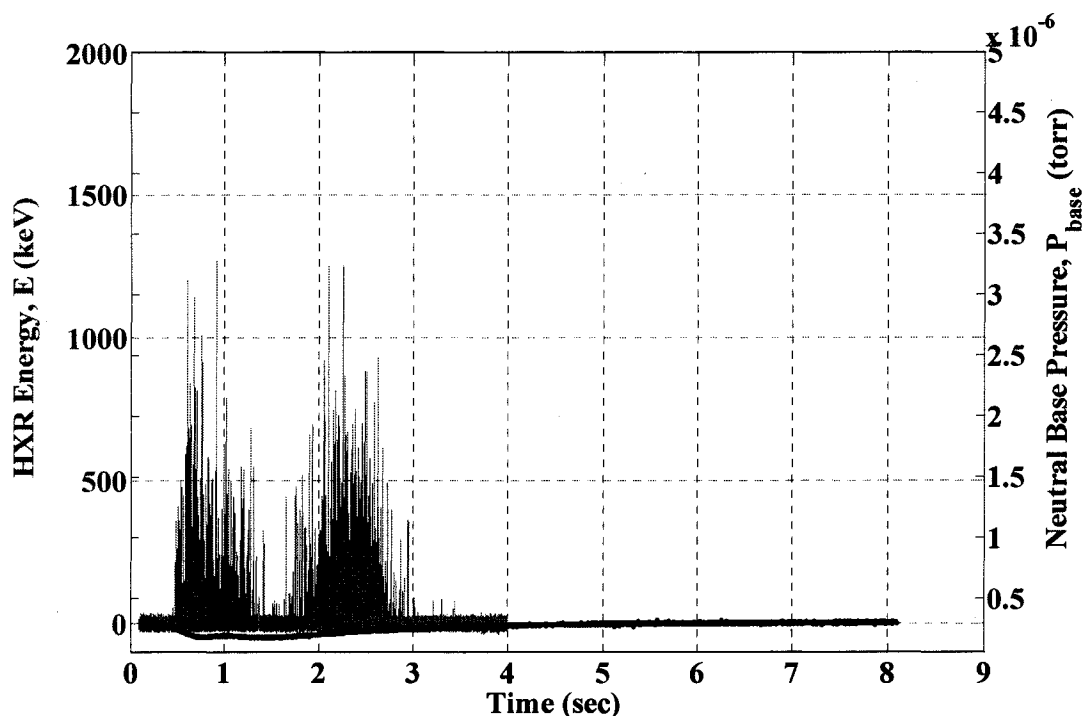


Figure 3.8: Hard x-ray signal during field ramping. No gas puff.

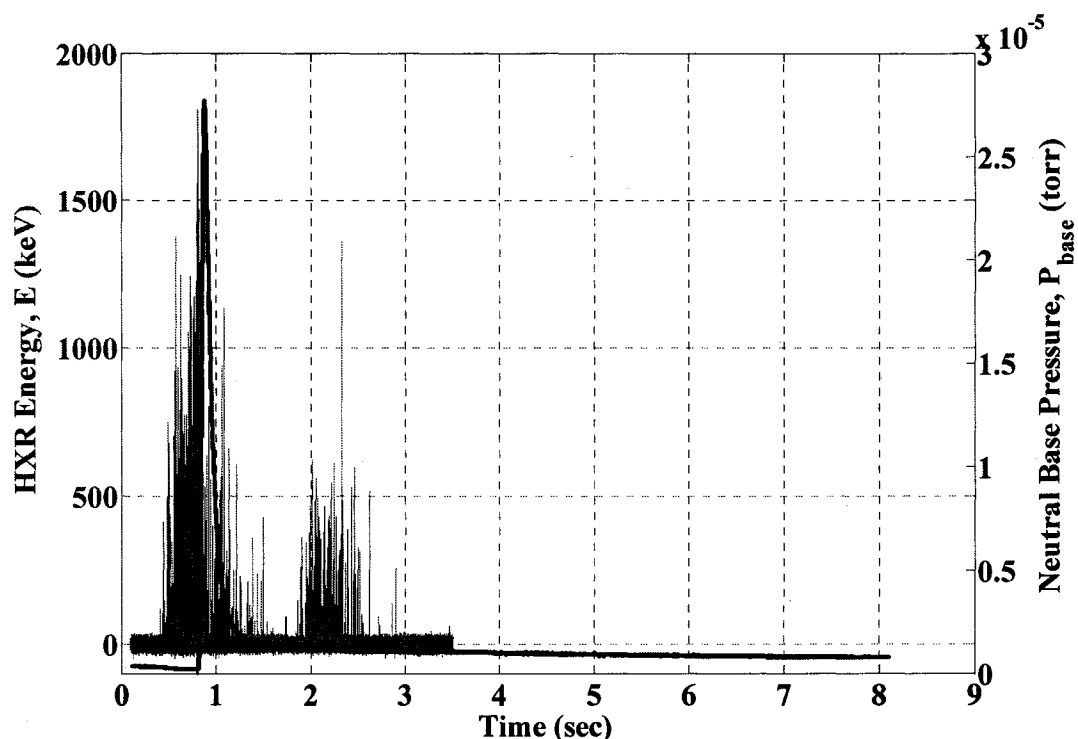


Figure 3.9: Hard x-ray signal during field ramping.

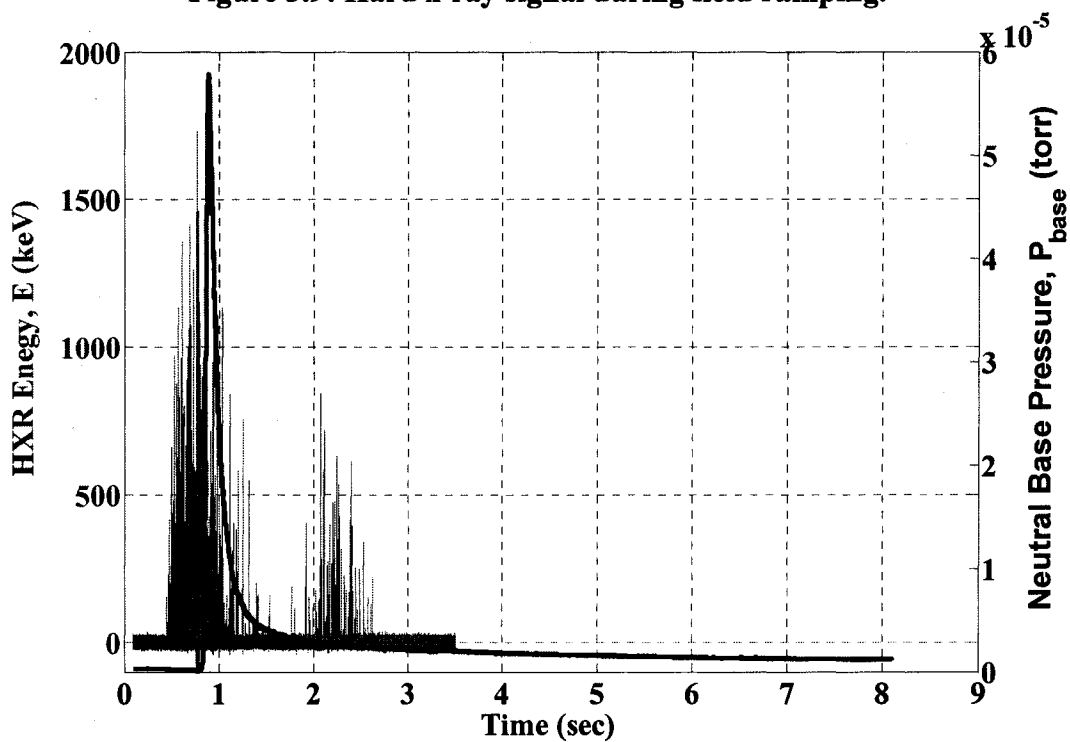


Figure 3.10: Hard x-ray signal during field ramping.

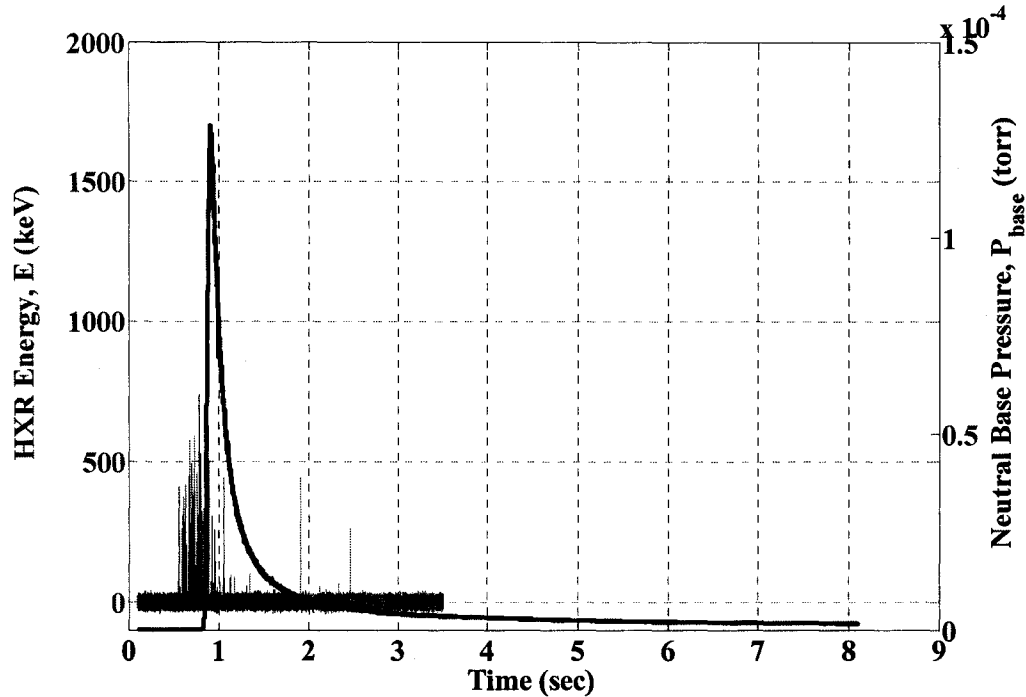
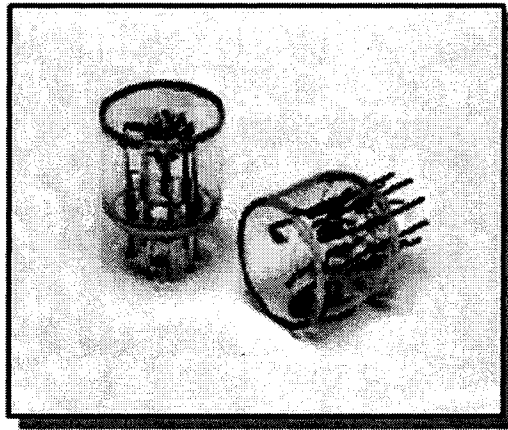


Figure 3.11: Hard x-ray signal during field ramping.

### 3.2.2 Ultraviolet Xenon Flash Lamp Method.

As stated earlier in Section 3.1.1, a thermionic filament was conventionally used in HSX to assist plasma breakdown. The problem with the filament was its continuous mode of operation, i.e. it emits electrons continuously during field ramping. Those electrons are accelerated by the toroidal loop voltage during field ramp-up and become runaways. One way to solve this problem and be able to control the production and acceleration of superthermal electrons during field ramp-up is to control the number of seed electrons and their injection time. This can be done by using a pulsed electron source. Using a pulsed source, electrons will be injected once into the machine during the ramp-up phase at a time where the loop voltage is small enough not to produce runaway electrons. Only low energy electrons will be present to assist the microwave breakdown without

producing hard x-rays during the ECRH discharge. Using the thermionic filament in pulse mode was not a good idea for two reasons (1) its long response time (2) biased injection and the problem of getting electrons into the confining region. For this reason, two different techniques were studied to produce pulsed seed electrons; (1) using a fast shutter in front of the thermionic filament to produce a pulse of electrons and (2) using a pulsed UV source to produce seed electrons through the photoelectric effect with neutral gas and vessel wall. The first technique was excluded because of the high cost of the shutter and its expected mechanical troubles.



**Figure 3.12: Xenon UV flash lamp.**

A Xenon UV flash lamp (shown in Figure 3.12) produced by Hamamatsu working in pulsed mode was used instead in HSX to produce the seed electrons needed to assist the plasma breakdown. The lamp works in pulse mode, the pulse duration is in the order of 100  $\mu$ seconds, and it has a maximum repetition rate of 100 Hz. The lamp is installed outside the vacuum vessel in HSX facing a glass window that permits ultraviolet light penetration to the machine. The lamp can be gated using a conventional TTL pulse for any period of time up to 1 sec. The output light spectrum emitted by the lamp is shown in

Figure 3.13. The lamp has a wide emission spectrum from 200 to 800 nm with the maximum emission concentrated mainly in the ultraviolet range from 200 to 300 nm. The lamp specifications are listed in Table 3.1.

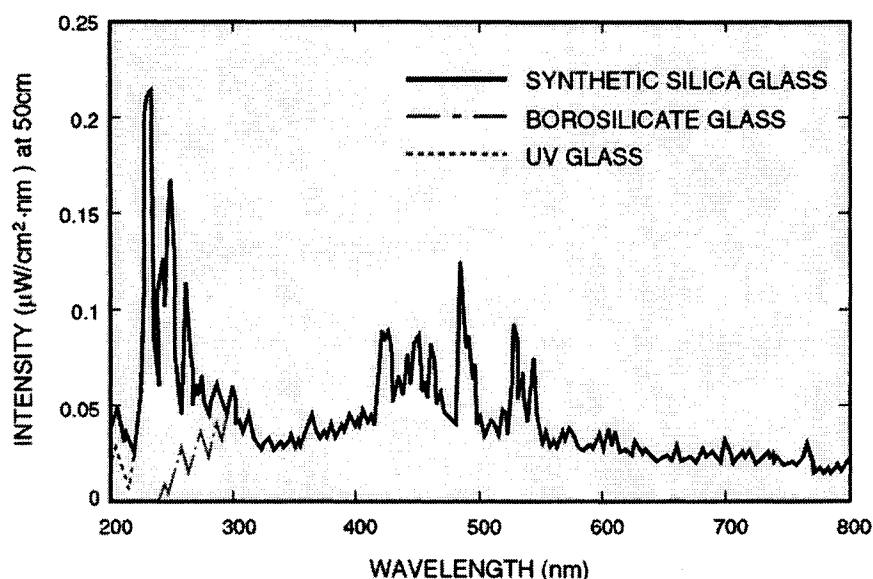


Figure 3.13: Xenon flash lamp output light spectrum.

Property	Value
Window Material	Synthetic Silica
Arc Size	8.0mm
Min Wavelength	160nm
Max Wavelength	2000nm
Max Average Input Power	15W
Repetition Rate Max	100Hz
Jitter	200ns
Output Fluctuation	2.5%
Guaranteed Life	$1.2 \times 10^9$ number of flashes
Cooling	Not required

Table 3.1: Xenon flash lamp specifications.

A candidate time window for injecting seed electrons into the machine is shown in Figure 3.14 between 500 to 700 msec. As will be discussed shortly, it was notice that if electrons are injected into the machine at times later than 500 msec no hard x-ray signal is

detected. This indicates that there is no superthermal electrons present in the machine with energies above the detector threshold energy of 20 keV.

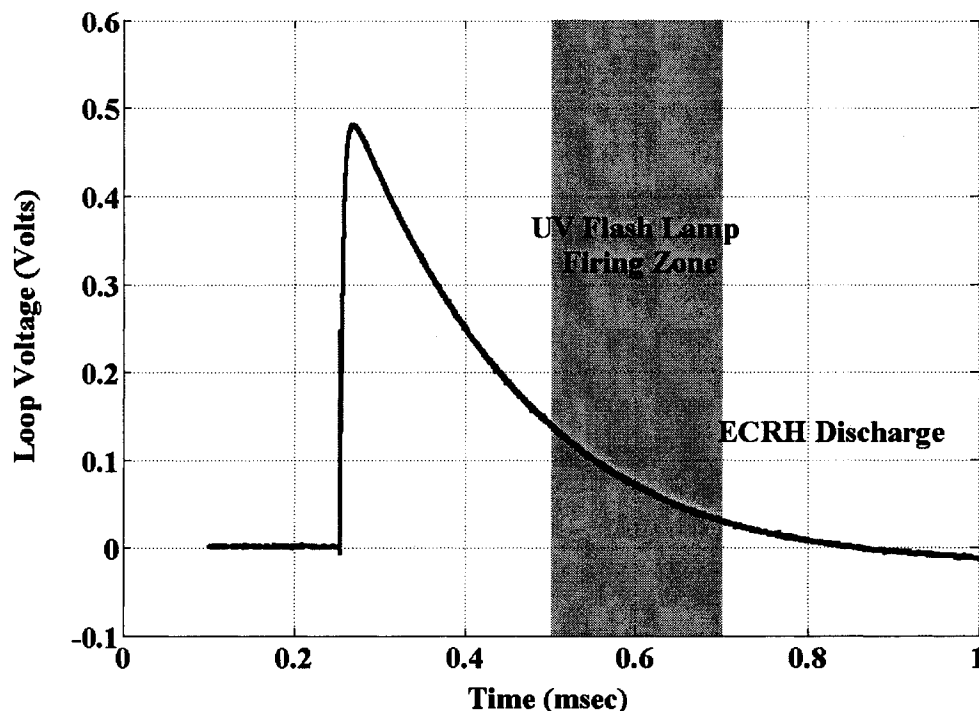


**Figure 3.14: Loop voltage during field ramping. Red strip indicates firing zone for UV flash lamp.**

Ultraviolet photons can ionize a neutral atom and produce seed electrons in the confinement volume. The birth time of those electrons can be set by the firing time of the UV flash lamp. Theoretically, it takes no time to produce seed electrons through the photoelectric effect, so electrons are considered to be produced at the same time the UV flash is fired into the machine.

The optimum time to trigger the UV lamp is picked so that we have no hard x-ray without plasma and prompt plasma breakdown. When UV lamp is triggered earlier than that, we will produce hard x-rays before the plasma, and when it is triggered later we have no hard x-ray without plasma but we have a large delay in breakdown from the

onset of the ECRH pulse. In order to study the effect of UV flash lamp firing time during field ramp-up on hard x-ray production, the lamp is triggered at various times during ramp-up from 300 to 700 msec and the hard x-ray signal and plasma breakdown time were measured. It was noticed that, when the lamp was fired earlier during the peak of loop voltage (i.e. around 300 msec), the hard x-rays are still detected around the machine and the plasma breakdown time is on the order of 2-3 msec, as was the case when the thermionic filament was used. When the firing time is advanced up to 500 msec, the hard x-ray signal decreases and the same plasma breakdown time was observed, as shown in Figure 3.15. When the flash lamp is triggered at times later than 500 msec, the hard x-ray signal disappeared, indicating runaway electrons with energies higher than the detector threshold (20 keV) were suppressed, and a delay in plasma breakdown time is observed. Figure 3.16 shows the hard x-ray signal for two different lamp firing times, 300 and 550 msec. Figure 3.16 shows that when the lamp is fired at 300 msec, the hard x-ray signal during the field ramp-up is still interfering with the signal generated during the plasma. On the contrary, when the lamp was fired at 550 msec, no hard x-ray signal is observed before the plasma. This indicates that the loop voltage at times later than 550 msec is not enough to overcome the electron-neutral collisionality and accelerate electrons to energies above the detector threshold energy of 20 keV. To suppress hard x-ray emission from runaway electrons during field ramp-up during the current research, the UV flash lamp was triggered at 550 msec.

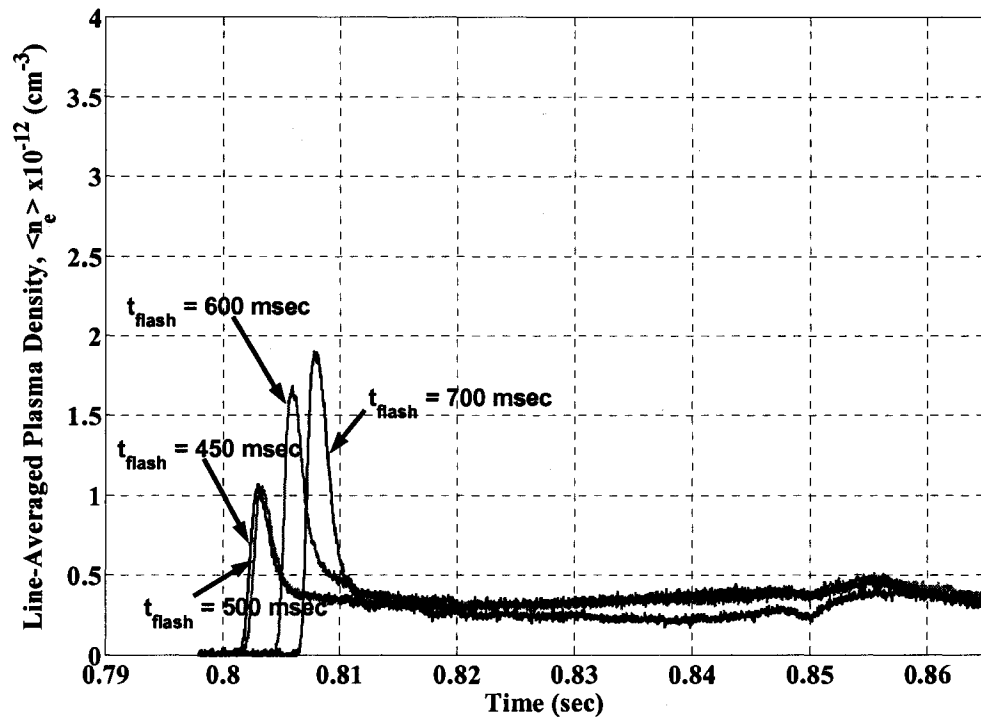


Figure 3.15: Plasma electron density time evolution at different UV flash lamp firing times

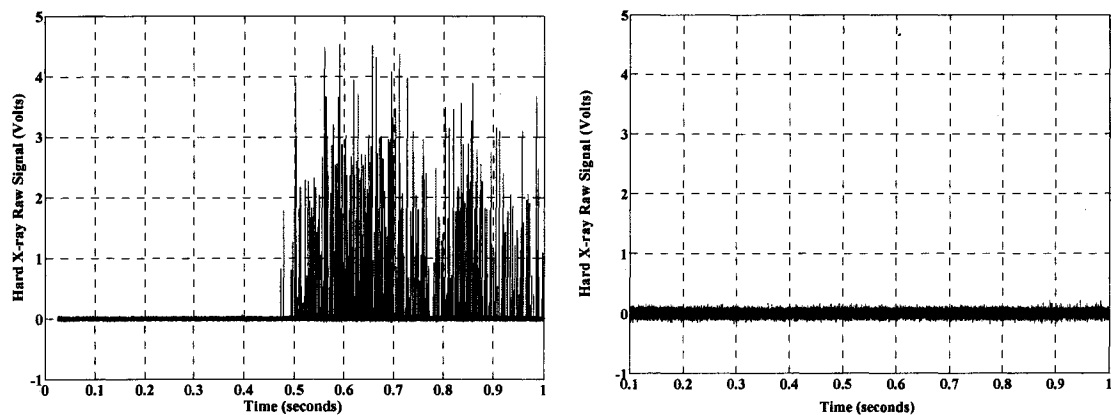


Figure 3.16: HXR signal for two different lamp firing times. (Left) lamp fired at 300. (Right) lamp fired at 550 msec.

### 3.3 Modeling of Electron Runaways during Field Ramping.

In order to study the dynamics of runaway electrons generated during field ramping, equation 3.2 was solved numerically with simplified assumptions. The

maximum runaway electron energy gained in the toroidal electric field as measured from hard x-ray signal is about 2 MeV, synchrotron and bremsstrahlung losses can be ignored at this energy range. The collision drag force was excluded from the Newton's second law equation in order to predict an upper bound to the electron energy gained in the loop electric field as a function of time. The following simplified version of equation of motion is numerically solved:

$$\frac{dm_e \gamma \vec{V}}{dt} = -e \vec{E} \quad (3.3)$$

All terms have the same meaning as equation 3.2. The initial electron kinetic energy is taken to be zero; this is a reasonable assumption since seed electrons are generated with a maximum kinetic energy of about 6 electron volts using UV flash lamp. The measured toroidal electric field generated during field ramping was used in the numerical calculations. If the particle is launched with zero initial kinetic energy at initial time  $t_{ini}$ , it can be followed in the accelerating toroidal electric field up to  $t_{final}$  and its final kinetic energy is determined. Because collisionality was neglected from the beginning, the electron final kinetic energy is considered the maximum energy the electron can gain in the accelerating field assuming  $t_{final} - t_{ini} \leq$  confinement time (otherwise the electron will be lost in a confinement time scale). To validate the modeling, the flash lamp was triggered once through the machine at specified time  $t_{ini}$  during field ramping, and hard x-ray was detected and compared to the maximum electron energy gain from the modeling. Figures 3.17 through 3.20 show the experimental results for different  $t_{ini}$ .

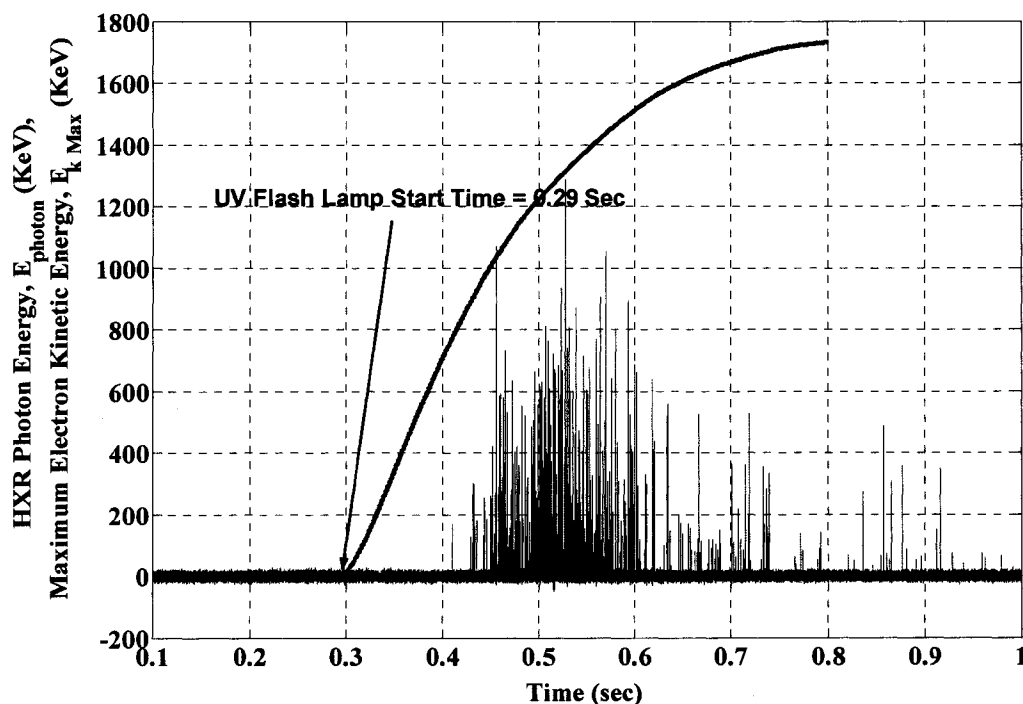


Figure 3.17: Hard x-ray generated when flash lamp was fired at 290 msec and the maximum electron energy gained with  $t_{\text{ini}} = 290$  msec.

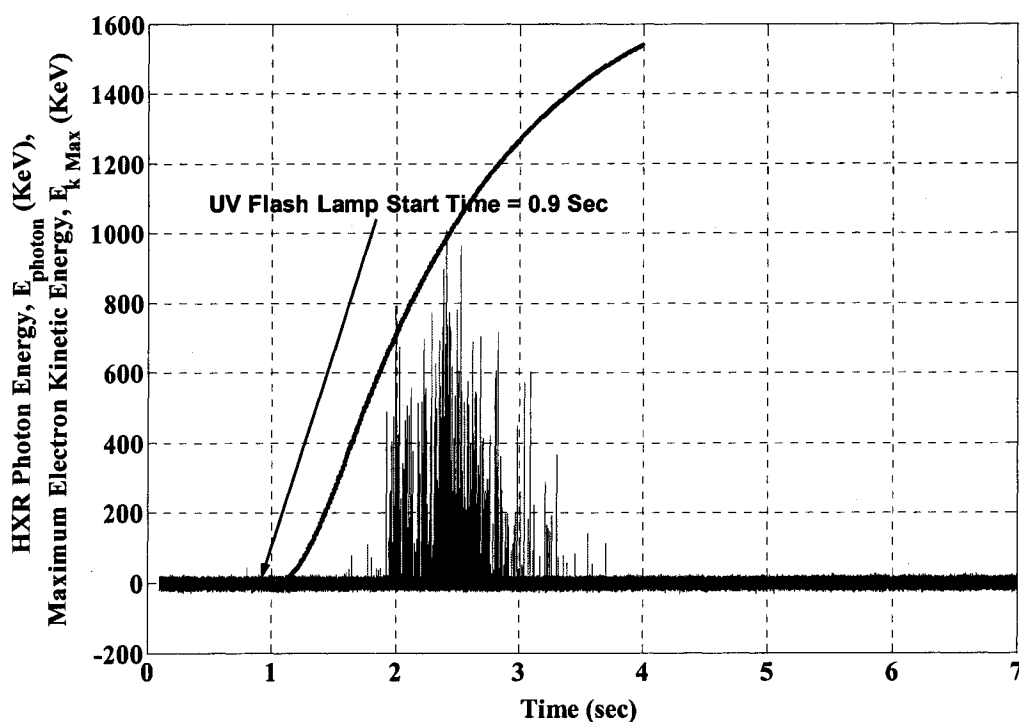


Figure 3.18: Hard x-ray generated when flash lamp was fired at 900 msec and the maximum electron energy gained with  $t_{\text{ini}} = 900$  msec.

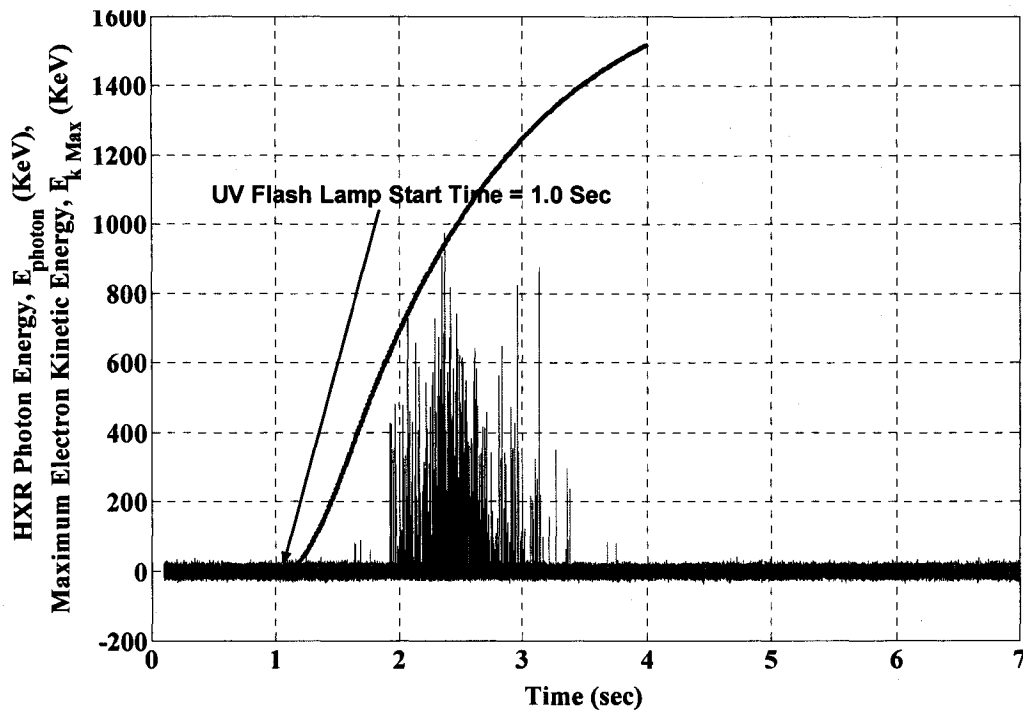


Figure 3.19: Hard x-ray generated when flash was lamp fired at 1000 msec and the maximum electron energy gained  $t_{ini} = 1000$  msec.

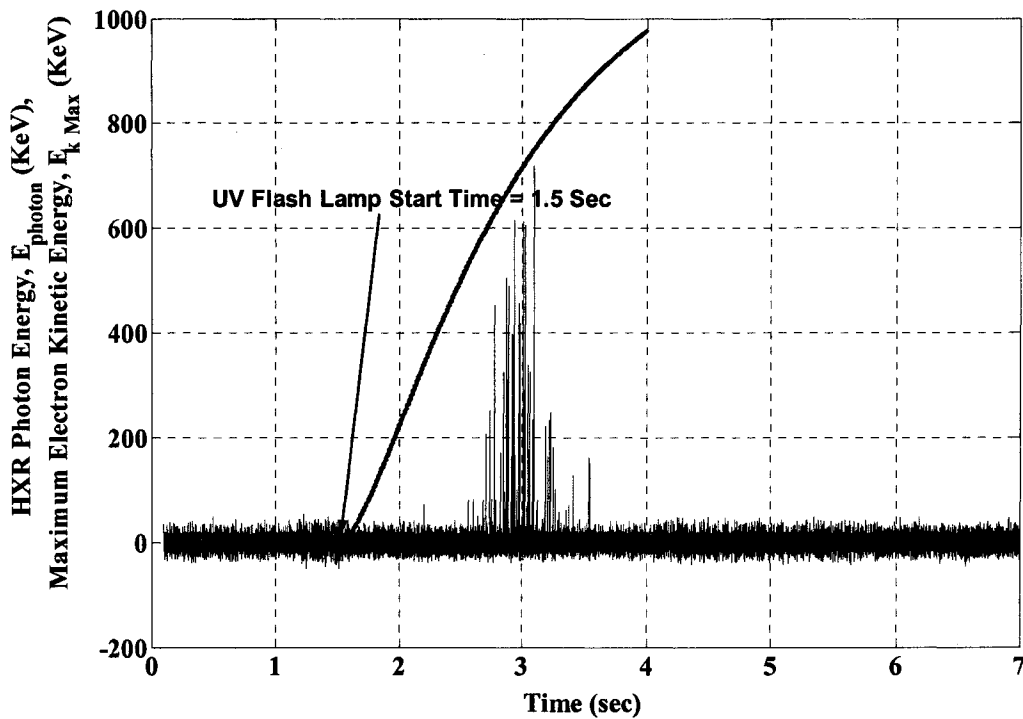


Figure 3.20: Hard x-ray generated when flash lamp was fired at 1500 msec and the maximum electron energy gained  $t_{ini} = 1500$  msec.

The x-axis represents the time in seconds and the y-axis represents the hard x-ray raw signal in keV (the x-rays spikes in volt are multiplied by the calibration factor to give the x-ray photon energy in keV) and the maximum electron energy in keV calculated from the model (red line). Figure 3.17 shows that when the UV lamp was triggered during the field ramp-up phase at 290 msec, it took  $\sim 130$  msec for the hard x-rays to appear. The energy gained by the launched electrons is not the same because of their stochastic collisionality behavior with the neutral gas molecules. Some electrons survive collisions and gain the maximum kinetic energy while others have the highest collisionality and gain the minimum kinetic energy. The un-collided electrons produce the maximum photon energy and they are shown in the figure at times when the hard x-ray spikes coincide with the calculated maximum kinetic electron energy. The results for triggering the UV flash lamp at three different times, 900 1000, and 1500 milliseconds respectively during the magnetic field ramp-down phase are shown in Figures 3.18 through 3.20. The figures show that the longer the lamp trigger time, the lower the hard x-ray signal. This is logical because electrons spend less time in the accelerating electric field and the field is weaker at longer times as shown in Figure 3.1.

### **3.4 Electron Runaways during ECRH Discharges.**

In the HSX stellarator, plasma is produced and heated using 2<sup>nd</sup> harmonic, X-mode ECRH. A linearly polarized microwave with frequency of 28 GHz is used for this purpose. To illustrate the production mechanism of runaway electrons during ECRH, a

brief description of the wave-particle interaction model for 2<sup>nd</sup> harmonic is given below; a detailed numerical analysis of the heating model will be given in Chapter 5.

The resonance condition for the  $n^{\text{th}}$  harmonic electron cyclotron resonance in plasma is given by<sup>11,12</sup>:

$$\omega - k_{\parallel} v_{\parallel} = n\Omega \quad (3.4)$$

Where  $\omega$  : microwave angular frequency,  $k_{\parallel}$  : parallel wave number,  $v_{\parallel}$  : electron parallel velocity,  $n$  : harmonic number, and  $\Omega = \frac{|e|B}{m_e}$  : electron cyclotron frequency. Equation 3.4 shows that the resonance will take place if the Doppler-shifted wave frequency in the reference frame of the particle  $\omega - k_{\parallel} v_{\parallel}$  is equal to the  $n^{\text{th}}$  harmonic of the cyclotron frequency  $n\Omega$ . In 2<sup>nd</sup> harmonic X-mode heating, the microwave propagates perpendicular to the local magnetic field in the resonance location and there is no parallel propagation,  $k_{\parallel} = 0$ ,  $\vec{k}_{\perp} \neq 0$ . The microwave electric field is linearly polarized and is directed in the perpendicular direction to both the local magnetic field and the wave perpendicular propagation vector  $\vec{k}_{\perp}$ . The electric field changes polarity twice as fast as the particle gyro frequency.

Conceptual pictures are shown in Figures 3.21 and 3.22 to illustrate the 2<sup>nd</sup> harmonic wave-particle interaction<sup>13</sup>. The electron is gyrating at frequency  $\Omega$  around magnetic field  $B_o \hat{z}$ . The electric field can be represented as  $\vec{E}(x, t) = E_o \cos(\omega t - k_{\perp} x) \hat{y}$  with a frequency  $\omega = 2\Omega$ . Two different situations are studied (1)  $\vec{k}_{\perp} = \frac{\pi}{2\rho_L}$  and (2)

$\bar{k}_\perp \neq \frac{\pi}{2\rho_L}$ , where  $\rho_L = \frac{v_\perp}{\Omega_e}$  is the electron gyro-radius as shown in Figures 3.21 and

3.22 respectively.

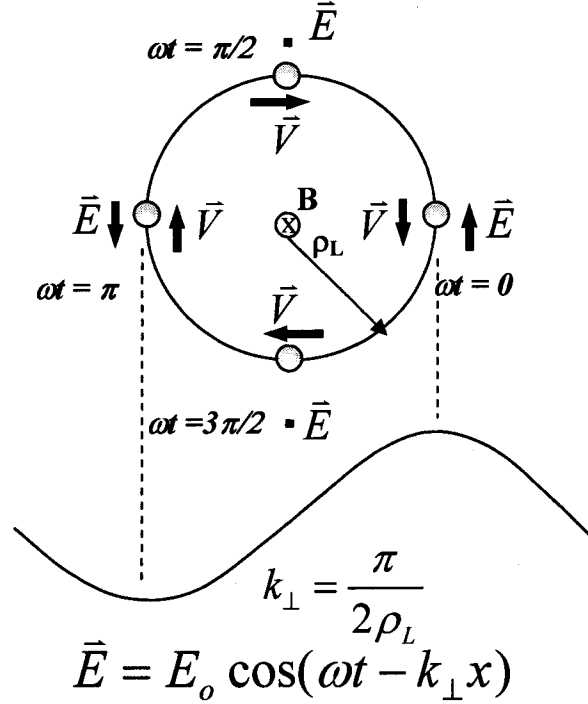
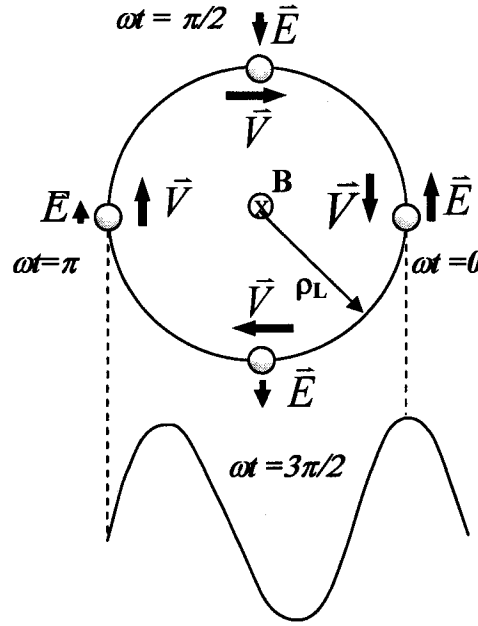


**Figure 3.21: Second harmonic, ECRH from wave-particle interaction perspective**

$$\text{for } \bar{k}_\perp = \frac{\pi}{2\rho_L}.$$

In the case shown in Figure 3.21 where  $\bar{k}_\perp = \frac{\pi}{2\rho_L}$  at  $\Omega t = 0$  and if the angle between the microwave electric field vector  $\bar{E}(x,0)$  and the electron velocity vector is  $180^\circ$  the electron will be accelerated by the wave electric field. At time  $\Omega t = \pi$ , although the temporal variation of the wave electric field vector  $\omega t = 2\Omega t = 2\pi$  has restored  $\bar{E}(x,t)$  to its initial value and direction at  $t = 0$ , the electric field spatial variation  $k_\perp \Delta x = \pi$  has reversed the direction of  $\bar{E}$  compared to its initial direction at  $t = 0$ . The

electron will be accelerated again at this location and there is net energy gain from the microwave. This situation represents the maximum energy an electron can gain from the electric field.



$$\vec{E} = E_o \cos(\omega t - k_{\perp} x)$$

$$k_{\perp} \neq \frac{\pi}{2\rho_L}$$

**Figure 3.22: Second harmonic, ECRH from wave-particle interaction perspective**

$$\text{for } \bar{k}_{\perp} \neq \frac{\pi}{2\rho_L}.$$

In the other case, if  $\bar{k}_{\perp} \neq \frac{\pi}{2\rho_L}$  at  $\Omega t = 0$  and if the angle between the microwave electric field vector  $\vec{E}(x,0)$  and the electron velocity vector is  $180^\circ$ , the electron will be accelerated by the wave electric field. At  $\Omega t = \pi$ , the electric field amplitude will be smaller than its corresponding value at  $t = 0$  and its direction will depend on the exact value of  $\bar{k}_{\perp}$ . It might be in the same or opposite direction of the electron motion. If the

electric field vector is directed parallel to the electron velocity vector as shown in Figure 3.22, the electron will be decelerating. Although the electron will be decelerating at  $\Omega t = \pi$ , there is net energy gain because the acceleration at  $t = 0$  is greater than the deceleration at  $\Omega t = \pi$ .

To give rudimentary explanation for the energies gained during ECRH, we will investigate the 2<sup>nd</sup> harmonic condition given by Equation 3.4. The resonance condition after simple algebraic manipulation can be written as:

$$\frac{2eB_o}{m_e \omega} + \left( \frac{2eB}{m_e \omega} \sqrt{1 - \beta^2} - \frac{2eB_o}{m_e \omega} \right) \pm N_{\parallel} \beta_{\parallel} = 1 \quad (3.5)$$

$$\beta = \frac{\sqrt{\left(\frac{\varepsilon}{m_e c^2}\right)^2 + 2\left(\frac{\varepsilon}{m_e c^2}\right)}}{\left(\frac{\varepsilon}{m_e c^2}\right) + 1} = \frac{\sqrt{\gamma^2 - 1}}{\gamma} = \frac{v}{c} \quad (3.6)$$

Where  $C$  the speed of light,  $m_e$  and  $e$  are the electron rest mass and charge,

$$\gamma = \sqrt{1 + \frac{p^2}{m_e^2 c^2}}, \quad B_o = 0.5 \text{ Tesla for, } B \text{ is the magnetic field at the particle location, } \parallel$$

denotes the component parallel to the magnetic field and  $\varepsilon$  is the relativistic kinetic energy of the electron. On the left hand side of Equation 3.5, the first term represents the resonance condition at  $\omega = 2\Omega_e = 2 \frac{eB}{m_e}$  without the relativistic shift and the electron motion parallel to  $B$ . The second term corresponds to the frequency shift from  $\omega = 2\Omega_e$  due to the relativistic mass variation and the spatial variation of  $B$ . The third

term represents the Doppler shift, whose sign is positive when the electron is moving parallel to the direction of the wave propagation and negative when the movement is anti-parallel.

The dominant part of the superthermal electrons are accelerated by perpendicular ECRH in the direction  $\theta \sim 90^\circ$  at  $B_0 = 0.5$  Tesla. When the microwave is injected into the machine, the electrons are accelerated and  $\gamma$  become greater than 1. Therefore the position of the resonance layer shifts toward the high field side of the machine satisfying the condition  $\omega = 2 \frac{eB}{m_e \gamma}$  as derived from Equation 3.5. The highest field across the machine is  $B \sim 0.6$  Tesla, which is 1.2 times the as large as  $B_0$ . Thus the maximum  $\gamma$  is 1.2. Substituting this value in Equation 3.6 we obtain for  $\varepsilon$  a maximum value of  $\sim 102$  keV. At low density single pass absorption is very low and microwave reflection from the back wall can take place, resulting in some parallel propagation of the microwave. Superthermal electrons moving in the high field side of the machine will be accelerated by this parallel wave and their energies are not governed by the maximum magnetic field value, as mentioned above for the case of perpendicular propagation, but by the value of  $N_{\parallel} \beta_{\parallel}$  near the plasma boundary in the high field side. An upper bound can be given by examining the resonance condition given by Equation 3.5 with a finite value of  $N_{\parallel} \beta_{\parallel}$ . Figure 3.23 is a graphical representation of the solution of Equations 3.5 and 3.6 for  $N_{\parallel} \sim 0.4$ . The solid curves show the results of the third term in Equation 3.5 indicating the Doppler effect of electrons with a pitch angle  $\theta$  from the direction of the magnetic field;

this term is positive when electrons are moving in the direction of the reflected microwave propagation.

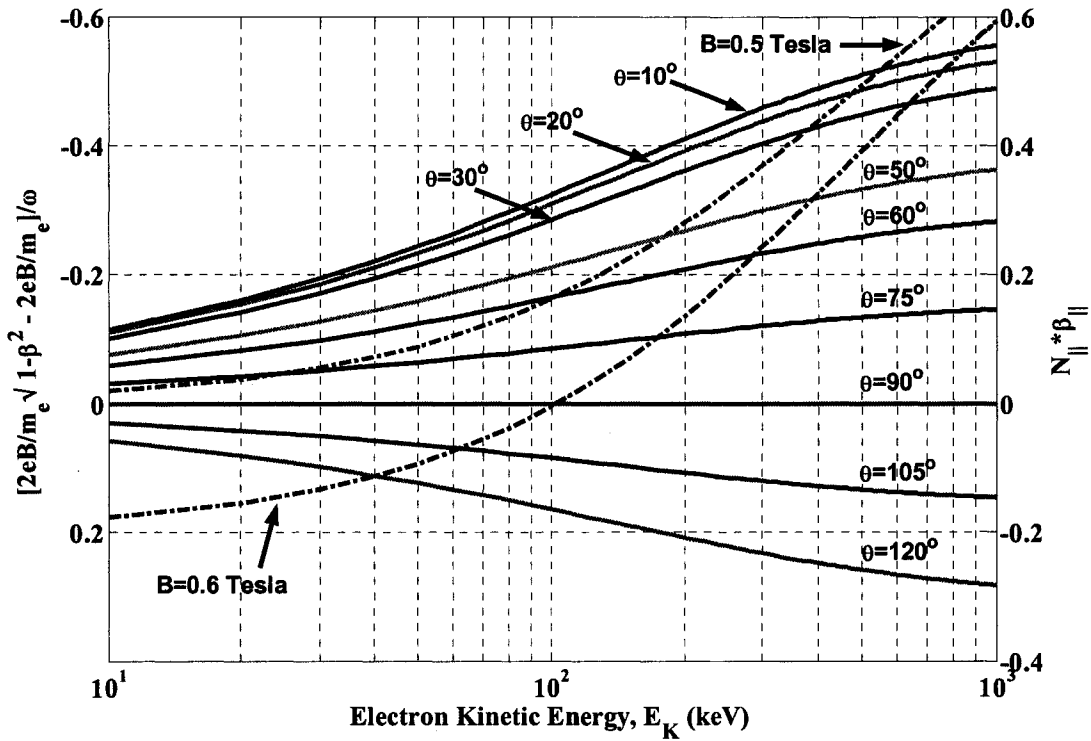


**Figure 3.23: Solution of equations 3.5 and 3.6 as a function of electron energy  $\epsilon$ .**

The dotted line shows the calculated results of the second term on the left hand side of Equation 3.5 indicating the relativistic mass variation effect on the ECRH condition corresponding to  $B = 0.5$  and  $0.6$  Tesla. The second harmonic ECRH condition is satisfied at the point of intersection of the two curves, where the effects of the second and third terms in the left hand side of equation 3.5 cancel each other. The higher energy electron resonates at the high field side can be determined from the figure. For example, an electron with  $\theta = 50^\circ$  resonates with  $\epsilon = 200$  keV at  $B = 0.5$  Tesla and with  $\epsilon \sim 400$  keV at  $B = 0.6$  Tesla, while electrons with  $\theta = 10^\circ$  resonates with  $\epsilon = 550$  keV at  $B = 0.5$

Tesla and with  $\varepsilon \sim 800$  keV at  $B = 0.6$  Tesla. Thus superthermal electrons can be heated in the region of  $B \sim 0.6$  with smaller values of  $\theta$  resulting from pitch angle scattering.

Because of the  $\frac{1}{v^3}$  dependence of the electron-electron and electron-ion collision frequencies, the electron collisionality will drop very fast at higher electron energy. If the accelerating force, i.e. the wave electric field is larger than the collision drag force, the electron energy will increase monotonically and the electron becomes runaway. At high electron energy, if the electron encounters a charge, either electron or ion, or if the electron leave the confining volume and hits the vessel wall or material objects like probes, it will emit hard x-rays. Figure 3.24 shows the hard x-ray signal emitted from electron runaways generated during 50 kW, 2<sup>nd</sup> harmonic X-mode ECRH plasma discharge from 800-850 msec.

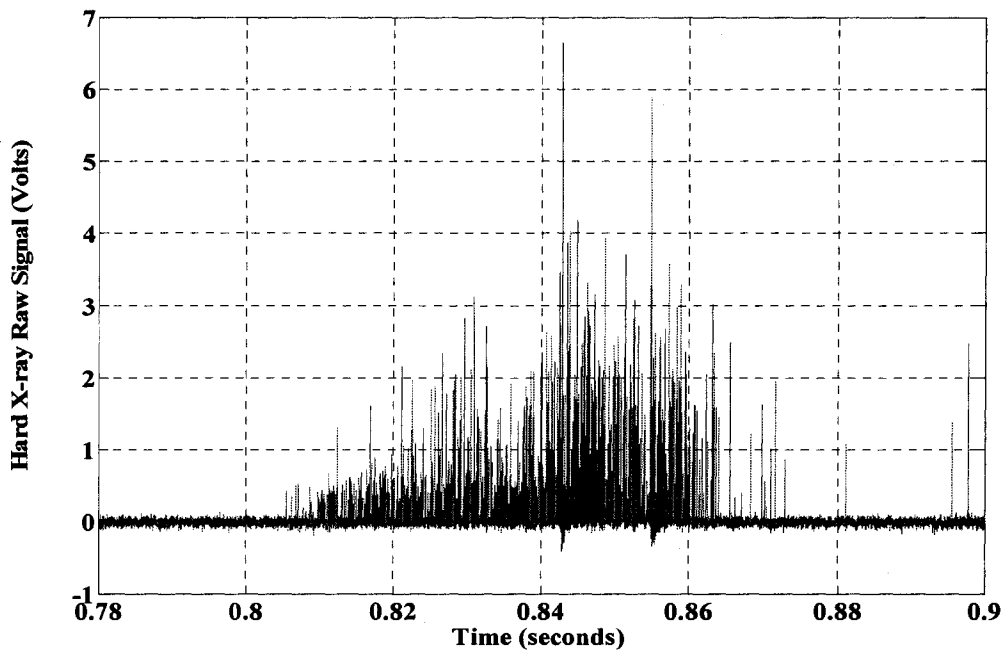


**Figure 3.24: Raw hard x-ray signal during the ECRH discharge.**

### 3.5 Summary

Superthermal electrons are generated in HSX in two different processes, from acceleration due to parallel electric field during field ramping, and during 2<sup>nd</sup> harmonic X-mode ECRH discharges. The hard x-ray generated during field ramping interferes with the signal generated during the plasma discharge. In order to focus the research on superthermal electrons during ECRH discharges, electrons generated during field ramping have been suppressed. Two techniques for suppressing superthermal electrons during field ramping were discussed, increasing vacuum base pressure and using UV xenon flash lamp. The energy gained by superthermal electrons in the toroidal loop electric field is measured using the maximum hard x-ray photon energy and it is in good agreement with modeling.

- 
- <sup>1</sup> B Esposito et al, Plasma Physics and Controlled Fusion, **38**, 2035, (1996)
- <sup>2</sup> H. Knoepfel et al, Physical Review Letter, **35**, 1340, (1975)
- <sup>3</sup> M. N. Rosenbluth, S. V. Putvinski, Nuclear Fusion, **37**(10), 1355 (1997)
- <sup>4</sup> A. C. England et. al, Physics of Fluids B **3**(7), 1671, (1991).
- <sup>5</sup> F. Medina et al, Plasma Physics and Controlled Fusion, **40**, 1897, (1998).
- <sup>6</sup> R. K. Janev, W.D. Langer, K. Evans, Jr., D.E. Post, Jr., "Elementary Processes in Hydrogen-Helium Plasmas", Springer-Verlag, (1987)
- <sup>7</sup> H. Boehmer et al., Physics of Fluids, **28**(10), 3099, (1985)
- <sup>8</sup> ALADDIN, online Atomic and Molecular Data Library, published by the International Atomic Energy Authority IAEA, <http://www-amdis.iaea.org/ALADDIN/>
- <sup>9</sup> A.C. England et al., Physics of Fluids B, **3**(7), 1671, (1991)
- <sup>10</sup> L. Rodrigues-Rodrigo et al., 26<sup>th</sup> EPS Conference on Controlled Fusion and Plasma Physics, Maastricht, 14-18 June 1999. Also ECA, **23**, 353, (1999)
- <sup>11</sup> T. H. Stix, Nuclear Fusion, **15**, 737 (1975)
- <sup>12</sup> R. Prater, Physics of Plasmas, **11**(5), 2349, (2004)
- <sup>13</sup> Thomas H. Stix, "Waves in Plasmas", 2<sup>nd</sup> edition, AIP Press, (1992).

# Chapter 4

## Hard X-ray Measurements in HSX

### 4.0 Introduction

Superthermal electrons generated during ECRH undergo small angle scattering with plasma electrons and comparatively stationary ions. As a result, they emit bremsstrahlung radiation in the soft to hard x-ray range (2-1000 keV), where the upper limit represents the maximum electron energy gained during ECRH. The emitted bremsstrahlung is related to the electron distribution function. By measuring the spectral emission, information about superthermal electron energies and populations can be obtained.

In this chapter, measurements of the hard x-ray emission from superthermal electrons in different magnetic configurations are discussed. The hard x-rays have been measured using the CdZnTe spectroscopic system described in Chapter 2. All the measurements described in this chapter were made by viewing the plasma through a line of sight perpendicular to the magnetic axis, and located nearly in the horizontal plane of the machine. Unless otherwise stated, data is taken during on-axis heating.

Section 4.1 describes the evidence of superthermal electron generation at low plasma line-averaged density ( $\bar{n}_e < 5 \times 10^{11} \text{ cm}^{-3}$ ) as obtained by different HSX diagnostics. The hard x-ray spectral differences between magnetic configurations are explained in Section 4.2 and the time evolution of the hard x-ray signal is discussed in Section 4.3. The dependence of

hard x-ray emission on plasma density, microwave input power and heating location are discussed in Sections 4.4, 4.5 and 4.6, respectively. The chapter concludes with a summary in Section 4.7.

## 4.1 Evidence of Superthermal Electron Generation in HSX

It is well known experimentally that 2<sup>nd</sup> harmonic X-mode electron cyclotron resonance heating produces a superthermal electron tail at low plasma density in fusion devices<sup>1,2</sup>. In the HSX stellarator, a superthermal electron population ( $E_{\text{tail}} > 20$  keV) is detected during on-axis ECRH at low plasma line-averaged density ( $\bar{n}_e < 5 \times 10^{11} \text{ cm}^{-3}$ ). The hard x-ray signal is extremely small in the AntiMirror configuration at all plasma densities. For this reason, our attention will be focused on studying hard x-ray emission from the two other magnetic configurations, QHS and Mirror.

The superthermal electron tail was detected using multiple HSX diagnostics sensitive to the presence of superthermal electrons. Figure 4.1 shows the time evolution of typical ECRH discharge operational signals for the QHS configuration at two different plasma line-averaged densities,  $\bar{n}_e \sim 5 \times 10^{11} \text{ cm}^{-3}$  and  $\bar{n}_e \sim 1.6 \times 10^{12} \text{ cm}^{-3}$ . The plasma density is kept constant during the ECRH discharge in both cases by using a programmable gas puff during the discharge. Higher hard x-ray counts are observed at low plasma density as shown in Figure 4.1(a), compared to high plasma density as shown in Figure 4.1(b), indicating higher superthermal electron population at low density. The soft x-ray emission (2-8 keV) measured using the PIPS detector described in Chapter 2 is constant during the discharge (for

Maxwellian plasma, the x-ray intensity scales linearly with plasma electron and ion densities and exponentially with electron temperature. See Appendix A for more details on x-ray generation theory).

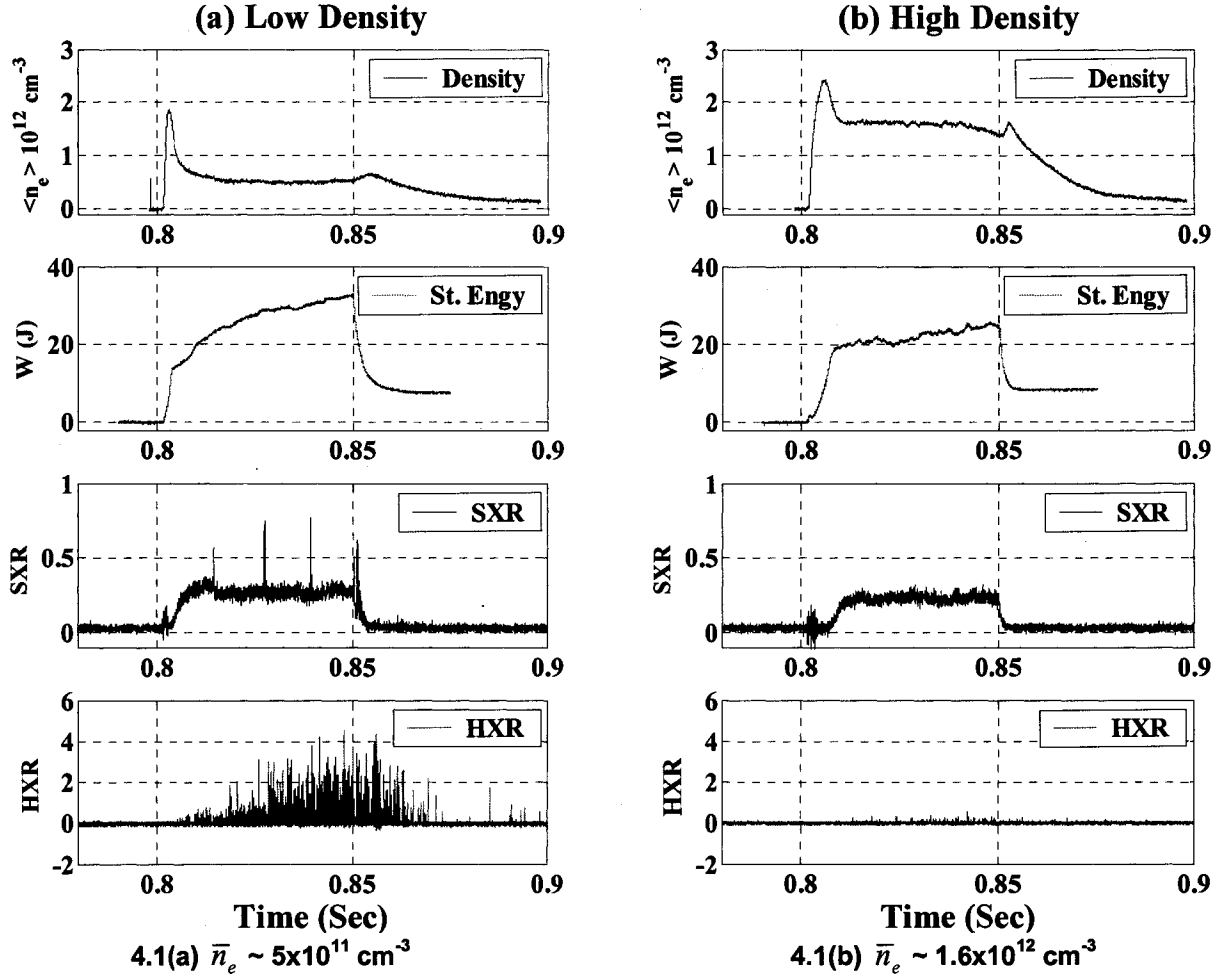


Figure 4.1: HSX discharge signals in QHS at low and high plasma line-averaged densities.

The plasma stored energy measured using diamagnetic flux loop is greater at low density compared to high density. As Figure 4.1(b) shows, at high electron plasma density ( $\bar{n}_e \sim 1.6 \times 10^{12} \text{ cm}^{-3}$ ), the stored energy is nearly constant during the discharge and hard x-ray

signal is very small, suggesting that no significant superthermal electron population exists at this density. This suggests that the stored energy is mainly carried by bulk electrons. At low density, where the stored energy increases monotonically during the discharge, the bulk plasma density and the soft x-ray signals are constant as shown in Figure 4.1(a). On the contrary, the hard x-ray signal is large and increases monotonically during the discharge as will be shown in Section 4.3. This indicates that a significant part of the stored energy is carried by the superthermal electron population at low density. The reason for the offset in the stored energy signal shown in Figure 4.1 after the microwave discharge is turned off is attributed to electronic pickup by the diamagnetic loop.

Figure 4.2 shows the density variation for several HSX diagnostics that are sensitive to the presence of superthermal electrons. Figure 4.2(a) shows the electron temperature versus density for the QHS configuration using the ECE radiometer and the Thomson scattering diagnostics. It is well known that when the plasma distribution deviates significantly from Maxwellian the ECE emission is sensitive to the tail of the distribution so that even a small population of superthermal electrons can dominate the emission<sup>3</sup>. Unlike the ECE radiometer, the Thomson scattering diagnostic is relatively insensitive to the presence of a small population of superthermal electrons. The difference between the two signals at low density, where the ECE radiometer measures higher electron temperature compared to Thomson scattering is indicative of energetic tail. The Thomson scattering measures the bulk electron temperature which appears nearly the same irrespective of plasma density.

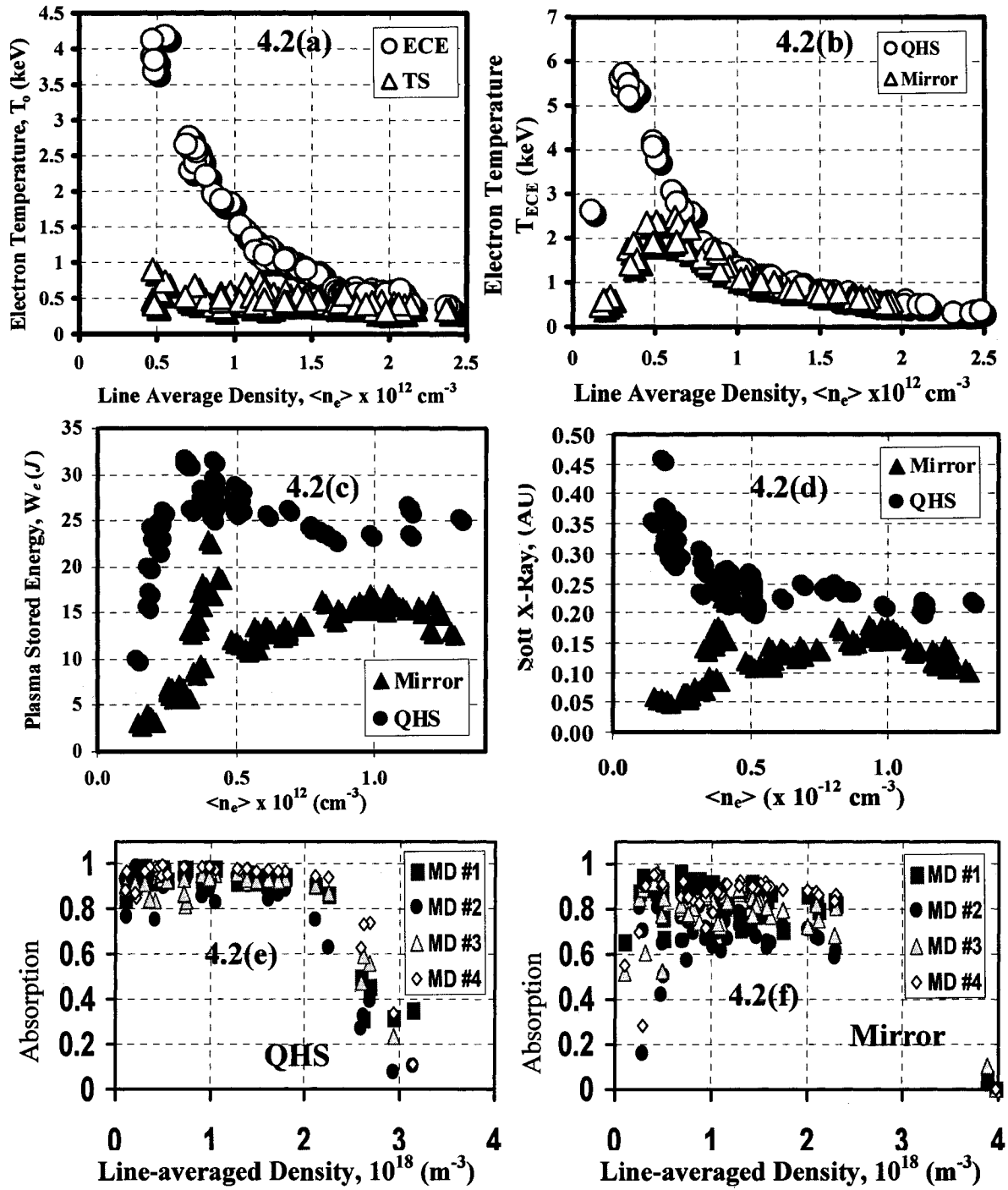


Figure 4.2: Different HSX diagnostics detect superthermal electrons at low density.

The density scan of the electron "temperature" measured using the ECE radiometer is shown in Figure 4.2(b) for both QHS and Mirror configurations. As the figure shows, at low density ( $\bar{n}_e < 5 \times 10^{11} \text{ cm}^{-3}$ ) higher ECE emission was measured in QHS compared to the Mirror configuration. This suggests that a higher superthermal electron population exists in QHS compared to Mirror at low density. As the density increases, the ECE radiation temperature decreases in the QHS configuration suggesting a reduction of the superthermal electron population at higher densities. The QHS and Mirror configurations have the same ECE temperatures at high density, indicating reduced superthermal populations in both configurations at high density. At high density the ECE temperature is somewhat lower than the Thomson temperature; this is consistent with the plasma "grey" emission (optically thin plasmas).

Figure 4.2(c) shows the density variation of the plasma stored energy as measured by diamagnetic loop. Higher stored energy is measured at low density in QHS compared to the Mirror configuration. Although the QHS configuration has a 10% bigger plasma volume compared to the Mirror configuration, this difference in volume alone can't account for the difference in stored energy at low density. Dr. K.M. Likin<sup>4</sup> of the HSX group shows that the difference in stored energy can be attributed to the energy carried by the higher superthermal electron population at low density in QHS compared to the Mirror configuration. In order to explain the high multi-pass microwave power absorption in QHS at low density (plasma absorption during multiple reflection of the microwave beam from the vessel's back wall), he uses a bi-Maxwellian distribution function model and showed that at low density ( $\bar{n}_e \sim 2 \times 10^{11}$

$\text{cm}^{-3}$ ) the data was consistent with nearly 40% of the electron population being superthermal and with a temperature of 16 keV. A high density ( $\bar{n}_e \sim 1.8 \times 10^{12} \text{ cm}^{-3}$ ) the superthermal population drops to  $\sim 3\%$  with a temperature of 1 keV.

Figure 4.2(d) shows the density variation of the soft x-ray signal in QHS and Mirror configurations. The data was obtained by averaging the SXR signal (shown in Figure 4.3) over 15 msec (835-850 msec) of the ECRH discharge at fixed density. The density scan shows higher SXR signal at all plasma densities in QHS compared to Mirror configuration.

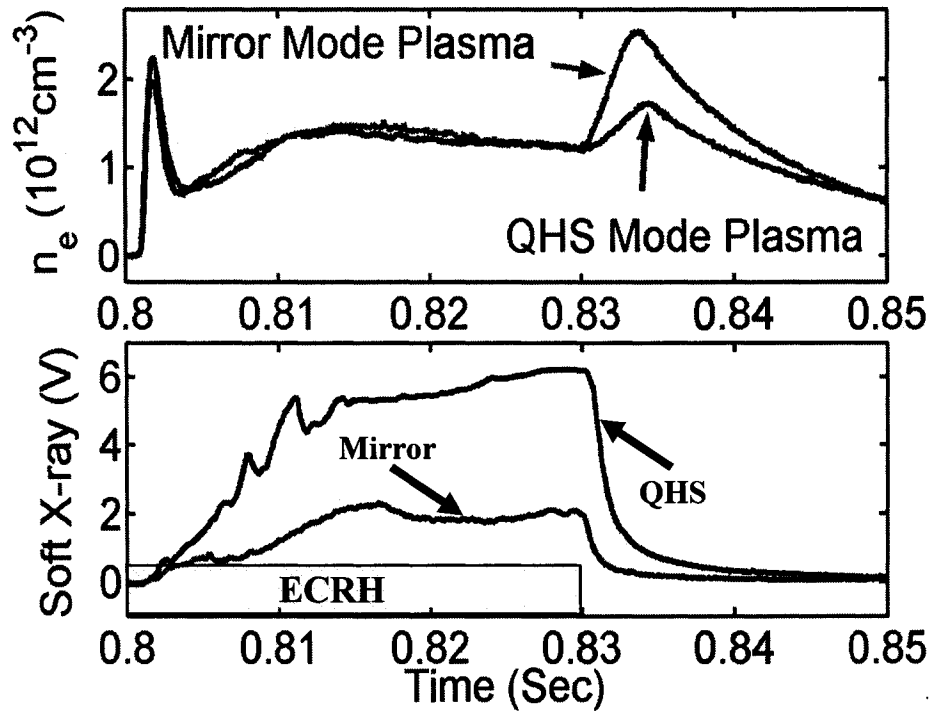


**Figure 4.3: Plasma line-averaged electron density (top) and soft x-ray (bottom) time evolution in QHS and Mirror configurations.**

Figure 4.3 shows the time evolution of the soft x-ray signal measured using the PIPS detectors for both QHS and Mirror configurations at a plasma line-averaged density  $\bar{n}_e \sim$

$1.3 \times 10^{12} \text{ cm}^{-3}$ . The figure shows that the soft x-ray signal in QHS is higher than in the Mirror configuration. The soft x-ray intensity is proportional to the square of plasma electron density and electron temperature in the soft x-ray region (see Appendix A). Because the plasma electron line-averaged density is the same for both cases during the ECRH discharge, a higher electron temperature is expected in the QHS compared to the Mirror configuration.

Figures 4.2(e) and 4.2(f) show the density variation of the multi-pass absorption efficiency in QHS and Mirror configurations<sup>4</sup>. The multi-pass absorption is defined as

$$\eta = 1 - \frac{P_{\text{non}}}{P_o}$$

where  $P_{\text{non}}$  is the measured non-absorbed power and  $P_o$  the reference power in

“cold plasma discharge” at plasma density above the cut-off. The microwave detectors MD#1 to MD#4 are installed toroidally around the machine to measure the non-absorbed microwave power. At low plasma line-averaged density ( $\bar{n}_e \sim 5 \times 10^{11} \text{ cm}^{-3}$ ), the absorption drops in the Mirror configuration while it remains high in QHS. In the AntiMirror configuration the multi-pass absorption efficiency does not exceed 0.5. In this configuration, electrons are deeply trapped in the local magnetic well and they leave the confinement region in a short time because they are on the so-called direct loss orbits. John Canik of the HSX group demonstrated this fact experimentally using a pair of collector plates installed on HSX at the toroidal location of the ECH antenna, at the top and bottom of the machine. One of the plates lies in the electron  $\nabla B$  drift direction, the other in the ion drift direction. These plates were used to detect any charge excess due to the direct orbit losses of deeply trapped particles.

Ray tracing calculations in HSX show that at low density the difference in microwave absorption between QHS and Mirror configurations is attributed to the higher absorption on the superthermal electron population existing in low plasma density QHS discharges<sup>5</sup>.

Among the various methods to diagnose superthermal electrons, the non-thermal bremsstrahlung hard x-ray emission, is one of the most efficient, as it offers quite direct insight on the build-up of the tail electron distribution function<sup>6,7</sup>. By measuring and analyzing the hard x-ray emission during ECRH discharges, differences in confinement of superthermal electrons in different magnetic configurations can be studied. The rest of this chapter will be devoted to studying hard x-ray emission in different HSX magnetic configurations, and its parametric dependencies. Single particle explanation of the results will be given in Chapters 5 and 6.

## 4.2 Spectrum Difference between Configurations

Plasma hard x-ray emission can be categorized into three different sources (for more details consult Appendix A), free-free, free-bound and line radiation. The free-free takes place when a free electron in the plasma encounters with a free charge either electron or ion (impurity or plasma species). The free-bound takes place when a free electron from the continuum is captured by one of the outer most electronic shells in ionic species and x-ray photon is emitted. The line radiation takes place when one of the electrons in the inner most atomic shells jumps to a higher energy level and returned back with the emission of a characteristic x-ray photon. At the energy range of interest in this work, the free-bound and

line radiation emissions are negligible compared to the free-free emission. The plasma impurity concentrations are almost the same at the same line-averaged density for both configurations. This is indicated from the radiated power signal measured using bolometer as shown in Figure 4.4 at line-averaged density  $\bar{n}_e \sim 4 \times 10^{11} \text{ cm}^{-3}$  for both configurations.

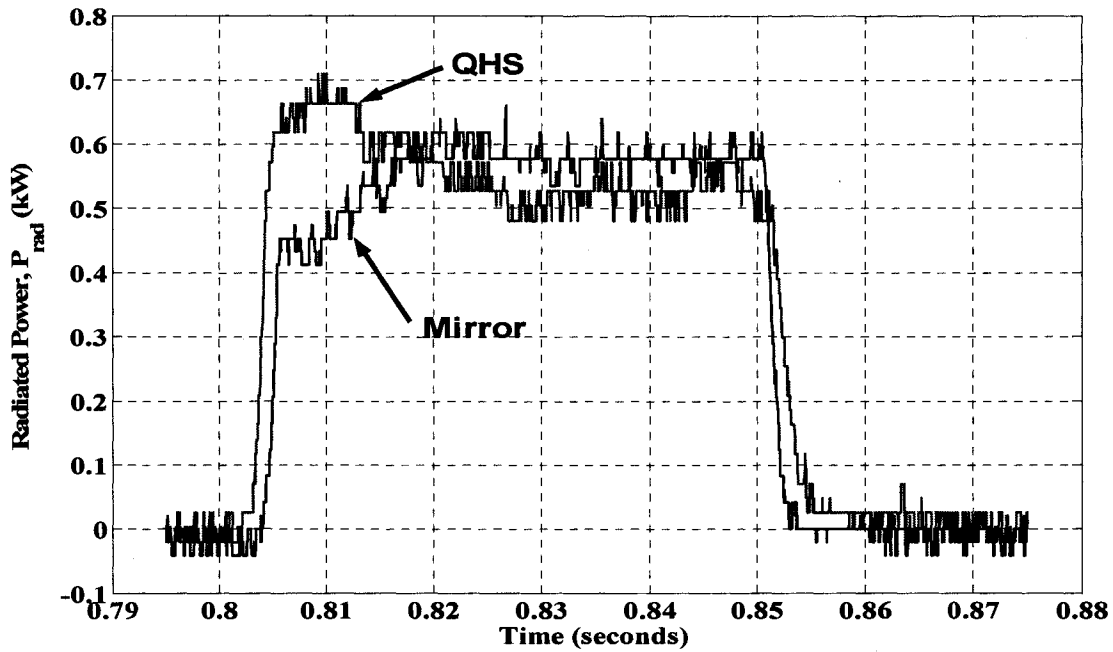


**Figure 4.4: Radiated Power measured using bolometer in HSX for QHS and Mirror configurations  $\bar{n}_e \sim 4 \times 10^{11} \text{ cm}^{-3}$ .**

Figure 4.5 shows the photon energy spectra collected from the plasma core during on-axis ECRH for both QHS and Mirror configurations. Each spectrum is collected over  $\sim 10$  similar 50 msec plasma shots ( $\bar{n}_e \sim 2 \times 10^{11} \text{ cm}^{-3}$ ,  $P_{\text{inj}} = 50 \text{ kW}$ ) to achieve adequate statistical resolution. The x-axis in Figure 4.5 represents the photon energy and the logarithmic y-axis represents the hard x-ray photon counts per energy bin. As the emitted photon energy spectrum is continuous, only a coarse number of bins is necessary, in contrast to the usual

needs in radiation spectroscopy for identification of specific emission lines. For this reason, a total of 200 energy bins ( $\Delta E = 10$  keV) were used to obtain the spectra shown in the figure.

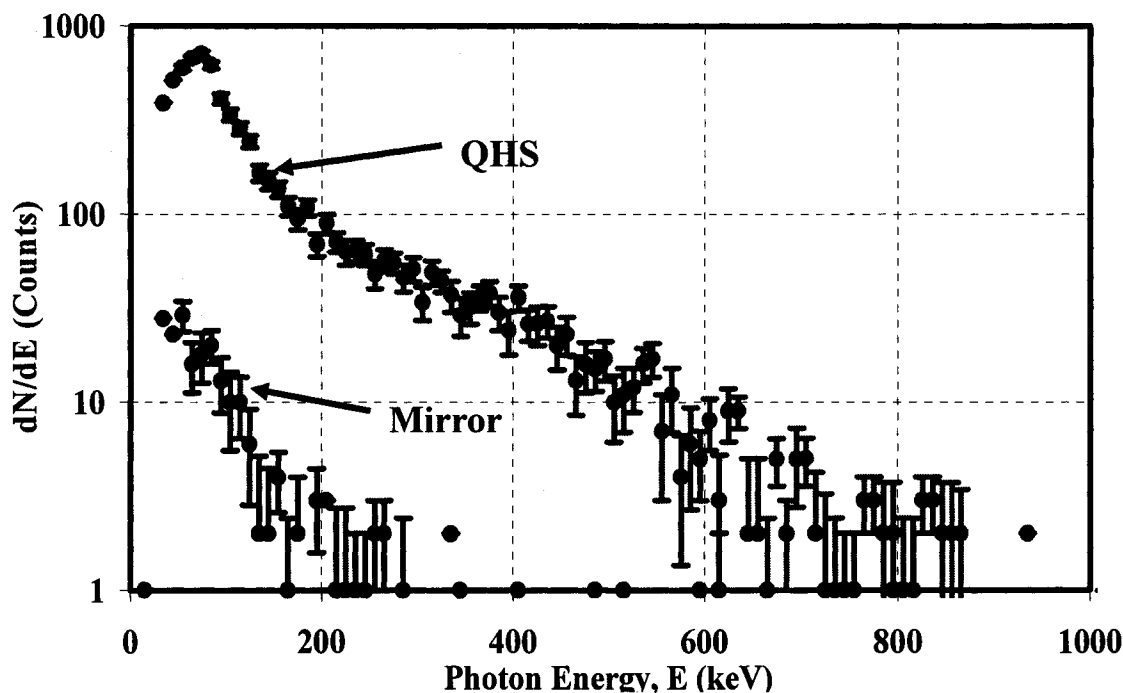


**Figure 4.5: Hard x-ray spectrum during on-axis ECRH for QHS and Mirror configurations.**

The figure shows that the hard x-ray tail extends to higher energy in QHS compared to Mirror ( $\sim 800$  keV compared to 200 keV). Hard x-rays below  $\sim 30$  keV are strongly absorbed by the stainless steel filter as discussed in Chapter 2. The total number of photon counts in QHS is  $\sim 7000$  compared to  $\sim 200$  in the Mirror case.

The portion of spectrum from 70 to 200 keV plotted in a semi-log scale is nearly linear; therefore each spectral tail can be characterized by an x-ray “temperature” or slope. In interpreting the meaning of this slope or temperature, caution must be exercised because unlike the case of soft x-ray, the slope here does not equal the mean energy of the emitting

electrons. The true mean energy is somewhat higher than the resulting hard x-ray spectrum slope. The reason is that as the electrons approach relativistic energies, the bremsstrahlung cross section tends to fall off with the emitted photon energy even for monoenergetic electrons. In spite of this limitation, the x-ray spectra slope provides a relative measure of the mean energy of the emitting electrons for the comparison of multiple spectra. As the figure shows, the QHS spectrum has two different slopes, a low energy slope of  $\sim 55$  keV between 70-200 keV and a high energy slope of  $\sim 176$  keV between 200-700 keV. The Mirror spectrum has a similar slope to the QHS spectrum of  $\sim 56$  keV between 70-200 keV, with no significant counts in the higher energy range.

The spectra indicate that electrons gain more energy in QHS than in Mirror. Also, at any energy the x-ray intensity is much higher in QHS than in the other two operating regimes (AntiMirror is not shown because no hard x-ray emission is detected during the ECRH discharge). This shows that the population of energetic electrons is much higher in QHS.

### 4.3 Hard X-ray Time Evolution

Superthermal electron temporal dynamics provides valuable details, especially on the underlying mechanisms of heating and energy confinement<sup>8</sup>. Figure 4.6 shows the hard x-ray count time evolution for QHS and Mirror configurations during on-axis ECRH discharges. Each plot is collected over  $\sim 10$  similar 50 msec plasma shots ( $\bar{n}_e \sim 2 \times 10^{11} \text{ cm}^{-3}$ ,  $P_{\text{inj}} = 50$  kW). The plots were obtained by counting the total number of hard x-ray photons in a

specified time window. A time window of 2 msec was used to measure accurately the hard x-ray temporal evolution for all the data presented in this work.

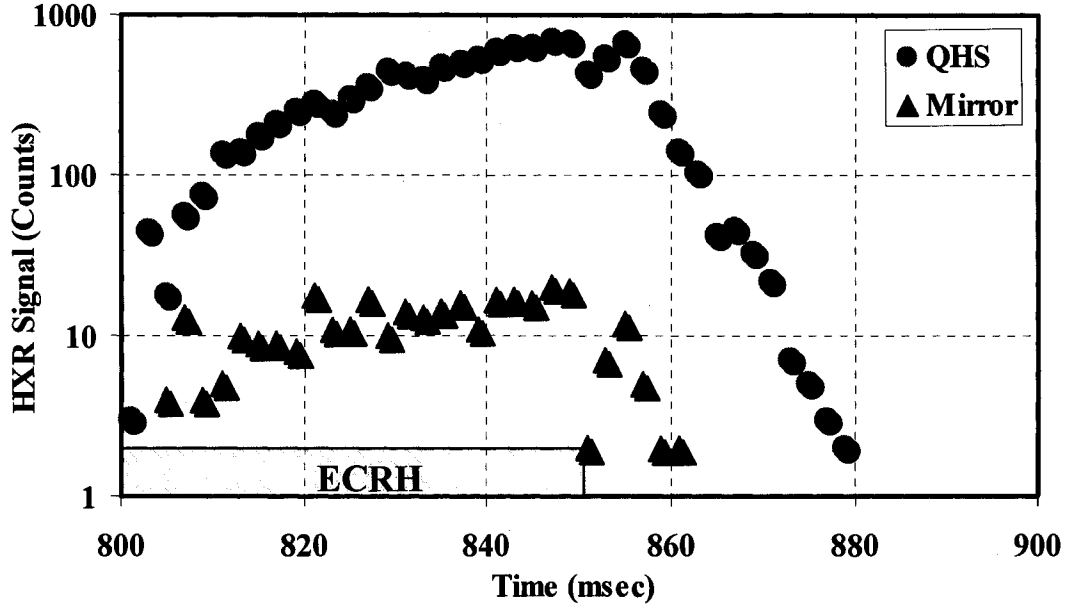


**Figure 4.6: HXR count time evolution for QHS and Mirror at line-averaged plasma density  $\bar{n}_e \sim 2 \times 10^{11} \text{ cm}^{-3}$ .**

The x-axis represents time in msec during the discharge (microwaves are on between 800-850 msec), while the y-axis represents total number of hard x-ray photons per time window. The figure shows that the hard x-ray counts are higher in QHS compared to Mirror at all times during and after the discharge. In QHS, the hard x-ray counts increase monotonically during the discharge, indicating higher superthermal electron production than loss. In the Mirror configuration, hard x-ray counts saturate very quickly and remain constant during the remainder of the discharge, indicating equal superthermal electron production and loss. After the microwave power is turned off the hard x-ray counts decay rapidly in Mirror compared to the QHS configuration. The decay constant, calculated from exponential curve fitting of the

hard x-ray signal after the microwave power is turned off is  $\sim 7$  msec in QHS compared to  $\sim 1$  msec in the Mirror case. The slower decay in the absence of heating and absorption issues indicates that the superthermal electrons are better confined in QHS as compared to Mirror.

Figures 4.7 and 4.8 show the time evolution of the hard x-ray average and maximum photon energies, respectively, during on-axis ECRH for the QHS and Mirror configurations. Figure 4.7 is obtained using the same set of discharges as Figure 4.6, by averaging over the photon energies in each time window. Figure 4.8 is obtained by measuring the maximum photon energy in each time window. In Figure 4.7, the x-axis represents the time in seconds and the y-axis is the averaged photon energy. The figure shows that in QHS, the average photon energy increases monotonically during the discharge, indicating continuous heating of superthermal electrons, and decays after the microwave power is turned off. In Figure 4.8, the x-axis represents the time in seconds and the y-axis is the maximum photon energy. The figure shows that higher maximum photon energy is attained in QHS compared to the Mirror configuration during the discharge. This result is also supported by the spectra shown in Figure 4.5 where higher maximum photon energies are measured in QHS compared to Mirror at low plasma density ( $\bar{n}_e \sim 2 \times 10^{11} \text{ cm}^{-3}$ ).

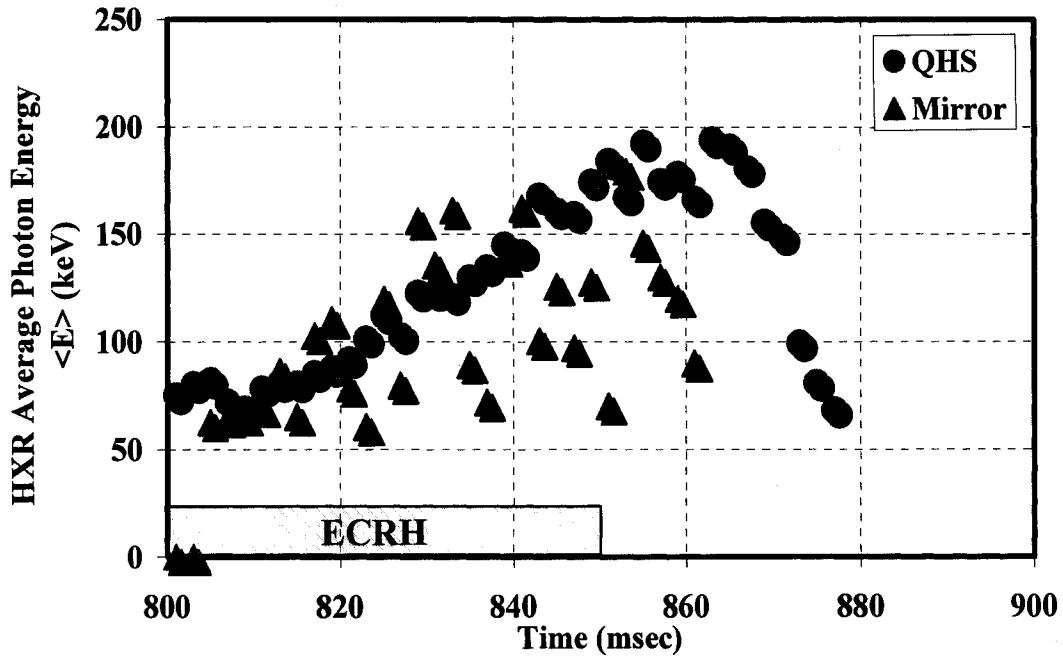


Figure 4.7: HXR average photon energy  $\langle E \rangle$  time evolution for QHS and Mirror at line-averaged plasma density  $\bar{n}_e \sim 2 \times 10^{11} \text{ cm}^{-3}$ .

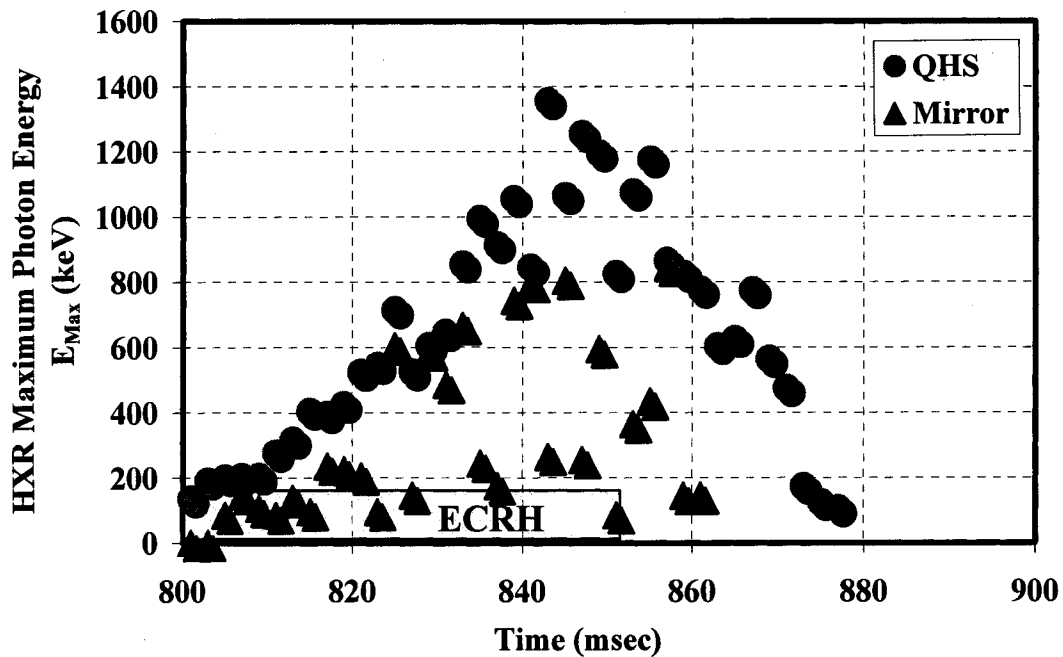
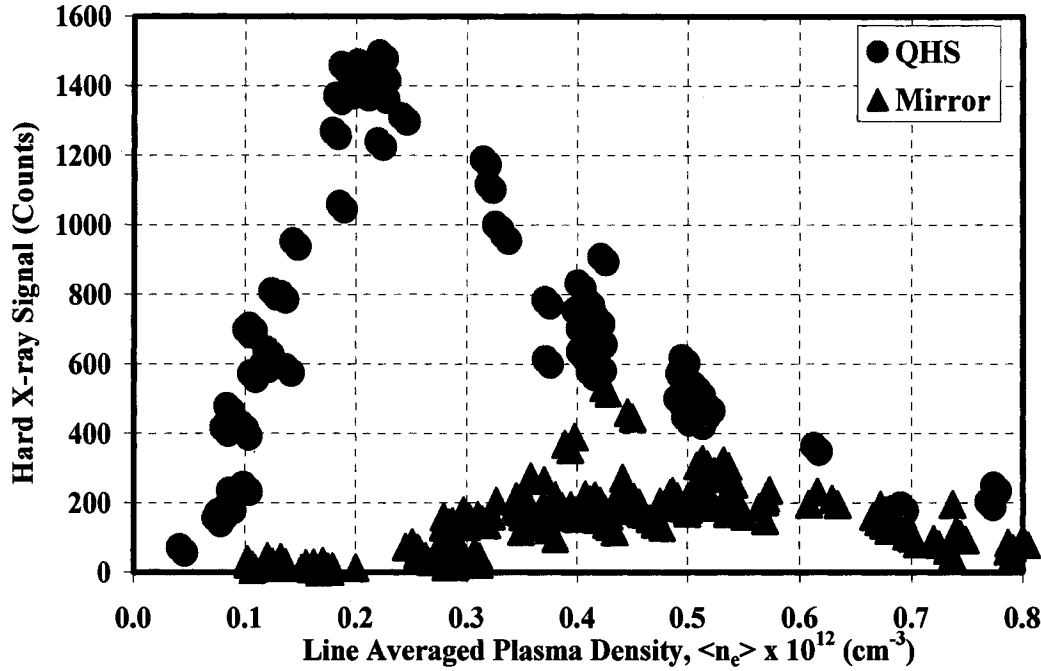


Figure 4.8: HXR maximum photon energy  $E_{\text{Max}}$  time evolution for QHS and Mirror at line-averaged plasma density  $\bar{n}_e \sim 2 \times 10^{11} \text{ cm}^{-3}$ .

#### 4.4 Hard X-ray Plasma Density Dependence

The variation of hard x-ray counts with plasma density for both QHS and Mirror configurations is shown in Figure 4.9.



**Figure 4.9: The variation of the hard x-ray counts with line-averaged plasma density for QHS and Mirror configurations.**

The x-axis represents the line-averaged plasma densities during the ECRH discharge (the plasma density was kept nearly constant during each discharge) and the y-axis represents the total hard x-ray counts during the 50 msec discharge. The figure shows a non-linear density dependence of the hard x-ray counts for both configurations. At very low plasma density ( $\bar{n}_e < 2 \times 10^{11} \text{ cm}^{-3}$ ) there is very little hard x-ray signal in Mirror configuration while the hard x-ray counts are maximum in the QHS configuration. For plasma densities higher than  $\bar{n}_e > 2 \times 10^{11} \text{ cm}^{-3}$ , the hard x-ray count decreases with increasing density in QHS, and increases

slightly in Mirror configuration up to a line-averaged density of  $\bar{n}_e \sim 4 \times 10^{11} \text{ cm}^{-3}$  then remains relatively constant up to  $6 \times 10^{11} \text{ cm}^{-3}$ . The figure shows clearly that the hard x-ray count is higher in QHS compared to Mirror configuration at line-averaged plasma densities  $\bar{n}_e < 6 \times 10^{11} \text{ cm}^{-3}$ , and they are nearly the same at higher densities. In order to understand the density dependence of the hard x-ray counts, a brief description of the production mechanism of superthermal electrons from a single particle perspective will be given. A detailed description of the single particle heating is given in Chapter 5.

During an ECRH plasma discharge, the electrons on average are accelerated by the wave electric field  $\vec{E}$  and decelerated by three different electron collisions: the electron-electron (e-e), electron-ion (e-i) and electron-neutral (e-n) collisions. The electron can also leave the confinement region in a confinement time scale. At low electron energy, electron-neutral collisions can be neglected during the discharge because transport calculations in HSX indicated that core neutral density is usually two orders of magnitude ( $\bar{n}_n \sim 10^{10} \text{ cm}^{-3}$ ) less than plasma electron density<sup>9</sup> at line-averaged plasma density  $\bar{n}_e \sim 10^{12} \text{ cm}^{-3}$ . Figure 4.10 shows the variation of electron-electron, electron-ion and electron-neutral collision frequencies with electron energy at different densities. The x-axis is the electron energy in eV and the y-axis represents the different collision frequencies. The figure show that at neutral density of  $n_n \sim 10^{10} \text{ cm}^{-3}$  and electron kinetic energy  $\varepsilon \sim 100 \text{ eV}$ , the electron-neutral collision frequency is nearly an order of magnitude less than the electron-electron collision frequency at electron density  $\bar{n}_e \sim 10^{11} \text{ cm}^{-3}$  and two order of magnitude less than the

electron-ion collision frequency at ion density  $\bar{n}_i \sim 10^{11} \text{ cm}^{-3}$ . The figure also shows that the electron-neutral collision frequency is higher than the electron-electron and electron-ion collision frequencies at electron energies larger than  $\sim 1 \text{ keV}$ , at  $n_n \sim 10^{10} \text{ cm}^{-3}$  and  $\bar{n}_e, \bar{n}_i \sim 10^{11} \text{ cm}^{-3}$ .

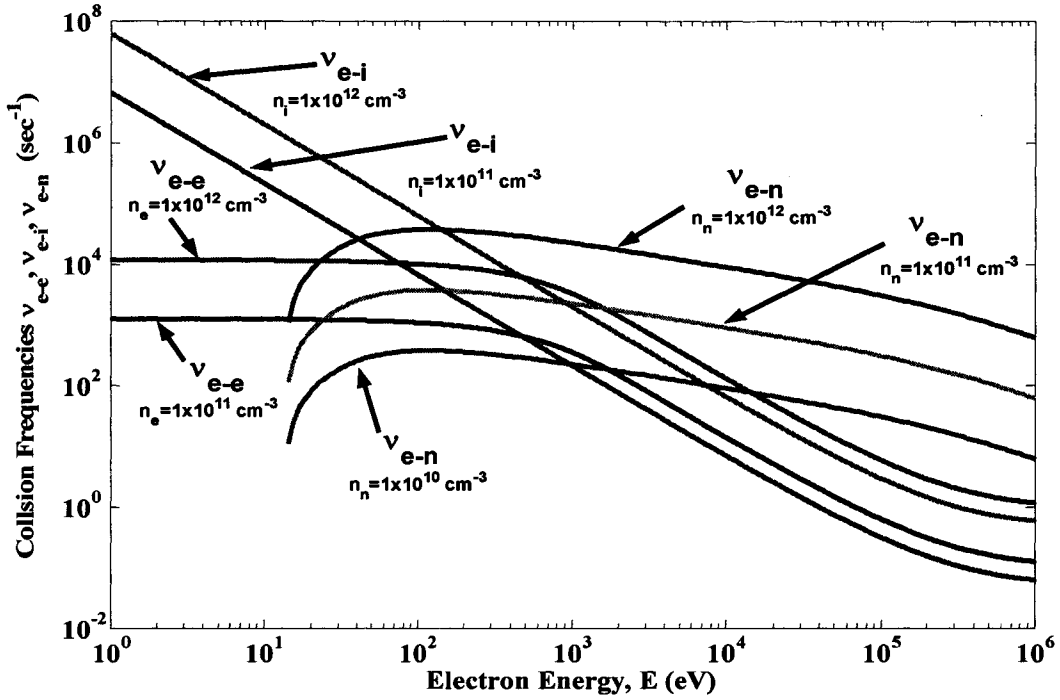


Figure 4.10: Comparison between various collision processes at different densities.

The electron equation of motion can be written as:

$$\frac{d}{dt} \left( \frac{1}{2} m_e v_e^2 \right) = -\langle e v_e \bar{E} \rangle + m_e v_e^2 \nu_e \quad (4.1)$$

Where,  $m_e$  and  $e$  are the electron mass and charge,  $v_e$  the electron speed,  $\nu_e$  the electron total collision frequency. The collision frequency assuming hydrogenic species ( $Z_{\text{eff}} = 1$ ) is given by:

$$\nu_e = \frac{n_e e^4 \ln \Lambda}{16\pi \varepsilon_0^2 m_e^2 \nu_e^3} \quad (4.2)$$

where,  $n_e$  the electron number density,  $\varepsilon_0$  the electric permittivity,  $\ln \Lambda$  a slowly varying function of plasma parameters, ( $\ln \Lambda \sim 17$  for fusion plasmas). The brackets  $\langle e\nu_e \bar{E} \rangle$  represent the time average over several periods of the EC wave for the fluctuating wave electric field and it is equal to the microwave input power per electron  $p_e = \langle e\nu_e \bar{E} \rangle$ . For the electrons to continuously accelerate and become superthermal, it must fulfill the condition  $p_e > m_e \nu_e^2 \nu_e$ . The minimum electron velocity that satisfies the last condition is called the critical velocity  $\nu_c$  and is given by:

$$\nu_c = \frac{n_e e^4 \ln \Lambda}{16\pi \varepsilon_0^2 m_e p_e} \quad (4.3)$$

Under the assumption of uniform heating power for all electrons in the heating zone,  $p_e$  can be given by  $p_e = \frac{P}{n_e V_{pd}}$ , where  $P$  is the microwave heating power, and  $V_{pd}$  is the power deposition volume. Although high energy electrons absorb more power in the heating zone than bulk electrons (due to their higher temperature), the assumption is reasonable if we take into account the relativistic detuning that causes electrons to fall off resonance before they are driven to very high energy. So the critical velocity can be written as:

$$v_c = \frac{n_e^2 e^4 \ln \Lambda V_{pd}}{16\pi\epsilon_0^2 m_e p} \propto \frac{n_e^2}{p} \quad (4.4)$$

The last equation (4.4) indicates that the critical velocity is proportional to the square of the electron density and inversely proportional to the microwave heating power, so for fixed microwave heating power, the electron density determines the critical velocity. Electrons can be accelerated to higher energies when they cross the resonance location during their bounce or passing motion. Since between crossings of the resonance zone the energies of the electrons are constant, the collision frequency is proportional to  $n_e$  and higher electron density suppresses the production of superthermal electrons. At lower density, the critical velocity is small and the collisionality is small and bulk electrons can more easily acquire energy and become superthermal. When the electron density is very small the microwave absorption is very low even for superthermal electrons and there are fewer ions for superthermal electrons to interact with and emit bremsstrahlung hard x-ray radiation. This picture is supported in Figure 4.9.

Figure 4.11 shows the density dependence of the hard x-ray average photon energy and Figure 4.12 shows the density dependence of the maximum photon energy for both QHS and Mirror configurations. As expected from the superthermal electron generation model described above, the lower the plasma density the more energetic the superthermal electron generated during the microwave discharges. The results in Figures 4.11 and 4.12 show that, at low line-averaged plasma density, the hard x-ray average and maximum photon energies are higher than at higher plasma densities.

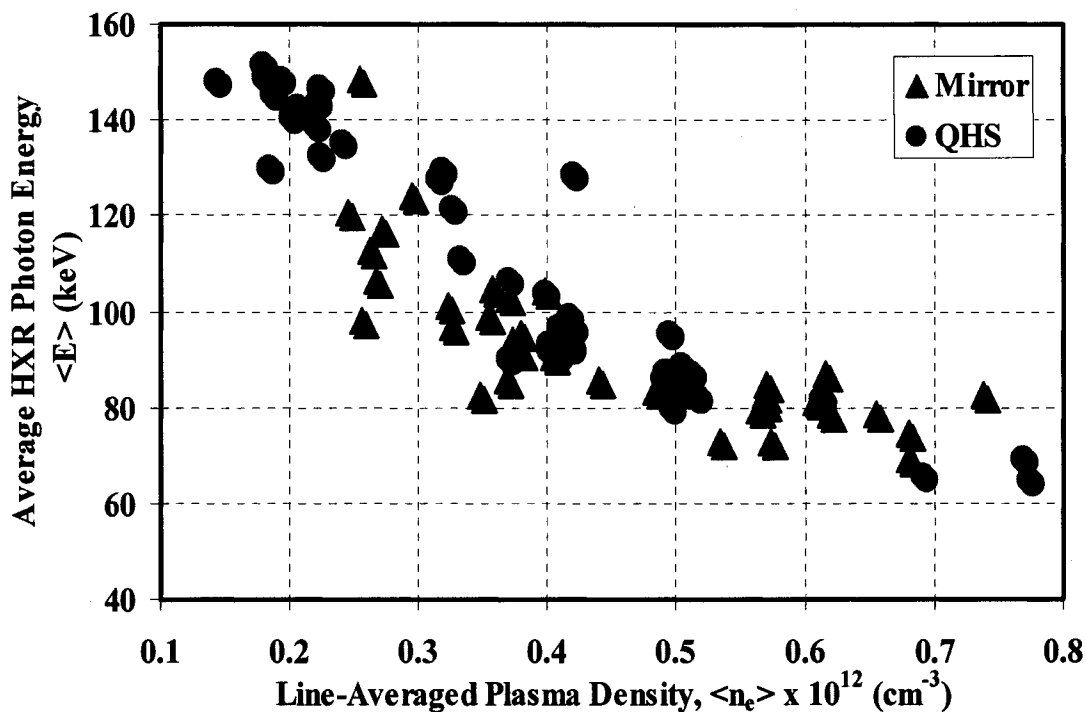


Figure 4.11: The variation of hard x-ray average photon energy  $\langle E \rangle$  with line-averaged plasma density for QHS and Mirror configurations.

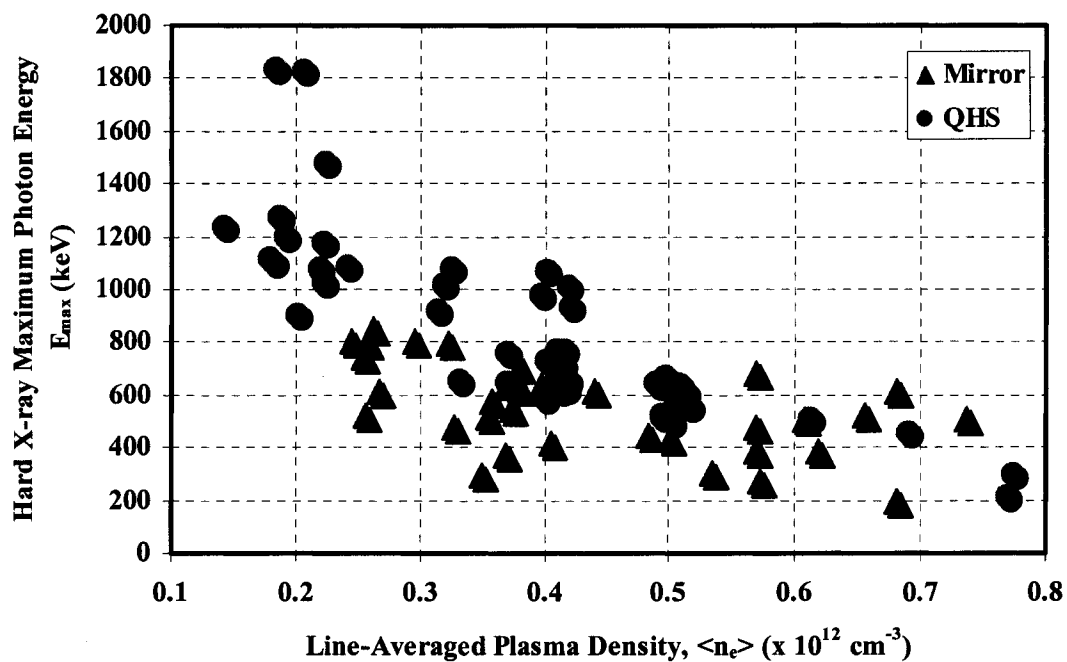


Figure 4.12: The variation of hard x-ray maximum photon energy  $E_{\max}$  with line-averaged plasma density for QHS and Mirror configurations.

The figures show that the average photon energy is almost the same for QHS and Mirror configurations at all line-averaged plasma densities, while higher maximum photon energy is detected in QHS compared to Mirror configuration at low density as previously noted in the spectrum difference between configurations.

To study the effect of plasma density on the hard x-ray spectrum and time evolution, the spectrum and time evolution were measured at three different plasma densities,  $\bar{n}_e \sim 2 \times 10^{11}$ ,  $4 \times 10^{11}$ , and  $8 \times 10^{11} \text{ cm}^{-3}$ , for both QHS and Mirror configurations. The density and the input microwave power are kept constant during the discharge and the plots were obtained by summing over  $\sim 10$  similar plasma shots. The results of this study are shown in Figures 4.13-4.16. The effect of plasma density on hard x-ray spectrum is more pronounced in QHS compared to Mirror as shown in Figures 4.13 and 4.14. In QHS, the increase in plasma density decreases the total number of photons produced during the 50 msec discharges, as well as the average and maximum energies. This indicates a smaller and less energetic population of superthermal electrons at higher densities. As the plasma density increases from  $\bar{n}_e = 2 \times 10^{11} \rightarrow 4 \times 10^{11} \rightarrow 8 \times 10^{11} \text{ cm}^{-3}$ , the maximum energy decreases from  $1000 \rightarrow 600 \rightarrow 200 \text{ keV}$ , respectively. The slope of the spectrum also increases as the density increases, indicating a decrease in the superthermal electron temperature.

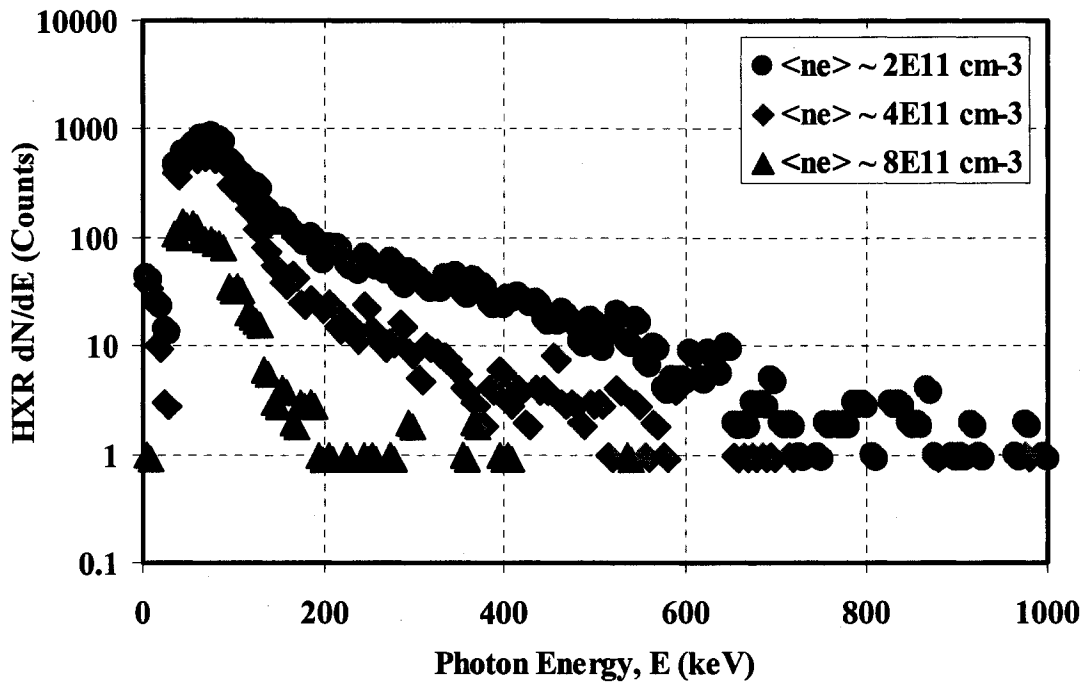


Figure 4.13: Hard x-ray spectrum at three different line-averaged plasma densities for the QHS configuration.

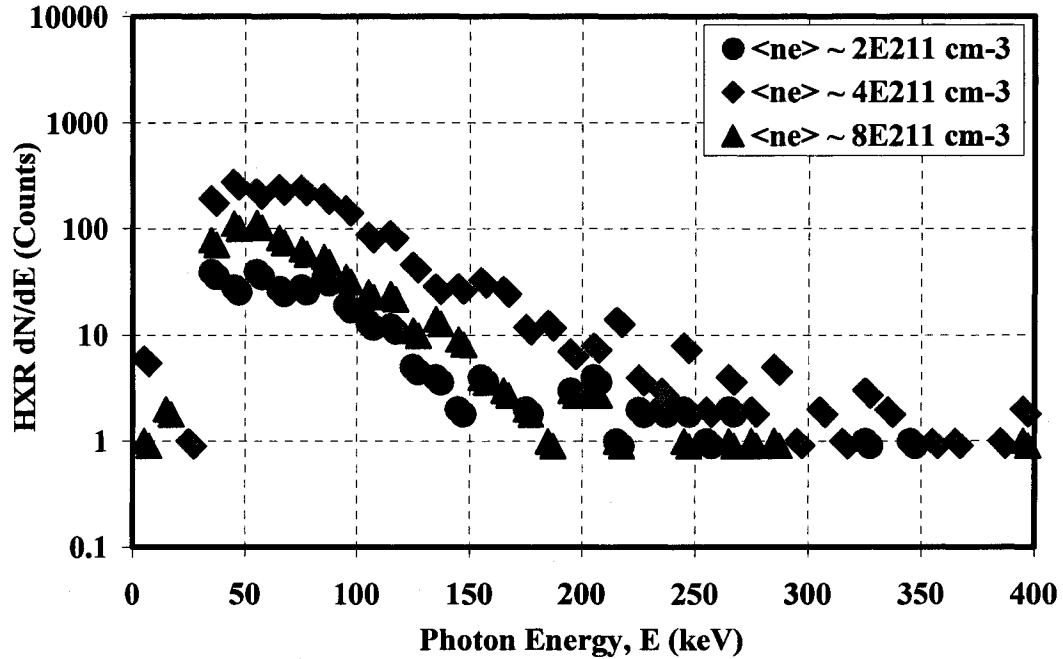


Figure 4.14: Hard x-ray spectrum at three different line-averaged plasma densities for the Mirror configuration.

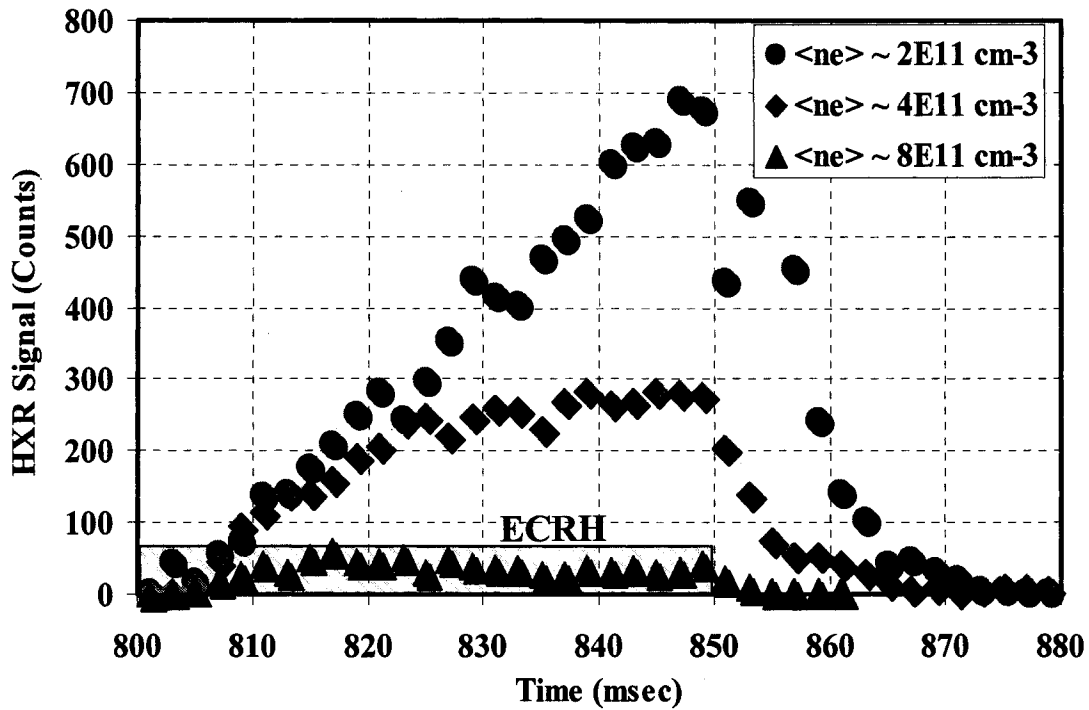


Figure 4.15: Hard x-ray counts time evolution at three different line-averaged plasma densities for the QHS configuration.

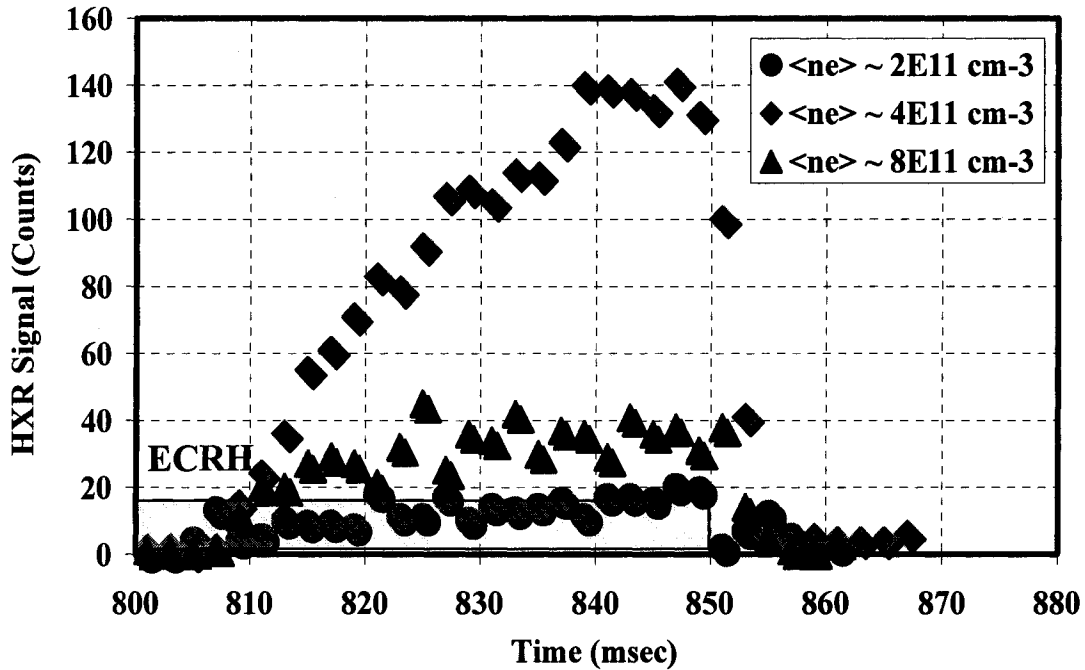


Figure 4.16: Hard x-ray counts time evolution at three different line-averaged plasma densities for the Mirror configuration.

The spectrum is nearly the same at all densities in Mirror configuration, with a slight increase in the hard x-ray photon counts at line-averaged plasma density  $\bar{n}_e = 4 \times 10^{11} \text{ cm}^{-3}$ . The superthermal electron confinement times measured from the decay time of the hard x-ray signal after the microwave power source is turned off is independent of plasma density up to  $\bar{n}_e = 6 \times 10^{11} \text{ cm}^{-3}$ , then decreases with increasing plasma density. In QHS the decay time is  $\sim 7$  msec while in the Mirror case it is roughly 1 msec for low density.

At low plasma density, if the electron velocity surpasses the critical velocity, the electron will be accelerated and its kinetic energy will monotonically increase. At fixed plasma density, the higher the electron velocity, the lower the electron collisionality as the electron collision frequency varies as  $\frac{1}{v_e^3}$ . The energy losses of the already formed superthermal electrons are composed of bremsstrahlung losses, synchrotron losses and collisional losses. The collisional loss process is dominant at electron kinetic energies less than 1 MeV as compared to the bremsstrahlung and synchrotron losses<sup>10</sup>.

In order to study the effect of collisionality on the already generated superthermal electrons during the ECRH discharge, a set of density ramping experiments were performed. In one experiment the plasma density was ramped up during the discharge and in the other the density was ramped down. This was accomplished by controlling the gas puff during the discharge either by increasing or decreasing the gas flow to the machine. The results were compared to similar shots with the same plasma parameters and fixed electron density.

Figure 4.17-4.20 shows the effect of ramping-up the electron density during the discharge on the hard x-ray production in QHS configuration. Figure 4.16 shows the plasma density from two different plasma shots, one with density fixed at  $\bar{n}_e = 2 \times 10^{11} \text{ cm}^{-3}$ , and the other with the same plasma density up to 825 msec and density ramp-up from 825-850 msec. The density was chosen at  $\bar{n}_e \sim 2 \times 10^{10} \text{ cm}^{-3}$ , because it corresponds to the maximum hard x-ray counts produced in QHS. The ramp-up starting time was chosen at the middle of the discharge so there is enough time from the beginning of the discharge to generate a significant population of superthermal electrons and enough time till the end of the discharge to see the density effects on the hard x-ray production. Figure 4.18 shows the hard x-ray count time evolution for the two different cases shown above. In the normal fixed density discharge, the hard x-ray count increases monotonically during the discharge indicating continuous production of superthermal electrons. In the density ramp-up case, the hard x-ray count is the same as the fixed density one up to  $\sim 830$  msec. Then it decreases indicating a suppression of the superthermal electron production due to increased collisionality (e-e, e-i, and e-n). The same behavior is seen in the time evolution of the average and maximum photon energies, as shown in Figures 4.19 and 4.20. The figures show that the hard x-ray average and maximum photon energies increase monotonically during the discharge in the fixed density case and decreases after the microwave power is turned off. On the other hand, in the density ramp-up case, the average and maximum photon energies have the same values as the fixed density case up to  $\sim 830$  msec, then decreases through the end of the discharge.

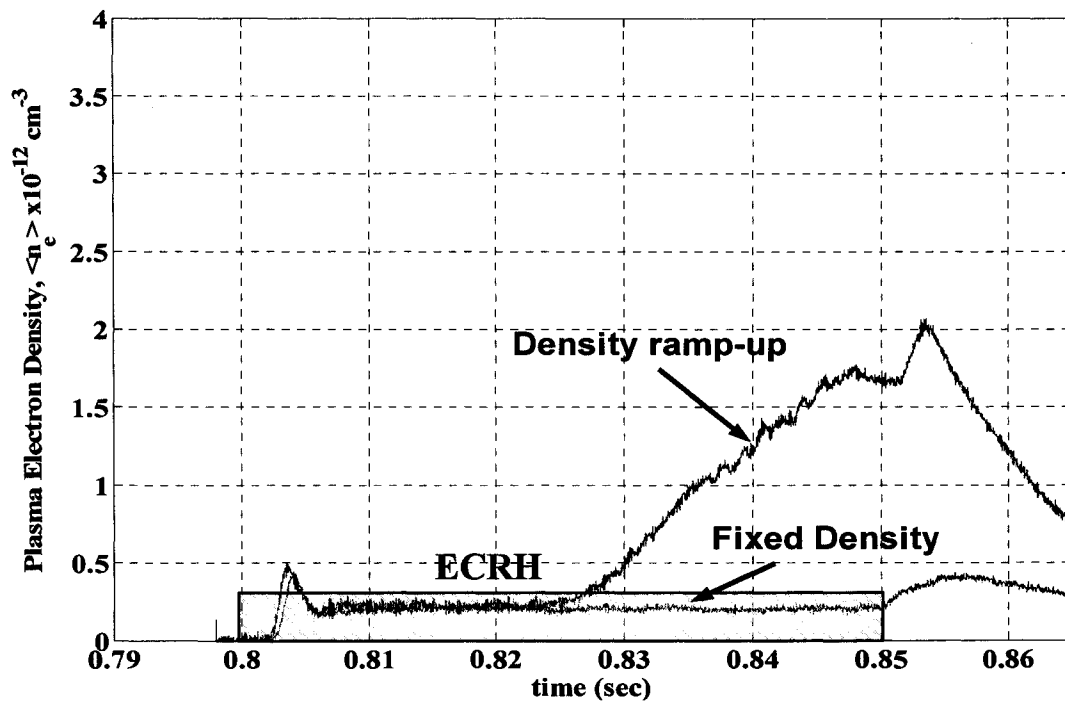


Figure 4.17: Line-averaged plasma density time evolution for QHS during ECRH discharges for two different situations, fixed density and density ramping up.

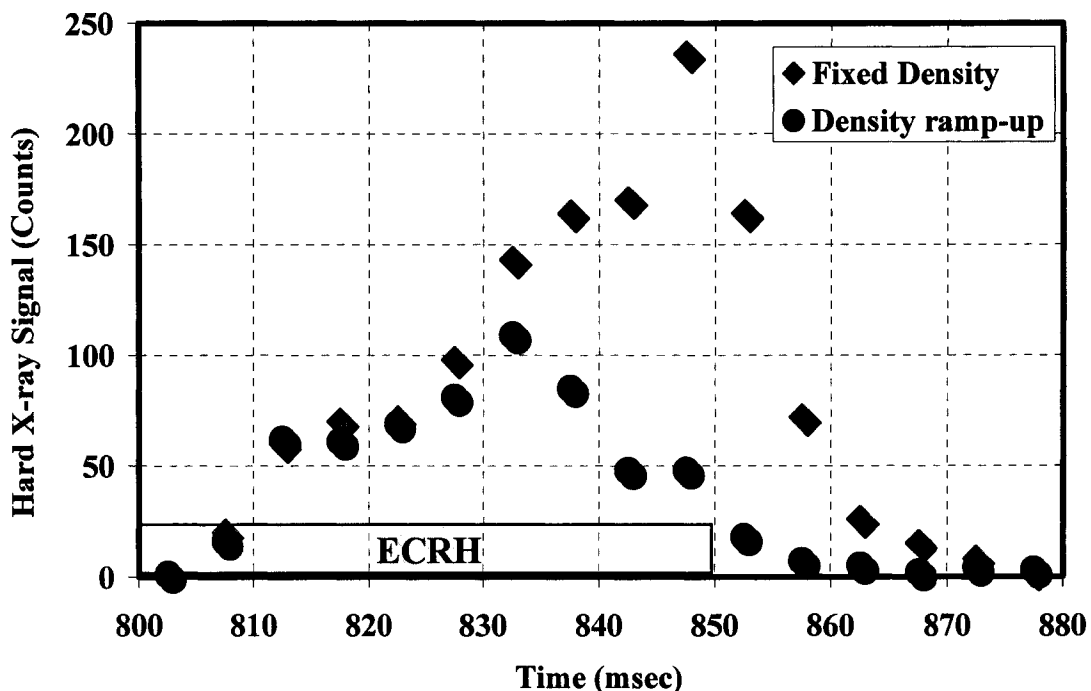


Figure 4.18: Hard x-ray counts time evolution for the two density cases shown in Figure 4.17 for the QHS configuration.

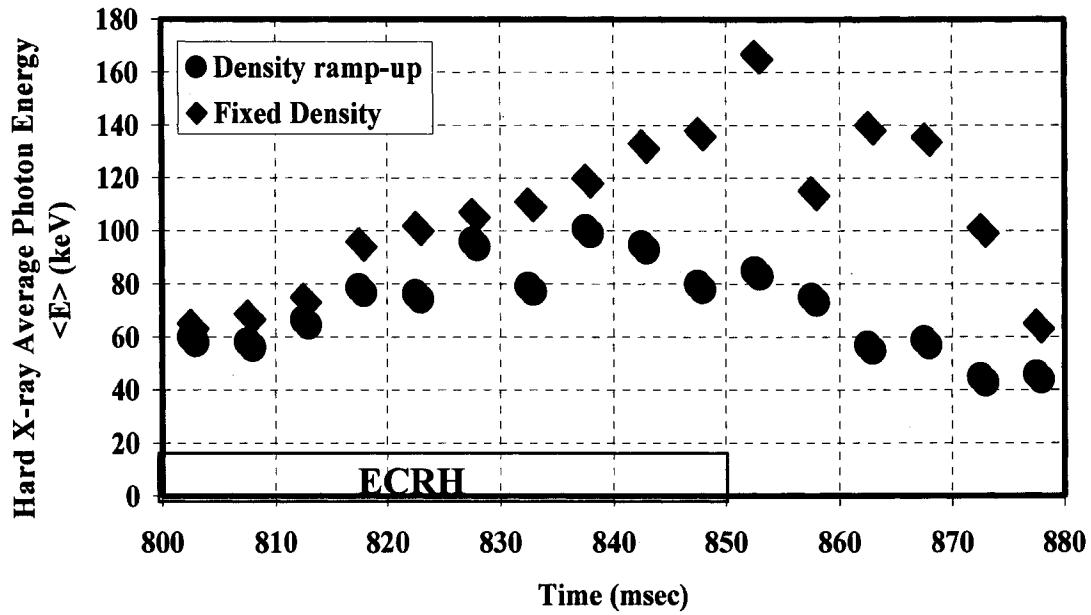


Figure 4.19: Hard x-ray average photon energy  $\langle E \rangle$  time evolution for the two density cases showed in Figure 4.17 for the QHS configuration.

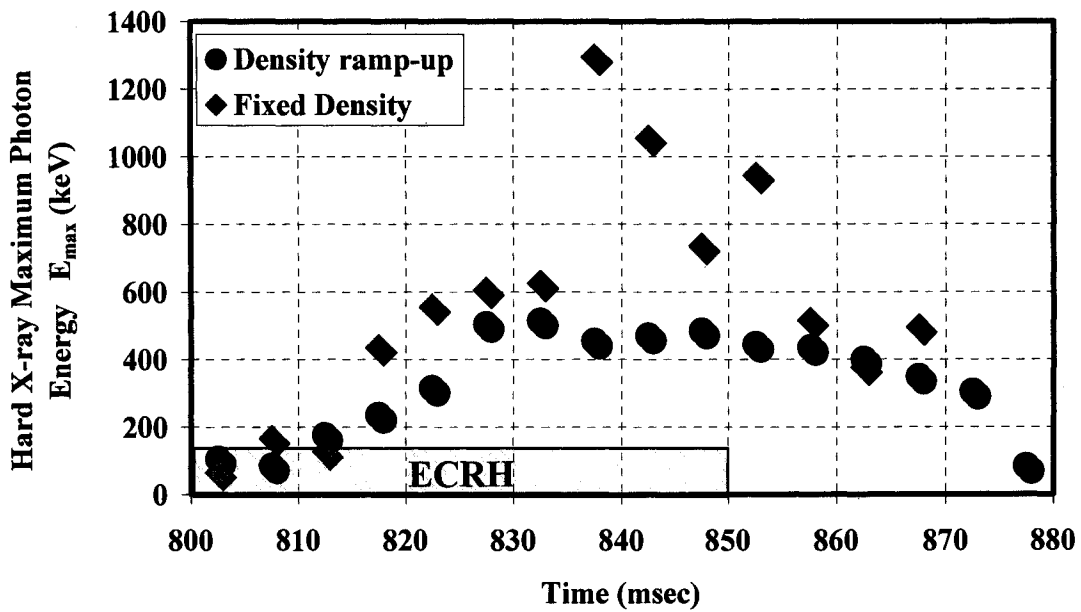


Figure 4.20: Hard x-ray maximum photon energy  $E_{\max}$  time evolution for the two density cases showed in Figure 4.17 for the QHS configuration.

This indicates that the increased collisionality (electron-electron, electron-ion and electron-neutral) prevents the electrons from gaining higher energies during the remainder of the discharge. A similar experiment was performed with the density ramped down instead of ramped up and the effect of collisionality on hard x-ray emission was studied. The results show that decreasing the plasma density increases the hard x-ray counts and the average and maximum photon energies as well.

## 4.5 Hard X-ray Microwave Power Dependence

In order to study the effect of heating power on superthermal electron production, a power scan was performed and the hard x-ray dependence on the microwave power was studied. Figure 4.21 shows the hard x-ray spectrum for the QHS configuration for three different microwave input power levels. The power scan was performed at constant line-averaged plasma density of  $\bar{n}_e \sim 1.6 \times 10^{12} \text{ cm}^{-3}$ , and constant microwave pulse duration of 50 msec. Each spectrum is collected over  $\sim 10$  similar plasma shots. In HSX, at high plasma density  $\bar{n}_e \sim 10^{12} \text{ cm}^{-3}$ , the microwave power absorption is nearly 100%, so the absorbed power is equal to the launched power. The figure shows that, the higher the microwave input power, the higher the hard x-ray counts. This indicates higher superthermal electron production. The slope of the hard x-ray spectrum is nearly constant at the three different microwave power levels shown in the figure. Figure 4.22 shows the variation of the hard x-ray average photon energy with the microwave input power for the above mentioned power scan.

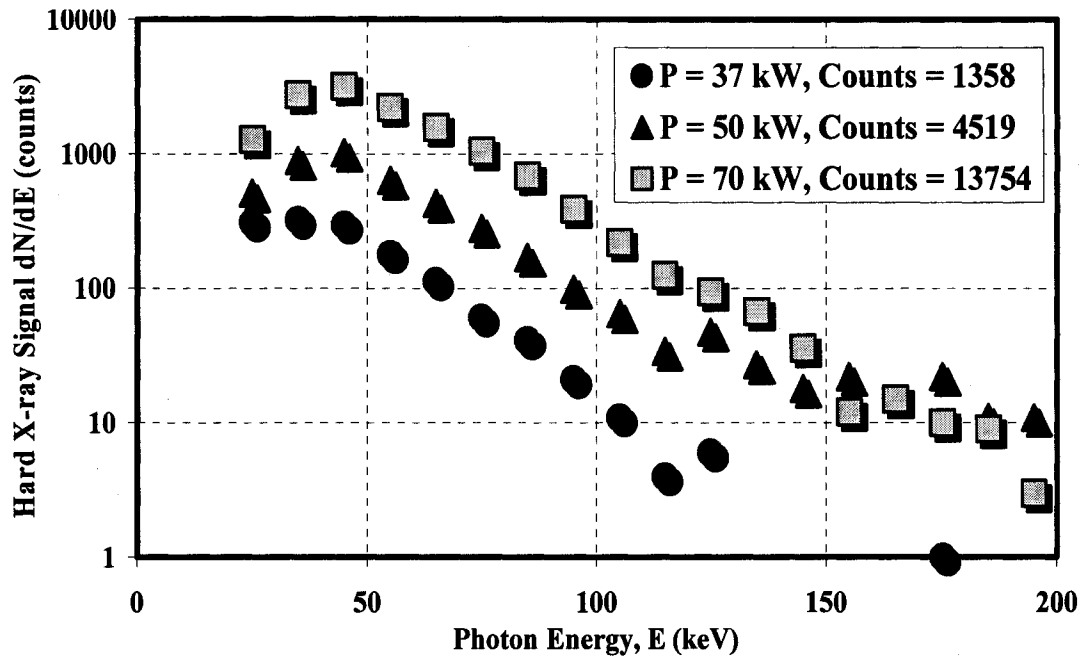


Figure 4.21: Hard x-ray spectrum for three different microwave input powers at the same line-averaged plasma density  $\bar{n}_e \sim 1.6 \times 10^{12} \text{ cm}^{-3}$  for QHS during ECRH discharge.

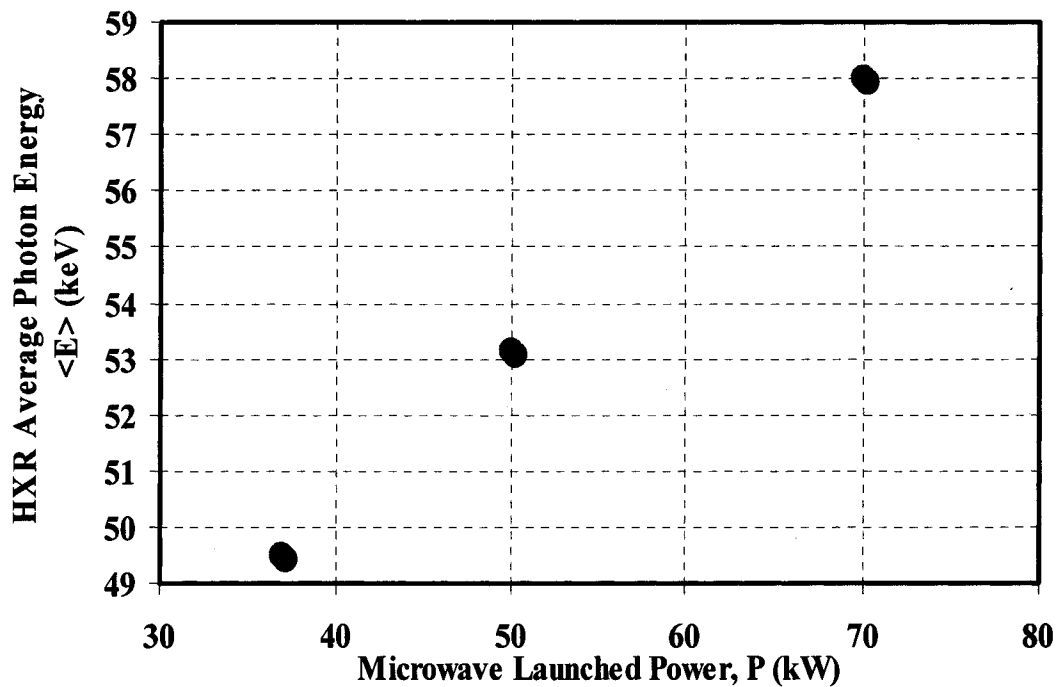


Figure 4.22: Hard x-ray average photon energy microwave power dependence for QHS at line-averaged plasma density  $\bar{n}_e \sim 1.6 \times 10^{12} \text{ cm}^{-3}$ .

The figure is obtained from the spectrum shown in Figure 4.21 by averaging over the photon energy during the 50 msec ECRH discharges. The x-axis represents the microwave launched power in kW and the y-axis represents the average photon energy in keV. The figure shows that the average photon energy has weak linear dependence on the microwave launched power, i.e. the higher the microwave input power, the higher the average photon energy. This scaling is in good agreement to results obtained from the single particle heating model discussed in Chapter 5.

The explanation of the power scan results based on the critical velocity model is as follows: the electron acceleration becomes larger with increasing microwave power (the wave electric field  $\bar{E} \sim P^{\frac{1}{2}}$ ), but the bulk plasma density does not change. This results in strong acceleration of the electrons during one collision time, which leads to efficient production of superthermal electrons as indicated in Figure 4.21. Once the electron velocity becomes large and the coulomb collisions can no longer compete with the acceleration produced by the wave electric field, the electrons are accelerated to become superthermal (until the relativistic mass variation limits their acceleration due to the relativistic detuning effect described above), and their average energy increases as shown in Figure 4.22.

## 4.6 Hard X-ray Resonance Location Dependence

All the results previously described in this chapter were obtained using on-axis ECRH. In order to study the effect of the microwave heating location on the production of

superthermal electrons and their confinement in different magnetic configurations, a scan of the microwave heating location was performed. The scan was obtained by altering the coil current values so that the resonant magnetic field is located at the specific location defined by the effective plasma radius  $r/a$ . For example, if we need the 2<sup>nd</sup> harmonic electron cyclotron resonance to take place at  $r/a \sim 0.5$  (positive values of the effective plasma radius  $r/a$  are located in the outboard side of the machine and negative values are located in the inboard side), the main coil current should be adjusted to produce a magnetic field of  $B = 0.5$  Tesla at  $r/a = 0.5$  in front of the microwave antenna. The scan was performed at constant line-averaged plasma density of  $\bar{n}_e \sim 2 \times 10^{11} \text{ cm}^{-3}$  for QHS and AntiMirror configurations and  $\bar{n}_e \sim 4 \times 10^{11} \text{ cm}^{-3}$  for Mirror configuration.

The variation of the plasma stored energy as measured by the diamagnetic loop and the hard x-ray counts with the microwave heating location is shown in Figures 4.23 and 4.24. The x-axis represent the effective plasma radius,  $r/a$ , of the resonance location and the y-axis is the stored energy in joules and the hard x-ray in counts. The figures show that the QHS has higher stored energy and hard x-ray counts compared to the Mirror and AntiMirror configurations. The figures also show that the maximum value of the stored energy and the hard x-ray counts are located near the magnetic axis  $r/a = 0$  for the QHS and Mirror configurations and is shifted toward the high field side for the AntiMirror configuration. The stored energy and the hard x-ray counts are nearly symmetric around the magnetic axis ( $r/a = 0$ ) for QHS and Mirror and are asymmetric for the AntiMirror configuration.

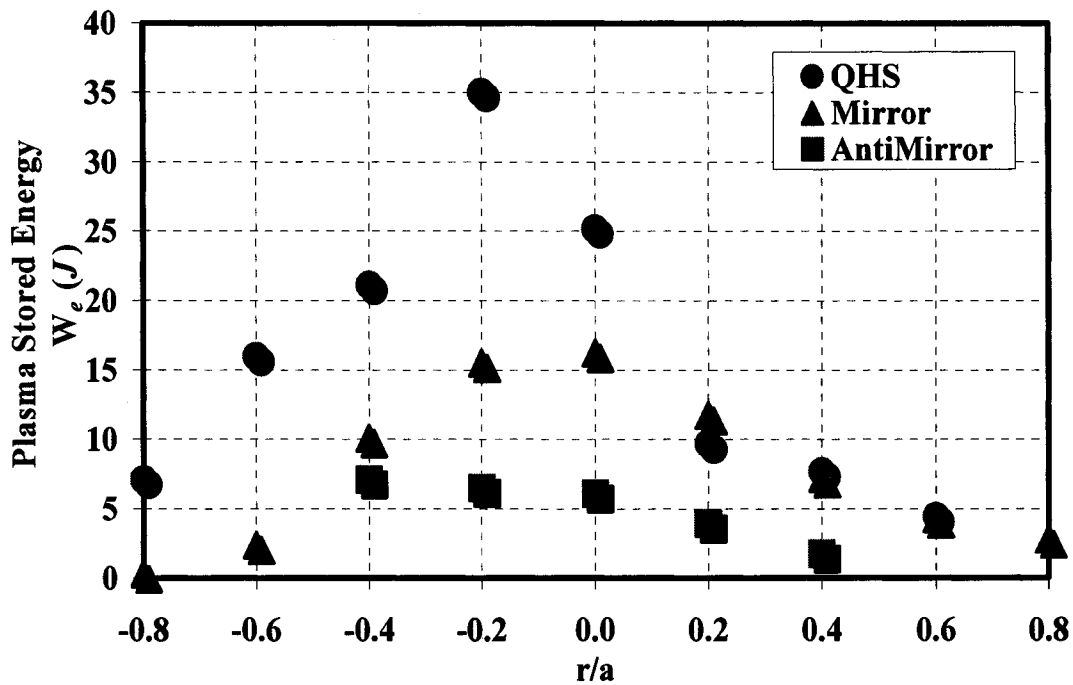


Figure 4.23: The variation of the plasma stored energy with resonance location for QHS, Mirror and AntiMirror configurations.

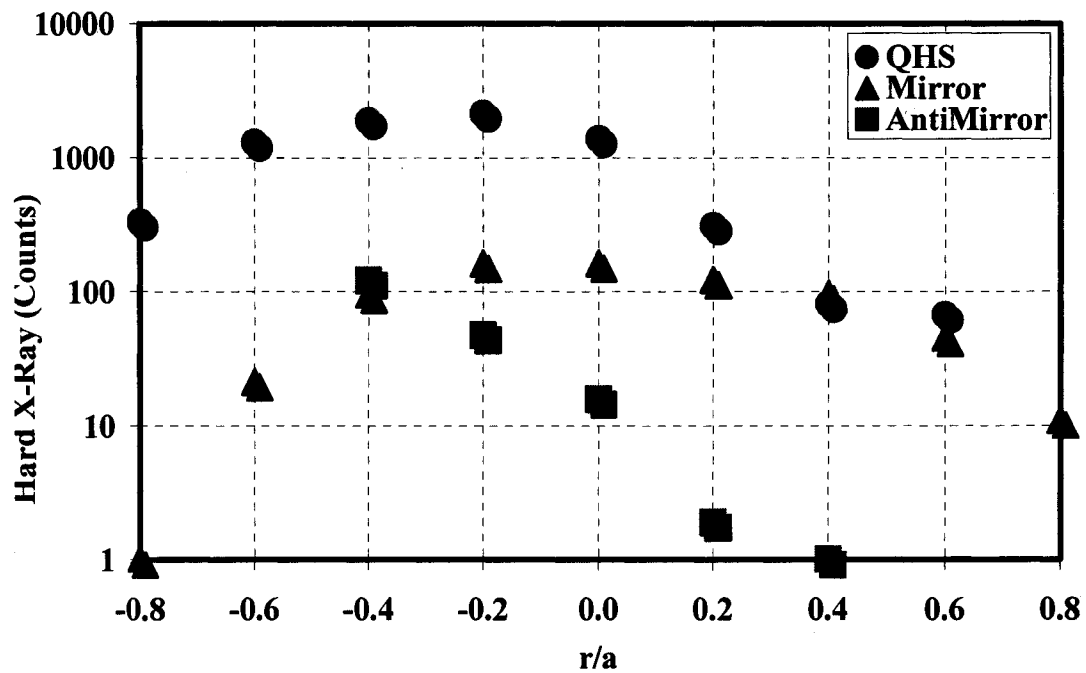


Figure 4.24: The variation of the hard X-Ray counts with resonance location for QHS, Mirror and AntiMirror configurations.

The 2<sup>nd</sup> harmonic X-mode ECRH increases electrons perpendicular energy so that the gyrotron is used to generate a population of trapped electrons at the launch location. In the QHS and Mirror configurations, the ECRH location is near a local maximum in the magnetic field strength, and hence little particle trapping occurs. In the AntiMirror configuration the opposite is true: the ECRH resonance is located at a minimum of the magnetic field strength, so many electrons are trapped and direct orbit losses are large. The magnetic well depth is higher in the outboard side of the machine in front of the microwave antenna and decreases towards the inboard direction. The smaller the well depth the smaller the fraction of electrons trapped in direct loss orbits. This explains the asymmetric behavior of the AntiMirror configuration in the last two figures. The maximum power density deposition is located on-axis for the QHS and Mirror configurations (the magnetic axis is shifted in the Mirror configuration with respect to the QHS configuration) and decreases with increasing the effective plasma radius; this explains the maximum near the magnetic axis in the last figures.

Figures 4.25-4.28 show the density variation of the plasma stored energy and hard x-ray counts for QHS, and Mirror configurations at three different microwave heating locations, inboard, on-axis and outboard, specified by  $r/a = -0.4, 0$ , and  $0.4$  respectively. The off-axis heating results show that the highest stored energy and x-ray signal are located near the magnetic axis, where the maximum power density deposition is expected, because the heating volume is minimum and the power per particle is maximum.

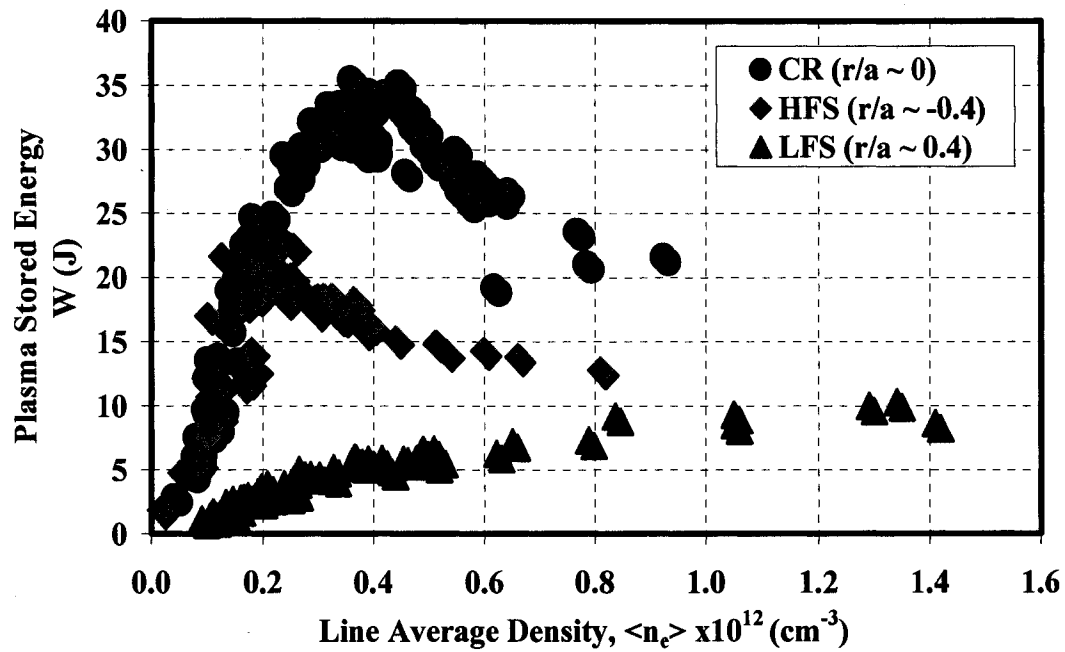


Figure 4.25: The variation of the plasma stored energy with plasma density for the QHS configuration at three resonance locations.

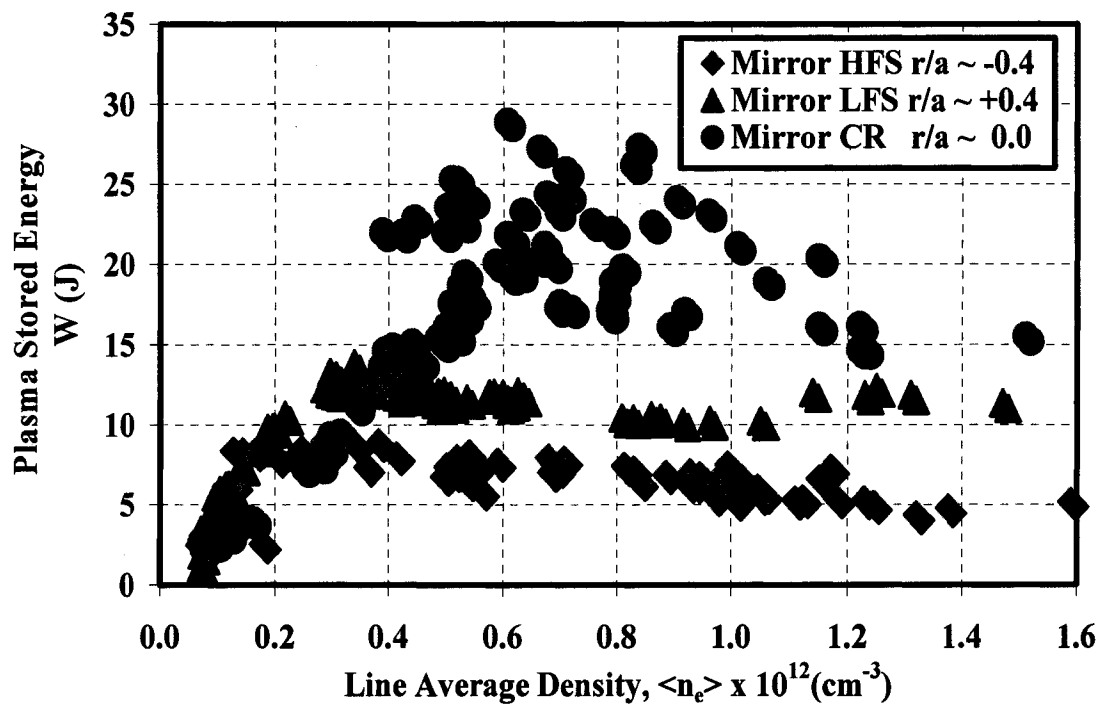


Figure 4.26: The variation of the plasma stored energy with plasma density for the Mirror configuration at three resonance locations.

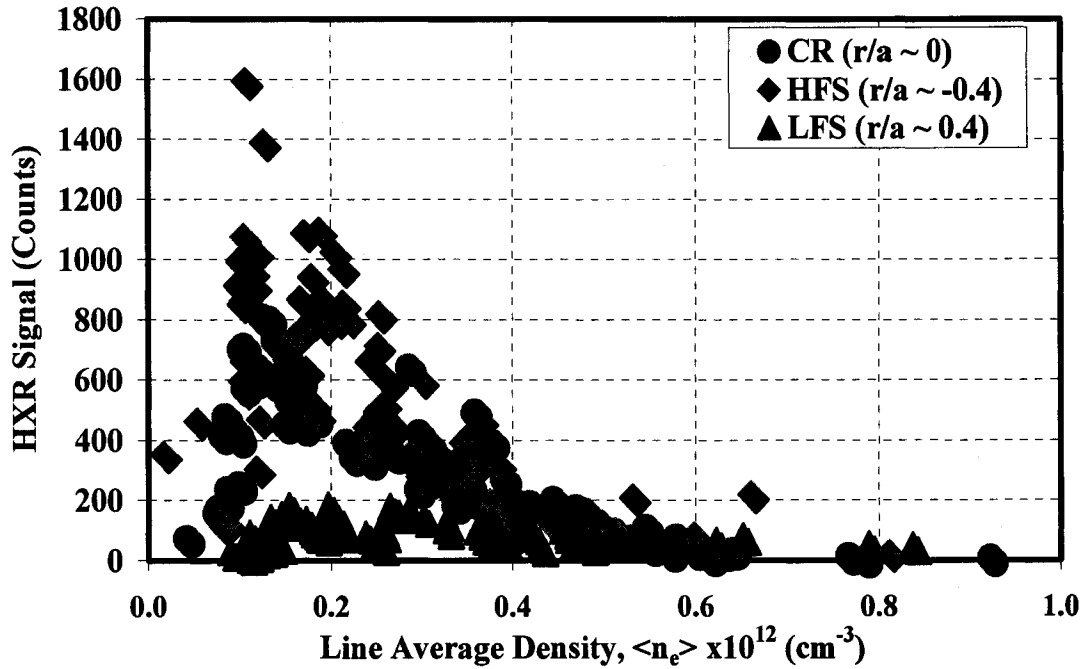


Figure 4.27: The variation of the hard x-ray counts with plasma density for the QHS configuration at three resonance locations.

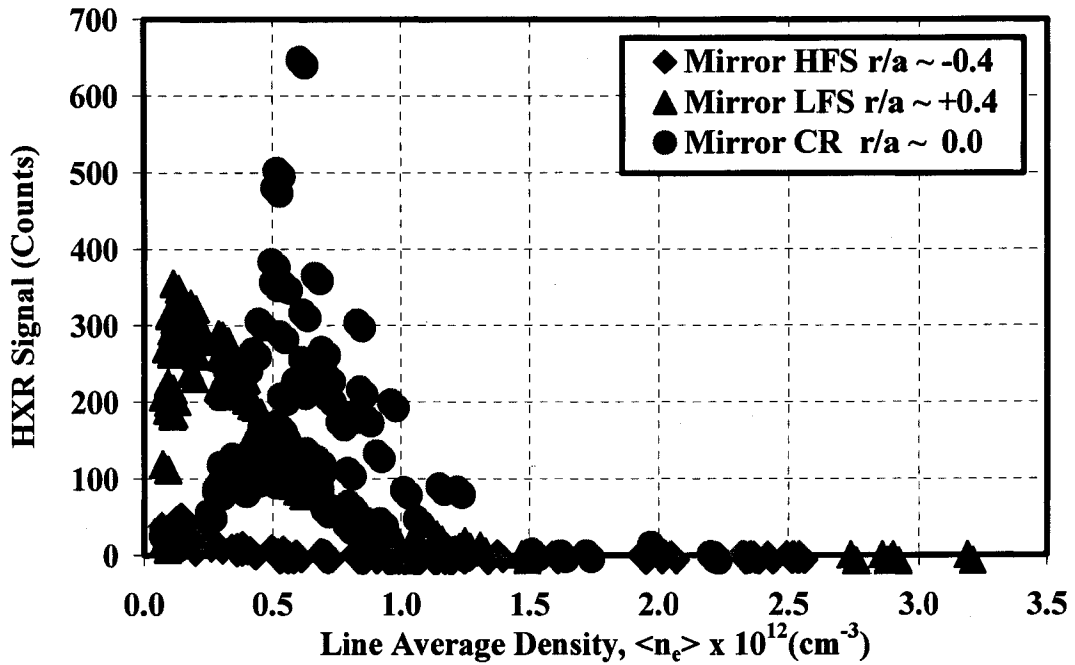


Figure 4.28: The variation of the hard x-ray counts with plasma density for the Mirror configuration at three resonance locations.

In QHS, at low plasma line-averaged density, the stored energy and hard x-ray counts is higher at the high field side as compared to the low field side. The situation is opposite in the Mirror configuration, the high field side is lower than the low field side. This can be explained in QHS as follows; electrons launched at the high field side in front of the antenna are on the top of the magnetic well and they are passing particles, while particles launched at the low field side are in the bottom of the magnetic field are most likely trapped. The majority of the particles are trapped because ECRH heating increases the electrons perpendicular energy as a result, increases their pitch angle as will be shown in Chapter 6.

## 4.7 Summary

The hard x-ray emission during ECRH in different magnetic configurations in the HSX stellarator was discussed. The spectral differences between configurations show that in QHS, a higher superthermal electron population with higher energy is present at low plasma density compared to the Mirror and the AntiMirror configurations. The time evolution of the hard x-ray signal shows longer decay time after the microwave source is turned off in QHS compared to Mirror indicating that superthermal electrons are better confined.

The hard x-ray density scan shows that the hard x-rays have a nonlinear density scaling. QHS has larger hard x-ray signal compared to Mirror configuration at low densities  $\bar{n}_e \sim 5 \times 10^{11} \text{ cm}^{-3}$  and they are nearly the same at higher density indicating better confinement in QHS compared to Mirror at low density. The power scan shows that the hard x-ray

average photon energy has weak linear dependence on the microwave input power at high plasma line-averaged density.

- 
- <sup>1</sup> M. Hirata et al., Japanese Journal of Applied Physics, **28**(1), 96, (1989).
- <sup>2</sup> S. Morimoto et al., Nuclear Fusion, **29**(10), 1697, (1989).
- <sup>3</sup> I.H. Hutchinson, "Principles of Plasma Diagnostics", 2<sup>nd</sup> edition, page 179, (2002).
- <sup>4</sup> K. Likin et al., AIP Conference Proceedings, **694**(1), 331, December 15, (2003).
- <sup>5</sup> K. Likin et al., Plasma Physics and Controlled Fusion, **45**, A133, (2003)
- <sup>6</sup> H. Knoepfel, "Hard X-Ray Measurements" in "Diagnostics for Fusion Experiments", Pergamon press, (1979).
- <sup>7</sup> I. H. Hutchinson, "Principles of Plasma Diagnostics", 2<sup>nd</sup> edition, Cambridge University Press, (2002).
- <sup>8</sup> Y. Peysson, Plasma Physics and Controlled Fusion, **35**, B253, (1993).
- <sup>9</sup> S. Gerhardt et al., Review of Scientific Instruments, **75**(9), 2981, (2004).
- <sup>10</sup> H. Boehmer et al., Physics of Fluids, **28**(10), 3099, (1985).

# Chapter 5

## Single Particle Heating Model

### 5.0 Introduction

ECRH in non-uniform magnetic fields has been the subject of extensive theoretical and experimental research.<sup>1,2,3,4</sup> Numerous analytical and numerical studies have been performed regarding the dynamics of electrons under ECRH by a strong monochromatic wave in a non-uniform static magnetic field.<sup>2,3</sup> The response of the electrons to the microwave electric field is described in terms of gains in energy and magnetic moment. In a typical situation waves are absorbed in a narrow resonant zone where a particle gains or loses energy depending on the wave-particle phase. As the particle moves along magnetic field lines, its phase changes as a result of collisions, so that in a subsequent passage through the resonant zone the phase is randomized. In this case a particle acquires energy on average.

The experimental data presented in Chapter 4 shows substantial difference in hard x-ray emission between QHS and Mirror configurations. The first question that should be asked is what causes this difference? Is it a difference in microwave heating or a difference in electron confinement between the magnetic configurations, so that in QHS electrons are confined for longer times than in the Mirror configuration and gain more energy as a result of more passes through the heating zone? In order to answer the question a comparison of single particle ECR heating and confinement between the

magnetic configurations should be investigated. A single particle heating model in the HSX stellarator will be treated numerically in this chapter using the technique of integration of the Lorentz force equation. Single particle guiding center drift orbits and confinement will be studied in Chapter 6. Section 5.1 describes the model and its limitations and the code developed for the numerical solution of the equation of motion. The phase-averaged energy gain during a single pass through the heating zone is obtained analytically in Section 5.2. Section 5.3 then discusses the phase-averaged energy gain during a single pass through the heating zone calculated numerically as a function of multiple parameters, including the wave electric field  $E$ , the perpendicular wave number  $k_{\perp}$ , and the perpendicular and parallel kinetic energies  $W_{\perp}$  and  $W_{\parallel}$ . The experimental validation of the code is given in Section 5.4 and the chapter concludes with summary in Section 5.5.

## 5.1 Model Description

The relativistic equation of motion of an electron in electric and magnetic fields  $(\vec{E}, \vec{B})$  is:

$$\frac{dm_e \gamma \vec{v}}{dt} = -e(\vec{E} + \vec{v} \times \vec{B}) \quad (5.1)$$

where,  $\gamma = (1 - \frac{v^2}{c^2})^{-\frac{1}{2}}$ ,  $m_e$  and  $-e$  are the electron rest mass and charge,  $\vec{v}$  the electron velocity,  $\vec{E}$  the linearly polarized wave electric field for X-mode heating,  $\vec{B}$  the magnetic field (the summation of the external static and wave magnetic fields).

### 5.1.1 Microwave Electric Field model

As stated before, the plasma is produced and heated in HSX using 28 GHz second harmonic, X-mode ECRH. The microwave beam is launched from the low field side in the  $-\hat{x}$  direction (in a Cartesian co-ordinate system with the origin located at the torus center and the x-axis is directed towards the box port C) perpendicular to the magnetic field line. The beam is focused using ellipsoidal mirror to the magnetic axis with a spot size of 4 cm (the beam radius is 2 cm and is defined as the distance at which the field falls to  $1/e$  relative to its on-axis value). A schematic of box port C showing the ellipsoidal mirror and the microwave beam is shown in Figures 5.1.

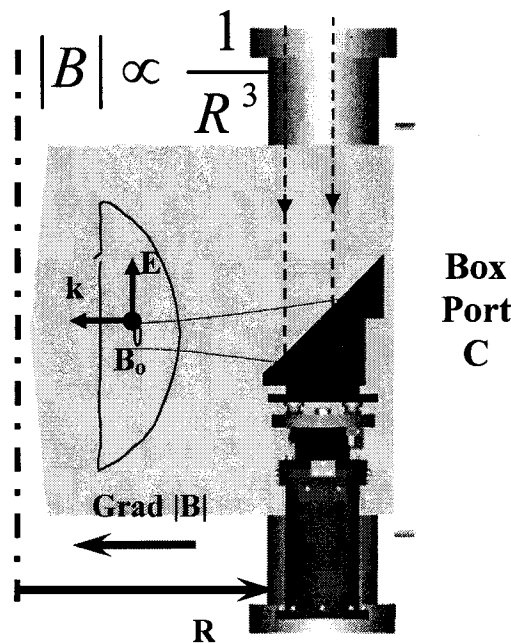


**Figure 5.1: Schematic of Box Port C showing the ellipsoidal mirror and the microwave beam. Figure courtesy of K. Likin.**

(The polarization of the wave electric field usually defines its direction in the co-ordinate system). Figure 5.2 shows the co-ordinate systems used in the numerical model. The Cartesian lab co-ordinate system centered at the machine geometrical center and the local Cartesian co-ordinate system at box port C is used to describe the microwave electric field. A transformation between the co-ordinate systems is done in the code.

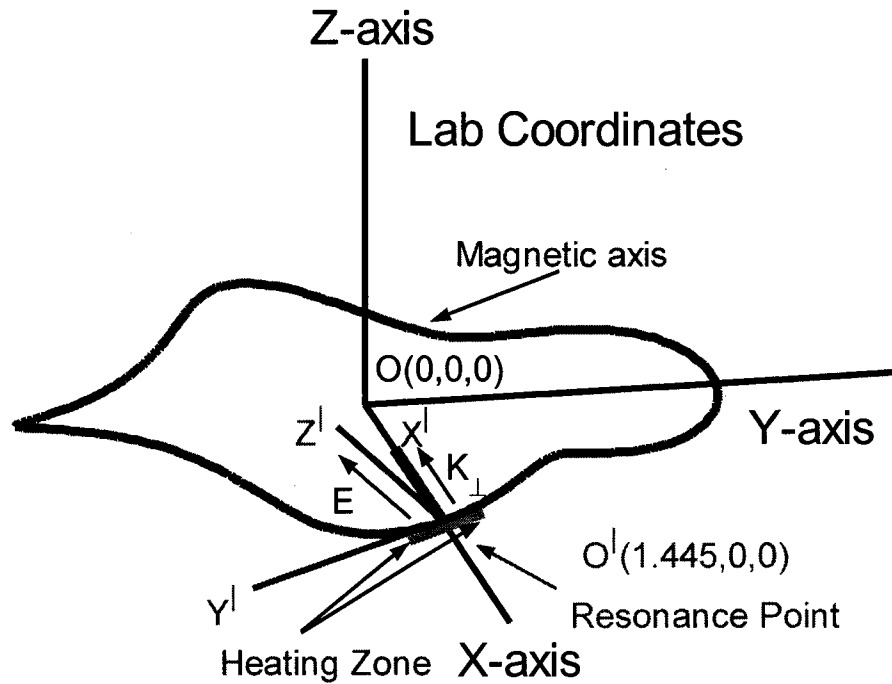


**Figure 5.2: View of HSX showing beam location and resonance point at (1.445,0,0) for the QHS configuration.**

With X-mode heating, at box port C, the wave electric field is perpendicular to the magnetic field on-axis and pointing in the  $\hat{Z}'$  direction as shown in Figure 5.2 (the resonance point where  $\omega = 2\Omega_e = 2\frac{eB}{m_e}$  for second harmonic is satisfied is located on-axis at  $O' = (1.445, 0, 0)$ ). The microwave electric field used in the Lorentz equation was modeled as follows: a Gaussian beam in the (Y,Z) directions with a beam width of 4 cm

is centered at the resonance point on-axis; the wave propagates perpendicular to the magnetic field on-axis in the  $-\hat{x}$  direction; it is linearly polarized in the  $\hat{z}'$  direction; and oscillates with a frequency 28 GHz. In mathematical form, the microwave electric field can be represented as:

$$\vec{E} = E_o e^{-\frac{y^2+z^2}{w^2}} \cos(\omega t - k_{\perp} x - \phi) \hat{z}' \quad (5.2)$$

where,  $E_o = \sqrt{\frac{2PR}{w^2}}$  is the amplitude of the microwave electric field, P the microwave power in Watts, R the resistance of free space  $\sim 377$  ohms,  $W = 4$  cm the microwave beam width,  $\omega = 2\pi f$  the wave angular frequency,  $f = 28$  GHz,  $k_{\perp} = \frac{N_{\perp}\omega}{c}$  the perpendicular wave number,  $N_{\perp}$  the perpendicular index of refraction, c the speed of light, and  $\phi$  (the wave-particle initial phase difference).

### 5.1.2 Magnetic Field model

The magnetic field used in the Lorentz equation is composed of two parts: the static field generated by the HSX modular coils and the time varying microwave magnetic field given by:

$$\vec{B}_{Microwave} = \frac{k_{\perp}}{\omega} \vec{E} \quad (5.3)$$

$$\vec{B} = \vec{B}_{HSX} + \vec{B}_{Microwave} \quad (5.4)$$

In order to calculate the HSX magnetic field, two separate methods are used. One of them is based on using lookup tables calculated from Biot-Savart law at a specified set of grid points, and simply interpolates the components of  $\vec{B}$  onto the required point. The other uses the Biot-Savart law directly to calculate the field using a segmented model of the coils. The major difference between the two methods is the lookup tables are fast, while the Biot-Savart code is more accurate. In the Biot-Savart program the main coils are represented by 14 turns, 60 segments per turn, and are closed at the feed block. The auxiliary coils are also closed, and are represented by a single turn. The Matlab single particle heating program can call the Biot-Savart program or the lookup tables (both methods were developed by J. Canik of the HSX group) to calculate the magnetic field at the particle location during the integration of the Lorentz equation. We tested both methods and noticed that the difference in the magnetic field calculated using the look-up tables and the Biot-Savart law is very small  $\sim 1\%$ . The error in the energy net energy gain introduced when using the look up tables is very small  $\sim 1-2\%$  so we decided to use the look up tables in calculating the magnetic field during the rest of the modeling in order to speed up the numerical calculations. Figure 5.3 shows the amplitude of the magnetic field on-axis for three different HSX magnetic configurations using the look up tables. The x-axis is the toroidal angle  $\varphi$  in degrees and the y-axis is the amplitude of the magnetic field along the field line. The microwave heating zone is located inside the circle shown in the figure at  $\varphi = 0$  and extends from  $\varphi \sim -1.5^\circ$  to  $\varphi \sim 1.5^\circ$  (-4 centimeters to 4 centimeters from the resonance point on axis).

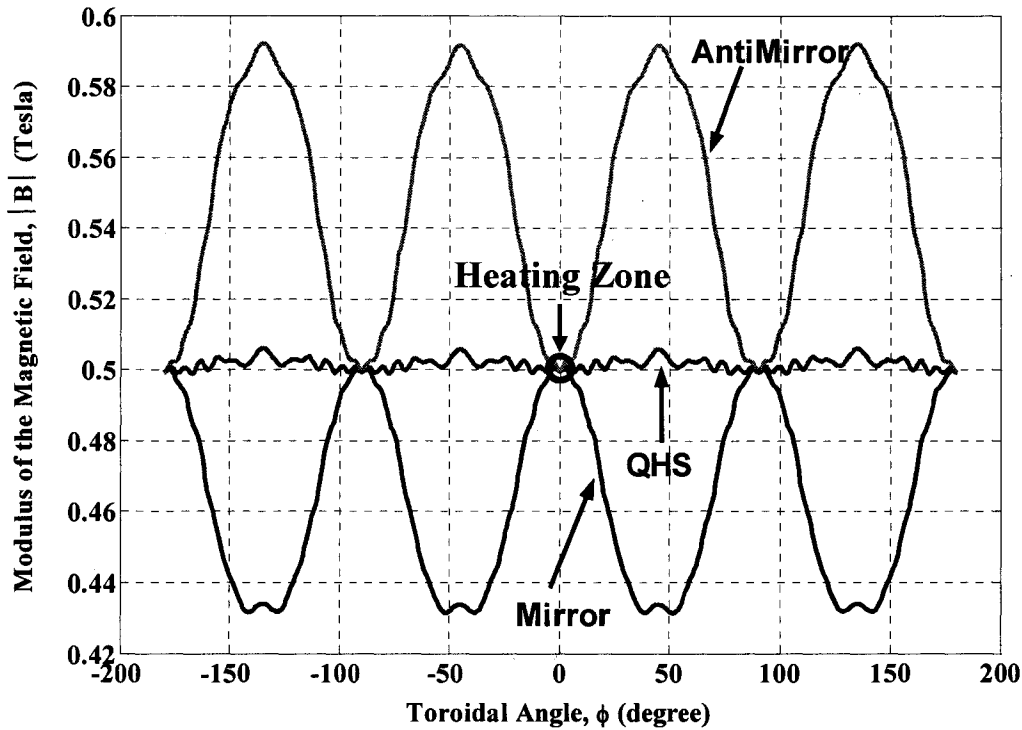
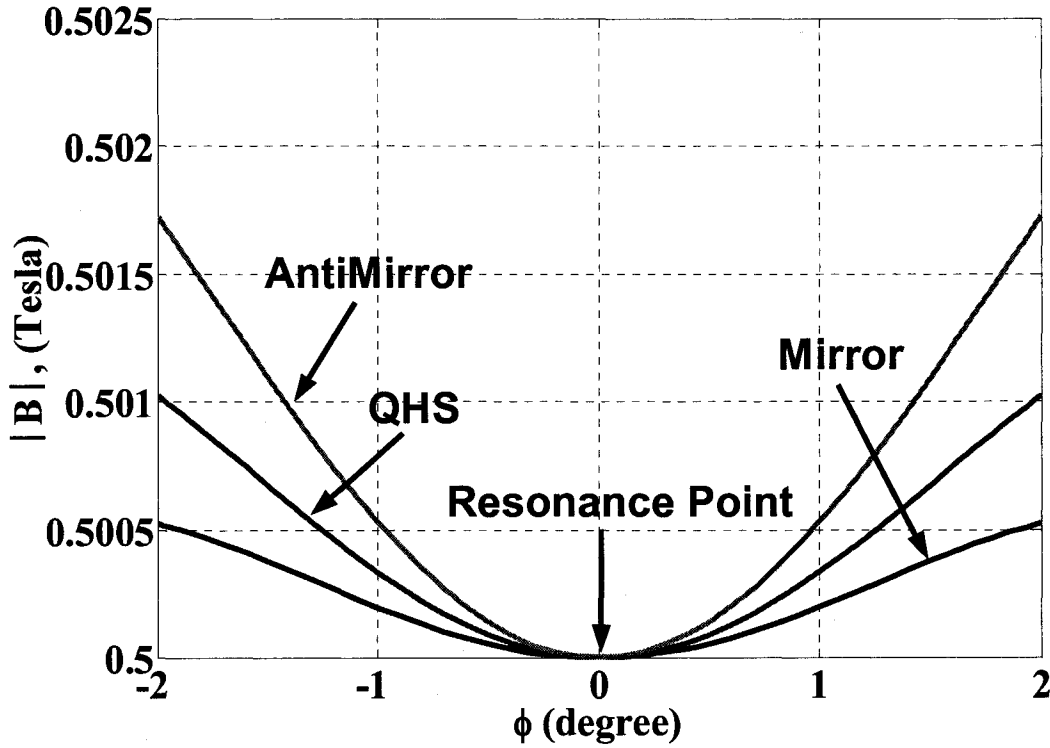


Figure 5.3: Toroidal variation of  $|B|$  on axis for QHS, Mirror and AntiMirror

### 5.1.3 Model Assumptions

In the model presented here the following assumptions are made which permit the estimation of the net energy gain during a single pass through the resonance zone in different HSX magnetic configurations:

- 1- The heating zone is localized in box port C and is defined as the region extending  $\sim 4$  cm from both sides of the resonance point on axis (point  $[1.445, 0, 0]$  for QHS). This is justified because the wave electric field is  $\sim 10\%$  at a distance of  $\sim 3$  centimeters from both sides of the resonance point and  $1\%$  at 4 centimeters. There is no microwave electric field component elsewhere in the machine (wall reflection was not taken into consideration). Figure 5.4 shows the magnitude of the magnetic field in the heating zone for different magnetic configurations.



**Figure 5.4: Toroidal variation of the magnitude of magnetic field  $|B|$  on axis along field line in the heating zone for QHS, Mirror and AntiMirror**

- 2- Although the code has the capability of solving the relativistic as well as the non-relativistic Lorentz equation, the non-relativistic equation only is solved because relativistic effects are negligible at electron energies ( $10^2$  to  $10^4$  eV) used to study the net energy gain during a single pass through the heating zone.
- 3- The electric field in the heating zone is purely transverse to the magnetic field and propagates in the  $-\hat{x}$  direction i.e.  $k_{\parallel} = 0$ .
- 4- The resonance time is defined as the time taken by the particle to cross the heating

zone  $\tau_{res} = \frac{L_{res}}{v_{\parallel}}$  where  $L_{res}$  is the resonance zone length and  $v_{\parallel}$ , the particle parallel velocity, is long enough so that the particle makes many cyclotron

gyrations, short enough so that no collisions take place during the resonance

$$\text{crossing } \frac{1}{v_{coll}} > \tau_{res} > \frac{2\pi}{\Omega_e}.$$

### 5.1.4 Code Description

A Matlab program (a detailed description of the code is presented in Appendix 4) was developed to solve both the relativistic and the non-relativistic equation of motion numerically and to obtain the trajectories and net energy gain of the test particles interacting with the microwave in the heating zone in different HSX magnetic configurations. The code uses the Matlab “ode45” solver. The “ode45” solver is based on an explicit Runge-Kutta (4,5) formula, the Dormand-Prince pair<sup>5,6</sup> (based on the fourth and fifth order Runge-Kutta pairs). The time step is adjusted automatically in Matlab to resolve the fine details of electron gyromotion. Each electron is launched -4 cm toroidally from the left of the resonance point on the magnetic axis and the integration time is adjusted so that at the end of the run, the particle will move to approximately +4 cm toroidally to the other side of the resonance point. Each electron is injected with initial kinetic energy  $W_{initial}$ , variable pitch angles  $\alpha$ , and initial phase  $\phi$  between gyro orbit and wave electric field. An example of the program output plots are shown in Figures 5.5, 5.6 and 5.7 for QHS configuration for the following parameters: starting position = -4 cm,  $W_{initial} = 200$  eV, pitch angle  $\alpha = 45^\circ$ , initial phase  $\phi = 0$ ,  $E_0 = 1.7 \times 10^5$  V/m (corresponding to a microwave power of 50 kW),  $N_\perp = \frac{ck_\perp}{\omega} = 1$ , and integration time =  $1.6 \times 10^{-8}$  sec. Figure 5.5 shows the electron trajectory following the magnetic field line in

the heating zone in the lab co-ordinates. The thickness of the line is the electron gyro-diameter. Figure 5.6 shows the toroidal variation of the magnitude of the magnetic field along the field line that passes through the particle starting point. As the figure shows, the magnetic field is symmetric around the resonance point on-axis ( $B = 0.5$  T). The time evolution of the electron energy and particle toroidal location through the heating zone is shown in Figure 5.7. The figure shows that when the wave-particle phase difference  $\phi = 0$  the particle kinetic energy increases from 200 to 260 electron volts after crossing the heating zone, while the particle toroidal location changes from -4 to 4 centimeters.

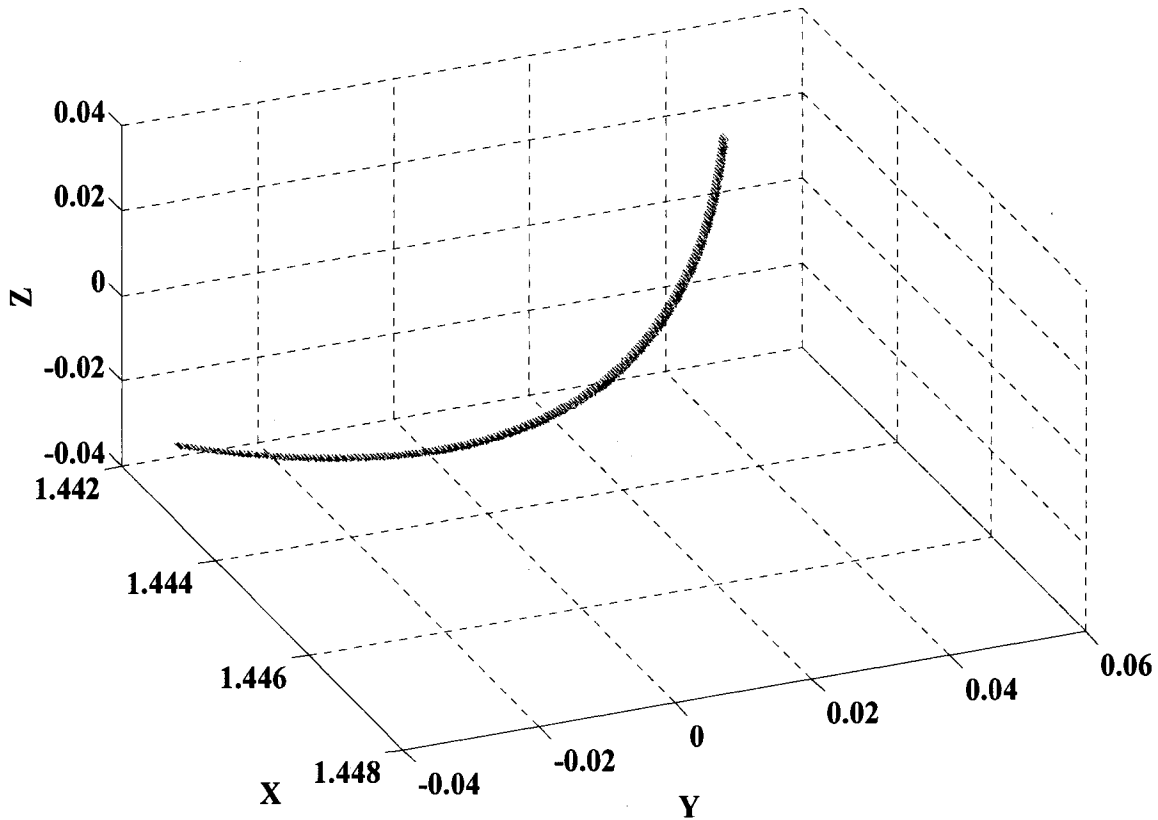


**Figure 5.5: Electron orbit in lab coordinates following magnetic-axis in the heating zone for QHS (thickness of the orbit is the electron gyro-diameter)**

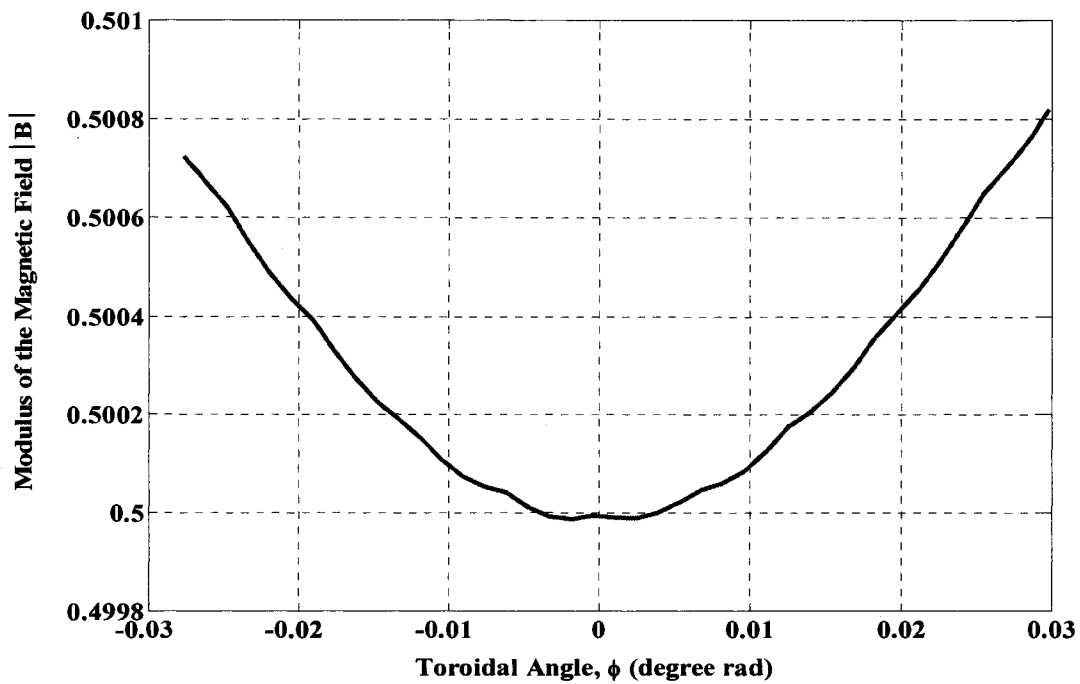


Figure 5.6: Magnetic field followed by the electron on-axis in the heating zone for QHS. Note the symmetry with respect to  $\phi$ .

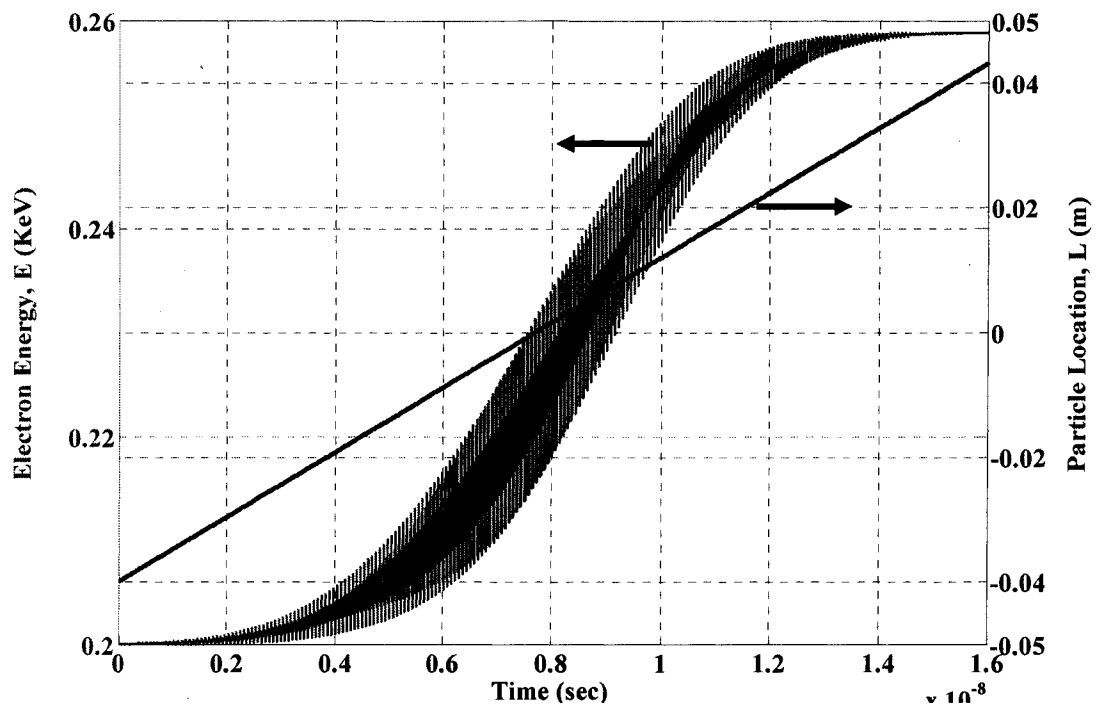
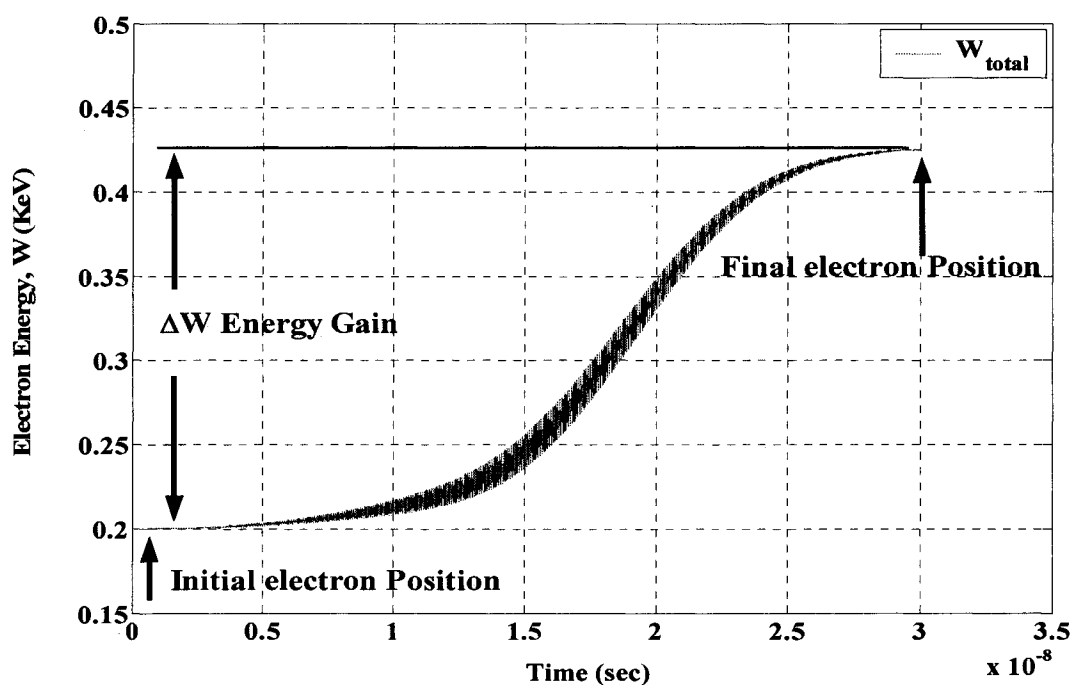


Figure 5.7: Electron total energy time evolution through the resonance zone (red) and particle location time evolution through resonance zone (blue) in QHS configuration.

At the initial launching location -4 cm from the resonance point, the wave electric field is almost 1% of its maximum value at  $\phi = 0$ . As the electron approaches the resonance zone, the wave electric field starts to increase and the electron couples to it. Depending on the initial phase between the electron and the microwave field, the electron begins to gain or lose energy. Figures 5.8 and 5.9 show the two different situations. The x-axis represents the time it takes the particle to cross the resonance zone and the y-axis represents the electron kinetic energy.



**Figure 5.8: Electron total energy time evolution through the resonance zone in QHS, pitch angle  $\alpha = 70^\circ$ , and initial phase  $\phi = 0^\circ$ .**

In the first case the electron gains energy from the microwaves when its initial phase =  $0^\circ$ , while in the second case, the electron loses energy when its initial phase =  $135^\circ$ . The rapid oscillations in energy are caused by the difference in the electric field amplitudes on

both sides of the gyro-orbit as discussed in Chapter 3. The oscillation has the same frequency as the electron gyro-frequency.

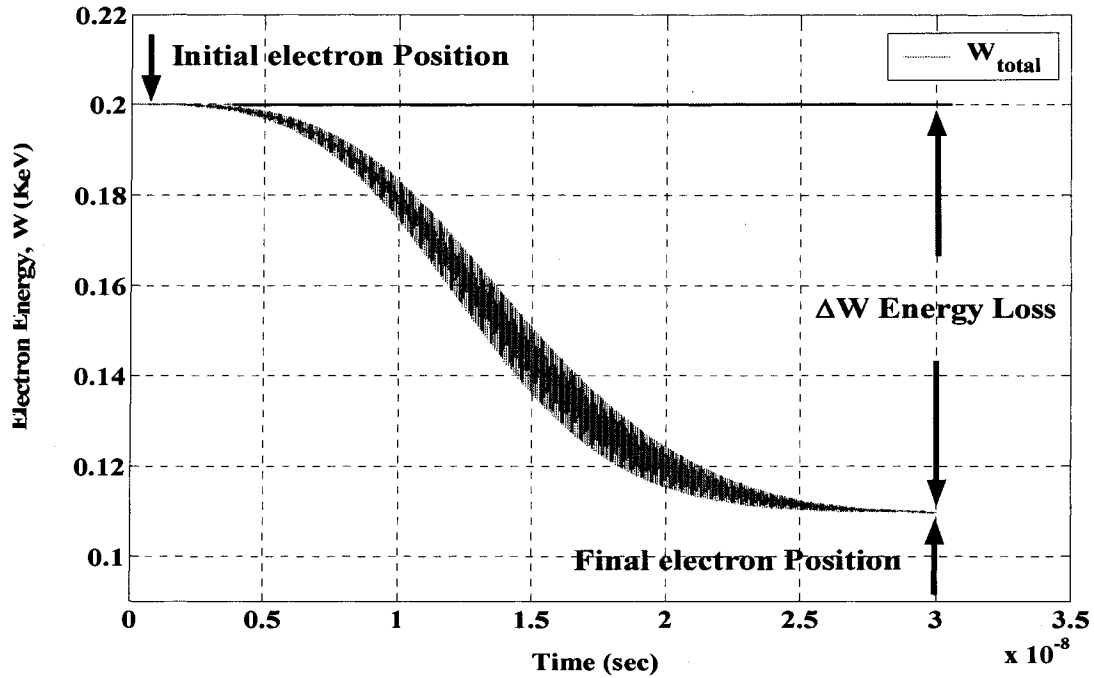


**Figure 5.9: Electron total energy time evolution through the resonance zone in QHS, pitch angle  $\alpha = 70^\circ$ , and initial phase  $\phi = 135^\circ$ .**

As stated before, the heating mechanism is a stochastic process, where a single electron can gain or lose energy from the microwave field. When the electron leaves the heating zone, it will follow field lines and on subsequent passes through the heating zone will have a different phase because of different effects while it was outside the heating zone including: coulomb collisions with other plasma species (electrons or ions) or neutral atoms, variations in drift orbit trajectories, and/or the fluctuation in density of the cold plasma which support the wave.

### 5.1.5 Energy Gain Dependence on Initial Phase

In order to study the phase dependence of the energy gain,  $\Delta W$ , in a single pass through the heating zone, the initial phase is varied in the range between 0 to  $2\pi$ , with an increment of  $2\pi/20$ , and the energy gain for each phase is calculated. The calculations were performed for the parameters; starting position = -4 cm,  $W_{\text{initial}} = 50\text{-}2000$  eV, pitch angle  $\alpha = [10^\circ \ 30^\circ \ 50^\circ \ 75^\circ]$ , initial phase  $\phi = 0\text{-}2\pi$ ,  $E_0 = 1.7 \times 10^5$  V/m,  $N_\perp = \frac{ck_\perp}{\omega} = 1$ , and integration time =  $1\text{-}5 \times 10^{-8}$  sec. Figure 5.10 shows the results for the case  $W_{\text{initial}} = 200$  eV, pitch angle  $\alpha = 75^\circ$ , initial phase  $\phi = 0\text{-}2\pi$ , for three different magnetic configurations, QHS, Mirror and AntiMirror. The x-axis is the wave-particle initial phase in radians and the y-axis is the kinetic energy gain,  $\Delta W$ , during a single pass through the heating zone.

The calculations show an offset sinusoidal dependence in the initial phase of the energy gain  $\Delta W$  (the reason for the offset will be described in the next section, analytical solution). A positive energy gain  $\langle \Delta W \rangle$  results if the energy gain is integrated uniformly over all initial phases. If there is an electron population with a specific energy distribution and random phases passing through the heating zone, the population will leave the heating zone with a net energy gain  $\langle \Delta W \rangle$ , where  $\langle \rangle$  represents averaging over all phases. Through the rest of the chapter our goal will be focused on studying the net energy gain  $\langle \Delta W \rangle$  in different magnetic configurations and its parametric dependence will be found for varying a number of parameters as detailed below.

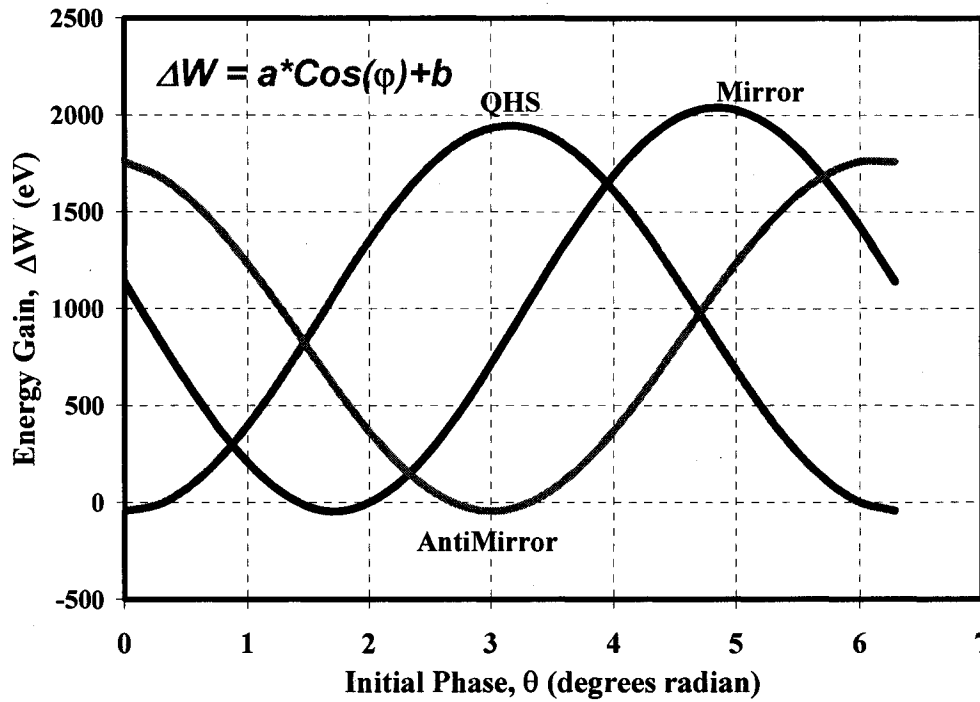


**Figure 5.10: Electron energy gain  $\Delta W$  as a function of initial phase  $\phi$  for  $W_{\text{initial}} = 200$  eV, pitch angle =  $75^\circ$  in QHS, Mirror and AntiMirror.**

## 5.2 Analytical solution

In their work to obtain a non-relativistic response function that connects the velocity distribution of electrons before and after a single pass through the heating zone during ECRH, Tatematsu et al<sup>7</sup> solved the Lorentz equation analytically and numerically. They evaluated the energy gain during a single pass through the microwave heating zone by calculating the electron orbit analytically and numerically. In the analytical treatment they evaluated the electron velocity and deviations of electron orbits from the non-perturbed ones to the first order of the microwave electric field amplitude. They studied higher harmonic X-mode ECRH and represented the right hand circularly polarized monochromatic wave by:

$$\vec{E} = \tilde{E} \cos(\omega t - k_{\parallel} z - k_{\perp} x) \hat{x} + \tilde{E} \sin(\omega t - k_{\parallel} z - k_{\perp} x) \hat{y} \quad (5.5)$$

Where  $\tilde{E}$  is the microwave electric field amplitude,  $\omega$  is the angular frequency of the wave, and  $k_{\parallel}$  and  $k_{\perp}$  are the wave number components parallel and perpendicular to the external magnetic field respectively. The z-axis was chosen in the direction of the external magnetic field. They adopt the paraxial approximation for the external magnetic field given by:

$$\begin{aligned} \vec{B} &= -\frac{1}{2} \frac{dB_o}{dz} \hat{x} + -\frac{1}{2} \frac{dB_o}{dz} \hat{y} + B_o(z) \hat{z} \\ B_o(z) &= B_{Ro} e^{\frac{z}{L_B}} \end{aligned} \quad (5.6)$$

Where  $L_B = B_o / \frac{dB_o}{dz}$  is the magnetic field scale length and it is considered much larger than the electron gyro-radius  $\rho_L$  i.e.  $L_B \gg \rho_L$ . They obtained the following formula for the electron energy gain during the heating interaction time  $\tau_i \sim \sqrt{L_B / \omega v_z}$  to the second order of  $\tilde{E}$ :

$$\begin{aligned} \Delta W &= -e v_{R\perp} \tilde{E} \cos(n\phi) J_{n-1}(k_{\perp} \rho_L) \tau_i + \\ &\quad \frac{e^2 \tilde{E}^2}{2m_e} \left(1 - \frac{k_{\parallel} v_{\parallel}}{\omega}\right) n J_{n-1}^2(k_{\perp} \rho_L) \tau_i^2 \end{aligned} \quad (5.7)$$

where  $v_{R\perp} = \rho_L \Omega_{ce}$  is the electron perpendicular velocity at the resonance point,  $J_{n-1}$  is the Bessel function of the first kind and order n-1 where n is the harmonic number. In order to obtain the phase-averaged net energy gain Equation 5.7 should be integrated over

the phase angle  $\varphi = 0 \rightarrow 2\pi$ . After integrating the equation and setting  $k_{\parallel} = 0$  for pure perpendicular propagation and  $n = 2$  for second harmonic one obtains the following expression for the net energy gain

$$\langle \Delta W \rangle = 2\pi \frac{e^2 \tilde{E}^2}{m_e} J_1^2(k_{\perp} \rho_L) \tau_i^2 \propto \tilde{E}^2 N_{\perp}^2 \frac{W_{\perp}}{W_{\parallel}} \quad (5.8)$$

for small values of  $k_{\perp} \rho_L$ . In the following section the parametric dependence of the phase-averaged net energy gain during single pass through the heating zone will be obtained by solving the Lorentz equation numerically.

### 5.3 Energy Gain Parametric Dependence

In this section we will study the dependence of the net energy gain  $\langle \Delta W \rangle$  on the microwave parameters like wave electric field and perpendicular wave number and particle perpendicular and parallel energies.

#### 5.3.1 Microwave Power Dependence

In order to study the microwave power dependence of the net energy gain  $\langle \Delta W \rangle$  in a single pass through the heating zone, the microwave power is varied in the range between 0 to 120 kW and the phase-averaged energy gain for each microwave power is evaluated. The calculations were performed for the parameters; starting position = -4 cm,  $W_{\text{initial}} = 500$  eV, pitch angle  $\alpha = [10^\circ \ 30^\circ \ 50^\circ \ 75^\circ]$ , initial phase  $\varphi = 0-2\pi$ ,  $P = 0-120$  kW,  $N_{\perp} = \frac{ck_{\perp}}{\omega} = 1$ , and integration time =  $1.5 \times 10^{-8}$  sec. Figure 5.11 shows the results for

the case  $W_{\text{initial}} = 500$  eV, pitch angle  $\alpha = 75^\circ$ , for the three different magnetic configurations QHS, Mirror and AntiMirror. The x-axis is the microwave power in kW and the y-axis is the net energy gain  $\langle \Delta W \rangle$  in eV.

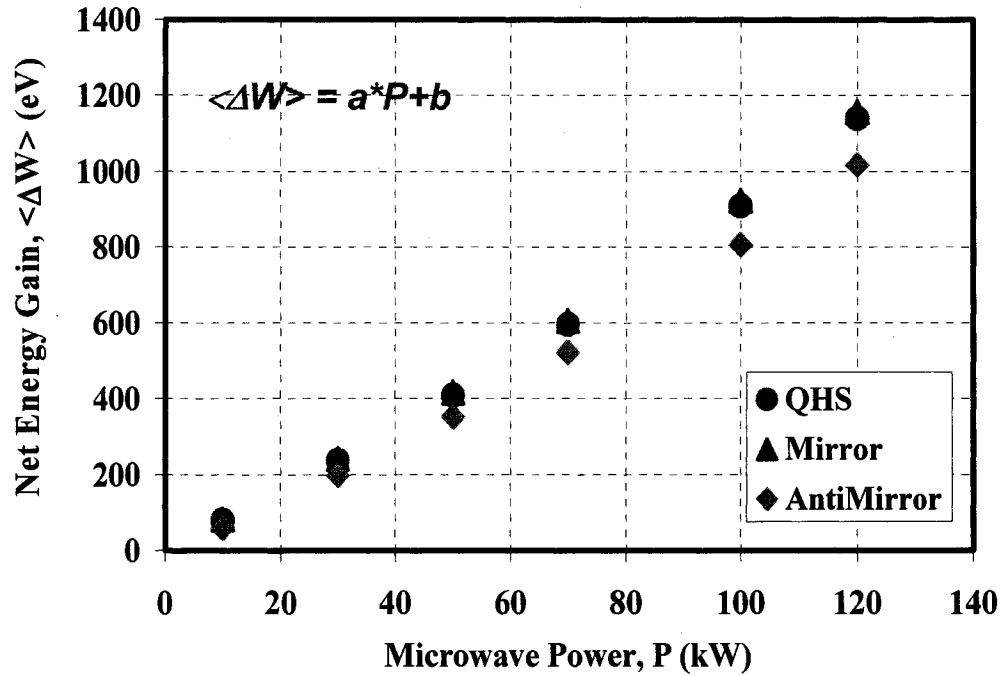


**Figure 5.11: Net Electron-energy gain  $\langle \Delta W \rangle$  as a function of microwave power.  $W_{\text{initial}} = 500$  eV, pitch angle  $\alpha = 75^\circ$  for QHS, Mirror and AntiMirror.**

The calculations showed that the net energy gain  $\langle \Delta W \rangle$  has a near linear dependence on the microwave power  $P$ . The result is in good agreement with Equation 5.8 as  $\langle \Delta W \rangle \propto E^2$ . Also the results show that the net energy gain  $\langle \Delta W \rangle$  is nearly independent of the magnetic configuration.

### 5.3.2 Perpendicular Index of Refraction Dependence

Although the perpendicular index of refraction should be determined from the dispersion relation in real plasma, we varied  $N_\perp$  in the range 0.2 to 1.2 to study the

dependence of the net energy gain  $\langle \Delta W \rangle$  in a single pass through the heating zone. The net energy gain  $\langle \Delta W \rangle$  for each  $N_{\perp}$  is evaluated. The calculations were performed for the parameters; starting position = -4 cm,  $W_{\text{initial}} = 500$  eV, pitch angle  $\alpha = [10^{\circ} 30^{\circ} 50^{\circ} 75^{\circ}]$ , initial phase  $\phi = 0-2\pi$ ,  $E_0 = 1.7 \times 10^5$  V/m, and integration time =  $1-5 \times 10^{-8}$  sec. Figure 5.12 shows the results for the case  $W_{\text{initial}} = 500$  eV, pitch angle  $\alpha = 75^{\circ}$ , initial phase  $\phi = 0-2\pi$ , for three different magnetic configurations, QHS, Mirror and AntiMirror. The x-axis is the perpendicular index of refraction and the y-axis is the net energy gain  $\langle \Delta W \rangle$  in eV.

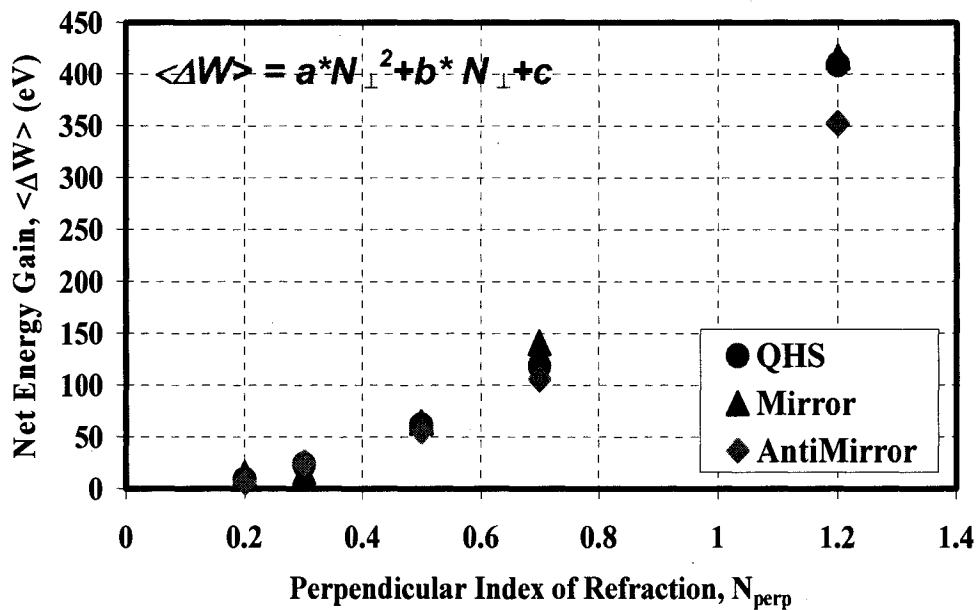


**Figure 5.12: Net Electron-energy gain  $\langle \Delta W \rangle$  as a function of  $N_{\text{perpendicular}}$ .  $W_{\text{initial}} = 500$  eV, pitch angle  $\alpha = 75^{\circ}$  for QHS, Mirror and AntiMirror.**

The calculations showed that the net energy gain  $\langle \Delta W \rangle$  has a parabolic dependence on the perpendicular index of refraction  $N_{\perp}$ . For small values of  $k_{\perp} \rho_L$ , the Bessel function term  $J_1^2(k_{\perp} \rho_L)$  can be approximated by  $(k_{\perp} \rho_L)^2$ . So for constant microwave power and

electron perpendicular and parallel velocities, the net energy gain from Equation

$$5.8 < \Delta W > \propto J_1^2(k_\perp \rho_L) \approx k_\perp^2 = \frac{\omega^2 N_\perp^2}{c^2} \text{ is proportional to the perpendicular index of}$$

refraction squared as the Figure 5.12 shows. The figure also shows that the net energy gain is nearly independent of magnetic configurations.

### 5.3.3 Perpendicular Velocity Dependence

In order to investigate the dependence of the net energy gain on the perpendicular velocity  $v_\perp$ , the parallel energy  $W_\parallel$  is kept constant at 100 eV and the perpendicular energy  $W_\perp$  varied in the range between 50 to 400 eV and the energy gain for each  $W_\perp$  is evaluated. The calculations were performed for the parameters; starting position = -4 cm,  $W_{\text{initial}} = 50\text{-}400$  eV, pitch angle  $\alpha = [10^\circ \ 30^\circ \ 50^\circ \ 75^\circ]$ , initial phase  $\phi = 0\text{-}2\pi$ ,  $E_0 = 1.7 \times 10^5$  V/m, and  $N_\perp = \frac{ck_\perp}{\omega} = 1$ , integration time =  $1\text{-}5 \times 10^{-8}$  sec. Figure 5.13 shows the results for the case  $W_\parallel = 50$  eV, pitch angle  $\alpha = 75^\circ$ , initial phase  $\phi = 0\text{-}2\pi$ , for three different magnetic configurations, QHS, Mirror and AntiMirror. The x-axis is the perpendicular energy  $W_\perp$  in eV and the y-axis is the net energy gain  $<\Delta W>$  in eV. The calculations showed that the net energy gain  $<\Delta W>$  has a linear dependence on the perpendicular kinetic energy  $W_\perp$ . Again for small values of  $k_\perp \rho_L$  the Bessel function term  $J_1^2(k_\perp \rho_L)$  in Equation 5.8 can be approximated by  $(k_\perp \rho_L)^2$ . At constant microwave power and wave number and electron parallel velocity the net energy gain can

be given by  $\langle \Delta W \rangle \propto J_1^2(k_\perp \rho_L) \approx \rho_\perp^2 = \frac{v_\perp^2}{\Omega_{ce}^2} \approx W_\perp$  is proportional to the perpendicular kinetic energy as shown in Figure 5.13. Also the results again show that the net energy gain  $\langle \Delta W \rangle$  is independent of magnetic configurations.

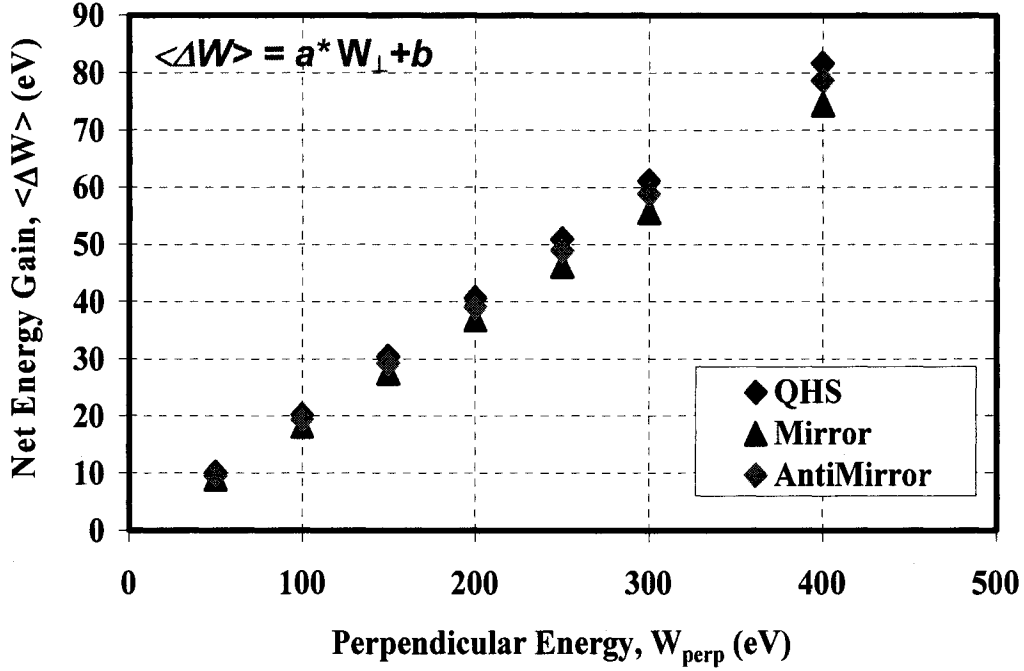


Figure 5.13: Net Electron-energy gain  $\langle \Delta W \rangle$  as a function of  $W_\perp$ , pitch angle  $\alpha = 75^\circ$ ,  $W_{\parallel \text{initial}} = 100$  eV for QHS, Mirror and AntiMirror.

#### 5.3.4 Parallel Velocity Dependence

In order to study the dependence of the net energy gain  $\langle \Delta W \rangle$  on parallel kinetic energy, two different calculations were performed, the total energy  $W$  is changed while the pitch angle is kept constant at  $75^\circ$ , and the pitch angle is changed while the initial energy is kept constant. The calculations were evaluated for the parameters; starting position = -4 cm,  $W_{\text{initial}} = 50\text{-}2000$  eV, pitch angle  $\alpha = [10^\circ 30^\circ 50^\circ 75^\circ]$ , initial phase  $\phi$

$= 0.2\pi$ ,  $E_0 = 1.7 \times 10^5$  V/m,  $N_{\perp} = \frac{ck_{\perp}}{\omega} = 1$ , and integration time =  $1.5 \times 10^{-8}$  sec. Figure

5.14 shows that with the pitch angle kept constant at  $\alpha = 75^\circ$ , the higher the electron initial energy the lower the net energy gain  $\langle \Delta W \rangle$  for all three configurations.

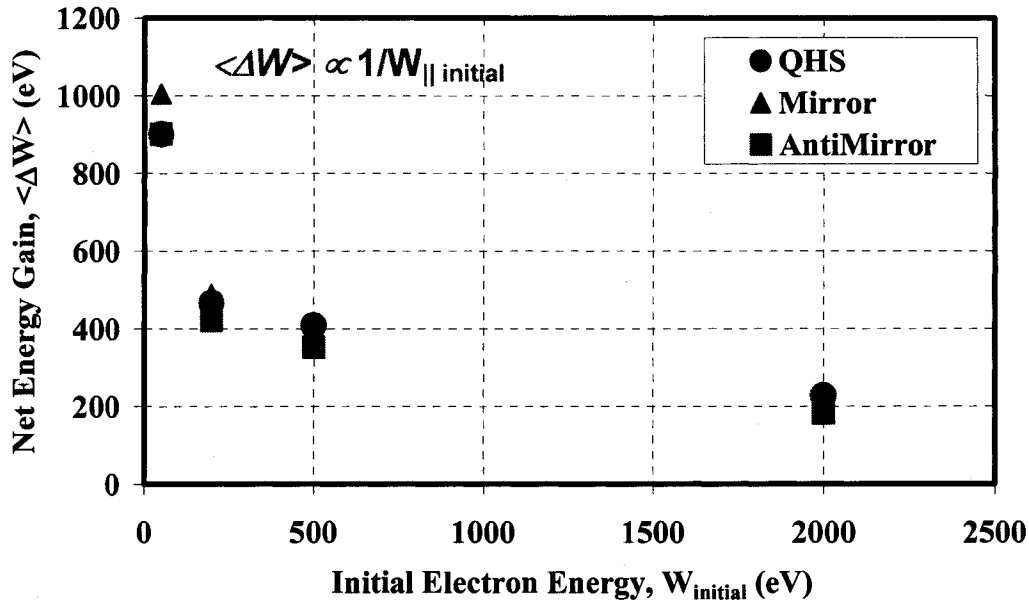


**Figure 5.14: Net Electron-energy gain  $\langle \Delta W \rangle$  as a function of  $W_{\text{initial}}$ , pitch angle  $\alpha = 75^\circ$ , for QHS, Mirror and AntiMirror.**

This can be explained as follows; with constant pitch angle  $\alpha$ , the higher the total energy, the higher the energy components both parallel and perpendicular to the field line  $W_{\parallel}$  and  $W_{\perp}$ . The higher the electron parallel velocity the shorter the resonance time (the electron will spend shorter time in the heating zone, the heating time is inversely proportional to  $W_{\parallel}$ ), the lower the energy gain from the microwave. Figure 5.15 shows the variation of the net energy gain with the pitch angle for different electron initial energies. The figure shows that, the higher the pitch angle the more energy the particle

gains from the microwave. This is true because the particle spends more time in coupled to the microwave at higher initial pitch angles.

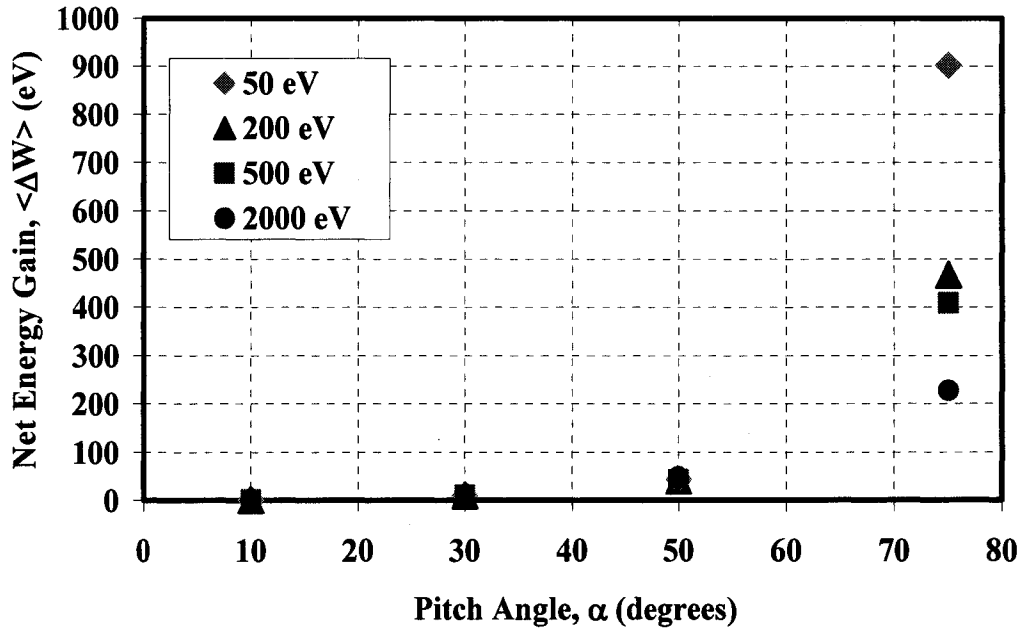


**Figure 5.15: Net Electron-energy gain  $\langle \Delta W \rangle$  as a function of pitch angle for QHS, Mirror and AntiMirror.**

As Equation 5.8 shows that for constant microwave power, wave number and electron

perpendicular velocity the net energy gain given by  $\langle \Delta W \rangle \propto \tau_i^2 = \frac{L_{res}^2}{v_{\parallel}^2} \approx \frac{1}{W_{\parallel}}$  is

inversely proportional to the square root of the electron parallel energy and is in good agreement with the results of figures 5.14 and 5.15 as the figure shown. Again the figure also shows the independence of the net energy gain on the magnetic configuration.

## 5.5 Summary

The single particle heating model and its assumptions were discussed in this chapter. A simplified analytical representation of the net energy gain is given in the

chapter to compare it with the numerical calculations. The parametric dependencies of net energy gain in single pass through the heating zone were evaluated. A comparison between different HSX magnetic configurations from the single pass heating point of view shows no difference in net energy gain  $\langle \Delta W \rangle$ .

- 
- <sup>1</sup> T.H. Stix, "Waves in Plasmas", American Institute of Physics, New York (1992).
- <sup>2</sup> F. Jaeger, A.J. Lichtenberg, and M.A. Lieberman, Plasma Physics, **14**, 1073, (1972).
- <sup>3</sup> M.A. Lieberman and A. J. Lichtenberg, Plasma Physics, **15**, 125, (1973).
- <sup>4</sup> H. Grawe, Plasma Physics, **11**, 151, (1969).
- <sup>5</sup> Matlab 6.5 Release 13 help file.
- <sup>6</sup> J.R. Dormand, and P.J. Prince, Journal of Computational and Applied. Mathematics, **6**, 19, (1980).
- <sup>7</sup> Y. Tatematsu et al., Physics of Plasmas , **4**(8), 2972, (1997).

# Chapter 6

## Single Particle Confinement in HSX

### 6.0 Introduction

The hard x-ray measurements in the HSX stellarator discussed in Chapter 4 showed that at low density during on-axis ECRH discharges superthermal electrons were generated with higher energies and populations in the QHS configuration compared to the Mirror and the AntiMirror configurations. The single particle heating model discussed in Chapter 5 showed that there is nearly no difference in energy gained during a single pass through the heating zone between magnetic configurations. As stated before in Chapter 5, it is assumed that heating only takes place inside the heating zone. For different magnetic configurations to have different electron energies and populations, differences in orbit topology and confinement outside the heating zone imply they will have different likelihoods of revisiting the heating zone. For example, in order to have a higher energy population as in QHS, electrons should have orbits that cause them to revisit the heating zone frequently. If the orbits have significant deviations, they will not revisit the heating zone as frequently, and fewer energetic particles would be expected (as in the Mirror and the AntiMirror configurations). In order to test these assumptions, single particle drift orbits have been examined in different magnetic configurations.

In this chapter, the electron guiding center drift orbits in the different magnetic configurations in HSX stellarator will be investigated. A description of the guiding center equations will be given in Section 6.1. The HSX magnetic spectrum will be described in Section 6.2. The microwave heating operator used in the calculations (based on the Lorentz model described in Chapter 5) will be discussed in Section 6.3. The numerical technique used in solving the guiding center equations and the code used are described in Section 6.4. Differences in particles orbits between magnetic configurations and their effects on heating during the ECRH will be discussed in Section 6.5. Energetic particle dynamics after the microwave heating power is turned off are discussed in Section 6.6.

## 6.1 Electron Guiding Center Equations

Energetic particle confinement represents an important issue in toroidal fusion devices for effective auxiliary heating or ignition. In conventional stellarators, as compared with tokamaks, the asymmetry of the magnetic configuration due to its three dimensional structures causes a serious energetic particle loss. In order to study these losses, attention has been paid to single-particle confinement<sup>1,2,3</sup> which is relevant in the low collisionality regime of a reactor. Such confinement is the first and one of the most important requirements for the feasibility of constructing a future fusion reactor on based on any type of confinement device.

Superthermal electrons in HSX stellarator can be considered as independent test particles and their confinement can be analyzed using the background magnetic field and

the guiding center approximation. When a charged particle moves at an angle with respect to an external magnetic field, it gyrates around the field with a gyration (also known as cyclotron) frequency that is directly proportional to the magnitude of its electronic charge and the applied magnetic field and inversely proportional to the mass of the particle. The center of gyration, called the guiding center has two velocity components: a fast component parallel to the magnetic field line and a slow drift component perpendicular to the magnetic field line. The drift is usually caused by (but not limited to): an external electrostatic force, a gradient of the magnetic field, curvature of the magnetic field, etc. The guiding center velocity is given by<sup>4</sup>:

$$\vec{V} = v_{\parallel} \frac{\vec{B}}{B} + \frac{m}{eB} (v_{\parallel}^2 + \frac{1}{2} v_{\perp}^2) \frac{\vec{B} \times \vec{\nabla} B}{B^2} + \frac{\vec{E} \times \vec{B}}{B^2} \quad (6.1)$$

where  $\parallel$  and  $\perp$  refers to parallel and perpendicular to the external magnetic field,  $\vec{E}$  is the electrostatic field and  $\vec{B}$  and  $\vec{\nabla} B$  are the magnetic field vector and the gradient of the magnetic field. It is advantageous to use magnetic co-ordinates in order to follow particle drift orbits in HSX. The use of Boozer co-ordinates<sup>5,6</sup> for calculating guiding center orbits in curl-free stellarator magnetic fields has been a standard procedure. The curl-free magnetic field can be represented by:

$$\begin{aligned} \vec{B} &= \vec{\nabla} \psi \times \vec{\nabla} \mathcal{G}_o \\ \vec{B} &= \vec{\nabla} \chi \end{aligned} \quad (6.2)$$

The co-ordinates  $(\psi, \vartheta_o, \chi)$  are such that  $2\pi\psi$  is the toroidal magnetic flux within a magnetic surface.  $\chi = g\varphi - I\vartheta$  is a co-ordinate along the field line proportional to the magnetic potential of a curl-free field, where  $g = RB_\varphi$  and  $I = rB_\vartheta$  are constants in the curl-free case and are related to the poloidal and toroidal currents.  $R$ ,  $r$ ,  $B_\vartheta$ , and  $B_\varphi$  are the major radius, minor radius, poloidal magnetic field and toroidal magnetic field respectively.  $\vartheta_o = \vartheta - \iota\varphi$  is a rotating helical angle that is constant on a given field line, where  $\iota$  is the rotational transform, and  $\vartheta$  and  $\varphi$  are the poloidal and toroidal angles respectively. The equations for the drift orbits are given by<sup>6</sup>:

$$\frac{d\vartheta}{dt} = \bar{V} \cdot \bar{\nabla} \vartheta_o, \quad \frac{d\psi}{dt} = \bar{V} \cdot \bar{\nabla} \psi, \quad \frac{d\chi}{dt} = \bar{V} \cdot \bar{\nabla} \chi \quad (6.3)$$

In order to evaluate each term we use:

$$\rho_{\parallel} = v_{\parallel} \left( \frac{m}{eB} \right), \quad \frac{1}{2} m v_{\perp}^2 = \mu B \quad (6.4)$$

$$v_{\parallel} \left( \frac{\bar{B}}{B} \right) = \left( \frac{e\rho_{\parallel}}{m} \right) \nabla \psi \times \nabla \vartheta_o \quad (6.5)$$

$$B \times \nabla \Phi = (\nabla \chi) \times \left( \frac{\partial \Phi}{\partial \vartheta_o} \nabla \vartheta_o + \frac{\partial \Phi}{\partial \psi} \nabla \psi + \frac{\partial \Phi}{\partial \chi} \nabla \chi \right), \quad \bar{E} = \nabla \Phi \quad (6.6)$$

where  $\rho_{\parallel}$  is the parallel gyro-radius,  $\mu$  is the magnetic moment, and  $\Phi$  is the scalar electric potential, this can be simplified to:

$$\frac{d\mathcal{G}_o}{dt} = \frac{\partial\Phi}{\partial\psi} + \left( \frac{\mu}{e} + \frac{eB}{m} \rho_{\parallel}^2 \right) \frac{\partial B}{\partial\psi} \quad (6.7)$$

$$\frac{d\psi}{dt} = -\frac{\partial\Phi}{\partial\mathcal{G}_o} - \left( \frac{\mu}{e} + \frac{eB}{m} \rho_{\parallel}^2 \right) \frac{\partial B}{\partial\mathcal{G}_o} \quad (6.8)$$

$$\frac{d\chi}{dt} = \frac{eB^2}{m} \rho_{\parallel} \quad (6.9)$$

The equation for  $\rho_{\parallel}$  can be obtained from the conservation of energy and the Hamiltonian,  $H$ , (defined as the total energy of particle) as follows:

$$\varepsilon = \frac{m}{2} v_{\parallel}^2 + \mu B + e\Phi \quad (6.10)$$

$$\frac{d\mathcal{G}}{dt} = \frac{\partial H}{\partial\psi}, \quad \frac{d\psi}{dt} = -\frac{\partial H}{\partial\mathcal{G}_o}, \quad \frac{d\chi}{dt} = \frac{\partial H}{\partial\rho_{\parallel}} \quad (6.11)$$

where  $\varepsilon$  is the total electron energy, and the conservation of energy implies  $\frac{dH}{dt} = 0$  or:

$$\frac{d\rho_{\parallel}}{dt} = -\frac{1}{g} \frac{\partial\Phi}{\partial\varphi} - \frac{1}{g} \left( \frac{\mu}{e} + \frac{eB}{m} \rho_{\parallel}^2 \right) \frac{\partial B}{\partial\varphi}, \quad (6.12)$$

The dependence of the magnetic field strength  $B$  on  $\psi$ ,  $\mathcal{G}_o$  and  $\chi$  depends on the specific configuration under study. The  $(\psi, \mathcal{G}_o, \chi)$  variables are the most convenient for calculating orbits, but it is convenient to use the coordinates  $(r, \mathcal{G}, \varphi)$  when summarizing results. Here  $r$  is the normalized radial variable and  $\mathcal{G}$  and  $\varphi$  are the poloidal and toroidal

angle variables. For a curl-free toroidal geometry like HSX stellarator the relation between  $\psi$ ,  $\vartheta_o, \chi$  and  $r, \vartheta, \phi$  is given by:

$$\vartheta = \vartheta_o + \iota\phi, \quad g = RB_o, \quad \chi = g\phi, \quad \text{and} \quad r = \sqrt{\frac{2\psi}{B_o}} \quad (6.13)$$

Using the above relations and transforming the guiding center equations from the  $(\psi, \vartheta_o, \chi)$  variables to  $(r, \vartheta, \phi)$  one obtains:

$$\frac{dr}{dt} = -\frac{1}{B_o r} \frac{\partial \Phi}{\partial \vartheta} - \frac{1}{B_o r} \left( \frac{\mu}{e} + \frac{eB}{m} \rho_{\parallel}^2 \right) \frac{\partial B}{\partial \vartheta} \quad (6.14)$$

$$\frac{d\vartheta}{dt} = \frac{1}{B_o r} \frac{\partial \Phi}{\partial r} + \frac{1}{B_o r} \left( \frac{\mu}{e} + \frac{eB}{m} \rho_{\parallel}^2 \right) \frac{\partial B}{\partial r} + \frac{\iota}{g} \frac{eB^2}{m} \rho_{\parallel} \quad (6.15)$$

$$\frac{d\phi}{dt} = \frac{1}{g} \frac{eB^2}{m} \rho_{\parallel} \quad (6.16)$$

$$\frac{d\rho_{\parallel}}{dt} = -\frac{1}{g} \frac{\partial \Phi}{\partial \phi} - \frac{1}{g} \left( \frac{\mu}{e} + \frac{eB}{m} \rho_{\parallel}^2 \right) \frac{\partial B}{\partial \phi} \quad (6.17)$$

## 6.2 The HSX Magnetic Spectrum

The main factor determining features of charged particle confinement in a non-axisymmetric toroidal magnetic device, such as torsatron, heliotron, or stellarator is the character of the magnetic field. The adequate representation of the magnitude of the actual magnetic field requires expanding it in Fourier series. It is known that in stellarator

devices, the behavior of the magnetic field strength along a field line can be represented adequately by Fourier-decomposition, in which a large number of harmonics with different toroidal ( $n$ ) and poloidal ( $m$ ) mode numbers should be taken into account. For the orbits studied in this chapter, we have chosen model magnetic fields for the three representative magnetic configurations; QHS, Mirror and AntiMirror. The model magnetic fields were calculated from the Biot-Savart law based on a segmented representation of the finite-size coil model. The spectrum is specified in Boozer coordinates as:

$$B = B_o \sum_{nm} b_{nm}(r) \cos(n\varphi - m\vartheta) \quad (6.18)$$

Where  $B_o = 1.0$  Tesla,  $b_{nm}(r)$  are the Fourier spectrum coefficients as a function of  $r$ ,  $n$  and  $m$  are the toroidal and poloidal mode numbers and  $\varphi$  and  $\vartheta$  are the toroidal and poloidal angles. Figure 6.1 shows the magnetic field spectrum for the QHS configuration based on the above model. The magnitude of the largest 15  $b_{nm}$  components at  $r/a = 0.9$  are plotted as a function of radius. The choice of the number of components used to represent the spectrum was based on truncating components that are less than 0.1% of the  $[0,0]$  component at  $r/a = 0.9$ . The mode numbers are defined as a pair  $[n,m]$  where  $n$  is the toroidal mode number and  $m$  is the poloidal mode number. The largest mode number for HSX is the  $[0,0]$ , which is the average magnetic field on the flux surface. The quantity  $(b_{0,0} - 1)$  is plotted and increases towards the edge, indicating a minimum-B configuration.

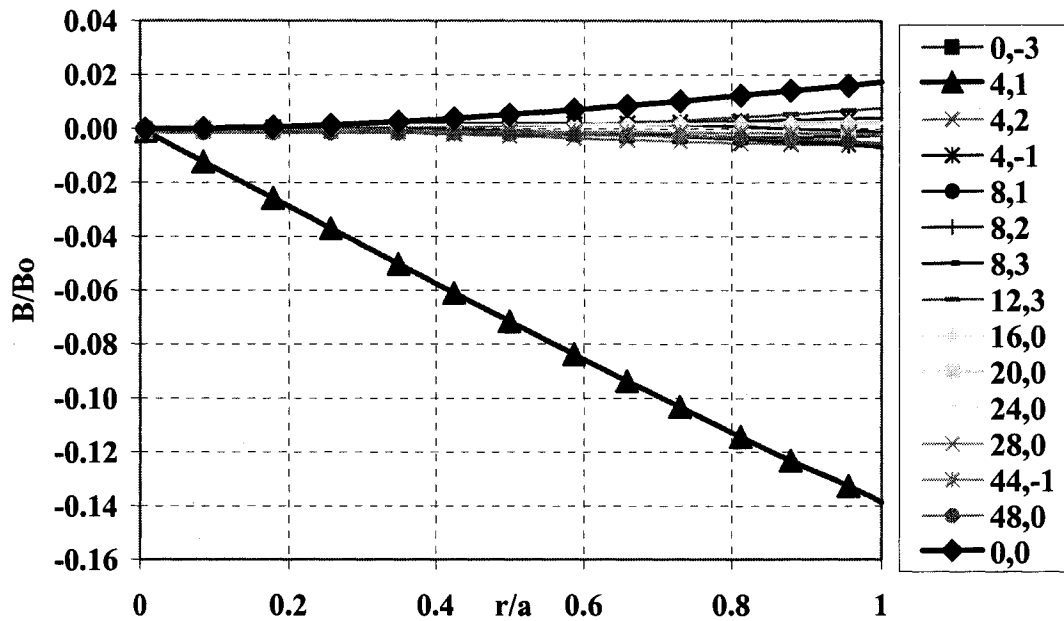


**Figure 6.1: The variation of QHS spectral components with minor radius.**

The second largest mode is the [4,1] helical mode which is the dominant mode contributing to the variation of the magnetic field on a flux surface. The principle symmetry breaking components are the [48,0] term and the [4,2] mode. The first mode is due to the modular ripple since there are a total of 48 coils in the machine. The magnitude of the symmetry breaking terms in the spectrum for the finite size HSX coils is below 1% at the edge. As stated in chapter one, HSX differs from a conventional stellarator in that it lacks significant toroidal curvature. The toroidal curvature term in the spectrum is  $\sim 0.0025$  or what one should expect in a device with a physical aspect ratio 400 although HSX has a physical aspect ratio  $\sim 8$ . If we want to break the quasi-symmetry, it is inefficient to break it by reintroducing the toroidal curvature; the [0,1] component of the

spectrum. Instead, the symmetry is broken with the excitation of a toroidal mirror term; the  $[4,0]$  component.

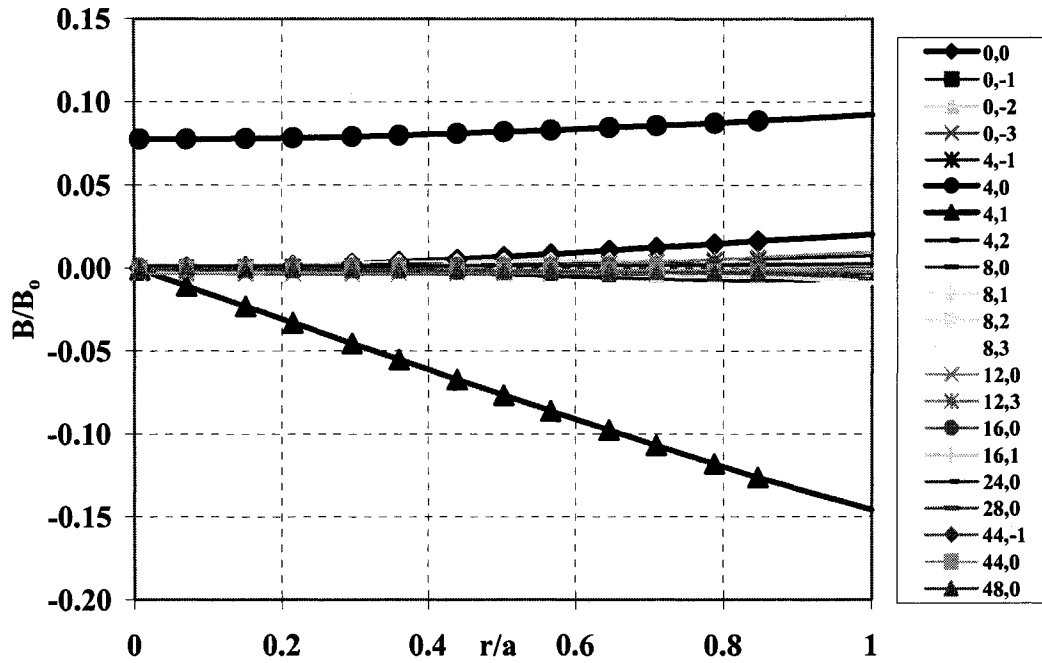


**Figure 6.2: The variation of Mirror spectral components with minor radius.**

Figure 6.2 shows the magnetic field spectrum for the 10% Mirror configuration. The magnitude of the largest 21  $b_{nm}$  components at  $r/a = 0.9$  are plotted as a function of radius. As stated earlier, the choice of the number of components used to represent the spectrum was based on truncating any component that is less than 0.1% of the  $[0,0]$  component at  $r/a = 0.9$ . The figure shows that the largest components are the  $[0,0]$ , and  $[4,1]$  components as in the case of QHS, but now a large  $[4,0]$  mode is excited, with only small changes in the other symmetry breaking components of the spectrum.

Figures 6.3 through 6.5 show the variation of the magnetic field amplitude along the field line for the three different configurations QHS, Mirror and AntiMirror at three

different locations, inboard side at  $r/a = -0.5$ , magnetic axis at  $r/a = 0$ , and outboard side at  $r/a = 0.5$ . The x-axis is the toroidal angle  $\phi$  in degrees and the y-axis is the modulus of the magnetic field  $|\mathbf{B}|$  in Tesla. The magnetic field was adjusted to  $|\mathbf{B}| = 0.5$  Tesla in the three different cases so that the 2<sup>nd</sup> harmonic resonance can take place. At  $\phi = 0$  (location of box port C where the microwave antenna is located). The figures show the quasi-symmetry of the magnetic field in the QHS as evidenced by the same magnitude of crests or troughs in  $|\mathbf{B}|$  as compared to the asymmetry evident in the magnetic field in the Mirror and AntiMirror configurations. At  $\phi = 0$  magnetic field is added to the QHS to produce the Mirror field and subtracted from the QHS to produce the AntiMirror field as discussed earlier in Chapter 1.

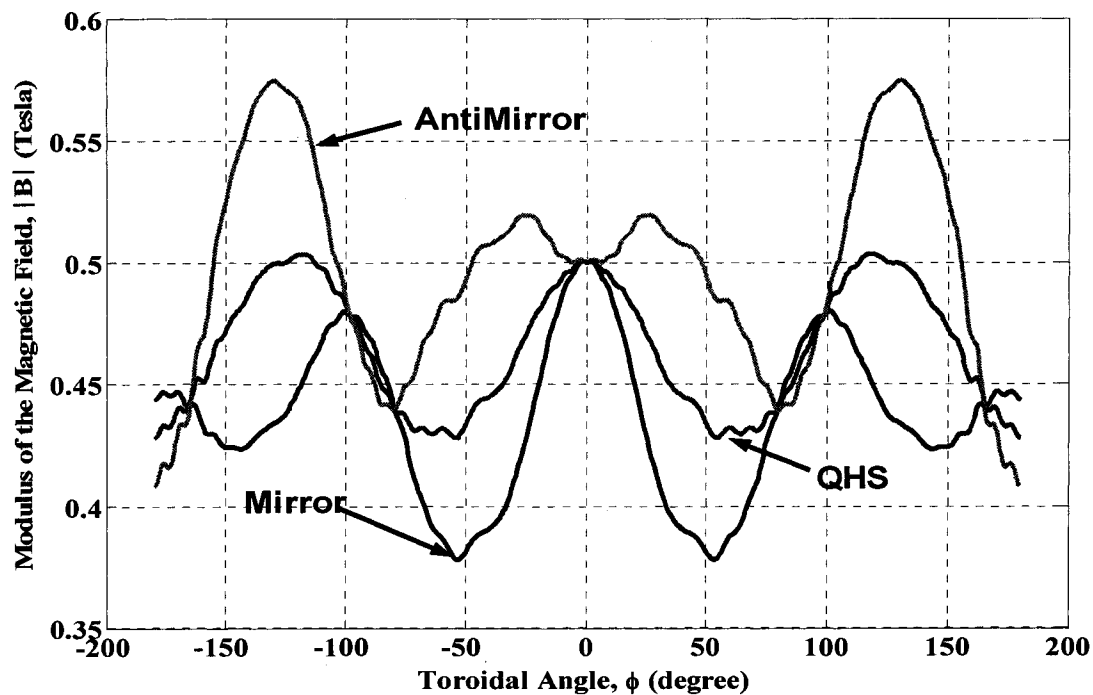


**Figure 6.3: Magnetic field variation along field line for QHS, Mirror and AntiMirror in the inboard side of the machine at  $r/a = -0.5$ .**

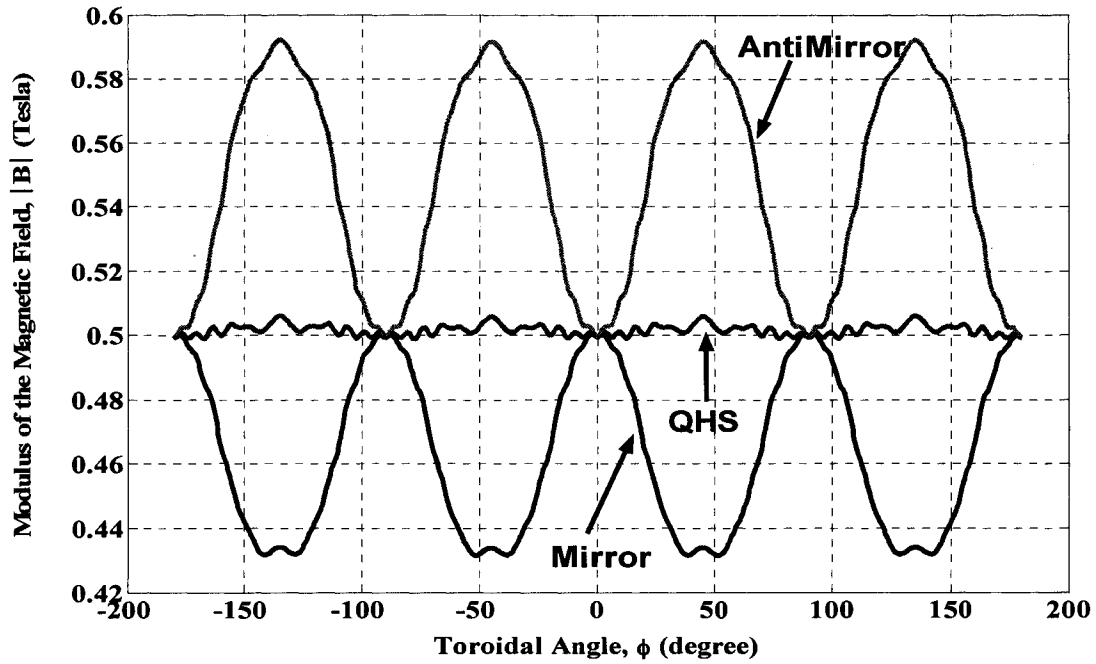


Figure 6.4: Magnetic field variation along field line for QHS, Mirror and AntiMirror in the inboard side of the machine at  $r/a = 0$ .

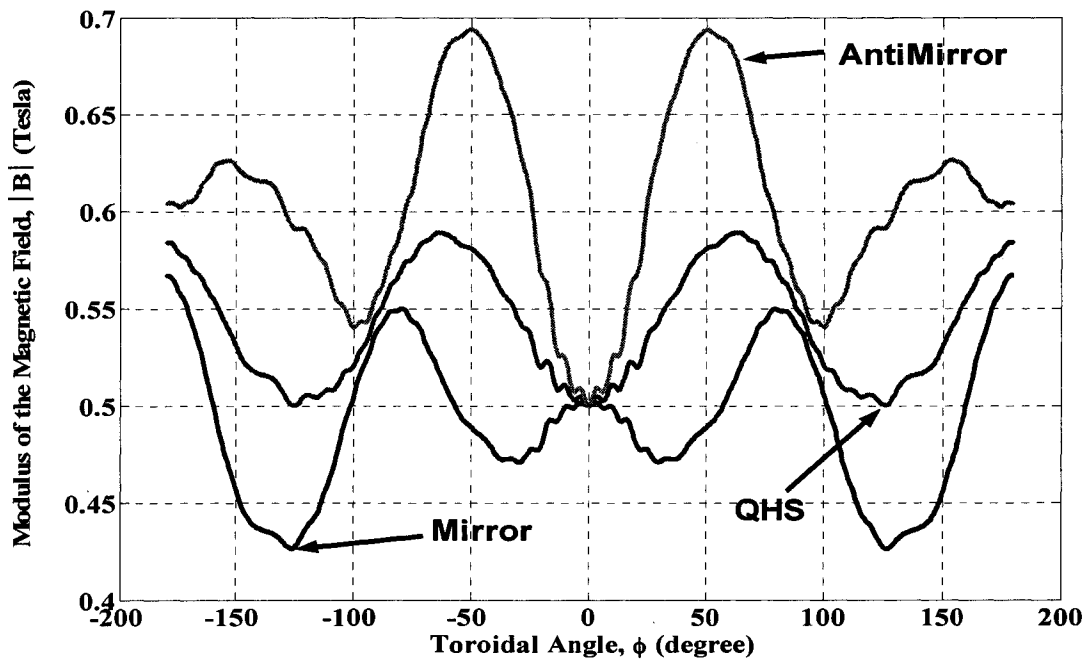


Figure 6.5: Magnetic field variation along field line for QHS, Mirror and AntiMirror in the inboard side of the machine at  $r/a = 0.5$ .

### 6.3 The Microwave Heating Operator

In Chapter 5, the Lorentz equation was solved numerically and the energy gain during single pass through the heating zone,  $\langle \Delta W \rangle$ , was obtained. In order to resolve the fine details of the electron gyro-orbit, Matlab automatically chooses a time step comparable to the shortest time scale in the problem i.e. the cyclotron time defined as  $t = 2\pi / \Omega_{ce} = 1/14 \times 10^9 \approx 7 \times 10^{-11}$  sec. Depending on their initial energies, bulk electrons of initial energy  $\sim 300$  eV take  $\sim 10^{-8}$  sec to cross the heating zone. It was very difficult to follow electrons for longer times using the Lorentz method because of the accumulation of numerical errors and the very long integration time. As a result, we solve the drift orbit guiding center equations with a microwave heating operator obtained from the single particle heating model to simulate the effect of ECRH heating on the electron orbits in different magnetic configurations. As described in Chapter 5, the heating zone is located on-axis in front of the microwave ellipsoidal antenna. For bulk electrons, the heating zone extends up to  $r/a \sim 0.1$  (determined by radius of power deposition region for bulk electrons). In evaluating the heating operator we assumed the following:

1. The  $|B|$  contours are almost straight vertical lines near the magnetic axis as shown in Figure 6.6. For the 2<sup>nd</sup> harmonic ECRH at 28 GHz, the resonant magnetic field of  $|B| = 0.5$  Tesla will be located along a vertical Z direction (in lab co-ordinates) and extends up to  $Z \sim 0.1$  from both sides of the magnetic axis, so the heating zone is nearly planar in shape and has a length of  $\sim 6$  cm centered at  $\phi = 0$ . This corresponds to the fact that Gaussian beam is well focused at this location while

limits heating at vertical distance off axis. We approximate the heating zone in Boozer co-ordinates as a cylinder centered at the magnetic axis with radius  $\sim 0.1$  of the effective plasma radius and  $\sim 6$  cm long. This approximation will be justified below.

2. Relativistic effects such as relativistic detuning and resonance shift toward the high field side are not treated in this model.
3. Electrons gain energy continuously while they are in the heating zone and the energy gain is completely in the perpendicular direction. As a result, the magnetic moment  $\mu$  and pitch angle  $\alpha$  change.
4. The energy gain per unit time is only a function of the flux surface variable  $r$  and pitch angle  $\alpha$ , and is independent of initial electron energy, but does depend on resonance time

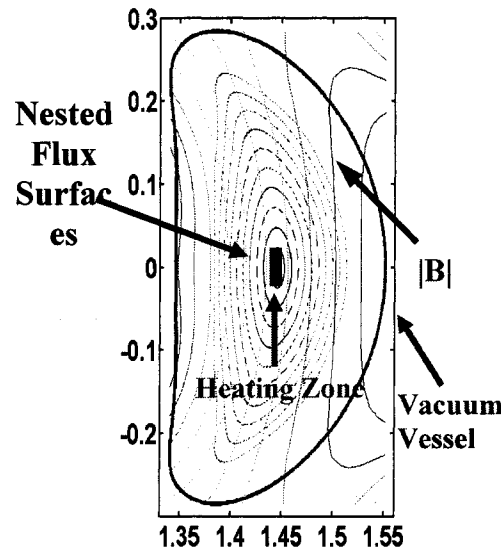


**Figure 6.6: Plasma cross section at box port C showing a cross section of the heating zone in lab co-ordinates (the red stick), the  $B$  contours, and the nested flux surfaces.**

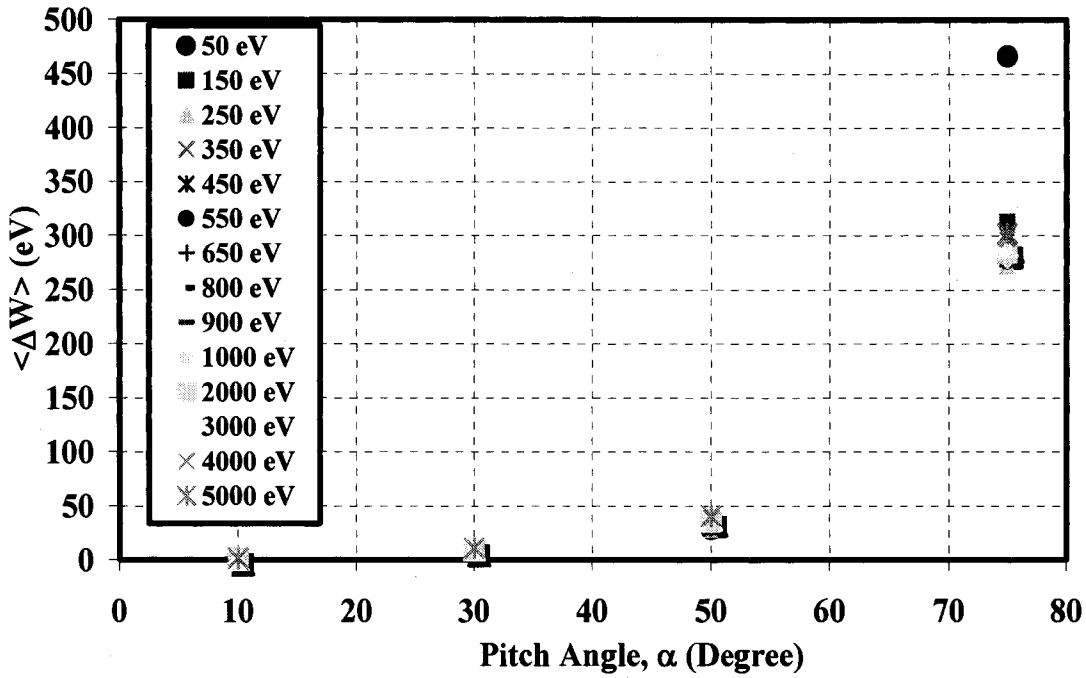


Figure 6.7: Net electron energy gain  $\langle \Delta W \rangle$  as a function of pitch angle  $\alpha$  at different initial electron energies for the QHS configuration.

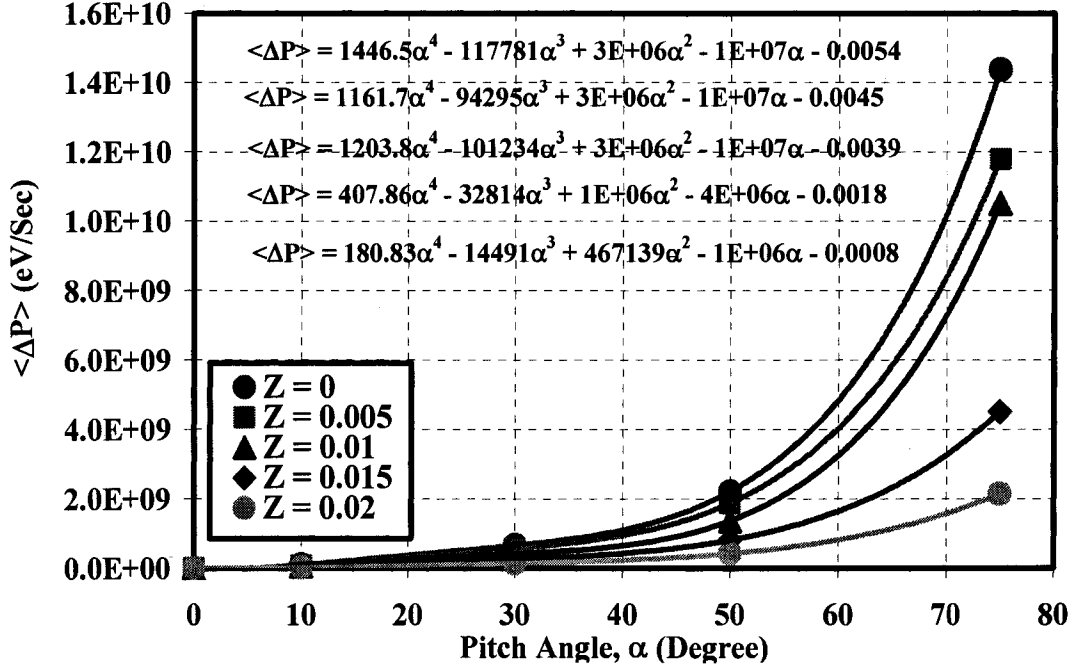


Figure 6.8: Net Electron power gain  $\langle \Delta P \rangle$  as a function of pitch angle  $\alpha$  at different Z locations in the QHS configuration.

The results are given by:

$$\begin{aligned}
 \langle \Delta P \rangle &= 1446.5\alpha^4 - 117781\alpha^3 + 3 \times 10^6 \alpha^2 - 10^{-7} \alpha - 0.0054 & z = 0 \\
 \langle \Delta P \rangle &= 1161.7\alpha^4 - 94295\alpha^3 + 3 \times 10^6 \alpha^2 - 10^{-7} \alpha - 0.0045 & z = 0.005 \\
 \langle \Delta P \rangle &= 1203.8\alpha^4 - 101234\alpha^3 + 3 \times 10^6 \alpha^2 - 10^{-7} \alpha - 0.0039 & z = 0.01 \\
 \langle \Delta P \rangle &= 407.8\alpha^4 - 32814\alpha^3 + 10^6 \alpha^2 - 4 \times 10^{-6} \alpha - 0.0018 & z = 0.015 \\
 \langle \Delta P \rangle &= 180.8\alpha^4 - 14491\alpha^3 + 467139\alpha^2 - 10^{-6} \alpha - 0.0008 & z = 0.02
 \end{aligned} \tag{6.19}$$

where  $\alpha$  is the initial electron pitch angle.

The heating operator is included in the guiding center equations when the particle is in the resonance zone by adding one more equation for the time rate of change of the magnetic moment  $\mu$ :

$$\frac{d\mu}{dt} = \frac{d}{dt} \left( \frac{\langle \Delta W \rangle}{B} \right) = \frac{\langle \Delta P \rangle}{B} \tag{6.20}$$

where  $\langle \Delta P \rangle$  is given by Equations 6.19 and  $B$  is the local magnetic field at the electron position. The solution of Equation 6.20 is given by  $\mu = t \langle \Delta P \rangle / B + \mu_o$ , where  $\mu_o = m_e v_{\perp}^2 / 2B$  is the electron initial magnetic moment entering the heating zone. Outside the heating zone the Matlab code solves the guiding center equations with  $\mu =$  constant. When the electron reenters the resonance zone, the code solves Equation 6.20 simultaneously with Equations 6.14-6.17. To evaluate  $\langle \Delta P \rangle$ , the program evaluates the local electron pitch angle  $\alpha$  and depending on the value of  $Z$  the program will pick up the right formula to use from Equations 6.19. If  $Z$  does not match any of the values

shown above the program will propose the same polynomial dependence for  $\langle \Delta P \rangle = a_1 \alpha^4 + a_2 \alpha^3 + a_3 \alpha^2 + a_4 \alpha + a_5$ . The individual polynomial coefficients  $a_1$  to  $a_5$  at any  $Z$  are obtained by substituting the value of  $Z$  in the following polynomial equation  $a_n = b_1 Z^4 + b_2 Z^3 + b_3 Z^2 + b_4 Z + b_5$ . The equation was obtained by fitting each of the five coefficients given in Equations 6.19,  $a_n(z = 0)$ ,  $a_n(z = 0.005)$ ,  $a_n(z = 0.01)$ ,  $a_n(z = 0.015)$ , and  $a_n(z = 0.02)$  to a fourth order polynomial and the coefficients  $b_1$  to  $b_5$  are obtained.

This heating zone model was checked by calculating the net energy gain during a single pass through the microwave heating zone  $\langle \Delta W \rangle$  from the Lorentz heating model and the guiding center (heating included) model. Both models gave nearly the same net energy gain  $\langle \Delta W \rangle$  for the same electron initial conditions (energy, pitch angle, etc).

## 6.4 The Numerical Solution

A computationally straightforward procedure was developed to study the particle orbits in HSX in different magnetic configurations. Since the guiding center equations in Boozer coordinates depend only on  $B(r, \vartheta, \varphi)$  and its derivatives, this function is the only information needed for computing the guiding center drift orbits. The influence of the ambipolar radial electric field is neglected ( $\nabla \Phi = 0$ ) because it has only a minor effect on the drift orbits of the high energy superthermal electrons. A Matlab program was

developed to solve the guiding center equations of motion (equations 6.14-6.17, 6.20) numerically and obtain the trajectories of the test particle in different HSX magnetic configurations. The code uses the Matlab “ode45” solver. The “ode45” solver is based on an explicit Runge-Kutta (4,5) formula, the Dormand-Prince pair<sup>7,8</sup>. The time step is adjusted automatically in the Matlab “ode45” solver. Each electron is launched with an initial energy  $\varepsilon$  and pitch angle  $\alpha$  at an effective plasma radius  $r/a$ , and toroidal and poloidal angles  $\varphi$  and  $\theta$ , respectively. The total integration time was set as an input parameter, and the Matlab code will run until either the integration time has elapsed or the particle leaves the confining volume defined by the last closed flux surface  $r/a = 1$ . A description of the guiding center drift orbit code is presented in Appendix 5.

Figures 6.9 and 6.10 show examples of  $r$ - $\theta$  and  $r$ - $\varphi$  polar plots of drift orbits for energetic electrons (5 keV, initial pitch angle  $\alpha = 85^\circ$ , initial poloidal angle,  $\vartheta = 0^\circ$ , initial toroidal angle,  $\varphi = 0^\circ$ , and  $r/a = 0.5$ ) in the Mirror magnetic configuration. Because electrons were launched outside the heating zone (defined by  $r/a < 0.1$ ), the microwave heating was not included in the calculations. The small blue circle at  $\varphi = 0^\circ$ ,  $\vartheta = 0^\circ$  and  $r/a = 0.5$  in both plots represents the electron starting location. The polar plots show that electrons launched with the above initial parameters are trapped and has big deviation from the home flux surface.

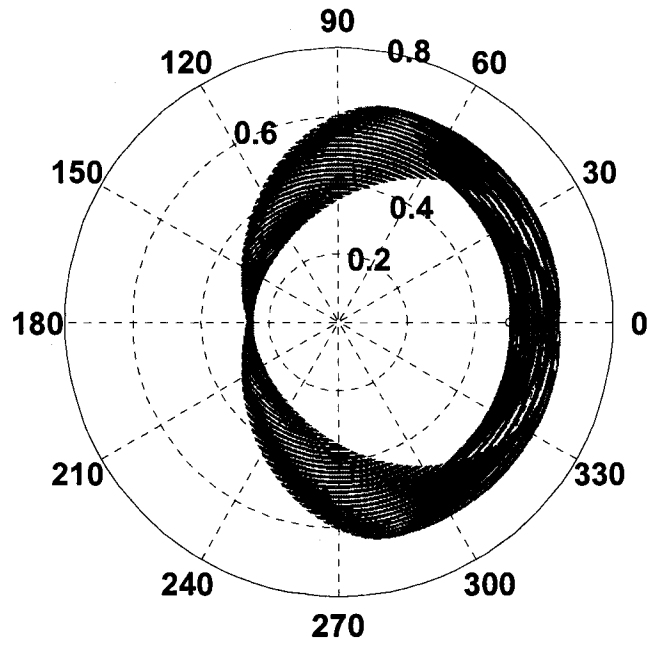


Figure 6.9:  $r$ - $\theta$  plot of electron drift orbit for  $\epsilon = 5$  keV,  $r/a = 0.5$ ,  $\alpha = 85^\circ$ ,  $\theta = 0^\circ$  and  $\varphi = 0^\circ$  in the Mirror configuration, integration time =  $5 \times 10^{-4}$  sec.

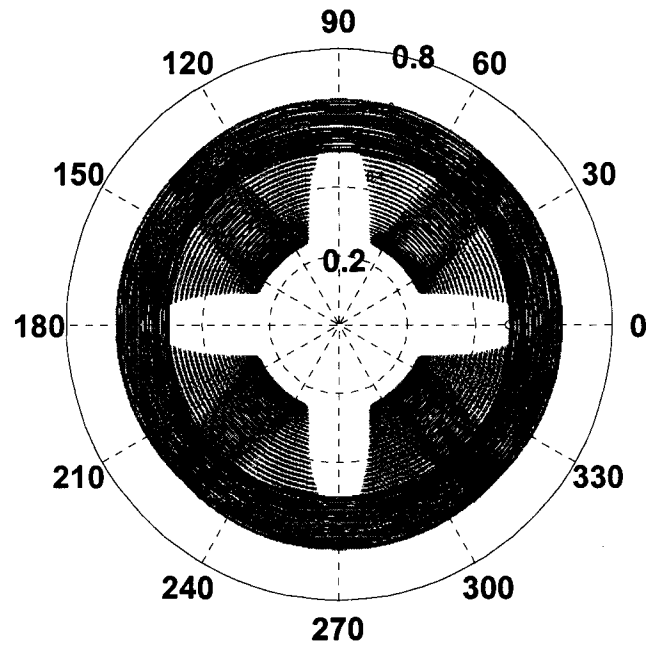
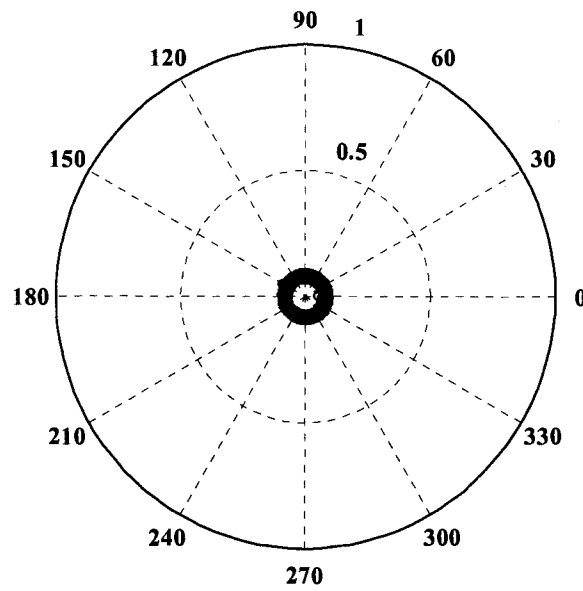


Figure 6.10:  $r$ - $\varphi$  plot of electron drift orbit for  $\epsilon = 5$  keV,  $r/a = 0.5$ ,  $\alpha = 85^\circ$ ,  $\theta = 0^\circ$  and  $\varphi = 0^\circ$  in the Mirror configuration, integration time =  $10^{-4}$  sec.

Figure 6.11 show the  $r$ - $\theta$  polar plot of an 100 eV electron orbit launched at  $r/a = 0.05$  inside the heating zone with initial pitch angle  $\alpha = 85^\circ$ ,  $\vartheta = 0^\circ$ ,  $\varphi = 0^\circ$ . The thickness of the orbit represents the electron deviation from the home flux surface. The blue circle represents the electron starting location and the black circle represents the electron final location.



**Figure 6.11:  $r$ - $\theta$  plot of electron drift orbit for  $\varepsilon = 100$  eV,  $r/a = 0.05$ ,  $\alpha = 85^\circ$ ,  $\theta = 0^\circ$  and  $\varphi = 0^\circ$  in the QHS configuration, integration time =  $10^{-4}$  sec.**

Figure 6.12 show the time evolution of the electron magnetic moment as a result of multiple passes through the heating zone. The x-axis is the time in seconds and the y-axis is the magnetic moment in units of Joules/Tesla. The steps in the magnetic moment indicate that the particle is inside the heating zone and has its energy is increasing while the plateaus represents when the electron is outside the heating zone. The final electron energy at the end of integration time is 75.63 keV.

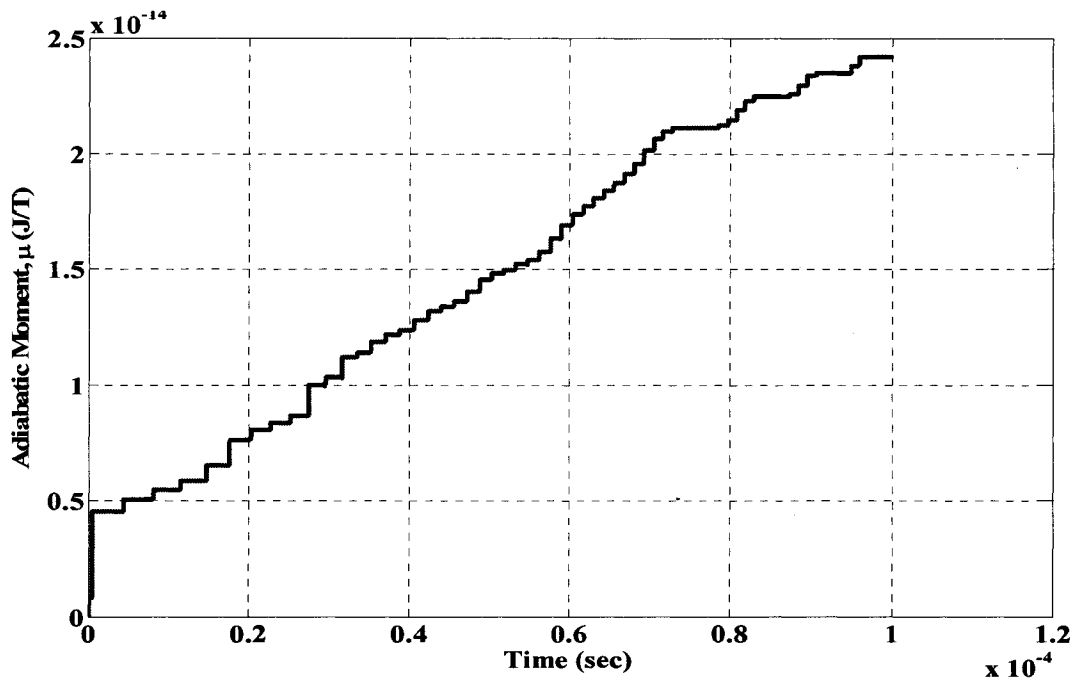


Figure 6.12: The time evolution for the magnetic moment for the electron shown in Figure 6.11

## 6.5 Confinement Differences between configurations during ECRH

The experimental results described in Chapter 4 show a clear difference in hard x-ray emission between different magnetic configurations. In order to prove that the difference is indeed caused by a difference in orbit trajectories outside the resonance zone, we will study the single electron confinement during the ECR heating in different magnetic configurations. By confinement we mean how often electrons leaving the heating zone in each configuration will revisit it again and increase its energy and population. In order to test this idea electrons are launched in each magnetic configuration with initial kinetic energy,  $\varepsilon$  (eV) at three different effective plasma radii near the magnetic axis  $r/a = 0, 0.05$ , and  $0.09$ . Five different values for the toroidal angle

$\varphi$  were specified at each  $r/a$ :  $\varphi = 0, \pi/8, \pi/4, \pi/2, \pi$ . At each initial toroidal location, the initial poloidal angle  $\vartheta$  is uniformly distributed between 0 and  $2\pi$ , and the pitch angle  $\alpha$  between  $10^\circ$  and  $88^\circ$ . The particles are followed in each configuration for the same period of time  $\sim 2 \times 10^{-4}$  sec. Collisions with background electrons, ions and neutral atoms are not included in the simulation. This is justified because for 100 eV electrons the electron-electron and electron-ion collision time is  $\sim 10^{-3}$  sec at low electron plasma density  $\bar{n}_e \sim 2 \times 10^{11} \text{ cm}^{-3}$ , while electron-neutral collision time is  $\sim 10^{-2}$  sec for  $\bar{n}_n \sim 10^{10} \text{ cm}^{-3}$ . The initial electron energies were chosen in the range between 100 and 500 eV, which is representative of the bulk electrons in the HSX. The initial  $r/a$  locations were chosen to make sure that the electrons are initially on flux surfaces that go through the microwave heating zone. HSX has four field periods i.e. the magnetic field replicate itself each  $\pi/2$ , this is why the values of the initial toroidal angle  $\varphi$  ranges from 0 to  $\pi$  (although  $\varphi = 0, \pi/2$  and  $\pi$  are magnetically identical, including the microwave heating at  $\varphi = 0$  makes particle orbits different for electrons launched at the three different toroidal locations). To obtain a quantitative difference between the configurations we define three parameters, the resonance zone crossing probability, the resonance zone crossing time fraction, the drift orbit relative width. The resonance zone crossing probability is defined as the number of times an electron crosses the heating zone cross section ( $r/a < 0.1$ ) at  $\varphi = 0$  divided by the total number of times an electron crosses the full plasma cross section at  $\varphi = 0$ . These two regions are illustrated in Figure 6.13. The resonance zone crossing

time fraction is the total time the electron spends in the heating zone ( $r/a < 0.1$ ,  $|\phi| < 4^\circ$ ) divided by the total time of the electron following. The drift orbit relative width is defined as the difference between the maximum and minimum  $r/a$  locations of the particle as shown in Figure 6.14.

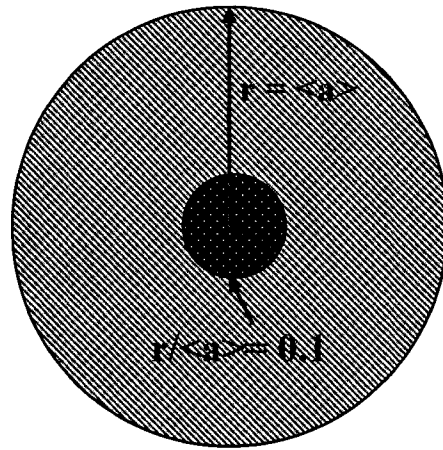


**Figure 6.13: Plasma cross section at  $\phi = 0$  in Boozer co-ordinates. The smaller circle is the heating zone cross section defined by  $r/\langle a \rangle = 0.1$ .**

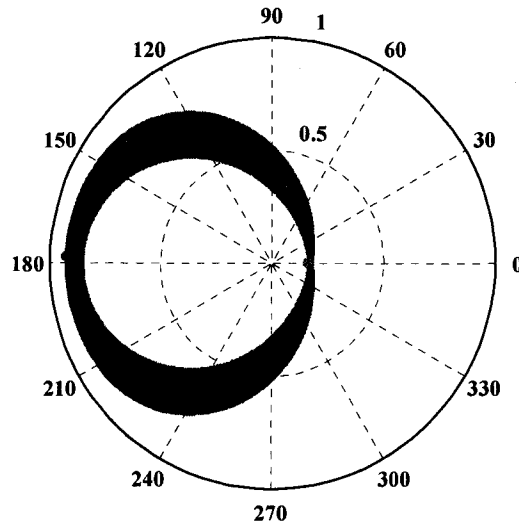


**Figure 6.14:  $r$ - $\theta$  plot of electron drift orbit for  $\varepsilon = 100$  keV,  $r/a = 0.5$ ,  $\alpha = 85^\circ$ ,  $\theta = \pi/2$  and  $\phi = 0^\circ$  in the AntiMirror configuration, integration time =  $10^{-4}$  sec. The 4 small circles indicate the electron initial and final locations (top 2 circles), the minimum  $r/a$  (right) and the maximum  $r/a$  (left).**

Those parameters were chosen as a figure of merit because they give a qualitative idea how good is the microwave heating mechanism. The higher the resonance crossing probability and time fraction the more likely the particle will become superthermal. If particles are launched inside the heating, the bigger the relative drift orbit width the more likely the particle will not revisit the heating zone again and stops gaining energy.

The results of the simulation for the case of  $r/a = 0.05$ ,  $\varepsilon = 500$  eV and simulation time  $= 2 \times 10^{-4}$  sec are shown in Figures 6.15 to 6.18. The figures show the variation of the resonance crossing probability, the electron final energy, the resonance crossing time fraction and the relative drift orbit width with the initial pitch angle  $\alpha$  at different poloidal locations around the machine for the three magnetic configurations. Each data point represents the average over 8 different values of the initial poloidal angle  $\vartheta$ .

The x-axis in Figure 6.15 is the initial pitch angle  $\alpha$  in degrees and the y-axis the resonance crossing probability. The figures show that an electron in the QHS configuration has the highest probability of crossing the resonance zone. The probability is nearly one at all toroidal locations and pitch angles except for the deeply trapped electrons. Electrons with initial pitch angles  $\alpha = 85^\circ$  and  $88^\circ$  have a probability between 60 % and 80 % depending on the electron initial toroidal location  $\varphi$ . The situation is different in case of the Mirror and AntiMirror configurations. In the Mirror configuration at initial pitch angles less than  $60^\circ$ , the probability is nearly one and drops significantly below one at higher pitch angles depending on the initial toroidal location.

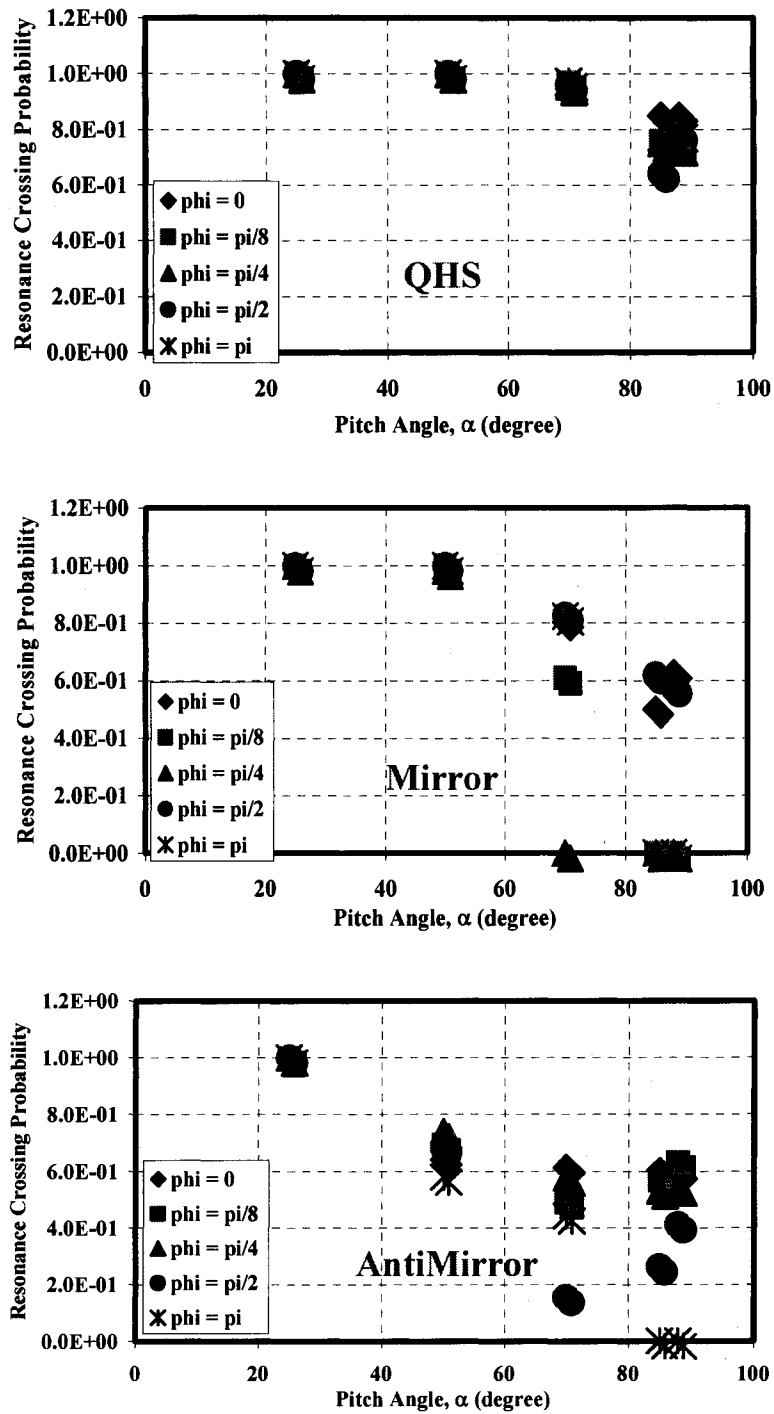
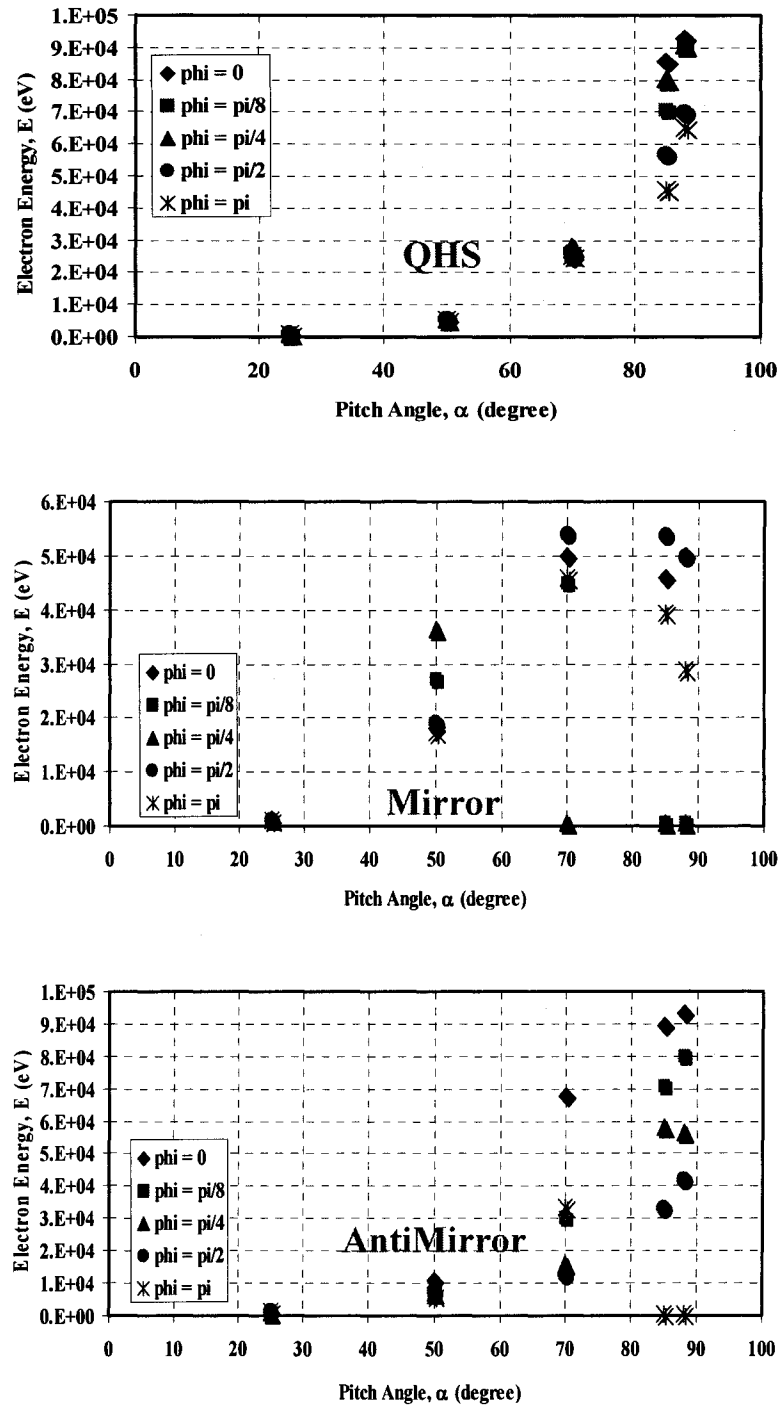


Figure 6.15: The variation of the resonance zone crossing probability for 500 eV electrons with pitch angle at  $r/\langle a \rangle = 0.05$  and different toroidal locations  $\phi$  in the QHS (top), Mirror (middle) and AntiMirror (bottom) configurations.

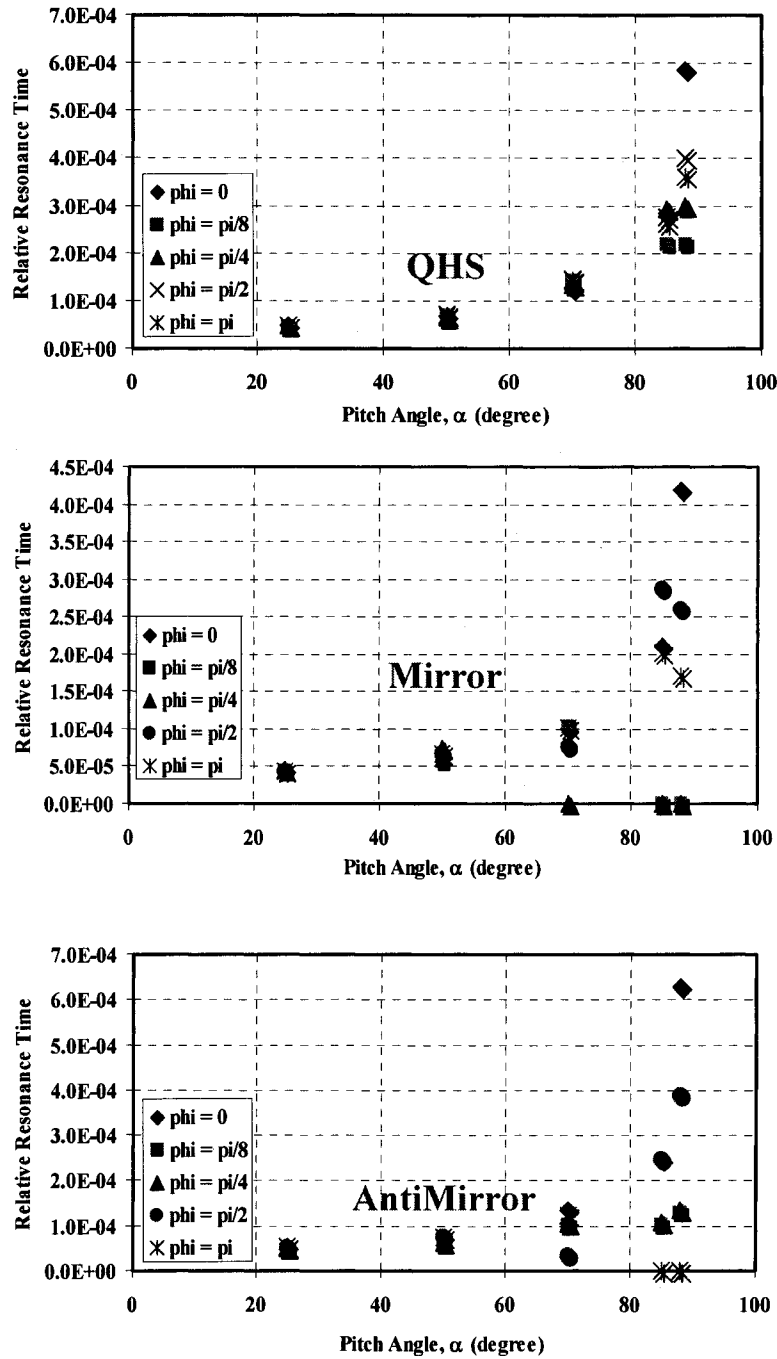
In the AntiMirror configuration the probability is small except at small pitch angle  $\sim 20^\circ$  and ranges between 0% and 60% depending on the initial toroidal location as in the Mirror case.

Figure 6.16 shows the electron final energy at the end of the particle following time ( $2 \times 10^{-4}$ ) seconds. The x-axis is the initial pitch angle  $\alpha$  and the y-axis is the final electron energy in eV. The figures show that the higher the initial pitch angle, the higher the final electron energy. In the QHS configuration, the final electron energy is independent of the initial toroidal location at all initial pitch angles except for the deeply trapped electrons with initial pitch angles  $\alpha = 85^\circ$  and  $88^\circ$ . The final energy ranges between 40 and 90 keV in the QHS configuration, 0 to 50 keV in the Mirror configuration and 0 to 90 keV in the AntiMirror configuration. As stated earlier, the relativistic effects are not considered in this model, and this is the reason why electrons gain such high energies in a short time scale. In reality electrons will fall off resonance at much lower electron energies. This is independent of magnetic configuration, however, so for the sake of comparison between the magnetic configurations neglecting relativistic effects is a good approximation.

Figure 6.17 shows the variation of the resonance crossing time fraction with the initial electron pitch angle at different electron initial toroidal locations for the three different configurations. The x-axis is the initial electron pitch angle  $\alpha$  and the y-axis is the resonance crossing time fraction. The figures show that the higher the electron initial pitch angle the longer the time the particle will spend in the resonance zone.



**Figure 6.16:** The variation of electron final energy for 500 eV electrons with pitch angle at  $r/a = 0.05$  and different toroidal locations  $\phi$  in the QHS (top), Mirror (middle) and AntiMirror (bottom) configurations.

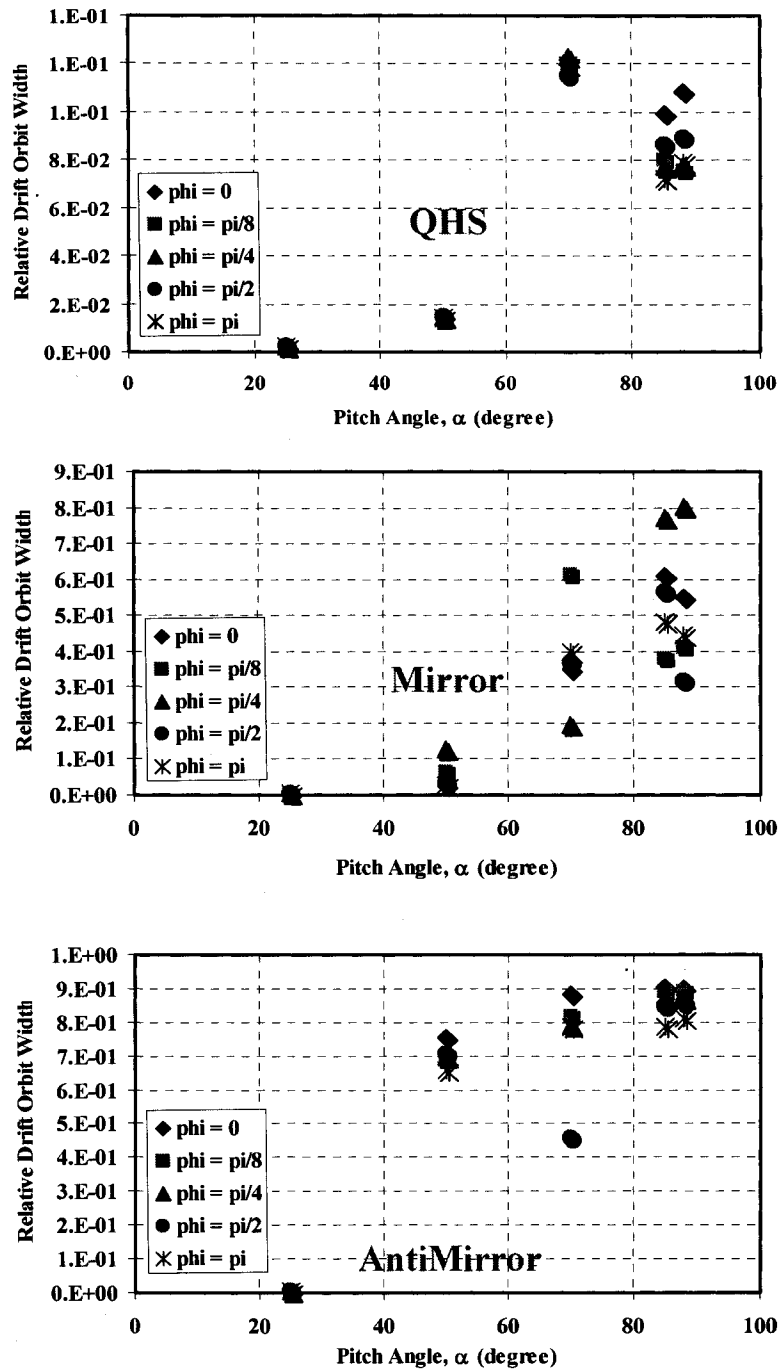


**Figure 6.17:** The variation of electron resonance zone crossing time fraction for 500 eV electrons with pitch angle at  $r/a = 0.05$  and different toroidal locations  $\phi$  in the QHS (top), Mirror (middle) and AntiMirror (bottom) configurations.

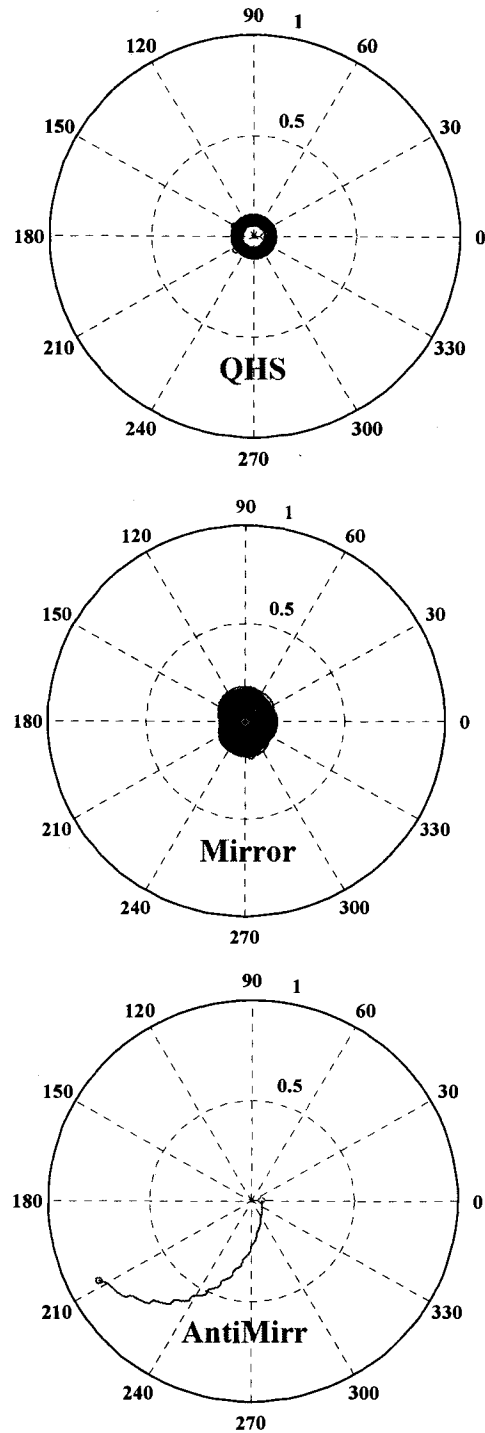
The figures also show that the deeply trapped electrons in the AntiMirror configuration spend nearly the same time in front of the microwave heating antenna at  $\varphi = 0$  as compared to the QHS configuration. The situation is different at the rest of the toroidal locations, with the resonance crossing time fraction ranging between 0 to  $\sim 3 \times 10^{-4}$ .

Figure 6.18 shows the variation of the relative drift orbit widths with the initial electron pitch angle at different electron initial toroidal locations for the three magnetic configurations. The x-axis is the initial pitch angle and the y-axis is the relative drift orbit width. The figures show that the higher the pitch angle, the bigger the relative drift orbit width. The QHS configuration has the minimum deviation from the home flux surfaces at all pitch angles and initial toroidal locations. At small pitch angles, the relative drift orbit width is on the order of 0.02 relative plasma radius ( $\Delta r/a$ ) and increases up to 0.1 plasma radius at an initial electron pitch angle  $\alpha = 70^\circ$ . For deeply trapped electrons at  $\alpha = 85^\circ$  and  $88^\circ$ , the scattering in the deviations is not big, it ranges between 0.08 and 0.1 plasma radius. The Mirror configuration has bigger deviations from the home flux surfaces especially, for the deeply trapped electrons with high initial pitch angle. The deviations range from 0.3 to 0.8 plasma radius. The situation is different in the AntiMirror configuration: at initial pitch angles greater than  $\sim 25^\circ$ , the deviation from the home flux surfaces are very large and are in the order of 0.8 to 0.9 plasma radius. As we will discuss soon those electrons are in the so called direct loss orbits.

Orbit trajectories and magnetic moment time evolution for the three different configurations are shown in Figures 6.19 and 6.20.



**Figure 6.18:** The variation of electron relative drift orbit width for 500 eV electrons with pitch angle at  $r/\langle a \rangle = 0.05$  and different toroidal locations  $\phi$  in the QHS (top), Mirror (middle) and AntiMirror (bottom) configurations.



**Figure 6.19:  $r$ - $\theta$  plot of electron drift orbit for  $\varepsilon = 100$  eV,  $r/a = 0.05$ ,  $\alpha = 85^\circ$ ,  $\theta = 0^\circ$  and  $\varphi = 0^\circ$  in different configurations, integration time =  $10^{-4}$  sec.**

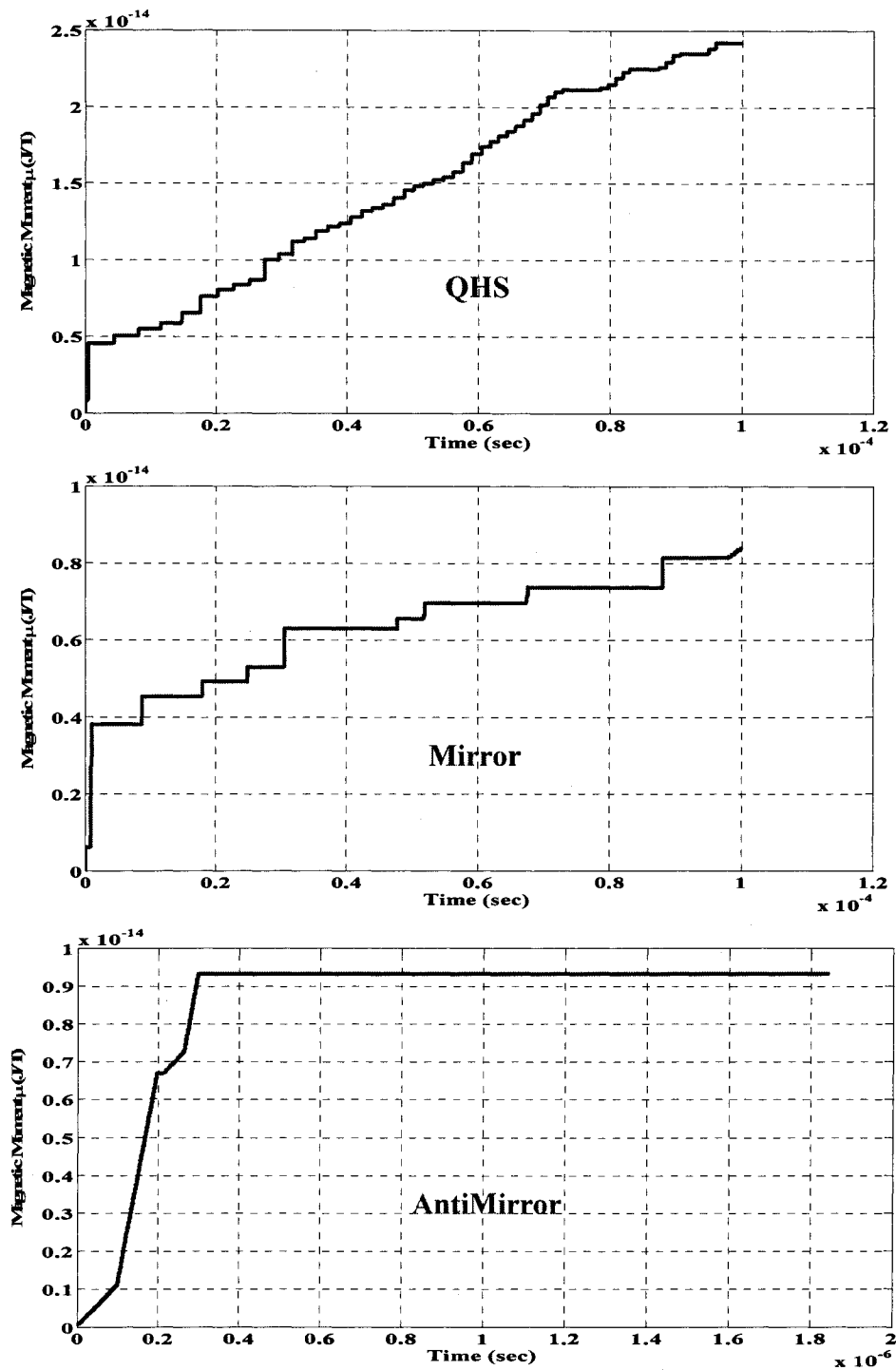


Figure 6.20: The time evolution for the magnetic moment for the electrons shown in Figure 6.19

The polar plots are for an 100 eV electrons launched at  $r/a = 0.05$  inside the heating zone with initial pitch angle  $\alpha = 85^\circ$ ,  $\theta = 0^\circ$  and  $\varphi = 0^\circ$  and integration time =  $10^{-4}$  sec. Figure 6.19 shows that, in QHS the particle orbits have the minimum deviation from the home flux surfaces (drift orbit width  $\sim 0.06$  plasma radius) compared to the Mirror and AntiMirror configurations. Electrons launched in the Mirror configuration at  $r/a = 0.05$  have higher deviations (drift orbit width  $\sim 0.18$  plasma radius) while electrons launched in the AntiMirror configuration are in direct loss orbit and leave the confinement region quickly. Figure 6.20 shows that, the magnetic moment increases monotonically in QHS, slowly in Mirror and saturates quickly in AntiMirror configurations during the integration time. This can be explained in light of Figure 6.19. In case of QHS, electron orbits have minimum deviation from home flux surface, so they will revisit the heating zone frequently and their energies will increase monotonically. In the Mirror configuration, electrons have larger deviates from the home flux surfaces. At the early stage they visit the heating zone frequently and gain energy, the higher the electron energy, the higher the deviation until the electron deviations bring the electron outside the heating zone, then their energy saturates. In the AntiMirror configuration, electrons spend the early stage of their life in the heating zone and gain energy from the microwave. Due to the asymmetry of the magnetic well in front of the microwave antenna and the increase in the electron pitch angle due to heating, electrons are in direct loss orbit and start to leave the confinement region. Once the electrons leave the heating

zone, it will stop gaining energy and their magnetic moment will saturate so quickly as shown in the figure.

The summary of the results are presented in Tables 6.1 to 6.4. The values are averaged over the initial toroidal angle  $\varphi$  at each initial pitch angle  $\alpha$  for the sake of comparison between the different magnetic configurations.

	25	50	70	85	88
	QHS				
$T_{\text{relative}}$	4.68E-05	6.80E-05	1.38E-04	2.66E-04	3.73E-04
$\sigma$	4.47E-07	1.58E-06	7.69E-06	2.94E-05	1.38E-04
	Mirror				
$T_{\text{relative}}$	4.45E-05	6.58E-05	7.00E-05	1.24E-04	1.70E-04
$\sigma$	5.77E-07	7.41E-06	4.81E-05	1.47E-04	2.06E-04
	AntiMirror				
$T_{\text{relative}}$	5.22E-05	7.30E-05	9.96E-05	1.40E-04	2.56E-04
$\sigma$	8.37E-07	5.20E-06	4.04E-05	1.06E-04	2.51E-04

**Table 6.1: Fraction of resonance zone crossing time at five different initial pitch angles  $\alpha$  in the QHS, Mirror and AntiMirror configurations.**

	25	50	70	85	88
	QHS				
$P_{\text{Crossing}}$	1.000	1.000	0.965	0.737	0.781
$\sigma$	0.000	0.000	0.007	0.080	0.043
	Mirror				
$P_{\text{Crossing}}$	1.000	0.996	0.561	0.280	0.300
$\sigma$	0.000	0.009	0.387	0.327	0.347
	AntiMirror				
$P_{\text{Crossing}}$	1.000	0.668	0.456	0.392	0.435
$\sigma$	0.000	0.061	0.181	0.257	0.257

**Table 6.2: Resonance zone crossing probability at five different initial pitch angles  $\alpha$  in the QHS, Mirror and AntiMirror configurations.**

	25	50	70	85	88
			QHS		
$\epsilon_{\text{final}}$	7.63E+02	5.40E+03	2.59E+04	6.78E+04	8.18E+04
$\sigma$	3.35E+01	2.41E+02	1.49E+03	1.65E+04	1.32E+04
			Mirror		
$\epsilon_{\text{final}}$	1.06E+03	2.51E+04	3.73E+04	2.51E+04	2.52E+04
$\sigma$	1.53E+02	8.52E+03	2.48E+04	2.86E+04	2.85E+04
			AntiMirror		
$\epsilon_{\text{final}}$	1.14E+03	7.70E+03	3.20E+04	5.05E+04	5.44E+04
$\sigma$	8.52E+01	1.87E+03	2.18E+04	3.46E+04	3.62E+04

**Table 6.3: Electron final energy at five different initial pitch angles  $\alpha$  in the QHS, Mirror and AntiMirror configurations.**

	25	50	70	85	88
			QHS		
$\langle \delta x \rangle / \langle a \rangle$	2.09E-03	1.42E-02	1.20E-01	8.32E-02	8.59E-02
$\sigma$	6.15E-05	5.96E-04	3.19E-03	1.03E-02	1.35E-02
			Mirror		
$\langle \delta x \rangle / \langle a \rangle$	2.64E-03	6.29E-02	3.83E-01	5.82E-01	5.19E-01
$\sigma$	2.32E-04	4.76E-02	1.73E-01	1.61E-01	2.11E-01
			AntiMirror		
$\langle \delta x \rangle / \langle a \rangle$	2.97E-03	7.01E-01	7.47E-01	8.60E-01	8.66E-01
$\sigma$	1.57E-04	3.47E-02	1.66E-01	4.52E-02	3.52E-02

**Table 6.4: Electron Drift orbit relative width at five different initial pitch angles  $\alpha$  in the QHS, Mirror and AntiMirror configurations.**

The tables show that on the average, QHS has the highest resonance zone crossing probability, resonance zone crossing time fraction, the highest final electron energy, and the minimum deviation from the home flux surfaces as expected because of its magnetic field helical symmetry. No matter where the electrons are launched on flux surfaces with  $r/a$  between 0 and 0.1 (flux surfaces passing through the microwave heating zone), they will revisit the heating zone frequently and they will have the minimum deviations from

those surfaces even for the deeply trapped electrons. The tables also show that the AntiMirror configuration comes second in the values of resonance zone crossing probability, time fraction and final energy to the QHS and is comparable to the Mirror configuration. This contradicts the experimental results described in Chapter 4 where no hard x-rays are measured in the AntiMirror configuration while moderate signal is measured in the Mirror configuration. This contradiction can be easily resolved if we look at the variation of  $|B|$  along field line at  $r/a = 0.05$  (field line that go through the heating zone) shown in Figure 6.21.

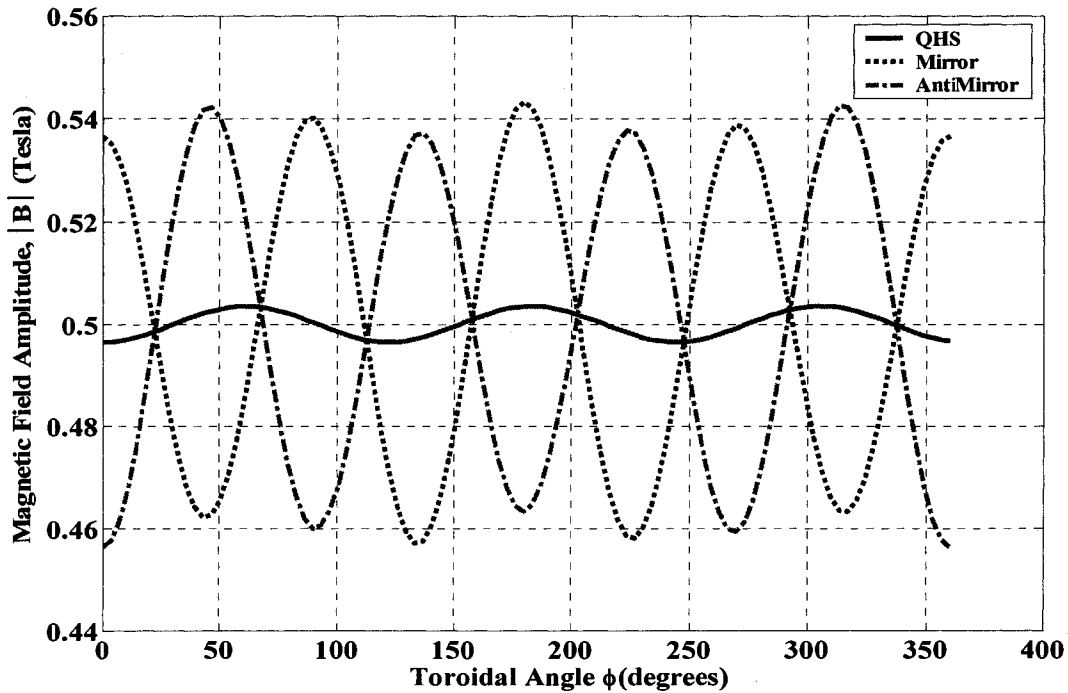


**Figure 6.21: The variation of the magnetic field amplitude along field line at  $r/a = 0.05$  in QHS, Mirror and AntiMirror configurations. Heating zone centered at  $\phi = 0$ .**

When the microwaves are injected into the machine, electrons are generated in the AntiMirror configuration at  $\phi = 0$  in front of the microwave antenna in the local

minimum of the magnetic field. Electron cyclotron heating is known to pump up the electron energy in the perpendicular direction and increase its pitch angle. Electrons deeply trapped in the asymmetric magnetic well will be on direct loss orbits and will leave the confinement region very rapidly after they are generated. To prove this idea, 25 keV electrons are launched at  $r/a = 0.1$  uniformly for  $5 \times 10^{-4}$  seconds with pitch angles  $\alpha > 70^\circ$ . If the particle location exceeds  $0.9 r/a$ , the particle will be considered as lost and the time taken by the particle to leave the confinement region is recorded. The total simulation time is divided to multiple time bins and the fraction of particles on direct loss orbits is obtained. The result of the simulation is shown in Figure 6.22.

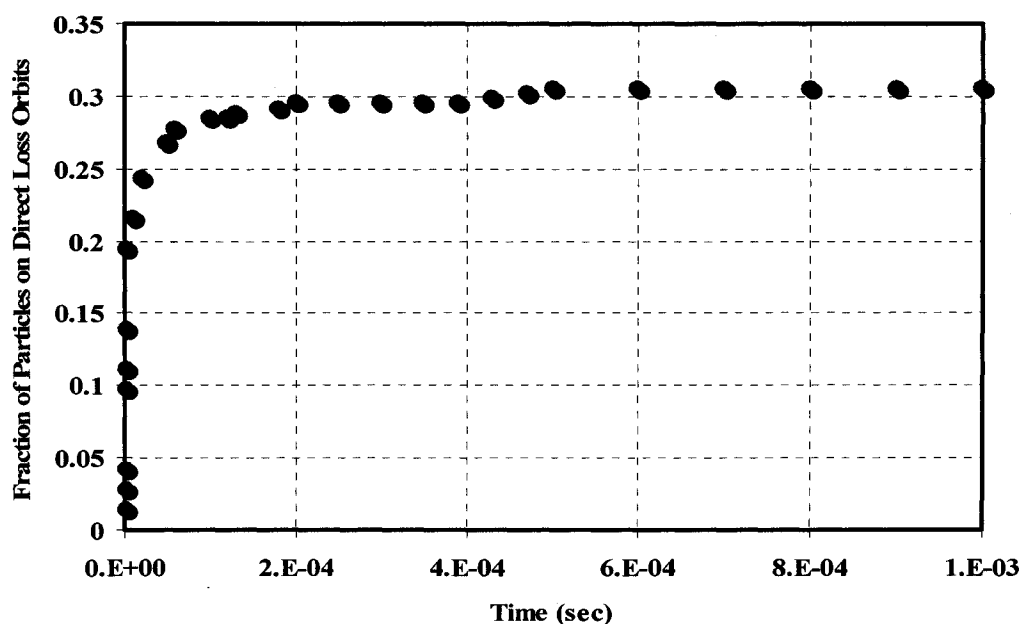


**Figure 6.22: The fraction of particles on direct loss orbits in AntiMirror configuration for 25 keV electrons launched at  $r/a = 0.1$  uniformly.**

The x-axis represents the time in seconds and the y-axis represents the fraction of particles on direct loss orbits. The figure shows that for electrons launched at  $r/a = 0.1$

and uniformly distributed around the machine, 30% are in direct loss orbits. The particles leave the confinement region in a short time scale ranging between a few  $\mu$ seconds and 0.2 msec after they are generated depending on the particle initial location and pitch angle. The 30% is not a huge direct loss in the AntiMirror and cannot explain why no hard x-ray signal is measured, but if we consider only the fraction of trapped particles in front of the microwave antenna the ratio will increase to almost 70% and the particles will be lost in less than  $\sim 20 \mu$ sec from the machine as shown in Figure 6.23.

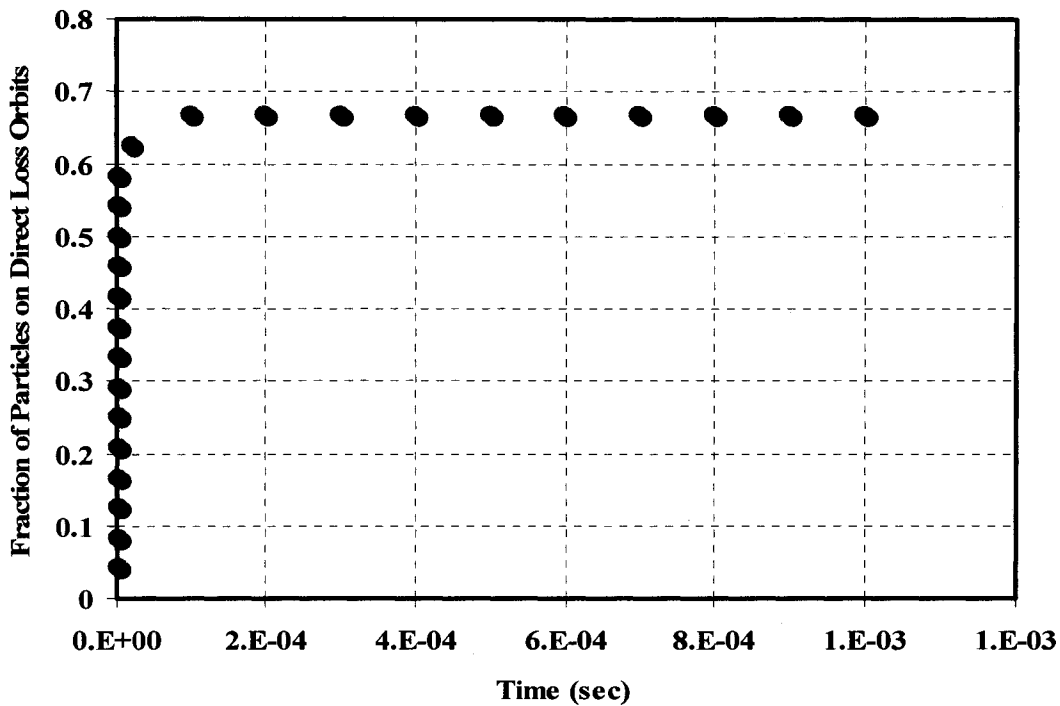


**Figure 6.23: The fraction of particles on direct loss orbits in AntiMirror configuration for 25 keV electrons launched at  $r/a = 0.1$  in front of the microwave heating antenna at  $\varphi = 0$ .**

The direct loss of electrons in the AntiMirror configuration was detected experimentally using a pair of plates<sup>9</sup> installed in the top and bottom of box port C where

the microwave antenna is located. The floating potential at each plate is monitored during HSX discharges, and is interpreted as being driven by direct losses of electrons at these locations. It was observed that in the QHS configuration, the potential at both plates is nearly zero. In AntiMirror, the plate in the ion drift direction remains nearly zero, while the plate in the electron drift direction shows a large negative floating potential of as much as  $-100\text{V}$  at low densities. This large potential is believed to be due to an excess of electrons at the plate in the electron drift direction, coming from direct orbit losses. In order to verify that the effect is indeed due to direct losses, the direction of the magnetic field is reversed to switch the ion and electron drift directions. In these experiments, the plate that was in the electron drift direction again showed a large, negative floating potential. This data verifies that in the QHS configuration, direct orbit losses have been significantly reduced compared to the AntiMirror configuration. The experimental results are shown in Figures 6.24 and 6.25. The x-axis represents the line-averaged plasma density and the y-axis is the floating potential  $V_f$  measured in volts. The Mirror does not show loss from confinement volume or voltages driven on plates. This is because; in front of the microwave antenna electrons are generated at the top of the magnetic well and are passing particles at this location. The Figure 6.25 shows that the floating potential in the AntiMirror configuration is higher at low density and decreases with increasing the plasma density. This is caused by increasing the de-trapping effects as a result of pitch angle scattering of electrons with background electrons and ions at higher plasma electron.

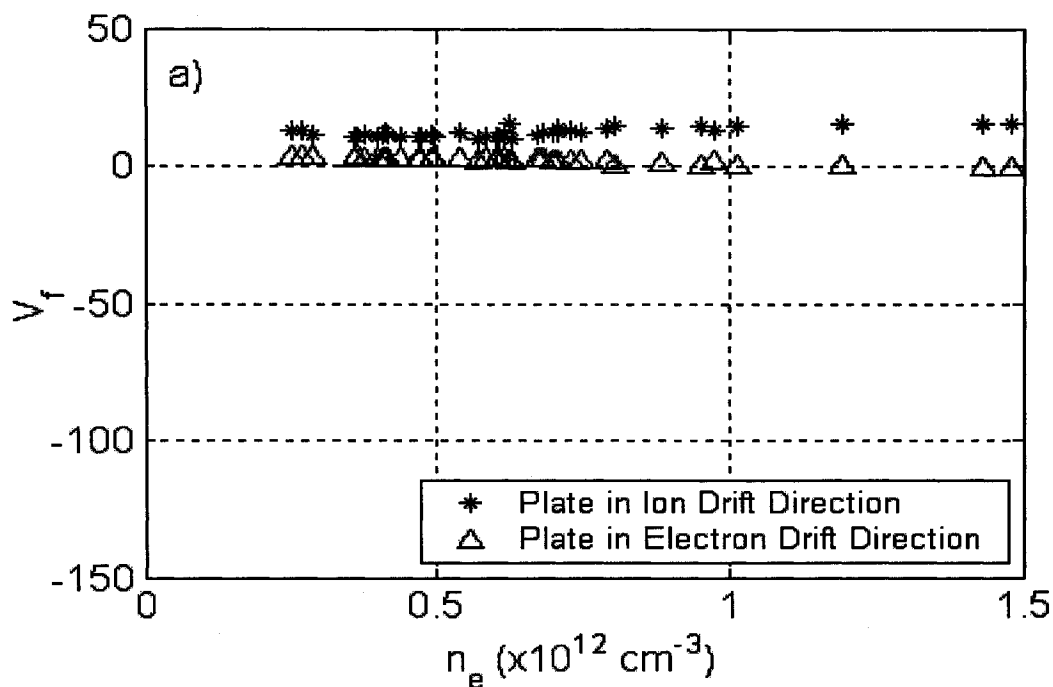


Figure 6.24: Floating potential on collector plates as a function of electron density in the QHS configuration<sup>9</sup>.

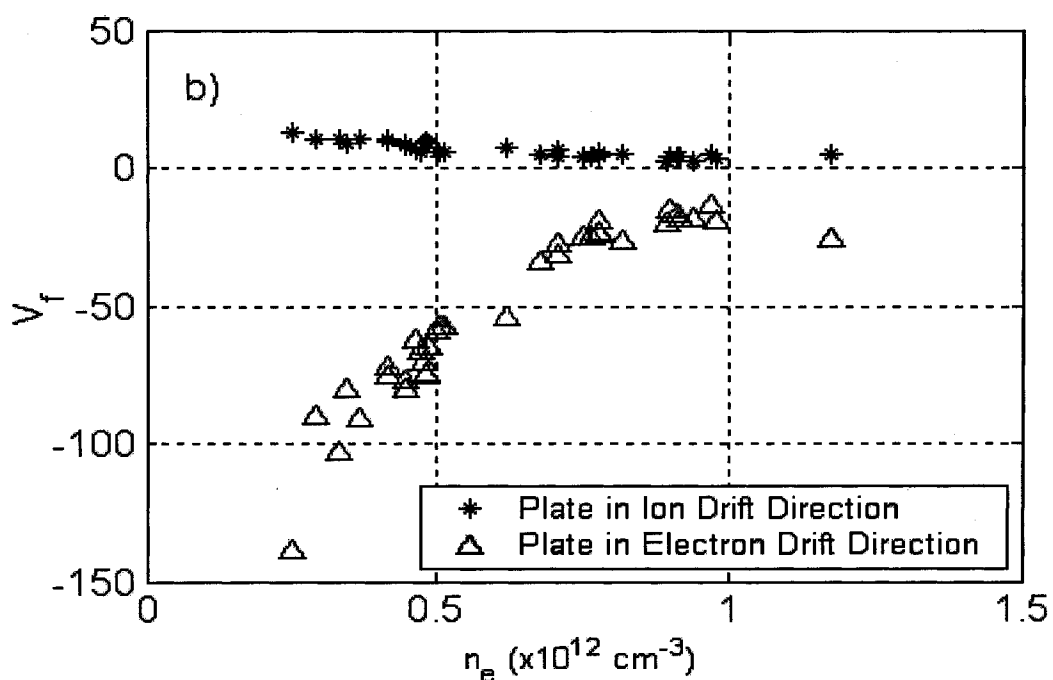


Figure 6.25: Floating potential on collector plates as a function of electron density in the AntiMirror configuration<sup>9</sup>.

## 6.6 Confinement Differences between configurations After ECRH is Turned Off

In this section we will study the difference in confinement between the magnetic configurations after the gyrotron power is turned off. The results of Chapter 4 show that after the microwave heating source is turned off, the hard x-ray emission decreases exponentially with time. The results also show that at low density,  $\bar{n}_e \sim 2 \times 10^{11} \text{ cm}^{-3}$ , the QHS configuration has longer superthermal electron confinement time  $\sim 7 \text{ msec}$  (measured from the exponential curve fitting of the decay of the hard x-ray emission after the microwave heating source is turned off) as compared to  $\sim 1 \text{ msec}$  in the Mirror configuration. At low plasma line-averaged density,  $\bar{n}_e \sim 4 \times 10^{11} \text{ cm}^{-3}$ , the average hard x-ray photon energy is  $\sim 100 \text{ keV}$  in both QHS and Mirror configurations, with a higher superthermal electron population in QHS as compared to Mirror. If superthermal electrons possess such high kinetic energy, they should have essentially no collisions with background electrons and ions. The electron-electron and electron-ion collision times are  $\tau_{e-e} \sim 410 \text{ msec}$ , and  $\tau_{e-i} \sim 816 \text{ msec}$  at line-averaged density  $\bar{n}_e \sim 4 \times 10^{11} \text{ cm}^{-3}$ . As the calculations in the last section show, the QHS configuration has a very small deviation from the home flux surfaces even for deeply trapped particles. One should expect that superthermal electrons should be confined in the QHS configuration for times at least comparable to the electron-electron collision time  $\tau_{e-e} \sim 410 \text{ msec}$ . The experimentally measured confinement time  $\sim 7 \text{ msec}$  is very short compared to the electron-electron collision time. This raises the question of why the electrons leave the

confinement region so quickly. HSX has a small minor radius and relatively low plasma density, so neutrals can easily penetrate to the core. The fact that there is a significant neutral density in the core leads us to study the electron-neutral collisionality and see if it dominates the electron-electron and/or electron-ion collisionality. If the electron-neutral collisionality dominates, the transport of superthermal electrons can be represented as a diffusive process with a scale length  $\Delta x$  corresponding to the drift orbit width and  $\Delta t$  being the electron-neutral collision time. In the next subsections we will describe the methods of evaluating the neutral density and the scale lengths  $\Delta x$  and  $\Delta t$ .

### 6.6.1 Neutral Gas Densities in the HSX Stellarator

$H_\alpha$  emission measurements of the absolutely calibrated  $H_\alpha$  detectors in HSX and the 3D simulation using the neutral gas code DEGAS<sup>10</sup> show that the neutral gas densities of atomic and molecular hydrogen are comparable in HSX during the ECRH discharges. Figure 6.26 shows the neutral density profile for atomic and molecular hydrogen. The figure shows that the atomic hydrogen density is  $\sim 10^{10} \text{ cm}^{-3}$  at line-averaged electron density  $\bar{n}_e \sim 5 \times 10^{11} \text{ cm}^{-3}$  and is constant across plasma minor radius while the molecular density shows an exponential decay into the core. In the HSX stellarator the base pressure is kept nearly constant at  $P_{\text{base}} \sim 10^{-7} \text{ torr}$  before the plasma discharge corresponding to a neutral density of  $n_n \sim 10^{10} \text{ cm}^{-3}$ . The micro-ion gauge signal shown in Figure 6.27 shows that after the microwave heating source is turned off a sudden increase in the neutral gas pressure takes place.

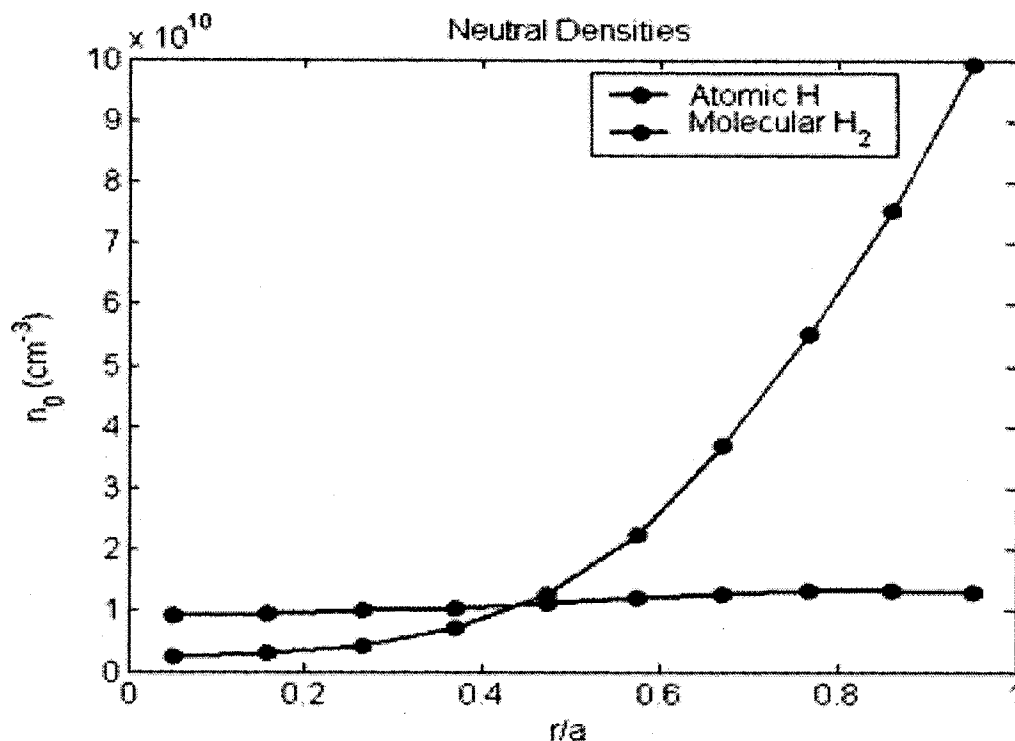


**Figure 6.26: The profiles of neutral densities for atomic and molecular hydrogen<sup>10</sup>.**

The maximum value of the base pressure depends on the sequence of gas puff used during the ECRH discharge and the location of the puffer toroidally around the machine. The figure shows that after the microwave heating source is turned off, the value of neutral gas density ranges between 1 and  $5 \times 10^{10} \text{ cm}^{-3}$ . The measurements of the micro-ion gauge are not precise because it is mounted on the plasma periphery and it has a slow response time, so the true neutral density is expected to be higher than the measured one.

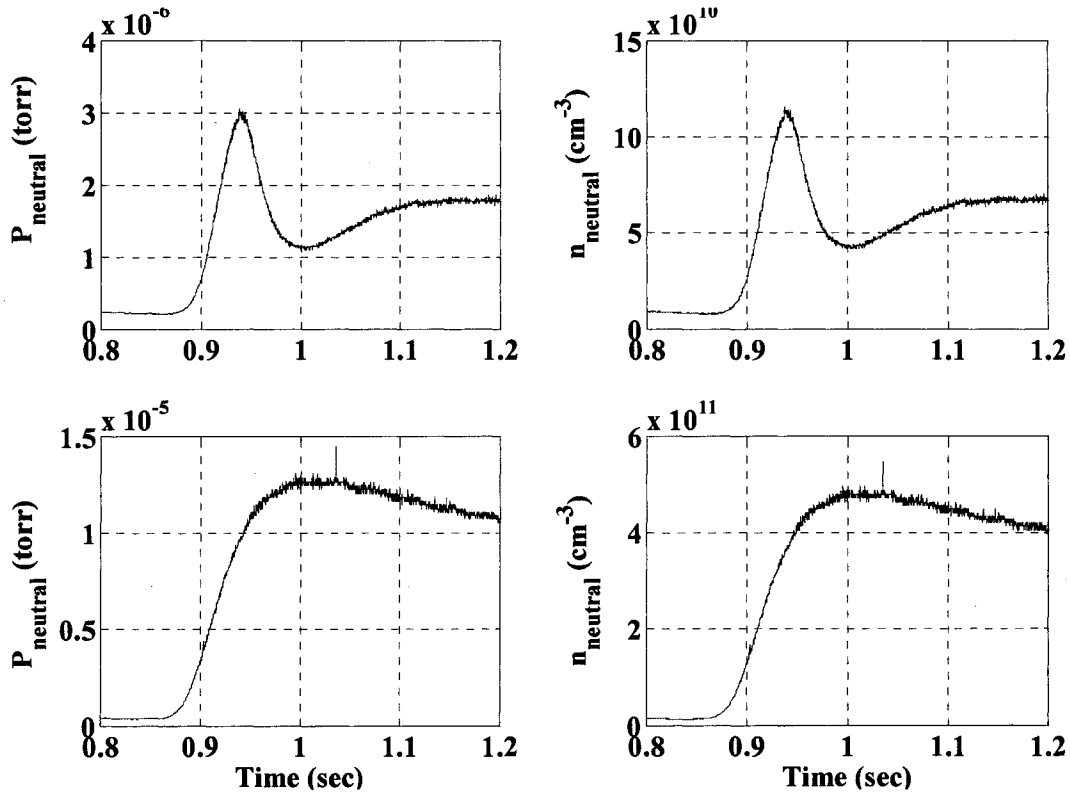


**Figure 6.27: The neutral base pressure measured using the micro-ion gauge left and the corresponding neutral density (right) using two different gas puffing sequences.**

Knowing the neutral gas density and the electron-neutral collision cross section it is easy to calculate the collision frequencies and collision times. The electron-neutral ionization collision frequency is given by<sup>11</sup>:

$$\nu = n_n \sigma_{e-n} v \quad (6.22)$$

where  $\epsilon$  is the electron kinetic energy in eV and the electron-neutral collision cross section is given by:

$$\sigma_{e-n} = \frac{3.123 \times 10^{-15}}{\epsilon} (\log_{10} \epsilon + 0.792) \quad (cm^2) \quad (6.21)$$

where  $v$  is the particle velocity. The collision time is the inverse of the collision

$$\text{frequency } \tau_{e-n} = \frac{1}{\nu_{e-n}}.$$

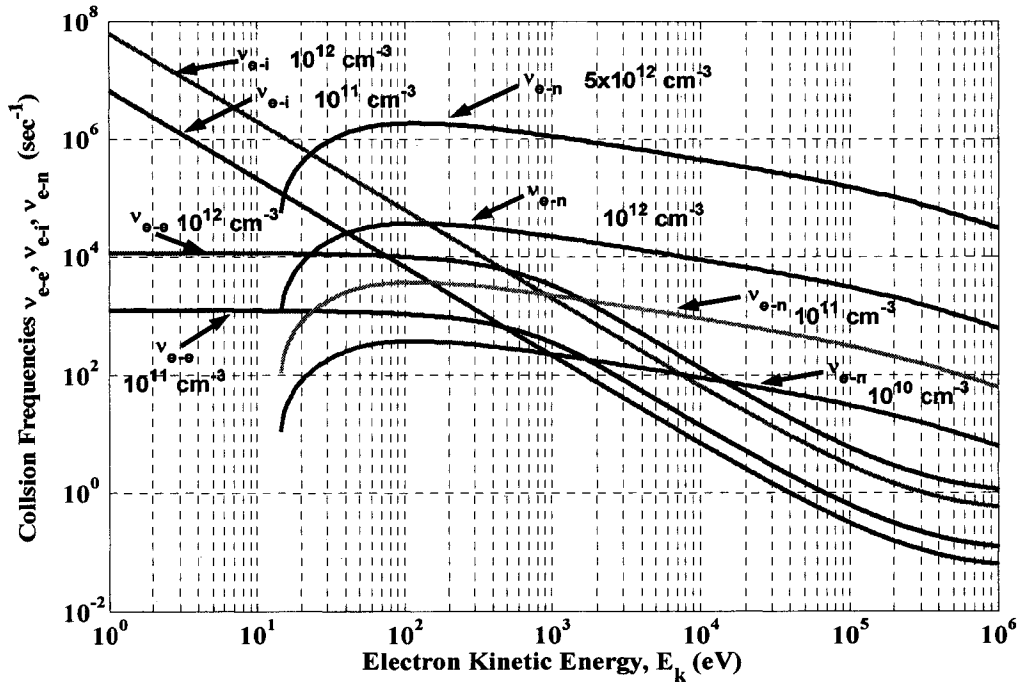


**Figure 6.28: The energy variation of the electron collision frequencies at different densities.**

Figure 6.28 shows the variation of the electron collision frequencies with electron kinetic energy at different plasma and neutral densities. The x-axis is the electron kinetic energy in eV and the y-axis is the electron-electron, electron-ion and electron-neutral collision frequencies. As the figure shows, at electron kinetic energies greater than  $\varepsilon = 1$  keV and neutral gas densities greater than  $n_n \sim 10^{10} \text{ cm}^{-3}$ , the electron-neutral collision frequency is larger than the corresponding electron-electron and electron-ion collision frequencies for electron and ion densities in the order of  $10^{11} \text{ cm}^{-3}$ . As we stated earlier

the neutral density after the gyrotron is turned off can go as high as  $n_n \sim 10^{12} \text{ cm}^{-3}$ , with the corresponding electron-neutral collision time is  $\tau_{e-n} \approx 10^{-4} \text{ sec}$ .

### 6.6.2 Estimation of Superthermal Electron Confinement Times

A simple formula for estimating the superthermal electron confinement time is given by:

$$\tau = \frac{\bar{a}^2}{5.8D} \quad (6.23)$$

Where  $\bar{a}$  is the plasma minor radius and D the diffusion coefficient given by  $D = \frac{\Delta x^2}{\Delta t}$

for a random walk process where  $\Delta x$  is the step size and  $\Delta t$  is the step time.

Particle following calculations were used to calculate the drift orbit width in different magnetic configurations, which are used as the step size. 1000 particles are launched in each magnetic configuration uniformly at  $r/a = 0.5$  with initial electron kinetic energy of 100 keV. The location  $r/a = 0.5$  is chosen based on an experiment where an electrostatic probe is inserted into the machine and the hard x-ray counts are recorded for each probe location. The results show that the hard x-ray counts drop significantly at  $r/a < 0.5$ . This indicates that superthermal electrons diffuse radially in the machine and are most likely to be present at half plasma minor radius. The result of the experiment is shown in Figure 6.29.

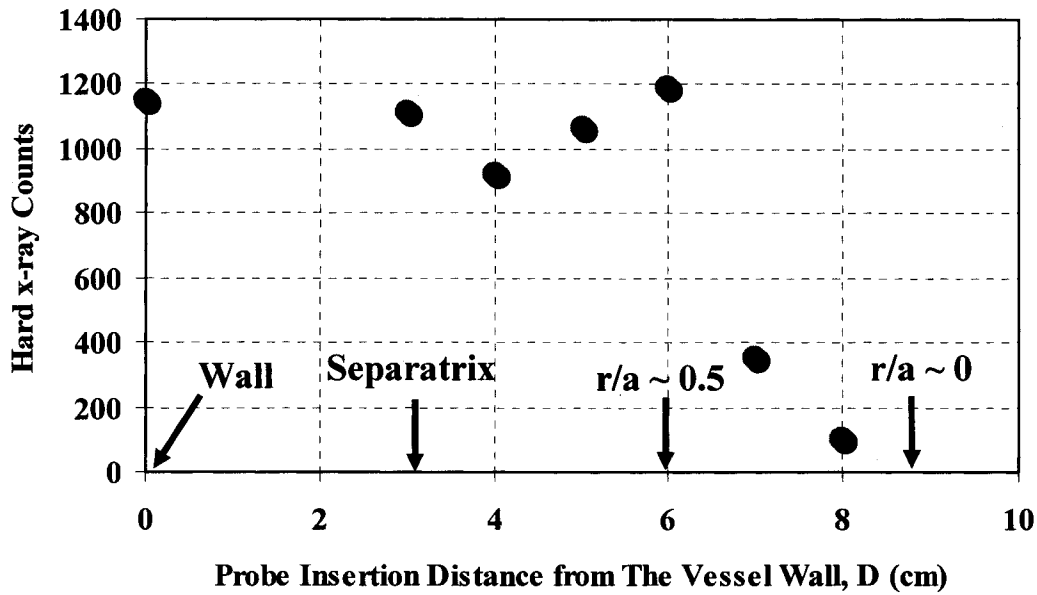


**Figure 6.29: The energy variation of the electron collision frequencies at different densities.**

The x-axis is the probe insertion distance in centimeters and the y-axis is the average hard x-ray counts at the probe location. The separatrix is at 3 cm from the vessel wall, and the magnetic axis is nearly 5.5 to 6 cm from the separatrix. The results of the calculations are shown in Table 6.5 for the three different configurations. Using  $\Delta x$  from the table and  $\Delta t \sim 10^{-4}$  second one obtains  $0.3249 \text{ m}^2/\text{sec}$  for the diffusion coefficient for the QHS configuration and  $20.52 \text{ m}^2/\text{sec}$  for the Mirror. The corresponding confinement times for the QHS configuration are  $\sim 6.7 \text{ msec}$  and  $0.1 \text{ msec}$  for the Mirror configuration. This is in reasonable agreement to the experimentally measured one.

Property	QHS	Mirror	AntiMirror
Drift Orbit Width $\Delta x$ (m)	$0.0057 \pm 0.0031$	$0.0453 \pm 0.04$	$0.0434 \pm 0.04$

**Table 6.5: Drift orbit width in different magnetic configurations.**

In order to study the effect of electron-neutral collisionality on superthermal electron confinement after the gyrotron is turned off, a gas puff was introduced just at the end of the discharge at 850 msec, and the hard x-ray decay time was compared to a normal shot without the gas puff at the end. The time variation of the neutral density calculated using the neutral base pressure measured with the micro-ion gauge is shown in Figure 6.28. The x-axis is the time in sec and the y-axis is the neutral density in  $\text{cm}^{-3}$  as inferred from the micro-ion gauge. Figure 6.29 shows the effect of increasing neutral density on the hard y-ray counts time evolution. The x-axis is the time in second and the y-axis is the hard x-ray count.

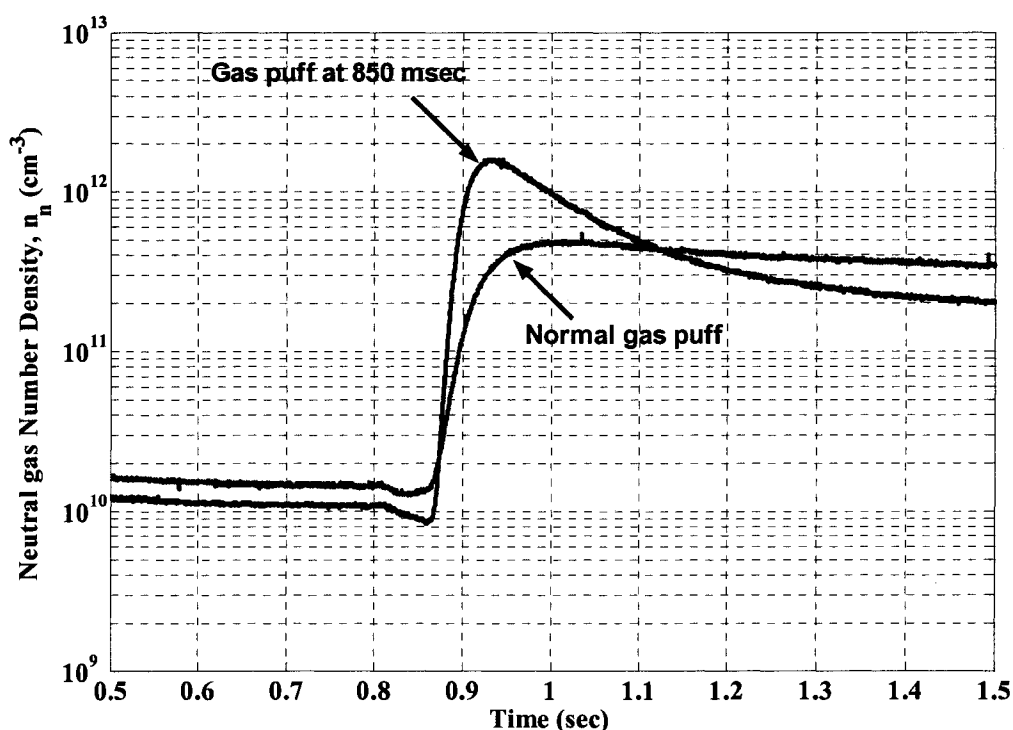
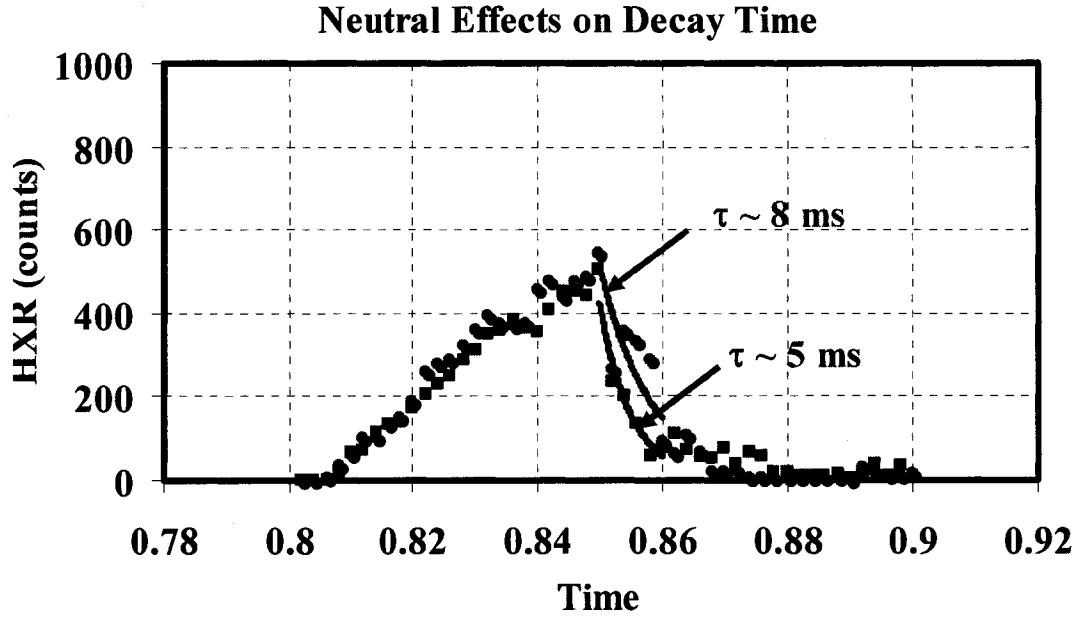


Figure 6.30: The time evolution of neutral gas density in two different gas puff shots.



**Figure 6.31: The time evolution of the hard x-ray counts at two different gas puff scenarios.**

Figure 6.30 shows that the neutral density is doubled after the gyrotron is turned off. Doubling the neutral density will double the electron-neutral collision frequency and decreases the electron-neutral collision time by half. This leads to decreasing the superthermal electron confinement time by the same factor. The confinement time calculated from the decay of the hard x-ray after the gyrotron power is turned off shows that the time is decreased by nearly a factor of half  $\sim 8$  to  $\sim 4$  msec as shown in Figure 6.31.

## 6.7 Summary

In this chapter, the guiding center drift equations were solved with a microwave heating operator included to study the effect of particle orbits on microwave heating. The

calculations show that the QHS configuration has better confinement properties than both Mirror and AntiMirror configurations. Specifically, electrons have the minimum deviation from the home flux surfaces and revisit the heating zone more frequently compared to the Mirror and AntiMirror configurations. This explains why we have higher hard x-ray photon population and energies in QHS compared to both Mirror and AntiMirror. The calculations also shows that the Mirror and the AntiMirror configurations are almost identical from the magnetic point of view (they have a phase difference of  $\pi/2$  in the mirror term) in contrast to the experimental results described in Chapter 4. However, the heating takes place at the minimum of the magnetic ripple in case of the AntiMirror and the majority of the energetic particles will leave the machine in a very short time scale due to direct loss orbits. In the Mirror configuration, the heating takes place on the top of the magnetic ripple and the particles are passing at the location of the microwave antenna, but they get lost because of the asymmetry of the magnetic ripple at different toroidal locations and have less interaction with the microwave field in the after glow phase.

The results also give an explanation of why the superthermal electrons will be lost on a time scale shorter than the electron-electron and electron-ion collision time scales. The penetration of neutrals into the HSX core caused by the low plasma density and small size of the machine is responsible for the higher electron-neutral collisionality compared to electron-electron and electron-ion collisionality for high electron energy. Modeling superthermal electron transport as a diffusion process with scale length  $\Delta x$

comparable to the drift orbit width and scale time  $\Delta t$  given by electron-neutral collision time gives a confinement time that is in good agreement with the experimentally measured confinement time from the decay of the hard x-ray after the microwave power is turned off.

- 
- <sup>1</sup> M. Wakatani et al, Nuclear Fusion, **21**, 175, (1981).
- <sup>2</sup> K. Uo and M. Nakasuga, Nuclear Fusion, **22**, 1386, (1982).
- <sup>3</sup> J. R. Cary et al, Physics of Fluids, **31**, 1586, (1988).
- <sup>4</sup> F. Chen, "Introduction to Plasma Physics and Controlled Fusion", 2<sup>nd</sup> edition, Plenum Press, (1984).
- <sup>5</sup> A. H. Boozer, Physics of Fluids, **23**(5), 904, (1980).
- <sup>6</sup> A H. Boozer, Physics of Fluids, **24**(5), 851, (1981).
- <sup>7</sup> Matlab 6.5 Release 13 help file.
- <sup>8</sup> J. R. Dormand and P. J. Prince, Journal of Computational and Applied. Mathematics **6**,19, (1980).
- <sup>9</sup> J. Canik, 44<sup>th</sup> APS-DPP meeting, November 11-15, 2002, Orlando, Florida.
- <sup>10</sup> J. Canik, 47<sup>th</sup> APS-DPP meeting, October 24-28, 2005, Denver, Colorado.
- <sup>11</sup> R. K. Janev, W.D. Langer, K. Evans, Jr., D.E. Post, Jr., "Elementary Processes in Hydrogen-Helium Plasmas", Springer-Verlag, (1987)

# Chapter 7

## Conclusion and Future Work

### 7.1 Conclusion

The HSX experiment is a novel machine with quasi-helical symmetry in the magnitude of  $\bar{B}$  which promises improved single particle confinement. The HSX stellarator has the flexibility to run under multiple magnetic configurations: quasihelical symmetry where neoclassical transport is comparable to tokamaks, and with broken symmetry where neoclassical transport properties are degraded back to the level of a conventional stellarator.

In the HSX stellarator, superthermal electrons are generated by two different processes: electron acceleration in the parallel electric field developed during the magnetic field ramp-up and ramp-down, and acceleration in the microwave electric field during the 2<sup>nd</sup> harmonic X-mode ECRH discharges. In order to study the hard x-ray emission from ECRH generated superthermal electrons, a hard x-ray spectroscopy system was built based on a CdZnTe semiconductor detector and software pulse height analysis program. Preionization using filament results in a fraction of the superthermal electrons generated during the field ramp-up phase being present during the current flat top. They absorb part of the ECRH injected power and speed up the breakdown process. These fast electrons emit hard x-rays at the same time as those generated by ECRH, making it

difficult to differentiate the origin of the hard x-ray emission during the microwave discharge.

In order to suppress the generation of runaway electrons during the magnetic field ramp-up, it was necessary to understand their generation mechanism, and determine if they have any impact on plasma formation and properties. Two techniques were tried to control and suppress the generation of runaway electrons: (1) puffing gas into the vacuum vessel to increase the collisionality and suppress the superthermal electron production process, and (2) using a UV Xenon flash lamp to control the injection time of seed electrons into the machine so that they can be injected at a small enough loop voltage that is not capable of accelerating them to high energy. The first method was excluded because of the difficulty of controlling the plasma density during the discharge if the gas puff takes place before the plasma discharge.

The ECE radiometer, diamagnetic loop, soft x-ray detectors and microwave diodes were able to detect the presence of superthermal electrons at low plasma density ( $\bar{n}_e < 5 \times 10^{11} \text{ cm}^{-3}$ ) during the ECRH discharges in the HSX stellarator. The experimental data shows substantial difference in hard x-ray emission between magnetic configurations. The results show that at low plasma density,  $\bar{n}_e \sim 2 \times 10^{11} \text{ cm}^{-3}$ , the QHS configuration has a higher energetic superthermal electron population compared to the Mirror and AntiMirror configurations. There are no hard x-rays detected in the AntiMirror configuration at all densities which is attributed to large direct loss orbits. The hard x-ray count rate is as much as two orders of magnitude higher in the QHS compared to the Mirror configuration. After the microwave power source is turned off, the

superthermal electron confinement time calculated from the exponential fit to the decay of the hard x-rays is  $\sim 7$  msec in QHS compared to  $\sim 1$  msec in the Mirror configuration.

In order to explain the experimental results and investigate whether hard x-ray differences between the configurations is attributed to wave-particle interaction differences between configurations or particle orbit differences, single particle heating was studied in the different configurations. The Lorentz equation was solved numerically with the wave electric field represented as a Gaussian beam propagating perpendicular to the external magnetic field, and the HSX magnetic field is calculated from the Biot-Savart law. The comparison between magnetic configurations from a single particle heating point of view shows that the energy gained during a single pass through the heating zone is approximately the same in different configurations.

The single particle guiding center drift orbit model shows that the difference in the hard x-ray emission between magnetic configurations is indeed caused by a difference in electron orbit topology between the configurations. The results show that, in the QHS configuration, electrons have only a small drift from the home flux surfaces whether they are passing or trapped. This results in many passes through the small heating zone with a large gain in energy. In the Mirror configuration particles launched in the heating zone gain significant energy until the large drifts move particles away from resonance. The closed orbits within the separatrix permit these particles to return to the resonance occasionally and gain a more modest energy than those with QHS. In the AntiMirror configuration, the model shows particles gain significant energy when trapped in the  $|B|$  minimum at the microwave location. These particles, however, are on direct loss orbits

and quickly leave the confinement volume without contributing to the hard x-ray flux as measured at toroidal locations away from the heating. As a result, the symmetry in the QHS leads to higher electron energy and populations compared to the cases where the symmetry is broken in Mirror and AntiMirror.

The results also show that the confinement of superthermal electrons in HSX in the absence of heating can be explained by a diffusive process where the scale length is proportional to the particle drift width and the time scale is given by the electron-neutral collision time instead of the electron-electron collision time.

## 7.2 Future Work

There are different areas that can be explored in the future, some regarding expanding the current work while others are exploring new territories. The future work will be briefly described in this section.

The guiding center drift orbit model described in Chapter 6 does not take into consideration the relativistic detuning, which shifts the resonance towards the high field side, and the electron collisionality with background electrons, ions and neutrals. The code could be modified by including an enhanced version of the heating operator calculated using the Lorentz model described in Chapter 5 that takes into account the relativistic detuning and the resonance shift toward the high field side, and the electron collisionality using Monte Carlo techniques.

The guiding center model shows that in the Mirror configuration, particles trapped far away from the microwave heating zone have small likelihood of visiting the heating

zone. One expects that this will lead to toroidal asymmetry in particle energy and as a consequence the hard x-ray emission. This can be tested by measuring the hard x-ray emission toroidally around the machine.

Calculations show that particles generated in the heating zone in front of the microwave antenna in the AntiMirror configuration are in the so called direct loss orbit. Direct loss orbits are verified experimentally using the plates experiment described in Chapter 6 by measuring the floating potential on the plates caused by direct loss electrons. Another set of experiment can be performed to verify the direct loss orbits in the AntiMirror configuration using the hard x-ray by mounting the hard x-ray detectors in the same position of the plates (top and bottom of box port C where the microwave antenna is located) and measuring the hard x-ray signal.

The current research work was performed using a single chord hard x-ray detector. The hard x-ray intensity measured was integrated along the line of sight. In order to determine the superthermal electron profile in the machine, a multiple chord hard x-ray camera could be used along with an x-ray inversion technique (such as Abel inversion) to calculate the local hard x-ray emission.

The hard x-ray emission from the ECRH plasma can be treated as a complicated convolution process of the electron distribution function with the bremsstrahlung cross section and the relative particle velocities. Using the hard x-ray emission one can get a rough estimate of the electron distribution function. The procedure is as follows: A distribution function that represents the physics being studied should be proposed. For a first guess in the case of ECRH, a two temperature Maxwellian distribution function can

be tried. The distribution function should be convoluted with the bremsstrahlung cross section and the particle relative velocities to get the hard x-ray emission, and the results could be compared to the experimental results using a curve fitting technique. The right electron distribution function is the one that has the best fit to the experimental results and contains most of the physics being studied.

Another way to estimate the superthermal electron distribution function is to solve the 5-D Fokker-Planck equation with a quasi-linear ECRH operator included. Calculating the electron distribution function from the Fokker-Planck modeling will allow the estimation of the hard x-ray emission from the plasma to compare with the experimental results. This method was tried during the current research by using the CQL3D code as Fokker-Planck solver and the GENRAY for the ray tracing calculations. The code did not give the expected results due to the high power density (during the current research phase the plasma density was low  $\bar{n}_e \sim 5 \times 10^{11}$  and the microwave power was concentrated at very small spot. This leads to very high power density) that invalidate the quasi-linear model for microwave heating. This issue will be resolved in the next research phase when HSX will run at high plasma density.

The HSX is scheduled for 1 Tesla operation upgrade early fall of 2006. The plasma production and heating will be achieved by 1<sup>st</sup> harmonic O-mode ECRH. The guiding center drift orbit model can be used to calculate the electron heating and predict whether or not hard x-ray emission will take place during the 1 Tesla operation. The Lorentz model described in Chapter 5 should be modified to include the O-mode instead of the X-mode microwave heating.

# Appendix 1

## Plasma X-ray Generation Theory

### A1.0 Introduction

The mechanisms for producing X-rays are similar to those responsible for production of other energies of electromagnetic radiation<sup>1</sup>. All depend on the acceleration of charged particles. Bremsstrahlung<sup>2,3,4</sup>, is one of the production mechanisms of x-ray, an illustration of the free-free process is shown in figure A1.1. It originates from the acceleration of electrons in coulomb collisions with other electrons and with ions and nuclei. It comes from the German words, 'brems' for braking, and 'strahlung' for radiation. The most common situation in plasma is the emission as electrons collide with nuclei due to their random thermal motions. This is called 'thermal bremsstrahlung'. Bremsstrahlung can also occur when a beam of particles decelerates on encountering an obstacle.

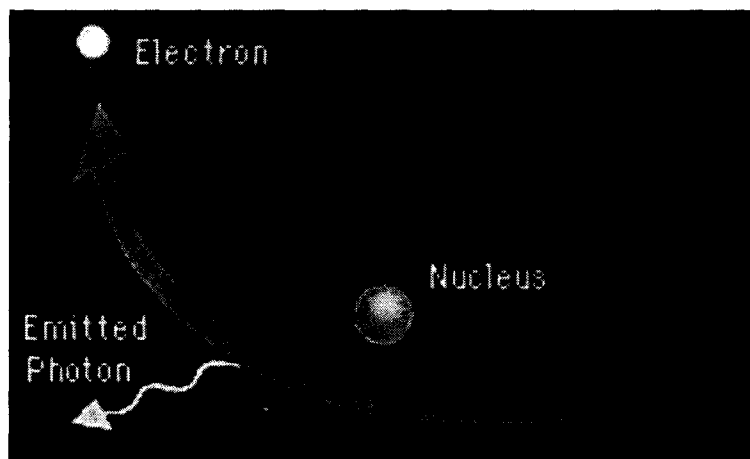


**Figure A1.1: Schematic drawing of the Bremsstrahlung process**

Thermal bremsstrahlung produces a characteristic spectrum. Each collision event can be regarded as producing a photon, and the energy of the photon corresponds approximately to the change in energy of the electron during the collision. The electrons have a distribution of energies, with the mean proportional to the temperature. The distribution of photon energies produced by bremsstrahlung reflects the electron energy distribution, and has an average which is proportional to temperature. Thus, a measurement of the bremsstrahlung spectrum can be used to determine the temperature of the electrons.

The emission of x-ray bremsstrahlung from plasmas was first observed around 1930 by Edlen and Erikson<sup>5</sup>, Ekefors<sup>6</sup> and others in high vacuum sparks. Grazing incidence spectrometers were also used to identify line spectra of highly ionized atoms. These experiments were not designed to evaluate plasma parameters such as density and temperatures. This was first attempted in 1936 by Robinson<sup>7</sup>. Much more attention has been concentrated on this subject since 1960, when several plasma devices developed for nuclear fusion research were expected to emit x-ray spectra. Hard x-rays below  $1 \text{ A}^\circ$  ( $\geq 12.41 \text{ keV}$ ) have often been observed in gas discharges<sup>8,9</sup>. In most cases they are emitted by electrodes or walls, which are bombarded by fast “runaway” electrons. In these high-power low-density discharges the x-rays result from the interaction of superthermal electrons with the walls.

X-ray emission has become an increasingly important feature from the standpoint of energy loss as well as from the diagnostic point of view. Bremsstrahlung enters Lawson's<sup>10</sup> criteria which is reason enough to monitor it carefully and to find out whether

there are stronger competing radiative processes. There are also experiments where the x-ray emission serves as a tool to diagnose various plasma parameters and properties. A well-known example is the determination of the electron temperature<sup>11,12</sup> from the slope of the x-ray continuum. Also, the ion temperature<sup>13</sup> was measured from the Doppler broadening of the x-ray impurity lines. The x-ray emission is used to diagnose the presence of impurities in the plasma and to investigate their spatial distribution and radial transport<sup>14</sup>. Finally x-rays are one of the main diagnostic tools in the investigation of the MHD fluctuations and disruptions<sup>15</sup> in tokamaks.

## **A1.1 Sources of X-ray in Plasma**

The x-ray spectrum emitted from the hot plasma consists of continuum Bremsstrahlung radiation, recombination radiation and line radiation. They will be described briefly in the following subsections

### **A1.1.1 Continuum Spectrum Source**

Bremsstrahlung and radiative recombination are the two dominant emission processes contributing to the continuum x-radiation. The former involves the scattering of a free electron by the coulomb field of an ion causing the electron to make a transition from one free state to another while emitting a photon. Photon production by the latter radiation mechanism results from the capture of a free electron into a bound state of an ion.

### A1.1.1.1 Free-Free Bremsstrahlung

The scattering of free electrons with a heavy charge center may give rise to radiation. In ionized plasma, free-free radiation comes from electrons encountering ions. The energy emitted per unit time, volume and frequency due to free-free Coulomb collision is<sup>16,17,18,19,20</sup>:

$$\frac{dW_{ff}}{dh\nu} = h\nu \sum_i \sum_z n_e n_i \int_0^\infty d\sigma_{ff}(E_c, h\nu, Z) v_e f(E_c) dE_c \quad (A1.1)$$

where,  $i$  ionic species,  $Z$  ionic charge state,  $n_e$  electron density,  $n_i$  ion density of atomic species  $i$  and charge state  $Z$ ,  $E_c$  kinetic energy of the electron,  $d\sigma_{ff}$  the free-free differential cross section (an example of cross section is shown in figure A1.2) and  $f(E_c)$  is the electron distribution function.

If the electron distribution is Maxwellian, the classical (Kramers) calculation gives energy dependence of the free-free emission as<sup>20</sup>:

$$\frac{dW_{ff}}{dh\nu} = \frac{6.4 \times 10^{-40}}{T_e^{\frac{1}{2}}} n_e \sum_i \sum_z n_i Z_{ffi}^2 \bar{g}_{ff}(T_e, E_\nu) e^{\left(-\frac{h\nu}{T_e}\right)} \quad (A1.2)$$

The units are in  $[erg\ cm^{-3}\ s^{-1}\ eV^{-1}]$ , where  $\frac{dW_{ff}}{dh\nu}$  is the power radiated per cm<sup>3</sup> and sec into the photon energy interval  $dh\nu$ ,  $Z_{ffi}$  is the ion charge relevant for free-free transitions, approximately equal to the nuclear charge,  $T_e$  is the electron temperature and  $\bar{g}_{ff}(T_e, E_\nu)$  is the temperature average Gaunt factor for free-free transitions which usually is close to one except in low- $Z$  cases.

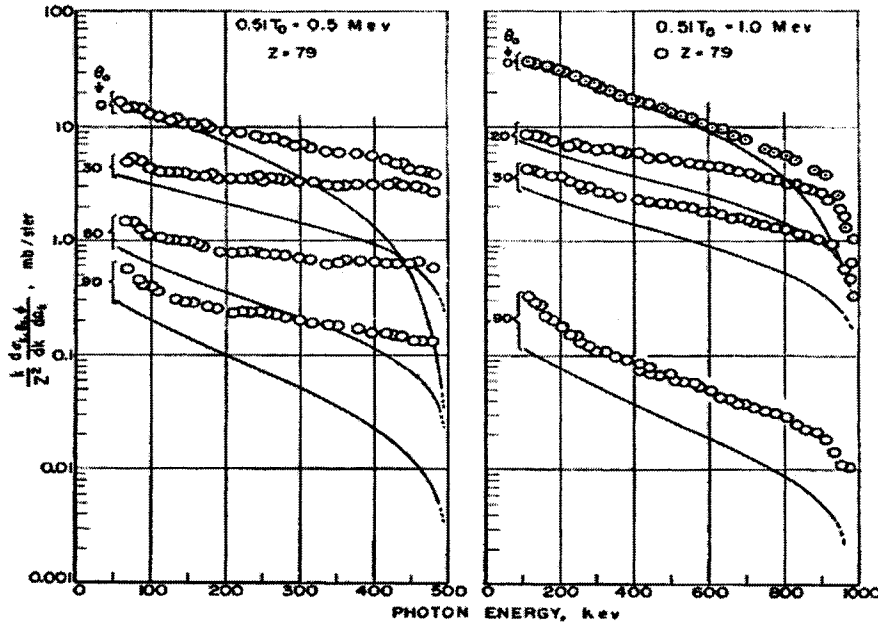


**Figure A1.2: Dependence of the Bremsstrahlung cross-section  $d\sigma$  on photon energy and angle  $\theta$  (angle between the incident electron direction and the emitted photon direction) for 0.5 and 10 MeV electrons (solid line is theory and circles are experiment)<sup>21</sup>.**

By integrating over energy we have:

$$W_{ff} = 1.53 \times 10^{-25} T_e^{\frac{1}{2}} n_e^2 Z_{eff} \bar{g}_{ff}(T_e) [\text{erg cm}^{-3} \text{s}^{-1}] \quad (\text{A1.3})$$

where,  $T_e$  is in eV,  $n_e$  is in  $\text{cm}^{-3}$ ,  $\bar{g}_{ff}(T_e)$  is the frequency integrated Gaunt factor and

$$Z_{eff} = \sum_i \sum_z \frac{n_{iz} Z^2}{n_e} \quad (\text{A1.4})$$

where  $n_{iz}$  is the ion density of atomic species  $i$  and charge state  $Z$ ,  $n_e$  is the electron density,  $Z$  is the ionic charge state. Figure A1.3 shows the Bremsstrahlung emission cones for relativistic electrons, moving from left to right<sup>22</sup>. Parameter of the curves is the energy of the emitted x-ray photons. Consider a vector from the origin to a point on one

of the curves; its length is proportional to the x-ray intensity emitted in the direction of the vector at the photon energy with the particular curve.

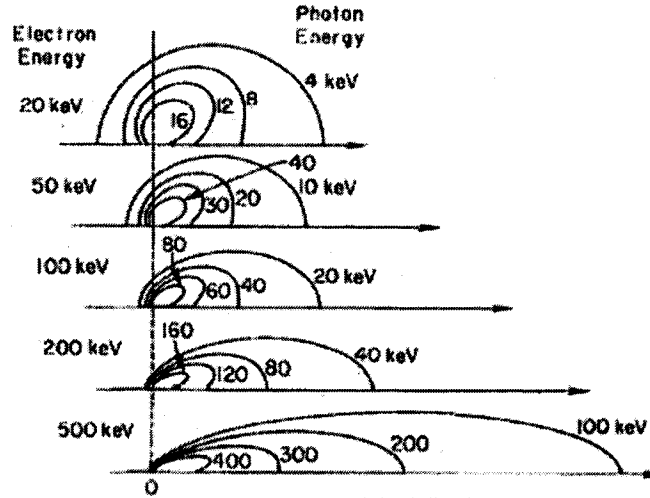


**Figure A1.3: Anisotropy of the Hard X-ray emission**

Another property of the free-free emission is that for long wavelengths ( $\lambda \gg \frac{hc}{kT_e}$ ), the spectral shape is independent of  $T_e$ . However, for short wavelengths ( $\lambda \leq \frac{hc}{kT_e}$  or  $h\nu \geq kT_e$ ) the spectrum is strongly temperature dependent and its analysis is thus especially suited to determination of the plasma electron temperature.

#### **A1.1.1.2 Free-Bound Recombination**

The capture of free electrons into a bound state of an ion, with the accompanying emission of radiation of energy  $h\nu = \frac{1}{2}mv^2 + \chi_n$ , produces a continuous spectrum of radiation for  $h\nu > \chi_n$ . The classical result for the cross section for the capture of an electron of energy  $W$  into a hydrogen like state  $n$  is  $\sigma_n(\nu) \sim 1/W(W + \chi_n)$ , and the

corresponding frequency dependence of the recombination radiation for the process  $N_{i+1}$

$+ e \rightarrow N_{i,n} + h\nu$  is<sup>23</sup>.

$$\frac{dW_{fb}}{dh\nu} = \frac{6.4 \times 10^{-40}}{T_e^{-\frac{1}{2}}} n_e n_{iz} Z^2 \sum_{n > n_{\min}} \bar{g}_{fb}(h\nu, Z, n) e^{\left(-\frac{h\nu}{T_e}\right)} \left( \frac{2}{3} \frac{Z^2 \chi_H}{T_e} e^{Z^2 \chi_H / n^2 T_e} \right) \quad [\text{erg cm}^{-3} \text{sec}^{-1} \text{eV}^{-1}] \quad (\text{A1.5})$$

where  $\bar{g}_{fb}$  the free-bound Gaunt factor and  $\chi_H$  the ionization potential of Hydrogen. If there are impurity ions in the plasma, the last equation must be multiplied by an enhancement factor (to account for the enhancement of the recombination radiation over the hydrogen bremsstrahlung) of the form<sup>24</sup>:

$$\xi = \frac{f_z Z^4 \chi_{n,\infty}}{kT_e} \quad (\text{A1.6})$$

where  $f_z$  is the impurity ions fraction in the charge-state  $Z$ . The impurity contribution is neglected compared to bremsstrahlung continuum at high energy (50 KeV – 800 KeV).

### A1.1.2 Line Emission Sources

Line radiation is the third important radiation mechanism occurring in the hot plasma. At photon energies greater than 1.5 keV, K, L, and M shell emission from high-Z impurities is predominant. Calculations of the excitation cross-sections for specific ionic charge states are quite complex. The power radiated during an instantaneous radiative decay of an ion in a charge state  $Z$  to all the  $N$  possible levels is<sup>25</sup>:

$$P_{line} = n_e n_{ion} f_z \sum_{n=0} Q_n \Delta E_n \quad (A1.7)$$

where  $f_z$  is the fraction of impurity ions in charge state  $z$ ,  $\Delta E_n$  are all the possible transitions and  $Q_n$  are the excitation rate coefficients. At high electron energies, bremsstrahlung radiation is dominant and the line radiation contribution can be neglected.

- 
- <sup>1</sup> A. Compton, "X-rays and Electrons, an Outline of Recent X-ray Theory", Macmillan and Co., (1927).
  - <sup>2</sup> J. D. Jackson, "Classical Electrodynamics", John Wiley & Sons, 3<sup>rd</sup> edition (1999).
  - <sup>3</sup> G. Bekefi, "Radiation Processes in Plasmas", John Wiley & Sons (1966).
  - <sup>4</sup> I. H. Hutchinson, "Principles of the Plasma Diagnostics" 2<sup>nd</sup> edition (2002).
  - <sup>5</sup> B. Edlen and A. Erikson, *Nature*, **125**, 233, (1930).
  - <sup>6</sup> E. Ekefors, *Z. Physik*, **31**, 737, (1930).
  - <sup>7</sup> H. A. Robinson, *Z. Physik*, **100**, 636, (1936).
  - <sup>8</sup> S. V. Lebedev, et al, *Soviet Physics JETP*, **37**, 248, (1960).
  - <sup>9</sup> R. Chodura, and M. Keilhacker, *Z. Naturforsch*, **17(a)**, 977, (1977).
  - <sup>10</sup> J. D. Lawson, *Proceedings of Royal Society*, **B70**, 6, (1957).
  - <sup>11</sup> D. A. Schaeglov, *Soviet Physics JETP Letters*, **6**, 365, (1967).
  - <sup>12</sup> S. Von Goeler, et al, *Nuclear Fusion*, **15**, 301, (1975).
  - <sup>13</sup> M. Bitter, et al, *Bull APS*, **23**, 698, 1978 and Princeton report PPPL-TM 321 paper 10, (1978).
  - <sup>14</sup> V. A. Vershkov, and S. V. Mirnov, *Proceedings of 5<sup>th</sup> European Conference on Controlled Fusion and Plasma Physics, Grenoble*, **vol I**, 1, (1972).
  - <sup>15</sup> S. Von Goeler, et al, *Physical Review Letters*, **33**, 1201, (1974).
  - <sup>16</sup> T. F. Straton, in *Plasma Diagnostic Techniques* (Huddleston, Leonard, eds.) Academic press, New York (1965).
  - <sup>17</sup> P. Bogen, "X-ray Diagnostics of Plasmas", in *Plasma Diagnostics* (W. Locher-Holtgreven) AIP (1995).
  - <sup>18</sup> S. Von Goeler, "Soft X-ray Measurements", in *Diagnostics for Fusion Experiments*, Pergamon Press, (1979).

- 
- <sup>19</sup> H. Knoepfel, "Hard x-ray Measurements", in *Diagnostics for Fusion Experiments*, Pergamon press, (1979).
- <sup>20</sup> H. Huchinson, "Principles of Plasma Diagnostics", Cambridge University Press, Cambridge, UK, (2003).
- <sup>21</sup> H. W. Koch and J. W. Motz, *Review of Modern Physics*, **31**(4), 920, (1959).
- <sup>22</sup> S. Von Goeler, et al, *Physics of Plasmas*, **2**(1), 205, (1995).
- <sup>23</sup> G. A. Chartas, "Manifestations of the MHD and Kinetic Dynamo through Soft X-rays", PhD thesis, University of Wisconsin, Madison, (1991).
- <sup>24</sup> R.W. P. McWhirter and H. P. Summers, "Applied Atomic Collision Physics Vol 2 Plasmas", Academic Press Inc, (1984).
- <sup>25</sup> P. G. Carolan and V. A. Piotrowicz, *Plasma Physics* **25**, 1065, (1983).

## Appendix 2

# Pulse Height Analysis Program

### A2.0 Introduction

In order to analyze the raw hard x-ray signal emitted during ECRH discharges in HSX and extract useful information regarding photon energy and intensity, a pulse height analysis technique should be used. A software based pulse height program is used instead of the conventional hardware one. The pulse height analysis program shown in Figure A2.1 is written in IDL language<sup>1</sup>. A program listing and a detailed description of the program functionality will be described in this appendix.

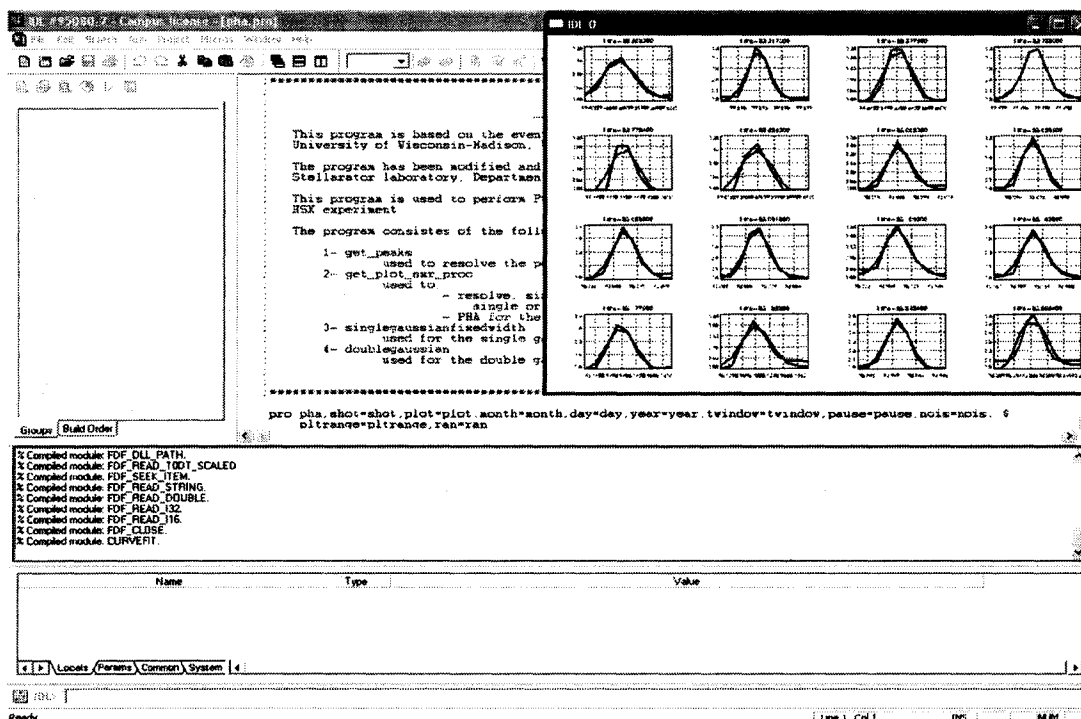


Figure A2.1: The Pulse Height Analysis Code running in plot mode 4.

## A2.1 The Pulse Height Analysis Program

The Pulse Height Analysis program is written by Dr. R. O'Connell<sup>2</sup> from the MST group at the University of Wisconsin Madison. The program was modified to fit our needs at HSX. The raw signal is sent through a shaping amplifier, which produces Gaussian pulses with amplitude proportional to the x-ray energy as shown in figure A2.2.

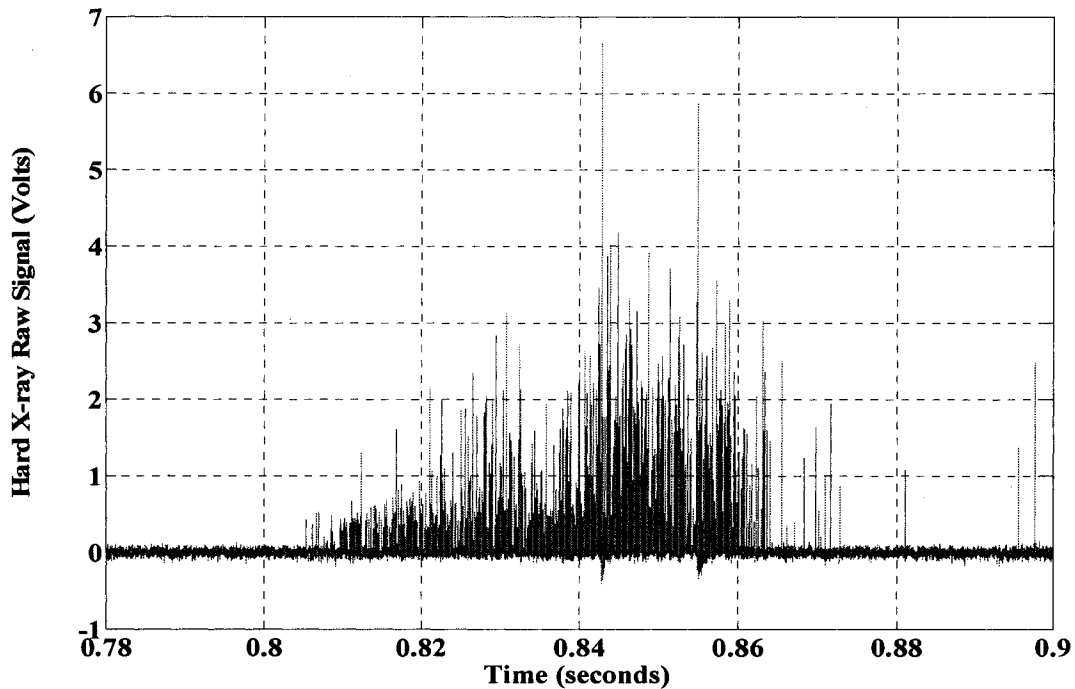
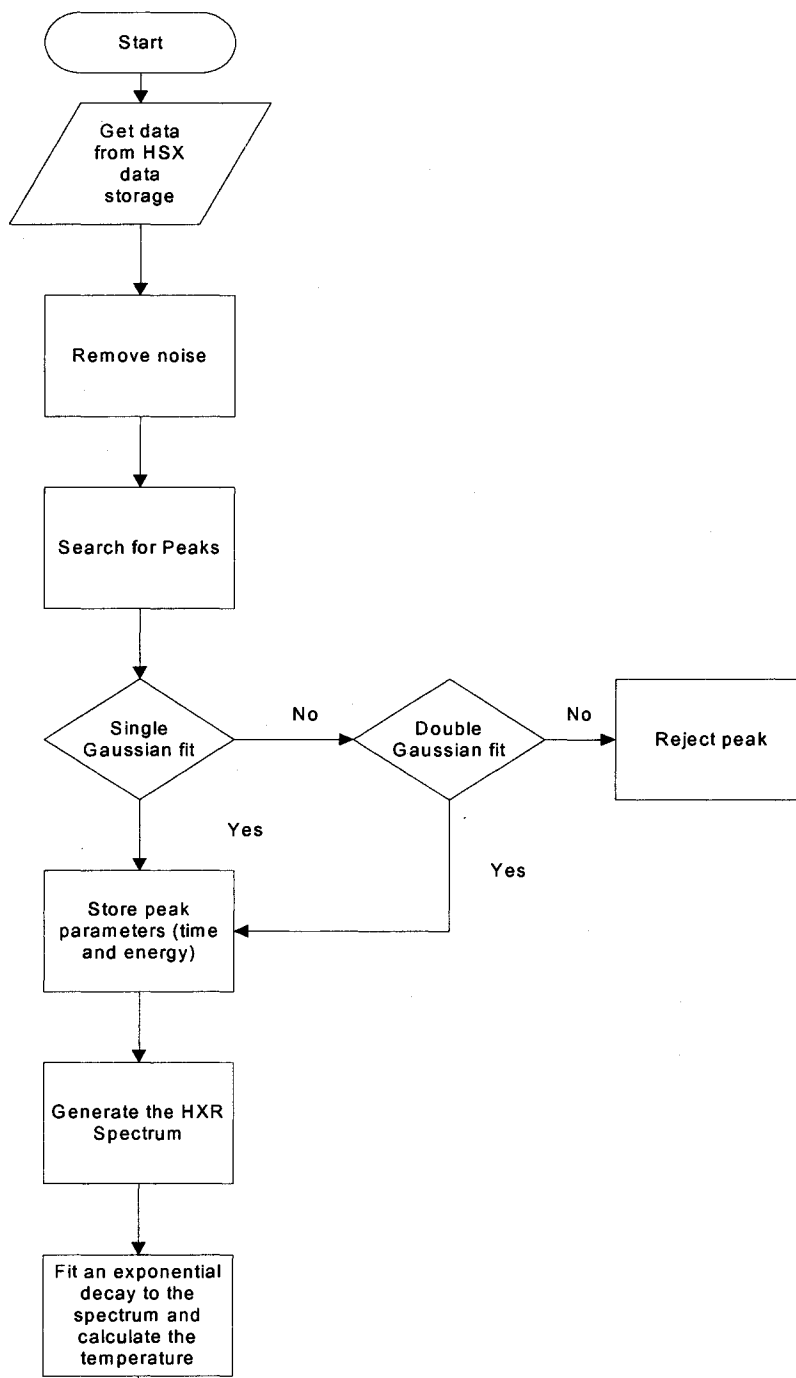


Figure A2.2: Raw hard x-ray signal during the plasma.

### A2.1.1 How the Program Works?

In Conventional hardware-based PHA, the signals at this stage are sent to a pulse height analyzer with predefined energy bins, and the x-ray pulses falling within a given bin are then counted using a scalar counter. The HSX hard x-ray diagnostic uses direct digitization of the signal, which allows for more sophisticated software techniques to analyze the data after the discharge. This gives improved pile-up and noise handling since

more information than just the pulse height is recorded. It also allows more flexible time and energy binning of x-ray events. Figure A2.3 shows the program flow chart.



**Figure A2.3 The Pulse Height Analysis (PHA) Program flow chart.**

The PHA program performs the following tasks:

- 1- Each pulse consists of many data points as shown in figure A2.4.
- 2- A data point is accepted as a real signal if it is above a noise level. Figure A2.5 shows the noise level in red.
- 3- A collection of data points are fitted into Gaussian shape using the known half width of the pulse as shown in figure A2.6
- 4- This leaves three fitting parameters: the time stamp, the amplitude and the base line shift.
- 5- Any fits with too high  $\chi^2$  are then fitted with a double Gaussian.
- 6- Events with still too high  $\chi^2$  are disregarded as either unsalvageable pile-up events or random noise.
- 7- The fraction of events flagged as double Gaussian or pile-up is monitored and can be set according to the balance of higher bandwidth vs. pile-up fraction.
- 8- At the end of the fitting procedure the hard x-ray intensity is stored as an array of precisely timed x-ray events.
- 9- The data can be histogrammed as shown in figure A2.7 in any convenient manner and correlation analysis with other plasma diagnostics is a possibility
- 10- Finally the hard x-ray spectrum shown in figure A2.7 is produced and an exponential fit is performed to obtain an estimate of the superthermal electron temperature (shown in figure 2.8) under the assumption of Maxwellian distribution

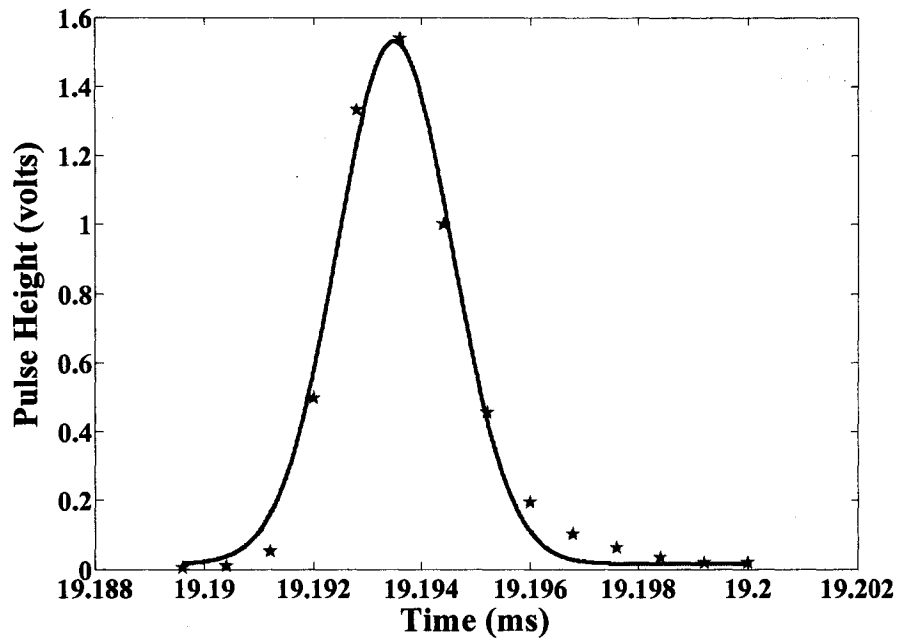


Figure A2.4: Raw hard x-ray single pulse with Gaussian fitting.

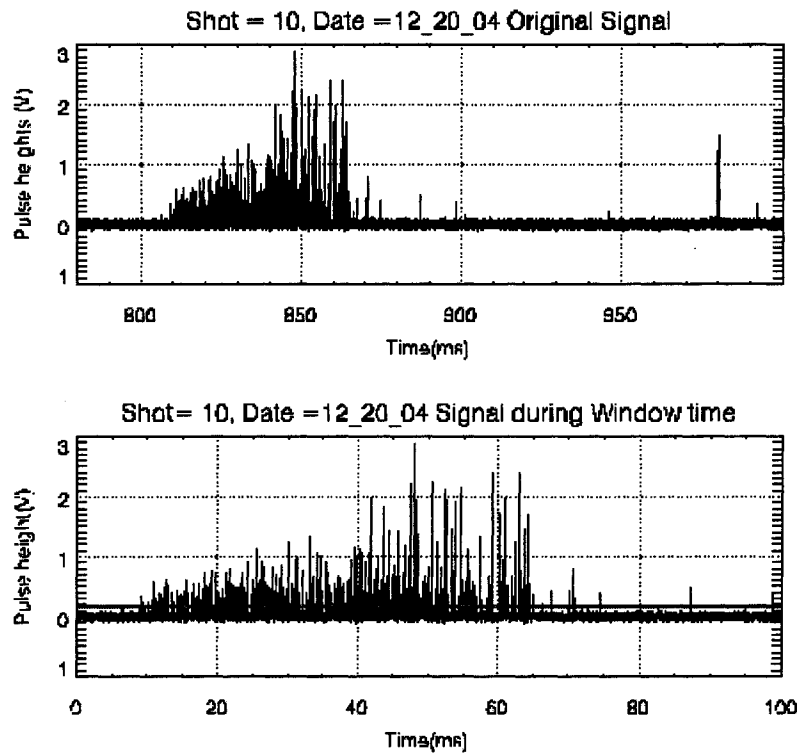
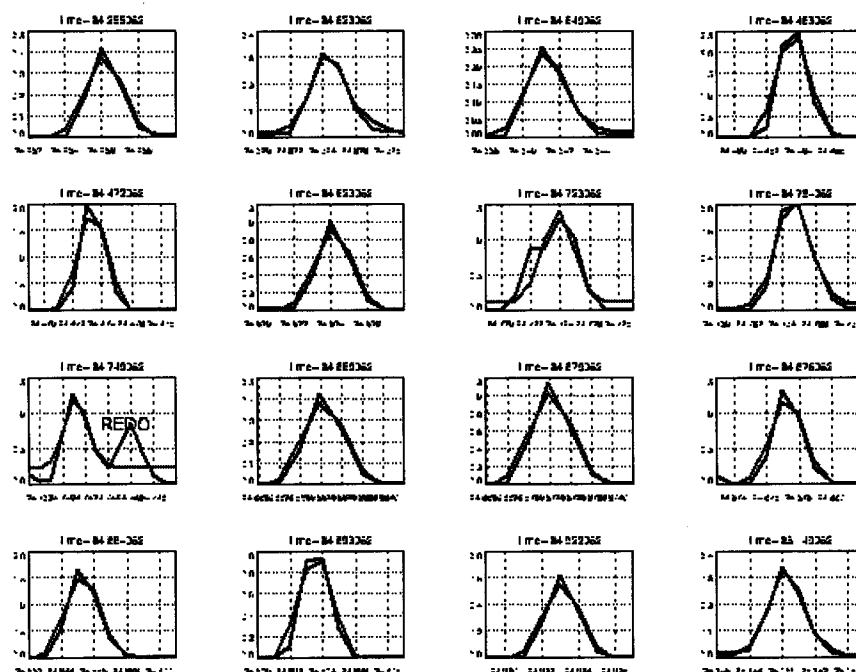
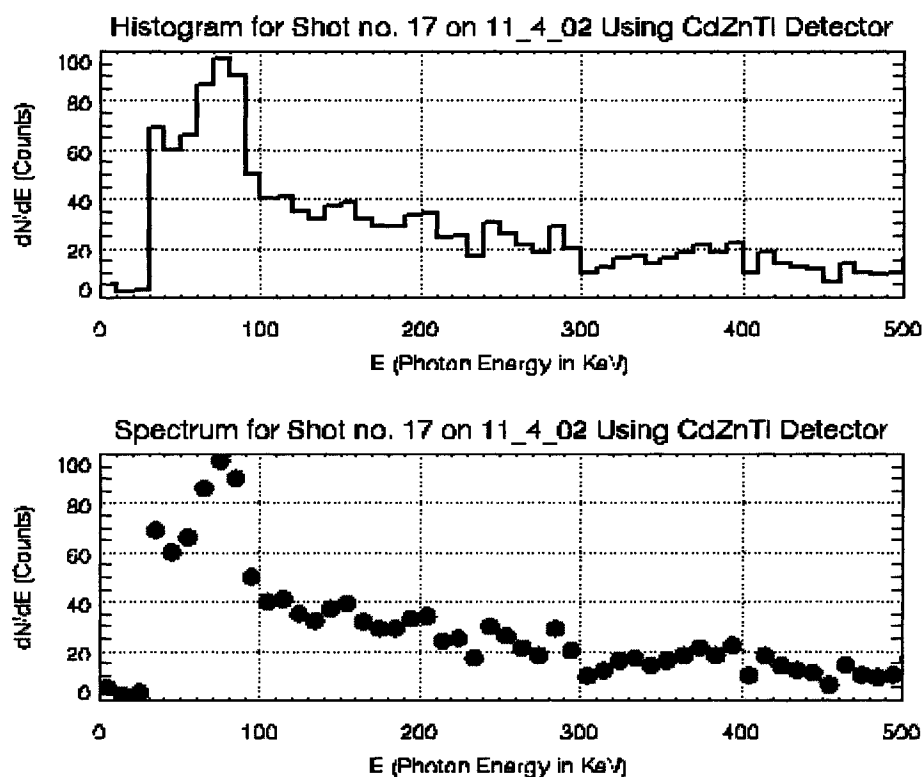


Figure A2.5: Hard x-ray signal and noise level in red. Time window 0-100 msec corresponds to 800-900 msec.



**Figure A2.6: Fitting the individual pulses to a single Gaussian.**  
**REDO: fails to fit single Gaussian and double Gaussian will be tried instead.**



**Figure A2.7 Hard X-ray histogram and spectrum.**

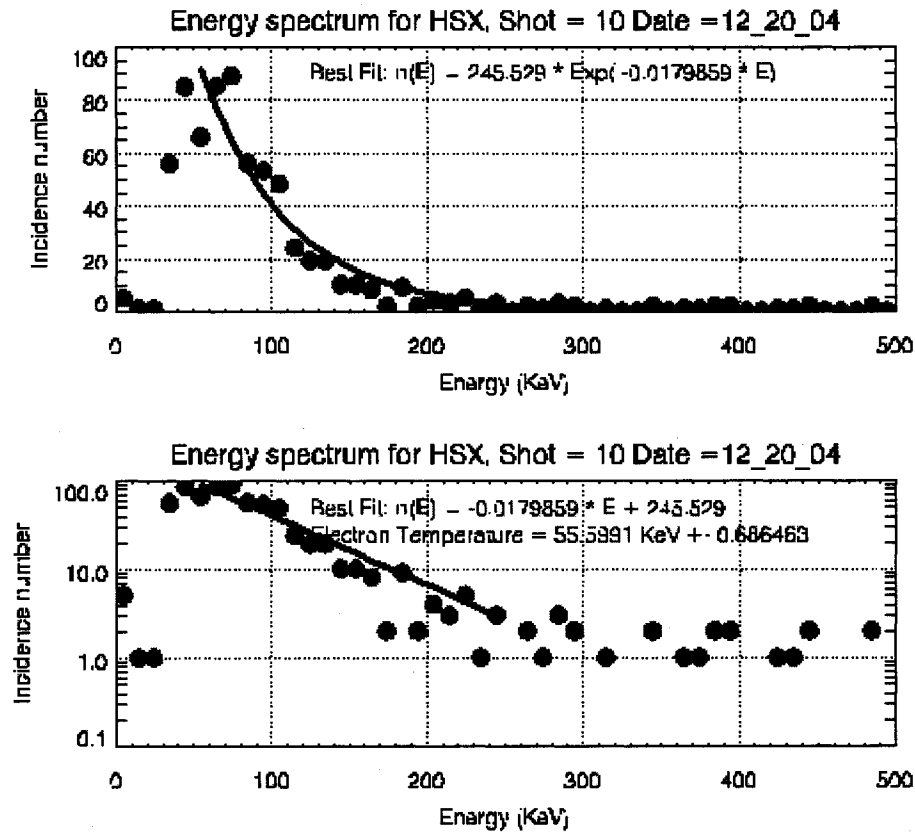


Figure A2.8: Curve fitting to calculate the electron temperature.

## A2.2 Program Input and Output

### A2.2.1 Program Input

The program accepts command line inputs as follows:

**pha**,**day**=*numeric*,**month**=*numeric*,**year**=*numeric*,**shot**=*numeric*,**twindow**=[*minimum*,*maximum*],**plot**=*numeric*,**pause**=*numeric*,**nois**=*numeric*,**pltrange**=[*minimum*,*maximum*],**range**=[*minimum*,*maximum*]

Where:

PHA: The program name.

Day: An integer number for the run day.

- Month:** An integer number for run month.
- Year:** An integer number for the run year.
- Shot:** An integer number for shot number, or the user can use the function `numrange(minimum,maximum)` to define a range of shots between minimum and maximum. A combination of both integers and the `numrange` function can be used.
- Twindow:** A real pair of numbers representing the minimum and the maximum of the time window for analyzing the hard x-ray.
- Plot:** An integer number represent the output format ranges from 0 to 4 as follows:
- 0 - Only the raw signal will be shown in the time window selected and the noise level. A sample output is shown in figure A2.5.
  - 1- The Gaussian curve fitting for individual pulses will be shown in the output as shown in figure A2.6
  - 2- The histogram and the spectrum of the hard x-ray signal for the input shot or range of shots are plotted as shown in figure A2.7.
  - 3- Superthermal electron temperature is estimated from the exponential curve fitting of the hard x-ray spectrum as shown in figure A2.8
- The spectrum of hard x-ray energy flux is plotted.
- Pause:** A integer that takes either 0 or 1 and used only with `plot = 1`. If `pause = 0`,

no pausing between individual pulse Gaussian fitting if `pause=1`, the program pauses for seconds to let the user check the quality of fitting.

**Noise:** A real input that represents the noise level in volts, usually its between 0.1-0.2 volts.

**Pltrange:** A real pair of numbers representing the minimum and the maximum of the plotting range of the hard x-ray spectrum in keV.

**Ran:** A real pair of numbers representing the minimum and the maximum of the temperature curve fitting range of the hard x-ray spectrum in keV.

A sample input case is given below:

```
pha,day=20,month=12,year=04,shot=[10,15,numrange(20,30)],twindow=[0,100],plot=  
1,pause=1,nois=0.15,pltrange=[0,500],ran=[50,250]
```

### **A2.2.2 Program Output**

The program produces two output files, a simple file that contains only the hard x-ray spectrum for easy handling and it has the format `month_day_year_shot.spectrum` and a detailed output and it is given the name `month_day_year_shot`. A list of both outputs is given below.

#### **A2.2.2.1 Simple Output**

5.00	0
15.00	0
25.00	0
35.00	1
45.00	0
55.00	0
65.00	0
75.00	0
85.00	0

95.00	0
105.00	0
115.00	0
125.00	0
135.00	0
145.00	0
155.00	0
165.00	0
175.00	0
185.00	0
195.00	0
205.00	0
215.00	0
225.00	0
235.00	0
245.00	0
255.00	0
265.00	0
275.00	0
285.00	0
295.00	0
305.00	0
315.00	0
325.00	0
335.00	0
345.00	0
355.00	0
365.00	0
375.00	0
385.00	0
395.00	0
405.00	0
415.00	0
425.00	0
435.00	0
445.00	0
455.00	0
465.00	0
475.00	0
485.00	0
495.00	0
505.00	0
515.00	0
525.00	0
535.00	0
545.00	0
555.00	0
565.00	0
575.00	0
585.00	0
595.00	0
605.00	0

615.00	0
625.00	0
635.00	0
645.00	0
655.00	0
665.00	0
675.00	0
685.00	0
695.00	0
705.00	0
715.00	0
725.00	0
735.00	0
745.00	0
755.00	0
765.00	0
775.00	0
785.00	0
795.00	0
805.00	0
815.00	0
825.00	0
835.00	0
845.00	0
855.00	0
865.00	0
875.00	0
885.00	0
895.00	0
905.00	0
915.00	0
925.00	0
935.00	0
945.00	0
955.00	0
965.00	0
975.00	0
985.00	0
995.00	0
1005.00	0
1015.00	0
1025.00	0
1035.00	0
1045.00	0
1055.00	0
1065.00	0
1075.00	0
1085.00	0
1095.00	0
1105.00	0
1115.00	0
1125.00	0

1135.00	0
1145.00	0
1155.00	0
1165.00	0
1175.00	0
1185.00	0
1195.00	0
1205.00	0
1215.00	0
1225.00	0
1235.00	0
1245.00	0
1255.00	0
1265.00	0
1275.00	0
1285.00	0
1295.00	0
1305.00	0
1315.00	0
1325.00	0
1335.00	0
1345.00	0
1355.00	0
1365.00	0
1375.00	0
1385.00	0
1395.00	0
1405.00	0
1415.00	0
1425.00	0
1435.00	0
1445.00	0
1455.00	0
1465.00	0
1475.00	0
1485.00	0
1495.00	0
1505.00	0
1515.00	0
1525.00	0
1535.00	0
1545.00	0
1555.00	0
1565.00	0
1575.00	0
1585.00	0
1595.00	0
1605.00	0
1615.00	0
1625.00	0
1635.00	0
1645.00	0

1655.00	0
1665.00	0
1675.00	0
1685.00	0
1695.00	0
1705.00	0
1715.00	0
1725.00	0
1735.00	0
1745.00	0
1755.00	0
1765.00	0
1775.00	0
1785.00	0
1795.00	0
1805.00	0
1815.00	0
1825.00	0
1835.00	0
1845.00	0
1855.00	0
1865.00	0
1875.00	0
1885.00	0
1895.00	0
1905.00	0
1915.00	0
1925.00	0
1935.00	0
1945.00	0
1955.00	0
1965.00	0
1975.00	0
1985.00	0
1995.00	0

#### A2.2.2.2 Detailed Output

---



---

PROGRAM Calibration VER 1.0  
 BY  
 ALI E. ABDOU,  
 UNIVERSITY OF WISCONSIN, MADISON,  
 DEPARTMENT OF ELECTRICAL AND COMPUTER ENGINEERING,  
 HELICALY SYMMETRIC EXPERIMENT (HSX) STELLARATOR LABORATORY,  
 ENGINEERING HALL, 1415 ENGINEERING DRIVE, MADISON, WI 53706,  
 USA  
 Tel: 608-265-3582  
 E-mail: abdou@cae.wisc.edu

---



---

THIS CASE IS RUNNING FOR:  
 -----

date = 1/24/05  
 Shot number = 7  
 Noise Level = 0.150 volt  
 Number of pulses = 1

Table 1: Individual Pulse Time and Height

i	pulse_time	t_left	t_right	Pulse Height
1	75.736000	75.735199	75.736801	0.180664

Table 2: Results from sigle Gaussian fitting routine

The Gaussian has the form  $F(x) = a[0]*EXP[(x-a[1])^2/w^2]+a[2]$

i	DgFred	Pulse_E	Pulse_t	a[0]	a[1]	a[2]	Chisq	RrdChisq	Status
1	6	0.1806641	75.7360001	0.108519	-0.000002	-0.002616	0.000194	0.001831	OK

Table 3: Results from double Gaussian fitting routine

The Gaussian has the form  $F(x) = a[0]*EXP[(x-a[1])^2/w^2]+a[2]*EXP[(x-a[3])^2/w^2]+a[4]$

i	DgFred	Pulse_E	Pulse_t	a[0]	a[1]	a[2]	a[3]	a[4]	Chisq	RrdChisq	Status
---	--------	---------	---------	------	------	------	------	------	-------	----------	--------

Table 4: Pulse Spectrum

bin#	Energy	Number of Photons
0	5.00	0
1	15.00	0
2	25.00	0
3	35.00	1
4	45.00	0
5	55.00	0
6	65.00	0
7	75.00	0
8	85.00	0
9	95.00	0
10	105.00	0
11	115.00	0
12	125.00	0
13	135.00	0
14	145.00	0
15	155.00	0
16	165.00	0
17	175.00	0
18	185.00	0
19	195.00	0
20	205.00	0
21	215.00	0
22	225.00	0
23	235.00	0
24	245.00	0

25	255.00	0
26	265.00	0
27	275.00	0
28	285.00	0
29	295.00	0
30	305.00	0
31	315.00	0
32	325.00	0
33	335.00	0
34	345.00	0
35	355.00	0
36	365.00	0
37	375.00	0
38	385.00	0
39	395.00	0
40	405.00	0
41	415.00	0
42	425.00	0
43	435.00	0
44	445.00	0
45	455.00	0
46	465.00	0
47	475.00	0
48	485.00	0
49	495.00	0
50	505.00	0
51	515.00	0
52	525.00	0
53	535.00	0
54	545.00	0
55	555.00	0
56	565.00	0
57	575.00	0
58	585.00	0
59	595.00	0
60	605.00	0
61	615.00	0
62	625.00	0
63	635.00	0
64	645.00	0
65	655.00	0
66	665.00	0
67	675.00	0
68	685.00	0
69	695.00	0
70	705.00	0
71	715.00	0
72	725.00	0
73	735.00	0
74	745.00	0
75	755.00	0
76	765.00	0

77	775.00	0
78	785.00	0
79	795.00	0
80	805.00	0
81	815.00	0
82	825.00	0
83	835.00	0
84	845.00	0
85	855.00	0
86	865.00	0
87	875.00	0
88	885.00	0
89	895.00	0
90	905.00	0
91	915.00	0
92	925.00	0
93	935.00	0
94	945.00	0
95	955.00	0
96	965.00	0
97	975.00	0
98	985.00	0
99	995.00	0
100	1005.00	0
101	1015.00	0
102	1025.00	0
103	1035.00	0
104	1045.00	0
105	1055.00	0
106	1065.00	0
107	1075.00	0
108	1085.00	0
109	1095.00	0
110	1105.00	0
111	1115.00	0
112	1125.00	0
113	1135.00	0
114	1145.00	0
115	1155.00	0
116	1165.00	0
117	1175.00	0
118	1185.00	0
119	1195.00	0
120	1205.00	0
121	1215.00	0
122	1225.00	0
123	1235.00	0
124	1245.00	0
125	1255.00	0
126	1265.00	0
127	1275.00	0
128	1285.00	0

129	1295.00	0
130	1305.00	0
131	1315.00	0
132	1325.00	0
133	1335.00	0
134	1345.00	0
135	1355.00	0
136	1365.00	0
137	1375.00	0
138	1385.00	0
139	1395.00	0
140	1405.00	0
141	1415.00	0
142	1425.00	0
143	1435.00	0
144	1445.00	0
145	1455.00	0
146	1465.00	0
147	1475.00	0
148	1485.00	0
149	1495.00	0
150	1505.00	0
151	1515.00	0
152	1525.00	0
153	1535.00	0
154	1545.00	0
155	1555.00	0
156	1565.00	0
157	1575.00	0
158	1585.00	0
159	1595.00	0
160	1605.00	0
161	1615.00	0
162	1625.00	0
163	1635.00	0
164	1645.00	0
165	1655.00	0
166	1665.00	0
167	1675.00	0
168	1685.00	0
169	1695.00	0
170	1705.00	0
171	1715.00	0
172	1725.00	0
173	1735.00	0
174	1745.00	0
175	1755.00	0
176	1765.00	0
177	1775.00	0
178	1785.00	0
179	1795.00	0
180	1805.00	0

181	1815.00	0
182	1825.00	0
183	1835.00	0
184	1845.00	0
185	1855.00	0
186	1865.00	0
187	1875.00	0
188	1885.00	0
189	1895.00	0
190	1905.00	0
191	1915.00	0
192	1925.00	0
193	1935.00	0
194	1945.00	0
195	1955.00	0
196	1965.00	0
197	1975.00	0
198	1985.00	0
199	1995.00	0

---

#### \* Statistics

---

Bin Size	= 0.050	Vol
Time Window	= 5.0	mSec
Maximum Energy	= 35.00	KeV
Average Energy	= 35.00	KeV
Detector Area	= 1.0	(10 mm x 10 mm) cm <sup>2</sup>
Detector Solid Angle	= 2.23E-003	SRadian
Total Number of pulses is	= 1	
Total Number of accepted pulses is	= 1	
Total Number of pile up pulses is	= 0	
Total Number of regicted pile up pulses is	= 0	
Percentage of accepted pulses	= *****	%
Percentage of pile up pulses	= 0.00	%
Percentage of regicted pile up pulses	= 0.00	%

## A2.3 Program Listing

### A2.3.1 The Main PHA Program

```

*****
;
;               Program Pulse Height Analysis (PHA)
;
;               _____
;
;This program is based on the event_proc program, Written by R. O'Connell, MST group,
;Department of Physics, University of Wisconsin-Madison, USA.
;

```

```

;The program has been modified and updated by, Ali E. Abdou, of the Helically
;Symmetric eXperiment (HSX), Stellarator laboratory, Department of ECE, University of
;Wisconsin-Madison
;
;This program is used to perform Pulse Height Analysis (PHA) of the Hard X-ray (HXR)
;signals generated in the HSX experiment
;
;The program consists of the following functions
;
; 1- get_peaks: used to resolve the peaks in the HXR signal
; 2- get_plot_sxr_proc: used to resolve, single and pile up pulses and fit a single or double
;Gaussian to it
;- PHA for the signal
; 3- singlegaussianfixedwidth: used for the single gaussian fixed width curve fitting
;4- doublegaussian: used for the double gaussian curve fitting
;
;*****
pro
pha,shot=shot,plot=plot,month=month,day=day,year=year,twindow=twindow,pause=pau
se,nois=nois, pltrange=pltrange,ran=ran
;-----
; Setting the output device, and calling the function get_plot_sxr_proc
;-----

forward_function get_plot_sxr_proc
set_plot,'win'
!P.BACKGROUND = 255+256L*(255+256L*255)
!P.COLOR = 0
!P.FONT = 1
DEVICE, SET_FONT = 'TIMES*BOLD*28'

if not keyword_set(twindow) then twindow=[0,100]
if not keyword_set(pause) then pause =0
if not keyword_set(nois) then nois = 0

err=get_plot_sxr_proc(shot=shot,twindow=twindow,plot=plot,month=month,day=day,year=year,pause=pause,nois=nois,pltrange=pltrange,ran=ran)
;-----
; End of main program event_proc
;-----

```

END

```

*****
;
; Function get_peaks
*****
function
get_peaks,t_left,t_right,hxr,t,t_xrays,twindow=twindow,noiselevel,outfile,f2,nopulse
;-----
; Reading data that lies in the window (twindow[0] -> twindow[1])
;-----

ind=where(t gt twindow[0] and t lt twindow[1])
num=n_elements(ind)
hxr2=hxr[ind]
nopulse =0
;-----
; getting data above the noise level
;-----
abovenoise=where(hxr2 gt noiselevel)
belownoise=where(hxr2 lt noiselevel)
hxr2[belownoise] = 0.0

if (abovenoise)(0) eq -1 then begin
printf,f2,FORMAT=(2x,A29,2x,F7.4,2x,A20)',No pulse above noise level
if',noiselevel,'volts, no data found'
    pulse_time=[0]
    energy_peak=[0]
    nopulse = 1
    return,0
endif

;-----
; Setting the borders for pulse search
;-----

if nopulse eq 0 then begin
    dummy=intarr(num)
    dummy[abovenoise]=1

    if dummy[num-1] eq 1 then dummy[num-1] = 0

    trigb=where(dummy-shift(dummy,1) gt 0)
    triga=where(dummy-shift(dummy,1) lt 0)

```

```

if      n_elements(trigb) eq 1 and n_elements(triga) eq 1 then begin
  if      trigb eq -1 and triga eq -1      then begin
    nopulse = 1
    return,0
  endif
endif

nev=n_elements(trigb)

t_left = fltarr(nev)
t_right= fltarr(nev)

printf,f2,FORMAT = '(x,A20,2x,I4)', 'Number of pulses  =',nev
printf,f2,"
energy_peak=fltarr(nev)
pulse_time=fltarr(nev)
printf,f2,FORMAT = '(x,A45)', 'Table 1: Individual Pulse Time and
Height'

printf,f2,FORMAT = '(A55)', '=====
printf,f2,FORMAT = '(3x,A51)', 'i  pulse_time  t_left   t_right Pulse Height'
printf,f2,FORMAT = '(A55)', '=====

;-----
; Searching for the peaks
;-----

for i=0,nev-1 do begin
  energy_peak[i]=      max(hxr2[trigb[i]:triga[i]],G)
  pp              =      trigb[i] + G
  pulse_time[i]  =      t[ind[pp]]
  t_left[i]      =      t[ind[trigb[i]]]
  t_right[i]     =      t[ind[triga[i]]]
  printf,f2,FORMAT =
  '(x,I3,2x,4(F10.6,2x))',(i+1),pulse_time[i],t_left[i],t_right[i],energy_peak[i]
endfor
t_xrays=pulse_time
return,energy_peak
printf,f2,FORMAT = '(A55)', '=====
printf,f2,"
endif
;-----

```

```

; End of function get_event
;-----
end

.*****
;
; Function get_plot_sxr_proc
.*****
function
get_plot_sxr_proc,shot=shot,twindow=twindow,plot=plot,month=month,day=day,year=y
ear,pause=pause,$
nois=nois,pltrange=pltrange,ran=ran
forward_function curvefit
;-----
; Constant definition
;-----
!P.MULTI=[0,1,2]
!x.style=1
!X.GRIDSTYLE = 1
!Y.GRIDSTYLE = 1
PLOTSYM, 0,1.2,color=250,fill=2
!P.FONT = 1
DEVICE, SET_FONT = 'TIMES*BOLD*20',/TT_FONT

ms=1000.0
noiselevel = nois
cal = [200,0.0]
;cal = [198.68,0.396]

;-----
; Constants used in calculation
;-----

maxv = 10
binsize = 0.05
noiselevel_1 = 0.0
time_ = (twindow[1]-twindow[0])/1e3 ; sec
area = 1.0 ;10mmx10mm=1cm^2
solangle = 0.00223; steradians

NumOfBins = (findgen((maxv-noiselevel_1)/binsize)*binsize+noiselevel_1)
n_shots_histogram = intarr(n_elements(NumOfBins))
Number_of_Shots = n_elements(shot)
month_ = string(month)

```

```

day_          = string(day)
year_         = string(year)
date_         = strcompress(month_+'_'+day_+'_'+0+year_,/rem)
shot_range    = string(shot(0))+ ' to '+string(shot(Number_of_Shots-1))
print,"
print,'#####'
print,'##### Hard X-ray Spectrum construction for #####'
print,'## + Date = ',date_
print,'## + Number_of_Shots = ',Number_of_Shots
print,'## + Shot Numbers = ',shot
print,'## + Binsize = ',binsize
print,'## + Noise Level = ',noiselevel
print,'## + Time Window = ',time_*1000, ' mSec. t1 =',twindow[0]+800,' and t2
=' ,twindow[1]+800
total_number_of_counts = intarr(Number_of_Shots)
standard_deviation    = intarr(Number_of_Shots)
for NS=0,Number_of_Shots-1 do begin
print,'/////////////////////////////////////'
print,'## + Now Processing Shot Number = ',Shot(NS)
;-----
; Defining input and output files
;-----

shot_          = string(shot(NS))
date_shot      = strcompress(month_+'_'+day_+'_'+0+year_+'_'+shot_,/rem)
outfile        = strcompress(date_+'_'_shot_+'_'_shot_+'.txt',/rem)
outfile1       = strcompress(date_+'_'_shot_+'_'_shot_+'_Spectrum'+'.txt',/rem)
;-----
; Opening the input and output files
;-----
openw,f1,outfile1,/get_lun
openw,f2,outfile,/get_lun
;-----
; writing the header to the output file
;-----
printf,f2,FORMAT='(A100)',$
'=====
printf,f2,FORMAT='(38x,A28)', 'PROGRAM Calibration VER 1.0'
printf,f2,FORMAT='(51x,A2)', 'BY'
printf,f2,FORMAT='(46x,A13)', 'ALI E. ABDOU,'
printf,f2,FORMAT='(36x,A33)', 'UNIVERSITY OF WISCONSIN, MADISON,'
printf,f2,FORMAT='(27x,A50)', 'DEPARTMENT OF ELECTRICAL AND COMPUTER
ENGINEERING,'

```

```

printf,f2,FORMAT='(22x,A59)',HELICALY SYMMETRIC EXPERIMENT (HSX)
STELLARATOR LABORATORY,'
printf,f2,FORMAT='(21x,A60)',ENGINEERING HALL, 1415 ENGINEERING DRIVE,
MADISON, WI 53706,'
printf,f2,FORMAT='(51x,A3)',USA'
printf,f2,FORMAT='(43x,A17)',Tel: 608-265-3582'
printf,f2,FORMAT='(39x,A26)',E-mail: abdou@cae.wisc.edu'
printf,f2,FORMAT='(A100)',$,
=====

printf,f2,'
printf,f2,FORMAT='(x,A25)',THIS CASE IS RUNNING FOR:'
printf,f2,FORMAT='(A27)','-----'
printf,f2,FORMAT='(x,A20,3x,A8)',date
=,strcompress(month_+'/'+'day_+'/'+'0'+year_,/rem)
printf,f2,FORMAT='(x,A20,2x,I3)',Shot number =,shot(NS)
printf,f2,FORMAT='(x,A20,2x,F6.3,2x,A4)',Noise Level =,noiselevel,"volt"
;-----
; Constants
;-----

out    = get_data(date_shot,'hard-x_1')
hxr    =out.data
t       =out.time*ms-800
t_original = out.time*ms

;-----
; Plotting the actual signal, and the window signal
;-----

set_plot,'win'
!P.BACKGROUND = 255+256L*(255+256L*255)
!P.COLOR = 0
!P.MULTI = [0, 1, 2]
PLOT,t_original,hxr,xtit='Time(ms)',ytit='Pulse heights (V)',tit='Shot
='+strcompress(shot_)+', Date =' +date_+' Original Signal',TICKLEN = 1
PLOT,t,hxr,xrange=twindow,xtit='Time(ms)',ytit='Pulse
height(V)',tit='Shot='+strcompress(shot_)+', Date =' +date_+' Signal during Window
time',TICKLEN = 1
oplot,!x.crangle,[noiselevel,noiselevel],color=255,thick=2
!P.MULTI = 0
;-----
; Calling the function get_peaks
;-----

xrays=get_peaks(t_left,t_right,hxr,t,t_xrays,twindow=twindow,noiselevel,outfile,f2,nopul
se)

```

```

if (nopulse eq 0) then begin
;-----
; Constant definition
;-----
!p.multi=[0,4,4]
nevents=n_elements(xrays)
xraysfit=fltarr(nevents)
t_xraysfit=fltarr(nevents)
pileup=intarr(nevents)
chisqmat=fltarr(nevents)
counter = 0
;-----
; First loop for single gaussian curve fitting
;-----
peak_E1 = fltarr(5000)
peak_T1 = fltarr(5000)
;-----
; Printing the 2nd table
;-----
printf,f2,FORMAT = '(x,A52)','Table 2: Results from sigle Gaussian fitting routine'
printf,f2,FORMAT = '(10x,A62)','The Gaussian has the form  $F(x) = a[0]*EXP[(x-a[1])^2/w^2]+a[2]$ '
printf,f2,FORMAT = '(A102)',$
'=====
printf,f2,FORMAT = '(3x,A98)','i DgFred Pulse_E Pulse_t a[0] a[1] a[2]
Chisq RrdChisq Status'
printf,f2,FORMAT = '(A102)',$
'=====

abovenoi=where(hxr lt 0.0)
hxr[abovenoi] = 0.0
for i=0,nevents-1 do begin
    ind = where(t gt t_left[i]-0.003 and t le t_right[i]+0.003,count)
    len = n_elements(ind)
    w = max(hxr[ind],s)
;-----
; Plotting each individual pulse
;-----
if plot eq 1 then
plot,t(ind),hxr(ind),tit='Time='+strcompress(string(t[ind[s]]),/print),/rem),thick=2,TICKLEN = 1
;-----
; Setting initial guiss
;-----

```

```

a=[1.0,0.0,0.0] ; h,t,base
weight=replicate(1.0,count)
k= 0
;-----
; Searching for the peaks of the pile up pulse
;-----
for j=1, len-2 do begin
if (((hxr[ind[j+1]]-hxr[ind[j]]) lt 0) and ((hxr[ind[j]]-hxr[ind[j-1]]) gt 0)) then begin
peak_at = j
if hxr[ind[j]] gt 0 then begin
peak_E1[k] = hxr[ind[j]]
peak_T1[k] = t[ind[j]]
k = k+1
endif
endif
endif
if (k eq 0 or 1) then begin
peak_E1[0] = max(hxr[ind])
peak_T1[0] = t_xrays[i]
endif else begin
a[0] = peak_E1[0]-hxr[ind[0]]
a[1] = peak_T1[0]-t_xrays[i]
endelse
;-----
; Calling curvefit function with the singlegaussianfixedwidth
; function
;-----
res=curvefit(t[ind]-t_xrays[i],hxr[ind]-hxr[ind[0]],weight,a,sigma,function_name=$
'singlegaussianfixedwidth',chisq=chisq,itmax=200,tol=0.000001,/noderiv)
;-----
; Plotting the fit for every individual pulse
;-----
if plot eq 1 then oplot,t(ind),res+hxr[ind[0]],col=255,thick=2
width=chisq
chisqmat[i]=chisq
h_en=a[0]
t_en=a[1]
;-----
; Testing the Goodness of the single gaussian fitting
;-----
if chisq/max(res) lt 0.045 then begin
printf,f2,FORMAT = '(x,2(I3,2x),2(F10.7,2x),5(F10.6,2x),2x,A2)',(i+1),(len-
3),xrays[i],t_xrays[i],$

```

```

a[0],a[1],a[2],chisqmat[i],chisqmat[i]/max(res),'OK'
endif else begin
printf,f2,FORMAT = '(x,2(I3,2x),2(F10.7,2x),5(F10.6,2x),2x,A4)',(i+1),(len-
3),xrays[i],t_xrays[i],$
a[0],a[1],a[2],chisqmat[i],chisqmat[i]/max(res),'REDO'
counter = counter +1
pileup[i]=1
endelse
if plot eq 1 then begin
if chisq/max(res) gt 0.05 then begin
x_ = (!x.crange[0]+!x.crange[1])/2.0
y_ = (!y.crange[0]+!y.crange[1])/2.0
xyouts,x_,y_,"REDO",color=256L*255*255,/data
endif
endif
;-----
; Saving the energy and time of the fitted data
;-----
t_xraysfit[i]=t_en+t_xrays[i]
if (h_en lt xrays[i] and h_en lt noiselevel) then begin
xraysfit[i]=xrays[i]
endif else begin
;xraysfit[i]=h_en
xraysfit[i]=xrays[i]
endelse
if pause eq 1 then begin
if (((i+1) MOD 16) eq 0 or i eq nevents-1) then begin
WAIT, 5
endif
endif
;-----
; End of the first for loop
;-----
endifor
;-----
; Printing
;-----
printf,f2,FORMAT = '(A102)',$
'=====
printf,f2,"
printf,f2,"
printf,f2,FORMAT = '(x,A53)', 'Table 3: Results from double Gaussian fitting routine'
printf,f2,FORMAT = '(10x,A87)', $

```

```

'The Gaussian has the form  $F(x) = a[0]*EXP[(x-a[1])^2/w^2]+a[2]*EXP[(x-a[3])^2/w^2]+a[4]$ '
printf,f2,FORMAT = '(A131)', $=====
printf,f2,FORMAT = '(3x,A124)', 'i DgFred Pulse_E Pulse_t a[0] a[1] a[2]
a[3] a[4] Chisq '+' RrdChisq Status'
printf,f2,FORMAT = '(A131)', '+++++++======
;-----
;now we go back over the data where the chisq is too high and try to fit with a double
gaussian
;-----
!p.multi=[0,4,4]
npileup=total(pileup)
pind=where(pileup eq 1)
rejected = 0
if pind[0] ne -1 then begin
npile=n_elements(pind)
;-----
; Second loop for pile up curve fitting
;-----
for i=0,npile-1 do begin
ind=where(t gt t_left[pind[i]]-0.05 and t le t_right[pind[i]]+0.05,count)
num=n_elements(ind)
r=max(hxr[ind],g)
;-----
; Plotting each pile up pulse
;-----
if plot eq 1 then plot,t[ind],hxr[ind],tit='pileup:
time='+strcompress(string(t[ind[g]]),/print),/rem),
thick=2,
TICKLEN = 1
peak_E= fltarr(num)
peak_T=fltarr(num)
k=0
;-----
; Searching for the peaks of the pile up pulse
;-----
for j=1, num-2 do begin
if (((hxr[ind[j+1]]-hxr[ind[j]]) lt 0) and ((hxr[ind[j]]-hxr[ind[j-1]]) gt 0)) then begin
peak_at= j
if hxr[ind[j]] gt 0 then begin
peak_E[k]= hxr[ind[j]]
peak_T[k]= t[ind[j]]
k=k+1

```

```

endif
endif
endifor
;-----
; Setting the initial guess
;-----
a=[0.5,0.002,0.5,0.008,0.0] ;h,t,h2,t2,base
a[0]=peak_E[0]
a[1]=peak_T[0]-t_xrays[pind[i]]
a[2]=peak_E[1]
a[3]=peak_T[1]-t_xrays[pind[i]]
weight=replicate(1.0,count)
;-----
; Calling the curve fitting function with the doublegaussian ; function
;-----
res=curvefit(t[ind]-t_xrays[pind[i]],hxr[ind],weight,a,sigma,itmax=200,tol=0.000001,$
function_name='doublegaussian',chisq=chisq/noderiv)
;-----
; Plotting the fit for every pile up function
;-----
if plot eq 1 then begin
oplot,t[ind],res,col=255,thick=2
;-----
; Labeling the failed to converge pile ups
;-----
if chisq/max(res) gt 0.2 then begin
x_=(!x.crange[0]+!x.crange[1])/2.0
y_=(!y.crange[0]+!y.crange[1])/2.0
xyouts,x_,y_,"REJECTED",color=256!*255*255,/data
endif
endif
if chisq/max(res) lt 0.2 then begin
printf,f2,FORMAT ='(x,2(I3,2x),9(F10.7,2x),2x,A2)',(i+1),(num-
5),xrays[pind[i]],t_xrays[pind[i]],a[0],a[1],a[2],a[3],a[4],chisq,chisq/max(res),'OK'
xraysfit[pind[i]]=a[0]
t_xraysfit[pind[i]]=a[1]
endif else begin
rejected = rejected + 1
printf,f2,FORMAT ='(x,2(I3,2x),9(F10.7,2x),2x,A8)',(i+1),(num-
5),xrays[pind[i]],t_xrays[pind[i]],a[0],a[1],a[2],a[3],a[4],chisq,chisq/max(res),'REJECTE
D'
endelse
;-----

```

```

; End of second loop
;-----
if pause eq 1 then begin
if (((i+1) MOD 16) eq 0 or i eq npile-1) then begin
WAIT,5
endif
endif
endif
;-----
; Opening the input and output files
;-----
printf,f2,FORMAT = '(A131)',$
'=====
printf,f2,"
;-----
; End of if statement
;-----
endif
;-----
; Beginning of the PHA part
;-----
!x.omargin=[0,10]
if n_elements(xraysfit) gt 0 then begin
voltage_bins = (findgen((maxv-
noiselevel_1)/binsize)*binsize+noiselevel_1)+(0.5*binsize)
histaxis1 = voltage_bins * cal[0] + cal[1]
;-----
; Printing table 4
;-----
printf,f2,FORMAT = '(x,A24)','Table 4: Pulse Spectrum'
printf,f2,FORMAT = '(A41)','=====
printf,f2,FORMAT = '(2x,A38)','bin#   Energy   Number of Photons'
printf,f2,FORMAT = '(A41)','=====
;-----
; Calculation of the histogram
;-----
histcnt1=(HISTOGRAM(xraysfit,BIN=binsize,MIN=noiselevel_1,MAX=maxv))
histcntl2=(HISTOGRAM(xraysfit,BIN=binsize,MIN=noiselevel_1,MAX=maxv))
Hist_multip = histaxis1*histcntl2
total_number = total(histcntl2)
sum_multip = total(Hist_multip)
average_energy = sum_multip/total_number
standarddeviation = sqrt(total((histaxis1-average_energy)^2*histcntl/total_number))

```

```

histnonzero=where(histcntl2 gt 0)
hist_element=N_elements(histnonzero)
Max_Photon_Energy = histaxisl(histnonzero(hist_element-1))
max_count = max(histcntl2)
max_count_position = where(histcntl2 eq max_count)
Energy_max_count = histaxisl(max_count_position)
total_number_of_counts(NS) = nevents
standard_deviation(NS) = sqrt(nevents)
print, '## + Total Number of counts =', nevents
print, '## + Standard deviation =', sqrt(nevents)
print, '## + Average Photon Energy =', average_energy, ' KeV'
print, '## + Standard Deviation =', standarddeviation
print, '## + Max Photon Energy =', Max_Photon_Energy, ' KeV'
print, '## + Max count rate =', max_count, ' at Energy =', Energy_max_count, ' KeV'
doylog=0
num = N_elements(histaxisl)
for i=0,num-1 do begin
printf,f2,FORMAT='(2x,I3,3x,F8.2,3x,I6)',i,histaxisl[i],histcntl[i]
printf,f1,FORMAT='(2x,F8.2,3x,I6)',histaxisl[i],histcntl[i]
endfor
if plot eq 2 then begin
SET PLOT, 'win'
!P.BACKGROUND = 255+256L*(255+256L*255)
!P.COLOR = 0
!p.multi=[0,1,1]
PLOT,histaxisl,histcntl,xrange=[pltrange[0],pltrange[1]],psym=2,xtit='E (Photon Energy
in KeV)',ytit='dN/dE (Counts)','$
,tit=strcmp('Spectrum for Shot no.'+shot_+' on '+date_+' Using CdZnTl
Detector'),TICKLEN = 1
endif
if plot eq 3 then begin
count =N_elements(histaxisl)
if not keyword_set(ran) then ran = [0,histaxisl[count-1]]
xran = ran
!p.multi=[0,1,2]
ind = where(histaxisl ge ran[0] and histaxisl le ran[1])
histcntl_ = histcntl[0:count-1]
yrng = [0.1,max(histcntl_)]
a = [60,0.016]
weight=replicate(1.0,count)
x=histaxisl[ind]
y=histcntl_[ind]

```

```

res=curvefit(x,y,weight,a,sigma,function_name='exponential',chisq=chisq,itmax=200,tol
=0.000001,/noderiv)
sigmaT = (1/a[1]^2)*sigma[1]
m = a[0]
b = a[1]
fitfun1=strcompress('Best Fit: n(E) =' + string(m) + ' * Exp(' + string(b) + ' * E)')
fitfun2=strcompress('Best Fit: n(E) =' + string(b) + ' * E + ' + string(m))
fitfun3=strcompress('Electron Temperature =' + string(abs(1/b)) + ' KeV +-'
+ string(sigmaT))
PLOT,histaxisl,histcntl,xrange=[pltrange[0],pltrange[1]],psym=8,ylog=0,xtit='Energy
(KeV)',ytit=$
Incidence number',tit=strcompress('Energy spectrum for HSX, Shot =' + shot_ + ' Date
=' + date_) $
,TICKLEN = 1
oplot,x,res,color=0+256L*(0+256L*255),thick=3
x_ = 0.5*(!x.crange[0]+!x.crange[1])/2.0
y_ = 1.75*(!y.crange[0]+!y.crange[1])/2.0
xyouts,x_,y_,fitfun1,color=256l*255*255,CHARSIZE = 1.0,/data
PLOT,histaxisl,histcntl,xrange=[pltrange[0],pltrange[1]],yrange=yrng,psym=8,ylog=1,xti
t='Energy (KeV)',ytit=$
'Incidence number',tit=strcompress('Energy spectrum for HSX, Shot =' + shot_ + ' Date
=' + date_) $
,TICKLEN = 1
oplot,x,res,color=0+256L*(0+256L*255),thick=3
x_ = 0.5*(!x.crange[0]+!x.crange[1])/2.0
y_ = 0.80*(!10^(!y.crange[0])+10^(!y.crange[1]))/2.0
xyouts,x_,y_,fitfun2,color=256l*255*255,CHARSIZE = 1.0,/data
xyouts,x_,0.5*y_,fitfun3,color=256l*255*255,CHARSIZE = 1.0,/data
endif
total_counts = total(total_number_of_counts)
n_shots_histogram = histcntl + n_shots_histogram
;-----
; printing the statistics
;-----
printf,f2,FORMAT = '(A41)', '=====
printf,f2,FORMAT = '(x,A12)', '* Statistics'
printf,f2,FORMAT = '(x,A13)', '-----'
printf,f2,FORMAT = '(x,A45,1x,F7.3,6x,A3)', 'Bin Size =',binsize,$
'Volts'
printf,f2,FORMAT = '(x,A45,1x,F7.1,6x,A4)', 'Time Window
=',(ms*time_) $, 'mSec'
printf,f2,FORMAT = '(x,A45,x,F9.2,4x,A3)', 'Maximum Energy           =', $
Max_Photon_Energy, 'KeV'

```

```

printf,f2,FORMAT = '(x,A45,x,F8.2,5x,A3)', 'Average Energy
=,average_energy, 'KeV'
printf,f2,FORMAT = '(x,A45,3x,F3.1,8x,A20)', 'Detector Area
=,area,$
'(10 mm x 10 mm) cm^2'
printf,f2,FORMAT = '(x,A45,3x,E9.2,2x,A7)', 'Detector Solid Angle
=,solangle,$
'SRadian'
printf,f2,FORMAT = '(x,A45,2x,I4)', 'Total Number of pulses is      =,nevents
printf,f2,FORMAT = '(x,A45,2x,I4)', 'Total Number of accepted pulses is
=,(nevents-rejected)
printf,f2,FORMAT = '(x,A45,2x,I3)', 'Total Number of pile up pulses is      =,counter
printf,f2,FORMAT = '(x,A45,2x,I3)', 'Total Number of regicte pile up pulses is
=,rejected
printf,f2,FORMAT = '(x,A45,3x,F5.2,x,A1)', 'Percentage of accepted pulses      =,$
(100.0*(nevents-rejected)/nevents),'%'
printf,f2,FORMAT = '(x,A45,3x,F5.2,x,A1)', 'Percentage of pile up pulses      =,$
(100.0*counter/nevents),'%'
printf,f2,FORMAT = '(x,A45,2x,F5.2,2x,A1)', 'Percentage of regicte pile up pulses
=,$
(100.0*rejected/nevents),'%'
endif
;-----
; End of function get_plot_sxr_proc
;-----
endif
if (nopulse eq 1) then begin
print,## + No date above noise for this shot'
endif
free_lun,f1
free_lun,f2
endfor
if (Number_of_Shots gt 1) then begin
num_hist = n_elements(n_shots_histogram)
outfile2= strcompress(date_+'_Shots_'+shot_range+'_Spectrum'+'.txt',/rem)
openw,f3,outfile2,/get_lun
for i=0,num_hist-1 do begin
printf,f3,FORMAT=(2x,I3,3x,F8.2,3x,I6)',i,histaxisl[i],n_shots_histogram[i]
endfor

if plot eq 2 then begin
SET_PLOT, 'win'
!P.BACKGROUND = 255+256L*(255+256L*255)

```

```

!P.COLOR = 0
!p.multi=[0,1,2]
if n_elements(shot) gt 1 then begin
shot = shot_range
endif else begin
shot = shot_
endif
PLOT,histaxisl,n_shots_histogram,xrange=[pltrange(0),pltrange(1)],psym=10,thick=2,xtitle='E (Photon Energy in KeV)',ytitle='dN/dE (Counts)'$
,tit=strcompress('Histogram for Shot no.'+shot+' on '+date_+' Using CdZnTi
Detector'),TICKLEN = 1
PLOTSYM, 0,1.2,color=250,fill=2
PLOT,histaxisl,n_shots_histogram,xrange=[pltrange(0),pltrange(1)],psym=8,xtitle='E
(Photon Energy in KeV)',ytitle='dN/dE (Counts)'$
,tit=strcompress('Spectrum for Shot no.'+shot+' on '+date_+' Using CdZnTi
Detector'),TICKLEN = 1
endif
if plot eq 3 then begin
SET_PLOT, 'win'
!P.BACKGROUND = 255+256L*(255+256L*255)
!P.COLOR = 0
!p.multi=[0,1,2]
if n_elements(shot) gt 1 then begin
shot = shot_range
endif else begin
shot = shot_
endif
count = N_elements(n_shots_histogram)
if not keyword_set(ran) then ran = [0,histaxisl[count-1]]
xran = ran
!p.multi=[0,1,2]
ind = where(histaxisl ge ran[0] and histaxisl le ran[1])
histcntl_ = n_shots_histogram[0:count-1]
yrng = [0.1,max(histcntl_)]
a = [60,0.016]
weight=replicate(1.0,count)
x=histaxisl[ind]
y=histcntl_[ind]
res=curvefit(x,y,weight,a,sigma,function_name='exponential',chisq=chisq,itmax=200,tol
=0.000001,/noderiv)
sigmaT = (1/a[1]^2)*sigma[1]
m = a[0]
b = a[1]

```

```

fitfun1=strcompress('Best Fit: n(E) =' + string(m) + ' * Exp(' + string(b) + ' * E)')
fitfun2=strcompress('Best Fit: n(E) =' + string(b) + ' * E + ' + string(m))
fitfun3=strcompress('Electron Temperature =' + string(abs(1/b)) + ' KeV +-'
' + string(sigmaT))
print,'## + Temperature = ',fitfun3,' KeV'
PLOT,histaxis1,n_shots_histogram,xrange=[pltrange[0],pltrange[1]],psym=8,ylog=0,xtit=
'Energy (KeV)',ytit=$
'Incidence number',tit=strcompress('Energy spectrum for HSX, Shot =' + shot_ + ' Date
=' + date_) $
,TICKLEN = 1
oplot,x,res,color=0+256L*(0+256L*255),thick=3
x_ = 0.5*((!x.crange[0]+!x.crange[1])/2.0)
y_ = 1.75*((!y.crange[0]+!y.crange[1])/2.0)
xyouts,x_,y_,fitfun1,color=256I*255*255,CHARSIZE = 1.0,/data
PLOT,histaxis1,n_shots_histogram,xrange=[pltrange[0],pltrange[1]],yrange=yrng,psym=
8,ylog=1,xtit='Energy (KeV)',ytit=$
'Incidence number',tit=strcompress('Energy spectrum for HSX, Shot =' + shot_ + ' Date
=' + date_) $
,TICKLEN = 1
oplot,x,res,color=0+256L*(0+256L*255),thick=3
x_ = 0.5*((!x.crange[0]+!x.crange[1])/2.0)
y_ = 0.80*((10^(!y.crange[0])+10^(!y.crange[1]))/2.0)
xyouts,x_,y_,fitfun2,color=256I*255*255,CHARSIZE = 1.0,/data
xyouts,x_,0.5*y_,fitfun3,color=256I*255*255,CHARSIZE = 1.0,/data
endif
if plot eq 4 then begin
SET_PLOT, 'win'
!P.BACKGROUND = 255+256L*(255+256L*255)
!P.COLOR = 0
!p.multi=[0,1,2]
if n_elements(shot) gt 1 then begin
shot = shot_range
endif else begin
shot = shot_
endif
count = N_elements(n_shots_histogram)
if not keyword_set(ran) then ran = [0,histaxis1[count-1]]
xran = ran
!p.multi=[0,1,2]
ind = where(histaxis1 ge ran[0] and histaxis1 le ran[1])
hist_energyflux = histcnt1*n_shots_histogram*1e3*1.6e-12/(area*solangle*time_)
total_energy = total(histcnt1*n_shots_histogram)*(1.0E+3*1.6E-
12*4*3.141592*time_*0.4*1.0E+6)/(2.0*solangle*1.0E+7)

```

```

print,'## + Total Energy Flux in this shot = ',total(hist_energyflux),'
egr/Cm2.Sec.Steradian'
print,'## + Total Energy radiated from HSX = ',total_energy,' Joule'
histcntl_ = hist_energyflux[0:count-1]
yrng = [1.0E-5,max(histcntl_)]
a = [60,0.016]
weight=replicate(1.0,count)
x=histaxisl[ind]
y=histcntl_[ind]
res=curvefit(x,y,weight,a,sigma,function_name='exponential',chisq=chisq,itmax=200,tol
=0.000001,$
/noderiv)
sigmaT = (1/a[1]^2)*sigma[1]
m = a[0]
b = a[1]
fitfun1=strcompress('Best Fit: n(E) =' + string(m) + ' * Exp(' + string(b) + ' * E)')
fitfun2=strcompress('Best Fit: n(E) =' + string(b) + ' * E + ' + string(m))
fitfun3=strcompress('Electron Temperature =' + string(abs(1/b)) + ' KeV +-'
'+string(sigmaT))
PLOT,histaxisl,hist_energyflux,xrange=[pltrange[0],pltrange[1]],psym=8,ylog=0,xtit='En
ergy (KeV)',ytit=$
'Erge/Kev.Cm2.Sec.Steradians',tit=strcompress('Energy spectrum for HSX, Shot =$
+shot_+' Date =' + date_) ,TICKLEN = 1
oplot,x,res,color=0+256L*(0+256L*255),thick=3
x_ = 0.5*((!x.crange[0]+!x.crange[1])/2.0)
y_ = 1.75*((!y.crange[0]+!y.crange[1])/2.0)
xyouts,x_,y_,fitfun1,color=256l*255*255,CHARSIZE = 1.0,/data
PLOT,histaxisl,hist_energyflux,xrange=[pltrange[0],pltrange[1]],yrange=yrng,psym=8,yl
og=1,xtit='Energy (KeV)',ytit=$
'Erge/Kev.Cm2.Sec.Steradians',tit=strcompress('Energy spectrum for HSX, Shot
= '+shot_+$
' Date =' + date_),TICKLEN = 1
oplot,x,res,color=0+256L*(0+256L*255),thick=3
x_ = 0.5*((!x.crange[0]+!x.crange[1])/2.0)
y_ = 0.60*((10^(!y.crange[0])+10^(!y.crange[1]))/2.0)
xyouts,x_,y_,fitfun2,color=256l*255*255,CHARSIZE = 1.0,/data
xyouts,x_,0.3*y_,fitfun3,color=256l*255*255,CHARSIZE = 1.0,/data
endif
Hist_multip_ = histaxisl*n_shots_histogram
total_number_ = total(n_shots_histogram)
sum_multip_ = total(Hist_multip_)
average_energy_ = sum_multip_/total_number_

```

```

standarddeviation_ = sqrt(total((histaxisl-
average_energy_)^2*n_shots_histogram/total_number_))
histnzero_ = where(n_shots_histogram gt 0)
hist_element_ = N_elements(histnzero_)
Max_Photon_Energy_ = histaxisl(histnzero_(hist_element_-1))
max_count_ = max(n_shots_histogram)
max_count_position_ = where(n_shots_histogram eq max_count_)
Energy_max_count_ = histaxisl(max_count_position_)
print,'#####'
print,'## + Time Window = ',time_*1000,' mSec. t1 =',twindow[0]+800,' and t2
=' ,twindow[1]+800
print,'## + Total counts for shots ',shot,'= ',total_counts
print,'## + Standard Deviation = ',sqrt(total_counts)
print,'## + Average Photon Energy = ',average_energy_, ' KeV'
print,'## + Standard Deviation = ',standarddeviation_
print,'## + Max Photon Energy = ',Max_Photon_Energy_, ' KeV'
print,'## + Max count rate = ',max_count_, ' at Energy = ', Energy_max_count_, ' KeV'
print,'#####'
free_lun,f3
endif
return, 0
end
;*****
; Program Singlegaussianfixedwidth
;*****
pro singlegaussianfixedwidth,x,a,f,pder
;-----
; Fitting functions - want a Gaussian - but want the pulse width constrained.
;-----
w=1.5e-3
bx=exp(-((x-a[1])^2/w^2))
f=abs(a[0])*bx+a[2]
;-----
; If called with 4 params - compute the partial derevatives
;-----
if n_params() ge 4 then $
pder=[[bx],[abs(a[0])*2*(x-a[1])/w^2*bx],[replicate(1.0,n_elements(x))]]
;-----
; End of function Singlegaussianfixedwidth
;-----
end
;*****
; Program Doublegaussian

```

```

*****
;
pro doublegaussian,x,a,f,pder
;-----
; Fitting functions - want a double Gaussian
;-----
w=1.5e-3
bx=exp(-((x-a[1])^2/w^2))
dx=exp(-((x-a[3])^2/w^2))
f=abs(a[0])*bx+abs(a[2])*dx+a[4]
;-----
; If called with 4 params - compute the partial derivatives
;-----
if n_params() ge 4 then $
pder=[[bx],[abs(a[0])*2*(x-a[1])/w^2*bx],$
[dx],[abs(a[2])*2*(x-a[3])/w^2*dx],[replicate(1.0,n_elements(x))]]
;-----
; End of function doublegaussian
;-----
end
*****
; Program exponential
*****
pro exponential,x,a,f,pder
;-----
; Fitting functions - want an exponential
;-----
bx=exp(a[1]*x)
f=abs(a[0])*bx
;-----
; If called with 4 params - compute the partial derivatives
;-----
if n_params() ge 4 then $
pder=[[bx],[abs(a[0])*x*bx]]
end
*****
; End of the program and it's functions
*****

```

### A2.3.2 Auxiliary Programs

```

*****
;
; Function numrange(x,y)
; This function return row vector containing the integers from x to y regularly-spaced

```

```

*****
;
function numrange,x,y
if x gt y then begin
    z=indgen(x-y+1)+y
endif else begin
    z=indgen(y-x+1)+x
endelse
return,z
end

*****
;
; Function plotsym
*****
pro plotsym, psym, psize, FILL=fill,thick=thick,Color = color
; NAME: PLOTSYM
; PURPOSE: Define useful plotting symbols not in the standard !PSYM definitions.
; EXPLANATION:
; After a symbol has been defined with PLOTSYM, a plotting command should
; follow with either PSYM = 8 or !P.PSYM = 8 (see USERSYM)
; For additional rotationally symmetric plotting symbols, see VSYM.PRO
; CALLING SEQUENCE:
; PLOTSYM, PSYM,[ PSIZE, /FILL, THICK=, COLOR=]
; INPUTS:
; PSYM - The following integer values of PSYM will create the
;         corresponding plot symbols
; 0 - circle
; 1 - downward arrow (upper limit), base of arrow begins at plot value      value
; 2 - upward arrow (lower limit)
; 3 - 5 pointed star
; 4 - triangle
; 5 - upside down triangle
; 6 - left pointing arrow
; 7 - right pointing arrow
; 8 - square
;
; Arrows are defined such that their base begins at their origin.
;
; OPTIONAL INPUTS:
; PSIZE - Size of the plotting symbol in multiples of the default size
;         (default PSIZE=1). Does not need to be an integer
;
; OPTIONAL INPUT KEYWORD:
; FILL - Parameter indicating whether to fill the symbol (see USERSYM)

```

```

; The default is 0, unfilled symbol. Does not affect arrows
; or character symbols.
; THICK - Thickness of unfilled symbols. Default is 1.
; COLOR - Color of the symbols, Default is !P.color
; OUTPUTS:
; None
;
; EXAMPLES:
; Plot Y vs. X with filled stars as the symbol, twice the default size
; IDL> PLOTSYM, 3, 2, /FILL ;Plotting symbol is a filled star,
; ;twice default size
; IDL> PLOT,X,Y,PSYM=8 ;Set PSYM = 8 to get star symbol
;
; Now plot Y vs. X with an open circle as the symbol
;
; IDL> PLOTSYM, 0 ;Plotting symbol is a circle
; IDL> PLOT,X,Y,PSYM=8
;
; METHOD:
; Appropriate X,Y vectors are used to define the symbol and passed to the
; USERSYM command.
;
; REVISION HISTORY
; Written W. Landsman June 1992
; 18-JAN-1996 Added a square symbol, HCW.
; 98Aug20 Added keyword thick parameter - RCB.
; April 2001 Added COLOR keyword WBL
;-
On_error,2

if N_elements(psym) LT 1 then begin
  print,'Syntax - PLOTSYM, psym, [ size, /FILL, THICK= ]'
  print,' PSYM values 0 - circle, 1 - down arrow, 2 - up arrow, 3 - star'
  print,' 4 - triangle, 5 - upside down triangle, 6 - left arrow'
  print,' 7 - right arrow, 8 - square'
  return
endif

if ( N_elements(psize) LT 1 ) then psize = 1 else psize = psize > 0.1

if not keyword_set(FILL) then fill = 0
if not keyword_set(thick) then thick=1

```

```

case psym of
0: begin           ;Circle
  ang = 2*!PI*findgen(49)/48.  ;Get position every 5 deg
  xarr = psize*cos(ang) & yarr = psize*sin(ang)
  end
1: begin           ;Down arrow
  xarr = [0,0,.5,0,-.5]*psize
  yarr = [0,-2,-1.4,-2,-1.4]*psize
  fill = 0
  end
2: begin           ;Up arrow
  xarr = [0,0,.5,0,-.5]*psize
  yarr = [0,2,1.4,2,1.4]*psize
  fill = 0
  end
3: begin           ;Star
  ang = (360. / 10 * findgen(11) + 90) / !RADEG ;star angles every 36 deg
  r = ang*0
  r[2*indgen(6)] = 1.
  cp5 = cos(!pi/5.)
  r1 = 2. * cp5 - 1. / cp5
  r[2*indgen(5)+1] = r1
  r = r * psize / sqrt(!pi/4.) * 2. / (1.+r1)
  xarr = r * cos(ang) & yarr = r * sin(ang)
  end
4: begin           ;Triangle
  xarr = [-1,0,1,-1]*psize
  yarr = [-1,1,-1,-1]*psize
  end
5: begin           ;Upside down triangle
  xarr = [-1, 0, 1, -1]*psize
  yarr = [ 1,-1, 1, 1]*psize
  end
6: begin           ;Left pointing arrow
  yarr = [0, 0, 0.5, 0, -.5]*psize
  xarr = [0,-2,-1.4,-2,-1.4]*psize
  fill = 0
  end
7: begin           ;Left pointing arrow
  yarr = [ 0, 0, 0.5, 0, -.5] * psize
  xarr = [ 0, 2, 1.4, 2, 1.4] * psize
  fill = 0
  end

```

```
8: begin                                ;Square
    xarr = [-1,-1,1, 1,-1] * psize
    yarr = [-1, 1,1,-1,-1] * psize
    end
else: message,'Unknown plotting symbol value of '+strtrim(psym,2)
endcase

if N_elements(color) GT 0 then $
usersym, xarr, yarr, FILL = fill,thick=thick, color = color else $
usersym, xarr, yarr, FILL = fill,thick=thick
return
end
```

---

<sup>1</sup> **IDL** The Data Visualization & Analysis Platform, <http://www.rsinc.com/idl/>

<sup>2</sup> R. O'Connell, MST plasma physics group, UW-Madison, private communication.

## Appendix 3

# Electron Collision Frequencies

### A3.0: Introduction

Collisions between charged particles in plasma differ fundamentally from those between molecules in a neutral gas because of the long range of the Coulomb force. When the plasma is fully ionized, all collisions are Coulomb collisions between charged particles. If the plasma is weakly ionized, collisions between plasma charged particles i.e. electrons and ions and neutral atoms are important and can dominate over Coulomb collisions. When an electron collides with a neutral atom, no force is felt until the electron is at a distance comparable to the atomic dimension; the collisions are billiard-ball like collisions. The situation is completely different when an electron collides with other charged particles in plasma, either electron or ion. The electron is gradually deflected by the long range Coulomb field of other charge. Coulomb collisions are, in fact, predominately small angle scattering events, so the collision frequency is not one over the typical time between collisions. Instead, it is one over the typical time needed for enough collisions to change the particle trajectory by  $90^\circ$ . For this reason, the collision frequency is sometimes termed the “ $90^\circ$  scattering rate”. Electron collisions in plasma can be divided to three types; electron-electron, electron-ion and electron-neutral. In this appendix, the electron collision frequencies will be evaluated.

### A3.1: Electron Coulomb Collisions

There are four types of Coulomb relaxation processes affecting the test particle velocity in plasma<sup>1</sup>; momentum loss or slowing down, perpendicular diffusion, parallel or speed diffusion and energy loss resulting from collision of test particle  $\alpha$  on a Maxwellian velocity distribution of background particle  $\beta$ . The collision frequencies of the above mentioned processes are given by<sup>2,3</sup>:

$$\nu_s^{\alpha\backslash\beta} = \left(1 + \frac{m_\alpha}{m_\beta}\right) \psi(x^{\alpha\backslash\beta}) \nu_o^{\alpha\backslash\beta} \quad (\text{A3.1})$$

$$\nu_\perp^{\alpha\backslash\beta} = 2 \left[ \left(1 - \frac{1}{2x^{\alpha\backslash\beta}}\right) \psi(x^{\alpha\backslash\beta}) + \psi'(x^{\alpha\backslash\beta}) \right] \nu_o^{\alpha\backslash\beta} \quad (\text{A3.2})$$

$$\nu_\parallel^{\alpha\backslash\beta} = \left[ \frac{\psi(x^{\alpha\backslash\beta})}{x^{\alpha\backslash\beta}} \right] \nu_o^{\alpha\backslash\beta} \quad (\text{A3.3})$$

$$\nu_\varepsilon^{\alpha\backslash\beta} = 2 \left[ \left(\frac{m_\alpha}{m_\beta}\right) \psi(x^{\alpha\backslash\beta}) - \psi'(x^{\alpha\backslash\beta}) \right] \nu_o^{\alpha\backslash\beta} \quad (\text{A3.4})$$

From the definitions A3.1-A3.4 we see that  $\nu_\varepsilon$  can be estimated also from  $\nu_\varepsilon = 2\nu_s - \nu_\perp - \nu_\parallel$ . And the reference frequency is given by:

$$\nu_o^{\alpha\backslash\beta} = \frac{4\pi e_\beta^2 e_\alpha^2 n_\beta}{\{4\pi\epsilon_o\}^2 m_\alpha^2 v_\alpha^3} \lambda_{\alpha\beta} \quad (\text{A3.5})$$

where  $\lambda_{\alpha\beta} = \ln \Lambda_{\alpha\beta} \sim 17$  for fusion plasmas,  $\psi(x^{\alpha/\beta})$  Maxwell integral,  $\nu_s$  slowing down collision frequency,  $\nu_{\perp}$  perpendicular diffusion collision frequency,  $\nu_{\parallel}$  parallel or speed diffusion collision frequency,  $\nu_e$  energy loss collision frequency,  $m_{\alpha}, m_{\beta}$  masses of test and background particles respectively,  $e_{\alpha}, e_{\beta}$  charges of test and background particles respectively,  $\epsilon_o$  electric permittivity,  $v_{\alpha}$  test particle velocity,  $k$  Boltzman constant =  $1.6 \times 10^{-19}$  J/eV,  $1.381 \times 10^{-23}$  J/k<sup>o</sup>,  $n_{\beta}$  background particle density in m<sup>-3</sup>, and the Maxwell integral is defined as:

$$\psi(x) = \frac{2}{\sqrt{\pi}} \int_0^x dt t^{1/2} e^{-t} \quad (\text{A3.6})$$

which has the following properties:

$$\psi + \psi' = \frac{2}{\sqrt{\pi}} \int_0^{\sqrt{x}} dy e^{-y^2} \equiv \text{erf}(\sqrt{x}) \quad (\text{A3.7})$$

$$\psi'(x) = \frac{d\psi}{dt} = \frac{2}{\sqrt{\pi}} \sqrt{x} e^{-x} \quad (\text{A3.8})$$

Physically the Maxwell integral is the normalized integral of a Maxwellian velocity distribution out to a sphere of radius  $v$ . The Maxwell integral and its related functions are

sketched in figure A3.1 versus  $x$ , where  $x^{\alpha/\beta} = \frac{m_{\beta} v_{\alpha}^2}{2kT_{\beta}} = \frac{v_{\alpha}^2}{v_{T\beta}^2}$  is the ratio of the test

particle speed to the thermal speed of the background particle of species  $\beta$ .

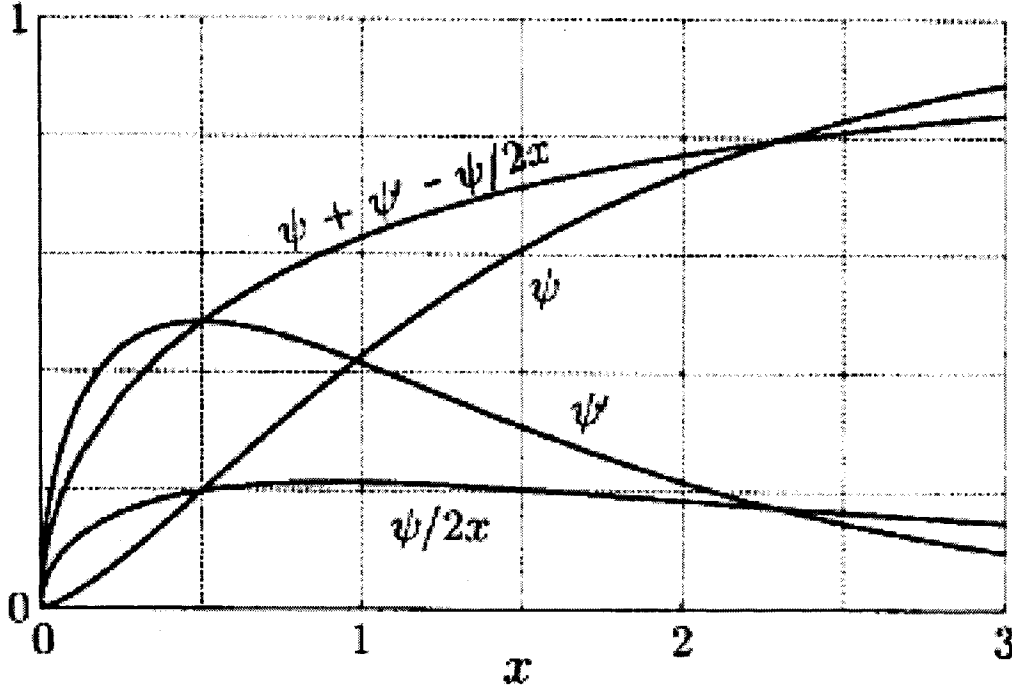


Figure A3.1: Maxwell Integral  $\psi$  and related functions<sup>2</sup>.

We now consider the various Coulomb collision effects on typical test electron in hydrogen plasma like the one under study during this research. So  $\alpha$  and  $\beta$  should be replaced by  $e$  and  $e$  for electron-electron ( $e-e$ ) and  $e$  and  $i$  ( $e-i$ ) for electron-ion collisions respectively. The reference collision frequencies for  $e-e$  and  $e-i$  collisions are related by

$$\nu_o^{e/e} = \nu_o^{e/i}, \text{ and the other parameters will be: } e_\alpha = e_\beta = e, \quad m_\alpha = m_e, \quad m_\beta = m_e, m_p$$

and  $\lambda_{ee} \approx \lambda_{ei} = 24 - \ln(n_e^{1/2} T_e^{-1})$ . Since the ratio of the proton mass to the electrons mass is very large ( $\sim 1836$ ), the relative speed parameters  $x^{\alpha/\beta}$  are given

$$\text{by } x^{e/i} = \frac{m_i}{m_e} \gg 1, \quad x^{e/e} = 1. \text{ Some expansions of interest in evaluating the values of the}$$

collision frequencies for the relative speed parameter are<sup>2</sup>:

$x \ll 1$

$$\begin{aligned}
 \psi(x) &\cong \left(\frac{4x^{\frac{3}{2}}}{3\sqrt{\pi}}\right)\left(1 - \frac{3x}{5} + \frac{3x^2}{14} - \dots\right) \\
 \psi'(x) &= \left(\frac{2\sqrt{x}e^{-x}}{\sqrt{\pi}}\right) \cong \left(\frac{2x^{\frac{1}{2}}}{\sqrt{\pi}}\right)\left(1 - x + \frac{x^2}{2} - \dots\right) \\
 \psi(x) + \psi'(x) - \frac{\psi(x)}{2} &\cong \left(\frac{4x^{\frac{3}{2}}}{3\sqrt{\pi}}\right)\left(1 - \frac{x}{5} + \frac{3x^2}{70} - \dots\right)
 \end{aligned} \tag{A3.9}$$

$x \gg 1$

$$\begin{aligned}
 \psi(x) &\cong 1 - \left(\frac{2\sqrt{x}e^{-x}}{\sqrt{\pi}}\right)\left(1 + \frac{1}{2x} - \frac{1}{4x^2} + \dots\right) \\
 \psi'(x) &= \frac{2\sqrt{x}e^{-x}}{\sqrt{\pi}} \\
 \psi(x) + \psi'(x) - \frac{\psi(x)}{2} &\cong 1 - \frac{1}{2x} + \left(\frac{e^{-x}}{x^{\frac{3}{2}}\sqrt{\pi}}\right)\left(1 - \frac{1}{x} + \dots\right)
 \end{aligned} \tag{A3.10}$$

Table A3.1 shows the relation between the various collisional processes.

Process	Symbol	e/e	e/i
Slowing Down	$\frac{v_s^{\alpha/\beta}}{v_o^{e/i}}$	0.86	1
Perpendicular Diffusion	$\frac{v_s^{\alpha/\beta}}{v_o^{e/i}}$	1.26	2
Speed Diffusion	$\frac{v_s^{\alpha/\beta}}{v_o^{e/i}}$	0.43	$\frac{m_e}{m_i}$
Energy Loss	$\frac{v_s^{\alpha/\beta}}{v_o^{e/i}}$	0.03	$2\frac{m_e}{m_i}$

**Table A3.1: Relation between various collisional processes<sup>2</sup>.**

The rates are referred to the electron-ion collision frequency  $\nu_o^{e/i}$ . The various Coulomb relaxation processes is calculated numerically using equations A3.1-A3.8 and the results are plotted in Figures A3.2 through A3.7. Figure A3.2 shows the electron energy variation of the various types of electron-electron collision frequencies. Figure A3.3 shows electron energy variation of the various types of electron-electron collision times. Similar plots for electron-ions are shown in Figures A3.4 and A3.5. Figure A3.6 shows the electron energy variation of the electron-electron slowing collision frequency at various plasma electron densities while Figure A3.7 shows the same variation for electron-ion slowing collision frequency.

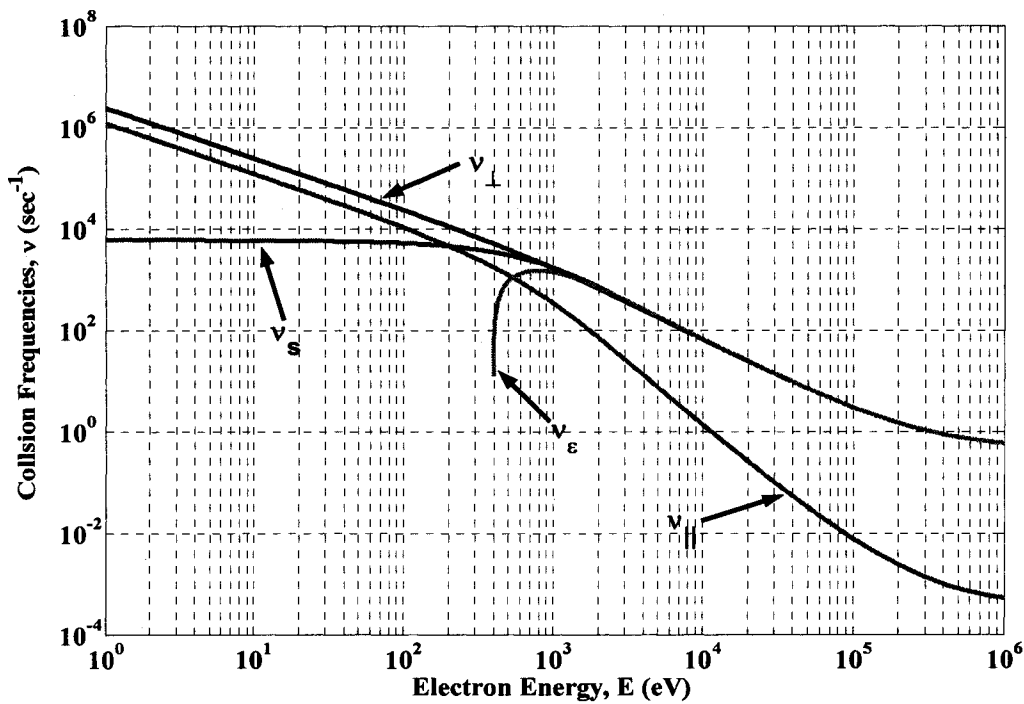


Figure A3.2: Electron-electron collision frequencies energy variation at  $n_e = 5 \times 10^{11} \text{ cm}^{-3}$ .

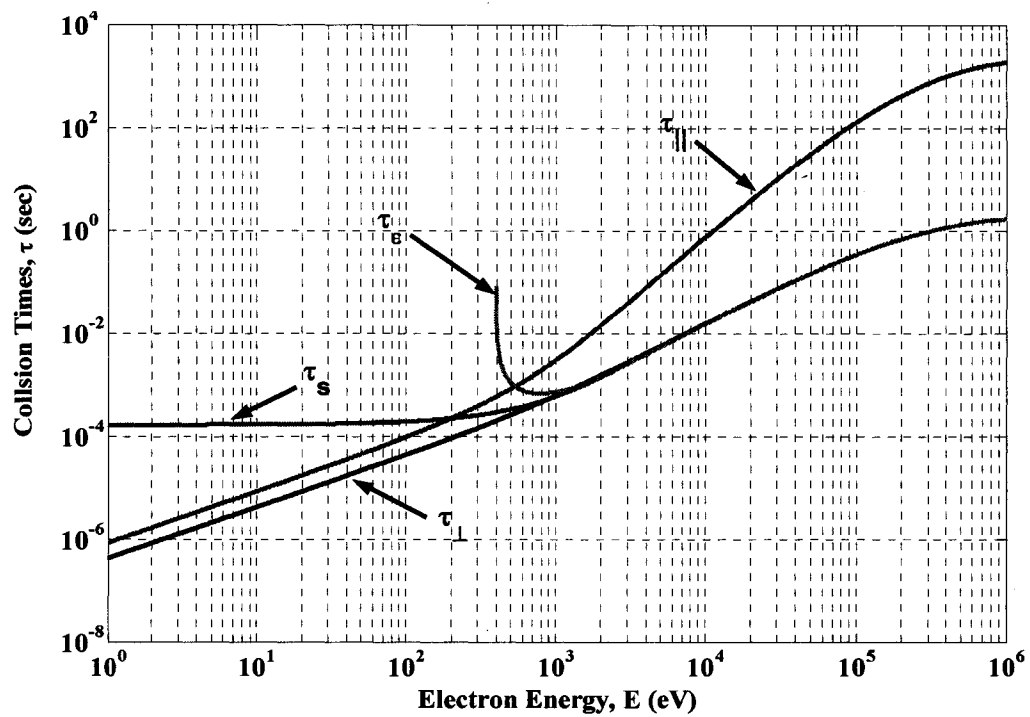


Figure A3.3: Electron-electron collision times energy variation at  $n_e = 5 \times 10^{11} \text{ cm}^{-3}$ .

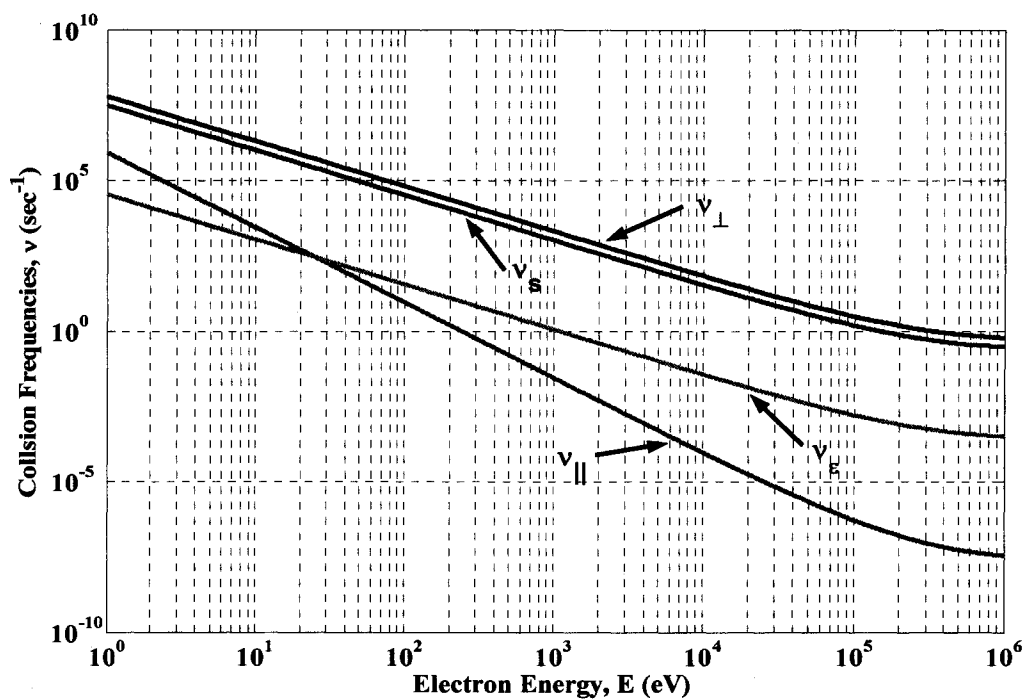


Figure A3.4: Electron-ion collision frequencies energy variation at  $n_e = 5 \times 10^{11} \text{ cm}^{-3}$ .

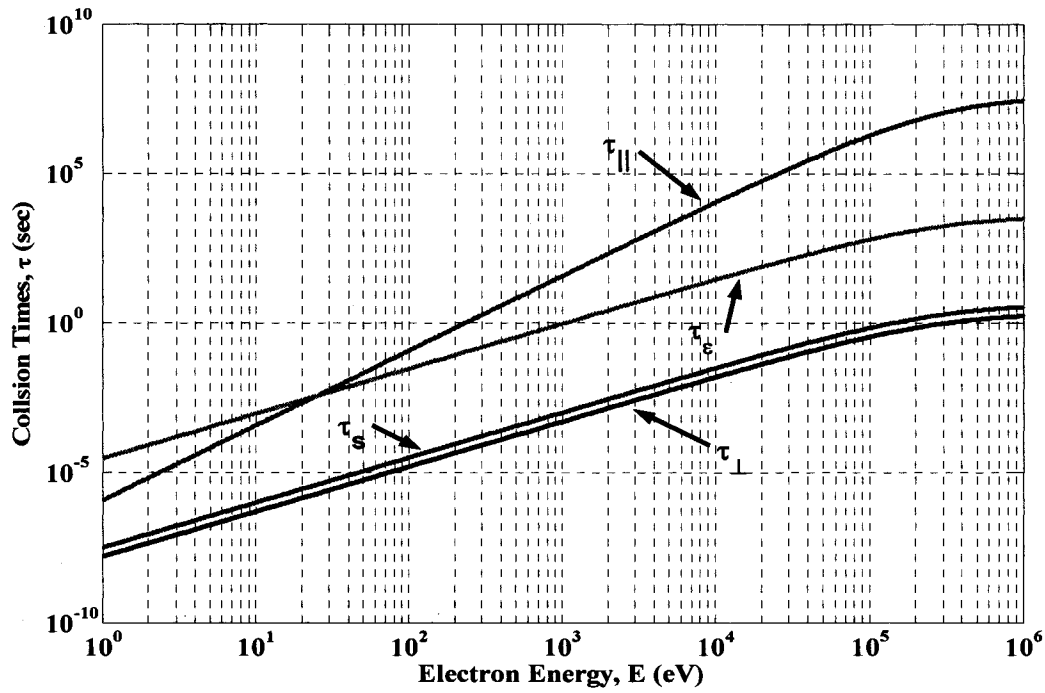


Figure A3.5: Electron-ion collision times energy variation at  $n_e = 5 \times 10^{11} \text{ cm}^{-3}$ .

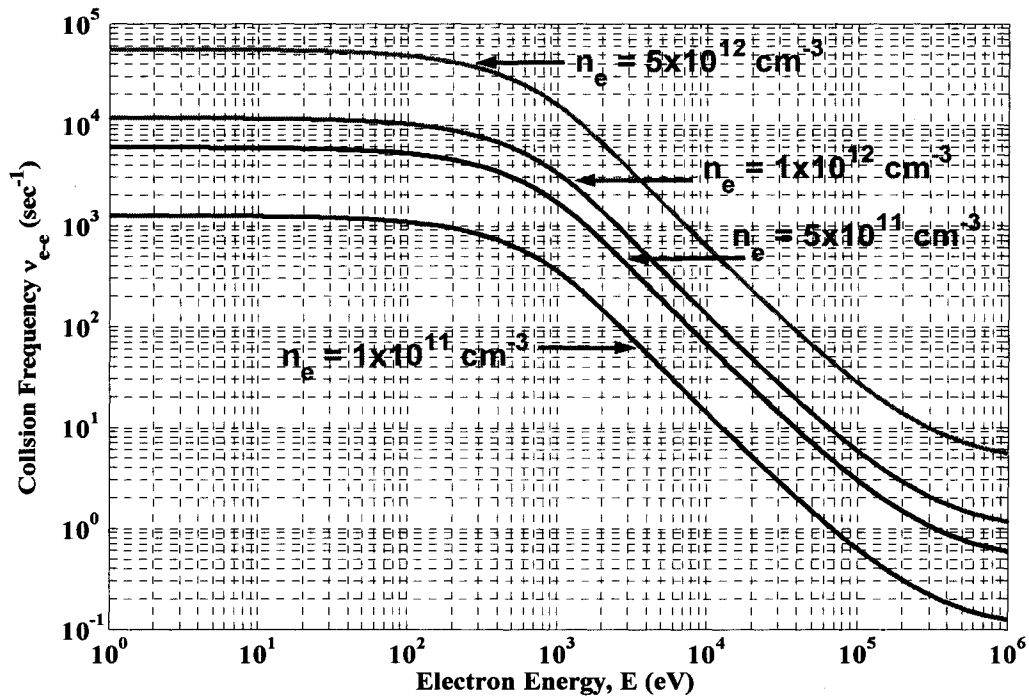


Figure A3.6: Electron-electron,  $\nu_s^{e/e}$ , collision frequency energy variation at different densities.

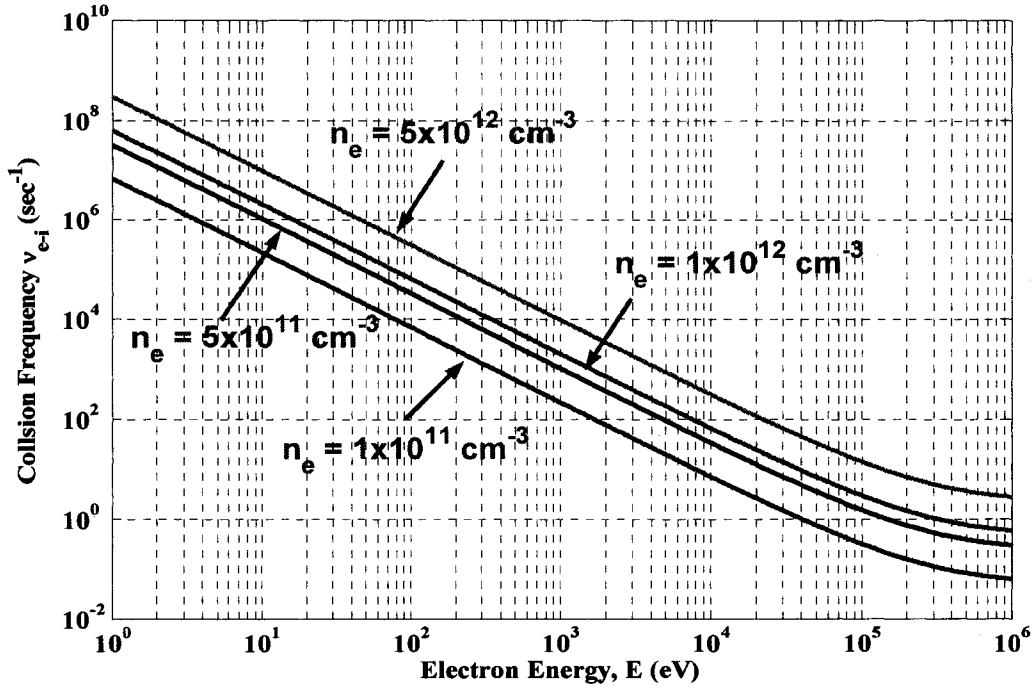


Figure A3.7: Electron-ion,  $\nu_s^{e/i}$ , collision frequency energy variation at different densities.

### A3.2: Electron Neutral Collisions

The electron neutral collision is calculated from the following formula:

$$\nu^{e/n} = n_n \sigma_{e-n} \nu_e \quad (\text{A3.11})$$

where  $n_n$  neutral atom density in  $\text{cm}^{-3}$ ,  $\sigma_{e-n}$  electron-neutral ionization cross section,  $\nu_e$  electron velocity. The cross section is given by<sup>4</sup>:

$$\sigma_{e-n} = \frac{3.123 \times 10^{-15}}{E} (\log_{10} E + 0.792) \quad (\text{cm}^2) \quad (\text{A3.12})$$

The electron neutral ionization cross sections for atomic and molecular hydrogen were obtained from online numerical data library<sup>5,6</sup> and were plotted in figure A3.8. The figure shows that the electron-H<sub>2</sub> ionization cross section is higher than the e-H at electron

energies higher than 200 eV. The figure also shows that the different evaluations (IAEA and NIST) for the ionization cross sections are identical.

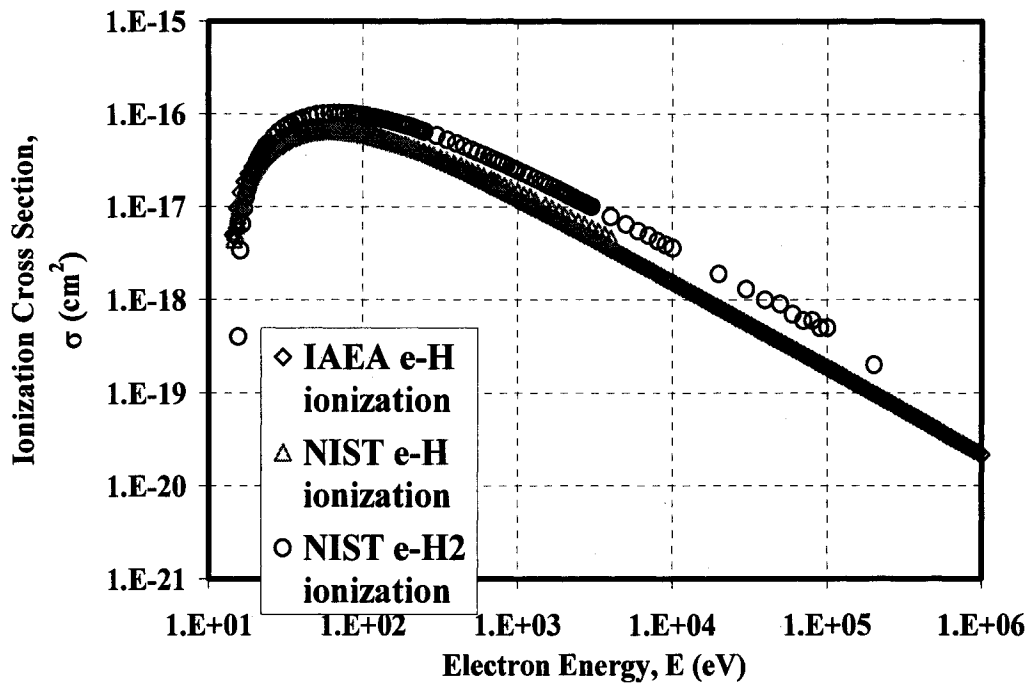


Figure A3.8:  $\sigma^{e/n}$  ionization cross section energy variation<sup>4,5</sup>.

The electron neutral collision frequency and time were evaluated numerically as plotted in Figures A3.9 and A3.10. Figure A3.9 shows the electron energy variation of the electron-H ionization collision frequency while Figure A3.10 shows the electron energy variation of the electron-H ionization collision time. Figure A3.11 shows the electron energy variation of the different types of electron collision frequencies (electron-electron, electron-ion and electron-neutral) at various plasma electron and neutral densities.

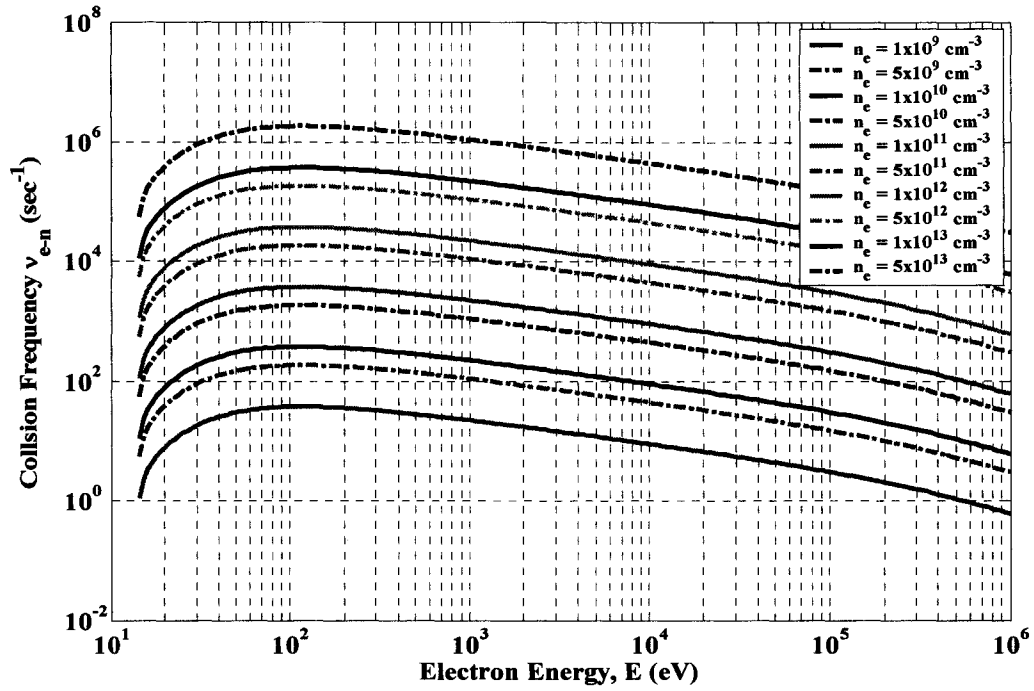


Figure A3.9: Electron-neutral,  $\nu^{e/n}$ , collision frequency energy variation at different densities.

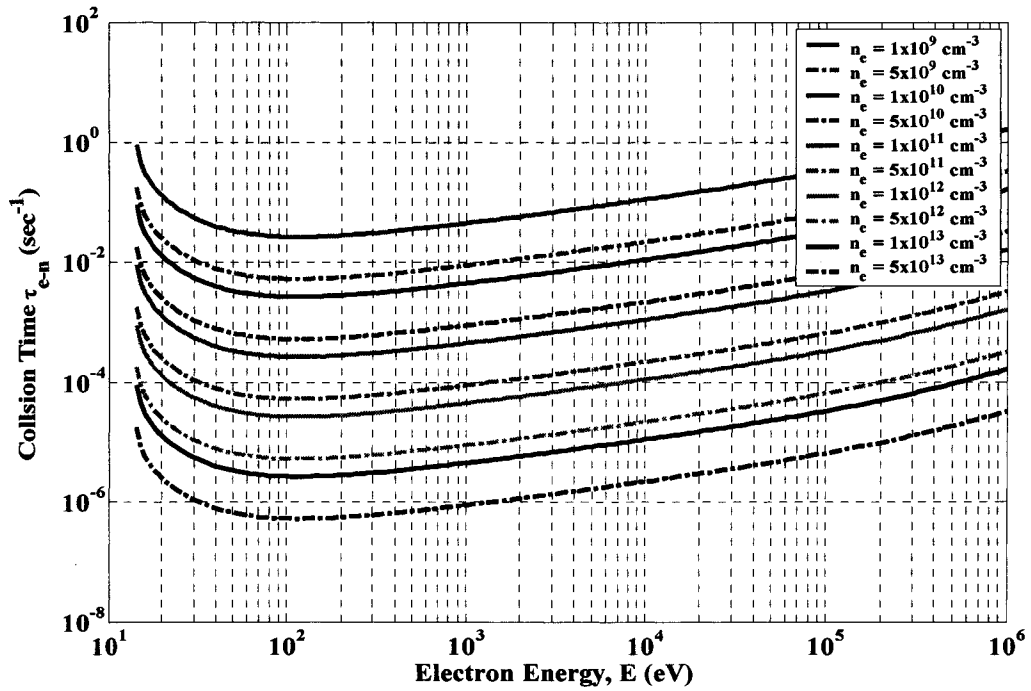
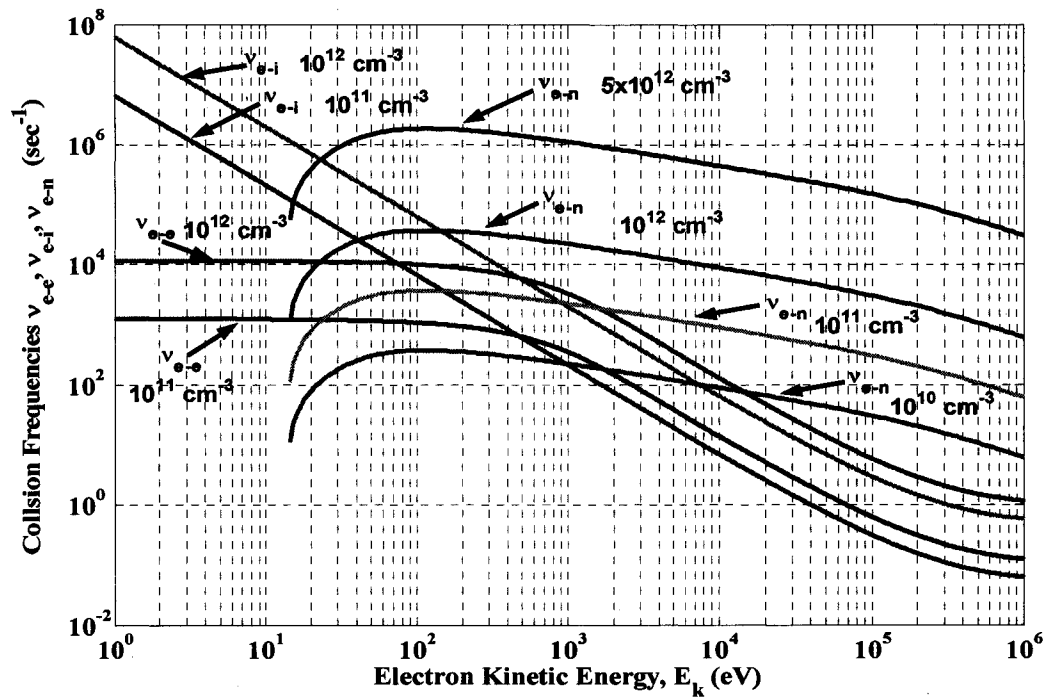


Figure A3.10: Electron-neutral,  $\tau^{e/n}$ , collision time energy variation at different densities.



**Figure A3.11: Comparison between various collision processes at different plasma electron and neutral densities.**

---

<sup>1</sup> B.A. Trubnikov, “Particle Interactions in a Fully Ionized Plasmas”, in Review of Plasma Physics, M.A. Leontovich, editor (Consultant Bureau, New York, 1966), Vol I, p. 105.

<sup>2</sup> J. D. Callen, “Fundamentals of Plasma Physics” book, to be published, can be accessed at <http://homepages.cae.wisc.edu/~callen/>

<sup>3</sup> J.D. Huba, NRL Plasma Formulary, Published by the Naval Research Laboratory, Washington, DC 20375 , (2002)

<sup>4</sup> R. K. Janev, W.D. Langer, K. Evans, Jr., D.E. Post, Jr., “Elementary Processes in Hydrogen-Helium Plasmas”, Springer-Verlag, (1987)

<sup>5</sup> IAEA, The numerical database ALADDIN, at <http://www-amdis.iaea.org/cgi-bin/ALADDIN/select.pl>

<sup>6</sup> The numerical database at National Institute of Standards and Technology NIST <http://www.nist.gov/>

## Appendix 4

# Single Particle Heating Program

### A4.0: Introduction

The single particle heating program used in calculating the net energy gain during single pass through the heating zone and described in Chapters 5 will be fully explained in this appendix.

### A4.1: The Single Particle Heating Model

The single particle heating program solves the electron equation of motion including a microwave electric field model and the Lorentz force:

$$\frac{dm_e \gamma \bar{v}}{dt} = -e(\bar{E} + \bar{v} \times \bar{B}) \quad (\text{A4.1})$$

where,  $\gamma = (1 - \frac{v^2}{c^2})^{-\frac{1}{2}}$ ,  $m$  and  $-e$  are the electron rest mass and charge,  $\bar{v}$  the electron velocity,  $\bar{E}$  the linearly polarized wave electric field,  $\bar{B}$  the magnetic field (the summation of the external static and wave magnetic fields). The electric field is represented by:

$$\bar{E} = E_o e^{-\frac{y^2 + z^2}{w^2}} \text{Cos}(\omega t - k_{\perp} x - \varphi) \hat{z}' \quad (\text{A4.2})$$

where  $E_o = \sqrt{\frac{2PR}{w^2}}$  is the amplitude of the microwave electric field,  $P$  the microwave power in Watts,  $R$  the resistance of free space  $\sim 377$  ohms,  $w = 4$  cm the microwave

beam width,  $\omega = 2\pi f$  the wave angular frequency,  $f = 28 \text{ GHz}$ ,  $k_{\perp} = \frac{N_{\perp}\omega}{c}$  the perpendicular wave number,  $N_{\perp}$  the perpendicular index of refraction,  $c$  the speed of light, and  $\varphi$  the wave-particle initial phase difference. The magnetic field used in the Lorentz equation is composed of two parts: the static field generated by the HSX modular coils and the time varying microwave magnetic field given by:

$$\vec{B}_{Microwave} = \frac{k_{\perp}}{\omega} \vec{E} \quad (\text{A4.3})$$

$$\vec{B} = \vec{B}_{HSX} + \vec{B}_{Microwave} \quad (\text{A4.4})$$

In order to calculate the HSX magnetic field, two separate methods are used. One of them is based on using lookup tables calculated from Biot-Savart law at a specified grid points, and simply interpolates the components of  $\vec{B}$  onto the specified point. The other uses the Biot-Savart law to calculate the field using a stick model of the coils. The major difference between the two methods is the lookup tables are fast, while the Biot-Savart code is more accurate.

## A4.2 Program Input

The program accepts Matlab command line inputs as follows:

```
[Energy_gain] = microwave_heating(mode,rovera,location,choice,PitchorEperp,
                                   ,initialphase,power,totaltime,N_perp,noplot,method)
```

where:

microwave\_heating: program name.

mode:	magnetic mode of operation, a string input takes one of three values 'QHS', 'Mirror' or 'AntiMirror'.
rovera:	particle radial location in unites of r/a.
location:	particle z location in unites of r/a
choice:	string input takes on of two values, 'pitch', or 'Eperp'
pitchorEperp:	[energy,pitch] for 'pitch' or [ $E_{\text{perpendicular}}$ , $E_{\text{parallel}}$ ] for 'Eperp'
relativistic:	0 for non-relativistic, or 1 for relativistic solution
initialphase:	electron-wave initial phase
power:	microwave initial power in kW
totaltime:	total electron integration time
N_perp:	perpendicular index of refraction
noplot:	0 for plotting the output, and 1 for no output plots
method:	1 for look up tables and 2 for Biot-Savart law.
Energy_gain:	the program outputs the electron energy gain

A sample input for electrons with initial energy = 200 eV, initial pitch angle  $\alpha = 85^\circ$ , initial phase  $\phi = 0$  launched at  $r/a = 0$ ,  $Z = 0$ , microwave input power of 50 kW and perpendicular index of refraction  $N_\perp = 1$ .

[Energy\_gain] = **microwave\_heating**('QHS',0,0,'pitch',[0.2 85],0,50,1e-8,1,0,1)

### A4.3 Program Output

The output is represented in graphical format and the final electron energy is dumped on the screen. Figure A4.1 shows the electron trajectory following the magnetic field line in the heating zone in the lab co-ordinates.

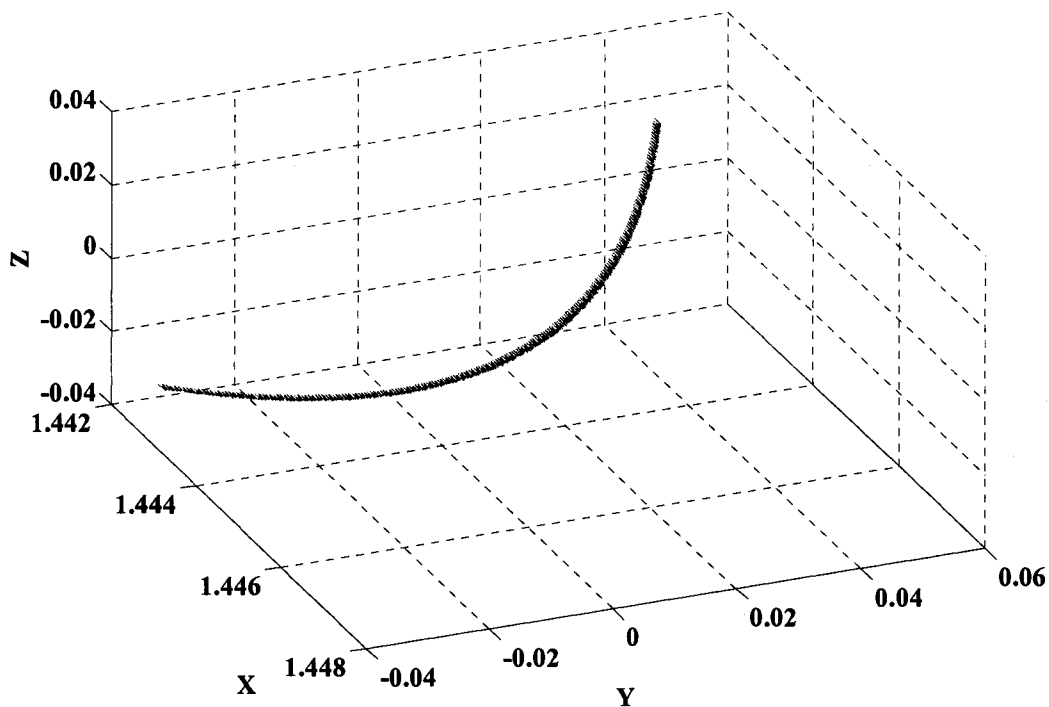


**Figure A4.1: Electron orbit in lab coordinates following magnetic-axis in the heating zone for QHS (thickness of the orbit is the electron gyro-diameter)**

The thickness of the line is the electron gyro-diameter. Figure A4.2 shows the toroidal variation of the magnitude of the magnetic field line that passes through the particle starting point. As the figure shows the magnetic field is symmetric around the resonance point on-axis ( $B = 0.5$  T). The time evolution of the electron energy and particle toroidal location through the heating zone is shown in Figure A4.3.

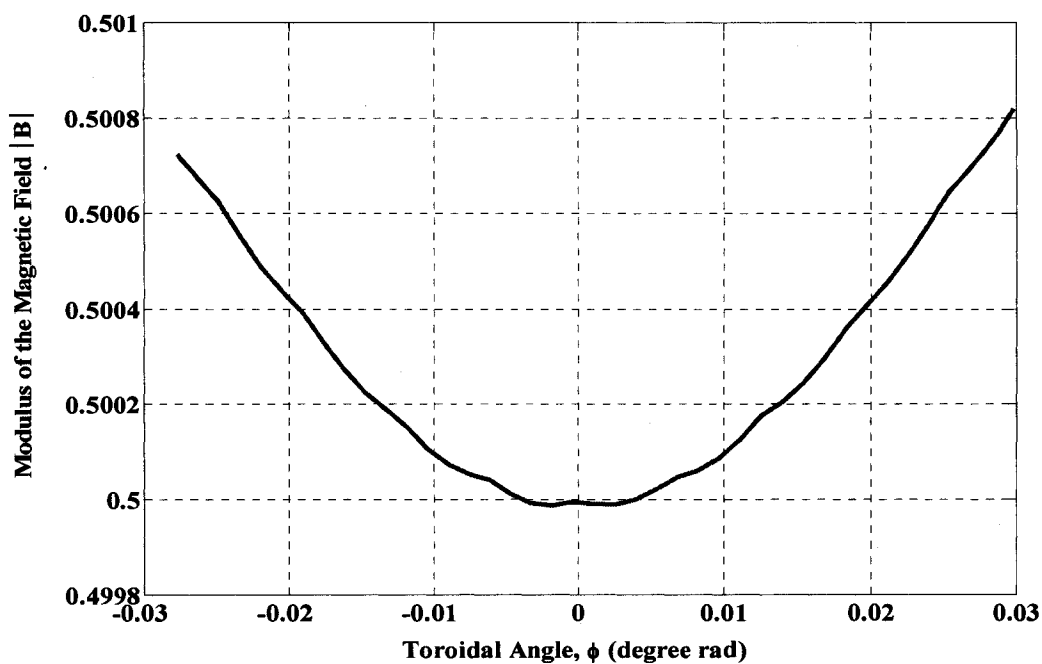


**Figure A4.2: Magnetic field followed by the electron on-axis in the heating zone for QHS**

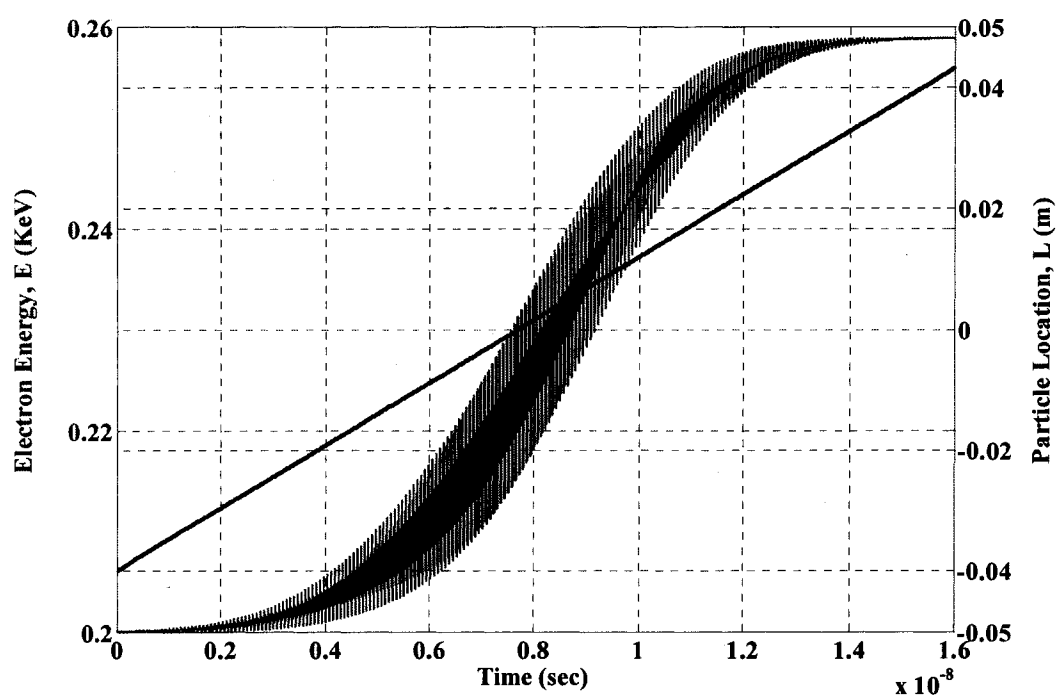


**Figure A4.3: Electron total energy time evolution through the resonance zone (red) and particle location time evolution through resonance zone (blue) in QHS configuration.**

## A4.4 Program Listing

### A4.4.1 Function microwave\_heating

Function [Energy\_gain] = microwave\_heating(mode,rovera,location,choice,PitchorEperp,relativistic,initialphase,power,totalltime,N\_perp,noplot,method)

```
%#####
% PROGRAM RFHEATING
%#####
close all;
%*****
% Constants
%*****
electron_mass = 9.1e-31; % electron mass in Kg
C_speed_of_light = 3e8; % speed of light
%*****
% Loading the needed lookup tables for calculating the magnetic fields
%*****
load coils;
load vessel;
load aux_coils;
if strcmpi(mode,'qhs') == 1
    display('Now loading QHS look up tables');
    load qhs_tables_cr_half;
elseif strcmpi(mode,'mirror') == 1
    display('Now loading Mirror look up tables');
    load mir_tables_cr_half;
elseif strcmpi(mode,'antimirror') == 1
    display('Now loading AntiMirror look up tables');
    load ant_tables_cr_half;
else
    display('You Entered Undefined Mode, modes are: QHS, Mirror and AntiMirror');
    return
end
%*****
% Initial position of the particle
%*****
if strcmpi(mode,'qhs') == 1
    a_qhs = 0.0707;
```

```

R_          = 1.4454+rovera*a_qhs;
[bx_,by_,bz_] = hsxfield_lin_interp(R_,0,0);
B_local     = sqrt(bx_^2+by_^2+bz_^2);
Ratio_local  = 0.5/B_local;
hsxbx       = Ratio_local*hsxbx;
hsxby       = Ratio_local*hsxby;
hsxbz       = Ratio_local*hsxbz;
[bs_bp,cs_bp,ds_bp] = get_coord(R_,0,0,method,mode);
if location == 0
    Ro = 1.4454+rovera*a_qhs;
    PHIo = 0;
    Zo = 0;
    R_axis_bp = Ro;
else
    R_axis_bp = 1.4454+rovera*a_qhs;
    PHI_axis_bp = 0;
    Z_axis_bp = 0;
    delta_phi = 0.01*location/R_axis_bp;
    [R_start,PHI_start,Z_start,ithit]
line_follow_modified(R_axis_bp,PHI_axis_bp,Z_axis_bp,delta_phi,method,mode);
    Ro = R_start(end);
    PHIo = PHI_start(end);
    Zo = Z_start(end);
end
elseif strcmpi(mode,'mirror') == 1
    a_mirror = 0.0564;
    R_       = 1.4364+rovera*a_mirror;
    [bx_,by_,bz_] = hsxfield_lin_interp(R_,0,0);
    B_local     = sqrt(bx_^2+by_^2+bz_^2);
    Ratio_local  = 0.5/B_local;
    hsxbx       = Ratio_local*hsxbx;
    hsxby       = Ratio_local*hsxby;
    hsxbz       = Ratio_local*hsxbz;
    [bs_bp,cs_bp,ds_bp] = get_coord(R_,0,0,method,mode);
    if location == 0
        Ro = 1.4364+rovera*a_mirror;
        PHIo = 0;
        Zo = 0;
        R_axis_bp = Ro;
    else
        R_axis_bp = 1.4364+rovera*a_mirror;
        PHI_axis_bp = 0;
        Z_axis_bp = 0;

```

=

```

    delta_phi = 0.01*location/R_axis_bp;
    [R_start,PHI_start,Z_start,ithit]
line_follow_modified(R_axis_bp,PHI_axis_bp,Z_axis_bp,delta_phi,method,mode);
    Ro = R_start(end);
    PHIo = PHI_start(end);
    Zo = Z_start(end);
end
elseif strcmpi(mode,'antimirror') == 1
    a_antimirror = 0.0871;
    R_ = 1.4559+rovera*a_antimirror;
    [bx_,by_,bz_] = hsxfield_lin_interp(R_,0,0);
    B_local = sqrt(bx_^2+by_^2+bz_^2);
    Ratio_local = 0.5/B_local;
    hsxbx = Ratio_local*hsxbx;
    hsxby = Ratio_local*hsxby;
    hsxbz = Ratio_local*hsxbz;
    [bs_bp,cs_bp,ds_bp] = get_coord(R_,0,0,method,mode);
    if location == 0
        Ro = 1.4559+rovera*a_antimirror;
        PHIo = 0;
        Zo = 0;
        R_axis_bp = Ro;
    else
        R_axis_bp = 1.4559+rovera*a_antimirror;
        PHI_axis_bp = 0;
        Z_axis_bp = 0;
        delta_phi = 0.01*location/R_axis_bp;
        [R_start,PHI_start,Z_start,ithit]
line_follow_modified(R_axis_bp,PHI_axis_bp,Z_axis_bp,delta_phi,method,mode);
        Ro = R_start(end);
        PHIo = PHI_start(end);
        Zo = Z_start(end);
    end
end

r_position = Ro;
z_position = Zo;
phi_position = PHIo;

Xo = r_position*cos(phi_position);
Yo = r_position*sin(phi_position);
Zo = z_position;
%*****

```

```

% Calculating the Energy of the particle in different coordinates
%*****
if strcmpi(choice,'Pitch') == 1
    Energy = PitchorEperp(1); % Energy in KeV
    Pitch_angle = PitchorEperp(2); % Pitch angle in degrees
    % Energy of the Particle with respect to a frame of reference moving with the field line
    V_total = sqrt(2*1.6e-16*Energy/electron_mass);
    V_parallell = V_total*cos(Pitch_angle*pi/180);
    V_perp = V_total*sin(Pitch_angle*pi/180);
    global_title = [mode,' E_t_o_t_a_l = ',num2str(Energy),' KeV \phi = ',num2str(Pitch_angle),'^o, \theta = ',num2str(initialphase),'^o'];
elseif strcmpi(choice,'Eperp') == 1
    E_parallel = PitchorEperp(1)
    E_perp = PitchorEperp(2)
    Energy = E_parallel+E_perp % Energy in KeV
    % Energy of the Particle with respect to a frame of reference moving with the field line
    V_total = sqrt(2*1.6e-16*Energy/electron_mass);
    V_parallell = sqrt(2*1.6e-16*E_parallel/electron_mass);
    V_perp = sqrt(2*1.6e-16*E_perp/electron_mass);
    v2overc2 = (V_total/C_speed_of_light)^2;
    gamma_initial = sqrt(1/(1-v2overc2));
    Pitch_angle = atan(V_perp/V_parallell)*180/pi % Pitch angle in degrees
    global_title = [mode,' E_p_a_r = ',num2str(E_parallel),' KeV ',E_p_e_r = ',num2str(E_perp),' KeV, \phi = ',num2str(Pitch_angle),'^o, \theta = ',num2str(initialphase),'^o'];
else
    display('You Entered Undefined Entry: Pitch for using pitch angle')
    display('You have to enter the Initial Energy and Pitch Angle')
    display('Or Eperp and you need to enter the Initial E_parallel and E_perpendicular');
    return
end
% Initial Phase of the particle
initial_phase = 0;
% Transforming the component of particle velocity between frames
[bs,cs,ds] = get_coord(Ro,PHIo,Zo,method,mode);
V_parallell_vector = V_parallell*bs;
V_perp_cos = V_perp*cos(initial_phase*pi/180)*cs;
V_perp_sin = V_perp*sin(initial_phase*pi/180)*ds;
Vx = V_parallell_vector(1)+V_perp_cos(1)+V_perp_sin(1);
Vy = V_parallell_vector(2)+V_perp_cos(2)+V_perp_sin(2);
Vz = V_parallell_vector(3)+V_perp_cos(3)+V_perp_sin(3);
%*****
% Initial conditions and the ode solver

```

```

%*****
tspan = [0 totaltime];
y_initial = [Vx;Vy;Vz;Xo;Yo;Zo];
options = odeset('AbsTol',1e-9,'RelTol',1e-7);
if relativistic == 1
    display('Relativistic Equation of Motion is being Used')
    [t,y] =
ode45(@relmwheating,tspan,y_initial,options,initialphase,power,bs_bp,cs_bp,ds_bp,N_p
erp);
else
    display('Non Relativistic Equation of Motion is being Used')
    [t,y] =
ode45(@nonrelmwheating,tspan,y_initial,options,initialphase,power,bs_bp,cs_bp,ds_bp,
N_perp);
end
sizeoft = size(t);
%*****
sizeofy = size(y);
%*****
% Calculating the particle energy along the trajectory
%*****
E_x = 0.5*electron_mass*(y(:,1).^2)/1.6e-16;
E_y = 0.5*electron_mass*(y(:,2).^2)/1.6e-16;
E_z = 0.5*electron_mass*(y(:,3).^2)/1.6e-16;
E_total = E_x+E_y+E_z;
E_average = mean(E_total);
length_of_time = length(t);
DE = 1000*(mean(E_total(end-1000:end))-mean(E_total(1:1000)));
Energy_gain = DE;
display(['Energy gain = ' num2str(Energy_gain),' (eV)']);
%*****
% Calculating the part of the magnetic Axis of the Machine the particle will follow
%*****
R_final = sqrt(y(end,4)^2+y(end,5)^2);
PHI_final = atan(y(end,5)/y(end,4))-PHIo;
Z_final = y(end,6);
[R_mag_axis,PHI_mag_axis,Z_mag_axis,ithit] =
line_follow_modiefied(Ro,PHIo,Zo,PHI_final,method,mode);
X_mag_axis = R_mag_axis.*cos(PHI_mag_axis);
Y_mag_axis = R_mag_axis.*sin(PHI_mag_axis);
%*****
% Calculating Mod B for this part.
%*****
num = length(R_mag_axis);

```

```

for j=1:num
    [bx_axis,by_axis,bz_axis]
hsxfield_lin_interp(R_mag_axis(j),PHI_mag_axis(j),Z_mag_axis(j));
    Mod_B(j) = sqrt(bx_axis^2+by_axis^2+bz_axis^2);
end
%*****
% Calculating the particle location.
%*****
R_location = sqrt(y(:,4).^2+y(:,5).^2);
PHI_location = atan(y(:,5)./y(:,4));
particle_location = R_axis_bp*PHI_location;
%*****
% Plotting the results
%*****
if noplot == 0
    % Plotting the particle energy with time
    figure(1)
    plot(t,E_x,t,E_y,t,E_z,t,E_total)
    h2 = title(['Electron Energy Time Variation for ',global_title]);
    h3 = xlabel('Time (sec)');
    h4 = ylabel('Electron Energy');
    h5 = legend('E_x','E_y','E_z','E_t_o_t_a_l');
    lh = [h2 h3 h4 h5];
    set(lh,'FontSize',10,'FontWeight','bold');
    grid on

    % Plotting the modelus of the field line
    figure(2)
    plot(PHI_mag_axis,Mod_B,'r','LineWidth',3)
    h2 = title(['midB\mid along particle trajectory for ',global_title]);
    h3 = xlabel('\phi (degree rad)');
    h4 = ylabel('mod B');
    lh = [h2 h3 h4];
    set(lh,'FontSize',10,'FontWeight','bold');
    grid on
    % Plotting the particle position x versus y
    figure(3)
    plot(X_mag_axis,Y_mag_axis,'k','LineWidth',3)
    hold on
    plot(y(:,4),y(:,5))
    h2 = title(['Electron Position Variation 2D for ',global_title]);
    h3 = xlabel('X');
    h4 = ylabel('Y');

```

```

lh = [h2 h3 h4];
set(lh,'FontSize',10,'FontWeight','bold');
grid on
% Plotting the particle position in real space
figure(4)
plot3(X_mag_axis,Y_mag_axis,Z_mag_axis,'k','LineWidth',3)
hold on
plot3(y(:,4),y(:,5),y(:,6),'r')
h2 = title(['Electron Position 3D Variation for ',global_title]);
h3 = xlabel('X');
h4 = ylabel('Y');
h5 = zlabel('Z');
lh = [h2 h3 h4 h5];
set(lh,'FontSize',10,'FontWeight','bold');
grid on
% Plotting the particle Energy change during the resonance
figure(5)
plot(t,E_total,'r')
h2 = title(['Electron Energy Time Variation for ',global_title]);
h3 = xlabel('Time (sec)');
h4 = ylabel('Electron Energy (KeV)');
h5 = legend('E_t_o_t_a_l');
lh = [h2 h3 h4 h5];
set(lh,'FontSize',10,'FontWeight','bold');
grid on

% Plotting the particle Energy change during the resonance
figure(6)
[AX,H1,H2] = plotyy(t,E_total,t,particle_location);
set(get(AX(1),'Ylabel'),'String','Energy Gain (KeV)','FontSize',12,'FontWeight','bold');
set(AX(1),'YColor',[1 0 0]);
set(get(AX(2),'Ylabel'),'String','ParticleLocation (m)','FontSize',12,'FontWeight','bold');
set(AX(2),'YColor',[0 0 1]);
h2 = title(['Electron Energy and Z position Time Variation for ',global_title]);
h3 = xlabel('Time (sec)');
lh = [h2 h3 AX(1) AX(2)];
set(lh,'FontSize',12,'FontWeight','bold');
set(H1,'LineWidth',2,'Color','red');
set(H2,'LineWidth',3,'Color','blue');
grid on
end
%#####
% End of the program RFHEATING

```

```
%#####
```

#### A4.4.2 Function nonrelmwheating

```
function ydot = nonrelmwheating(t,y,const,power,bs_bp,cs_bp,ds_bp,N_perp)
%*****
% Constants
%*****
Bo = 1.0; % Magnetic Field of 1 Tesla to calculate the wave angular
frequency ~ 28 Ghz
w = 0.02; % Microwave Gaussian Beam Width
e = 1.6e-19; % Electron Charge in Coloumb
m = 9.1e-31; % Electron mass in Kg
omega = e*Bo/m; % Microwave angular frequency f ~ 28 Ghz
e_over_m = e/m; % Electron Charge to Mass Ratio
speed_of_light = 3e8; % Speed of Light
Eo = sqrt(power*1e7*377/2/pi); % Electric Field in Volts/m
k_perp = N_perp*omega/speed_of_light; % Perpendicular wave number
%*****
% Calculating the particle position in r,phi,z format
%*****
r_position = sqrt(y(4)^2+y(5)^2);
z_position = y(6);
phi_position = atan(y(5)/y(4));

%*****
% Calculating the microwave Electric and Magnetic field components
%*****
phase_shift = const*pi;
y_compenent = cs_bp(2);
z_compenent = cs_bp(3);
r2_microwave_beam = y(5)^2+y(6)^2;
E_total = Eo*exp(-r2_microwave_beam/w^2)*cos(omega*t-k_perp*y(4)-phase_shift);
E_y = y_compenent*E_total;
E_z = z_compenent*E_total;
B_microwave_y = z_compenent*k_perp*E_total/omega;
B_microwave_z = -y_compenent*k_perp*E_total/omega;
%*****
% Using the look up tables to Calculate the HSX magnetic field
%*****
[bx,by,bz] = hsxfield_lin_interp(r_position,phi_position,z_position);
Bx = bx; % Magnetic Field on the X-direction in Tesla
By = by+B_microwave_y; % Magnetic Field on the Y-direction in Tesla
```

```

Bz = bz+B_microwave_z;      % Magnetic Field on the Z-direction in Tesla
%*****
% Setting the differential equations
%*****
y1dot = e_over_m*(By*y(3)-Bz*y(2));
y2dot = e_over_m*((Bz*y(1)-Bx*y(3))-E_y);
y3dot = e_over_m*((Bx*y(2)-By*y(1))-E_z);
y4dot = y(1);
y5dot = y(2);
y6dot = y(3);
ydot = [y1dot;y2dot;y3dot;y4dot;y5dot;y6dot];
%*****
% End
%*****

```

#### A4.4.3 Function relmwheating

```

function ydot = relmwheating(t,y,const,power,bs_bp,cs_bp,ds_bp,N_perp)
%*****
% Constants
%*****
Bo = 1.0;      % Magnetic Field of 1 Tesla to calculate the wave angular
frequency ~ 28 Ghz
w = 0.02;      % Microwave Gaussian Beam Width
e = 1.6e-19;    % Electron Charge in Coloumb
m = 9.1e-31;    % Electron mass in Kg
omega = e*Bo/m; % Microwave angular frequency f ~ 28 Ghz
e_over_m = e/m; % Electron Charge to Mass Ratio
speed_of_light = 3e8; % Speed of Light
Eo = sqrt(power*1e7*377/2/pi); % Electric Field in Volts/m
k_perp = N_perp*omega/speed_of_light; % Perpendicular wave number
%*****
% Calculating the particle position in r,phi,z format
%*****
r_position = sqrt(y(4)^2+y(5)^2);
z_position = y(6);
phi_position = atan(y(5)/y(4));
%*****
% Calculating the microwave Electric and Magnetic field components
%*****
phase_shift = const*pi;
y_compenent = cs_bp(2);

```

```

z_component = cs_bp(3);;
r2_microwave_beam = y(5)^2+y(6)^2;
E_total = Eo*exp(-r2_microwave_beam/w^2)*cos(omega*t-k_perp*y(4)-phase_shift);
E_y = y_component*E_total;
E_z = z_component*E_total;
B_microwave_y = z_component*k_perp*E_total/omega;
B_microwave_z = -y_component*k_perp*E_total/omega;
%*****
% Calculating the relativistic term
%*****
V_total2 = y(1)^2+y(2)^2+y(3)^2;
v2overc2 = V_total2/speed_of_light^2;
gamma = 1/sqrt(1-v2overc2);
one_over_gamma = 1/gamma;
%*****
% Using the look up tables to Calculate the HSX magnetic field
%*****
[bx,by,bz] = hsxfield_lin_interp(r_position,phi_position,z_position);
Bx = bx; % Magnetic Field on the X-direction in Tesla
By = by+B_microwave_y; % Magnetic Field on the Y-direction in Tesla
Bz = bz+B_microwave_z; % Magnetic Field on the Z-direction in Tesla
%*****
% Setting the differential equations
%*****
multiplier = (E_y*y(2)+E_z*y(3))/speed_of_light^2;
y1dot = one_over_gamma*e_over_m*((By*y(3)-Bz*y(2))+multiplier*y(1));
y2dot = one_over_gamma*e_over_m*((Bz*y(1)-Bx*y(3))-E_y+multiplier*y(2));
y3dot = one_over_gamma*e_over_m*((Bx*y(2)-By*y(1))-E_z+multiplier*y(3));
y4dot = y(1);
y5dot = y(2);
y6dot = y(3);
ydot = [y1dot;y2dot;y3dot;y4dot;y5dot;y6dot];
%*****
% End
%*****

```

## Appendix 5

# Single Particle Drift Orbit Program

### A5.0: Introduction

The single particle guiding center drift orbits program used in the calculations for Chapter 6 will be explained in this appendix.

### A5.1: The Single Particle Drift Orbit Model

The code solves the guiding center drift orbit equations given by:

$$\frac{dr}{dt} = -\frac{1}{B_o r} \frac{\partial \Phi}{\partial \vartheta} - \frac{1}{B_o r} \left( \frac{\mu}{e} + \frac{eB}{m} \rho_{\parallel}^2 \right) \frac{\partial B}{\partial \vartheta} \quad (6.14)$$

$$\frac{d\vartheta}{dt} = \frac{1}{B_o r} \frac{\partial \Phi}{\partial r} + \frac{1}{B_o r} \left( \frac{\mu}{e} + \frac{eB}{m} \rho_{\parallel}^2 \right) \frac{\partial B}{\partial r} + \frac{t}{g} \frac{eB^2}{m} \rho_{\parallel} \quad (6.15)$$

$$\frac{d\varphi}{dt} = \frac{1}{g} \frac{eB^2}{m} \rho_{\parallel} \quad (6.16)$$

$$\frac{d\rho_{\parallel}}{dt} = -\frac{1}{g} \frac{\partial \Phi}{\partial \varphi} - \frac{1}{g} \left( \frac{\mu}{e} + \frac{eB}{m} \rho_{\parallel}^2 \right) \frac{\partial B}{\partial \varphi} \quad (6.17)$$

where  $r$  is the normalized radial variable,  $\vartheta$  and  $\varphi$  are the poloidal and toroidal angle variables,  $\rho_{\parallel}$  the parallel gyro-radius,  $\mu$  the magnetic moment, and  $\Phi$  is the scalar electric potential. The spectrum is specified in Boozer co-ordinates as:

$$B = B_o \sum_{nm} b_{nm}(r) \cos(n\varphi - m\vartheta) \quad (6.18)$$

where  $B_o = 0.5$  Tesla,  $b_{nm}(r)$  are the Fourier spectrum coefficients as a function of  $r$ ,  $n$  and  $m$  the toroidal and poloidal mode numbers and  $\varphi$  and  $\vartheta$  the toroidal and poloidal angles.

## A5.2 Program Input

The program accepts Matlab command line inputs as follows:

**[t\_end\_out,p\_out,E\_out,w\_out,w\_a\_out] = particle\_drift\_heating(mode,heating,  
rovera,phi,theta,initialenergy,pitchangle,totaltime,noplot)**

where:

**particle\_drift\_heating:** program name.

**mode:** magnetic mode of operation, a string input takes one of three values 'QHS', 'Mirror' or 'AntiMirror'.

**Heating:** 0 for no microwave heating included, and 1 for adding microwave heating

**rovera:** particle radial location in unites of  $r/a$ .

**phi:** : particle initial phi location in radians

**theta:** particle initial theta location in radians

**initialenergy:** particle initial energy in keV

**pitchangle:** particle initial pitch angle

**total time:** particle total integration time

**noplot:** 0 for plotting the output, and 1 for no output plots

<code>t_end_out:</code>	program out, particle time at the last time step
<code>p_out:</code>	program out, resonance zone crossing probability
<code>E_out:</code>	program out, particle final kinetic energy in eV
<code>w_out:</code>	program out, particle drift orbit width in meters
<code>w_a_out:</code>	program out, particle drift orbit width in units of $r/a$

A sample input for 200 eV electrons launched at  $r/a = 0.05$  inside the heating zone with initial pitch angle  $\alpha = 85^\circ$ , initial toroidal angle  $\varphi = 0$ , initial poloidal angle  $\vartheta = \pi/2$ , and integration time  $10^{-4}$  seconds is given by:

```
[t_end_out,p_out,E_out,w_out,w_a_out] = particle_drift_heating('QHS',1,0.05,0,pi/2,0.2,85,1e-4,0)
```

### A5.3 Program Output

The program produces no output files. The output is dumped to the screen in text and graphical format. Figures A5.1, A5.2 show examples of  $r$ - $\theta$  and  $r$ - $\varphi$  polar plots of drift orbits for energetic electrons (5 keV, initial pitch angle  $\alpha = 85^\circ$ ,  $\vartheta = 0^\circ$ ,  $\varphi = 0^\circ$ ,  $r/a = 0.5$ ) in the Mirror magnetic configuration. Electrons were launched outside the heating zone ( $r/a = 0.1$ ) so the microwave heating was not included.

Figure A5.3 show the  $r$ - $\theta$  polar plot of the of 100 eV electron orbit launched at  $r/a = 0.05$  inside the heating zone with initial pitch angle  $\alpha = 85^\circ$ ,  $\vartheta = 0^\circ$ ,  $\varphi = 0^\circ$ . Figure A5.4 show the time evolution of the electron magnetic moment as a result of multiple passes through the heating zone.

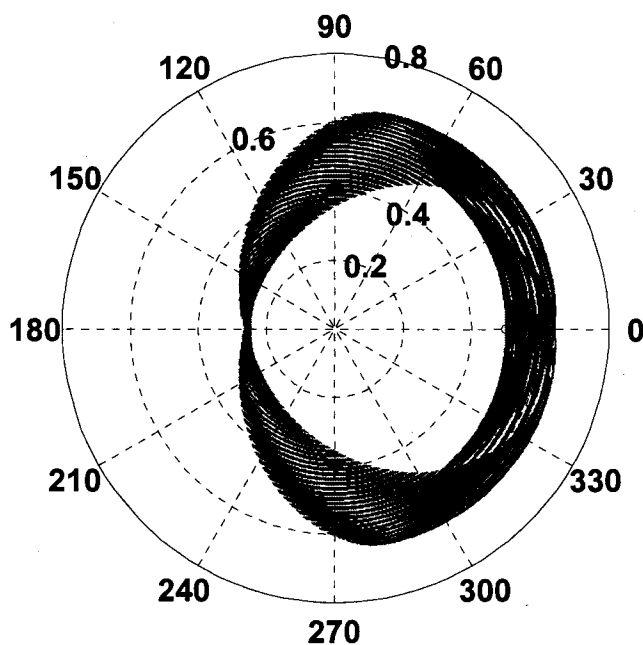


**Figure A5.1:**  $r$ - $\theta$  plot of electron drift orbit for  $\varepsilon = 5$  keV,  $r/a = 0.5$ ,  $\alpha = 85^\circ$ ,  $\theta = 0^\circ$  and  $\varphi = 0^\circ$  in the Mirror configuration, integration time =  $5 \times 10^{-4}$  sec.

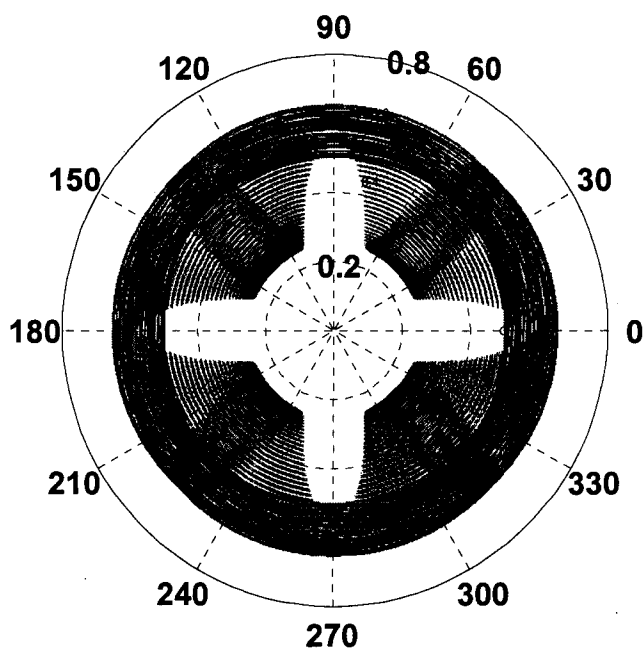


**Figure A5.2:**  $r$ - $\phi$  plot of electron drift orbit for  $\varepsilon = 5$  keV,  $r/a = 0.5$ ,  $\alpha = 85^\circ$ ,  $\theta = 0^\circ$  and  $\varphi = 0^\circ$  in the Mirror configuration, integration time =  $10^{-4}$  sec.

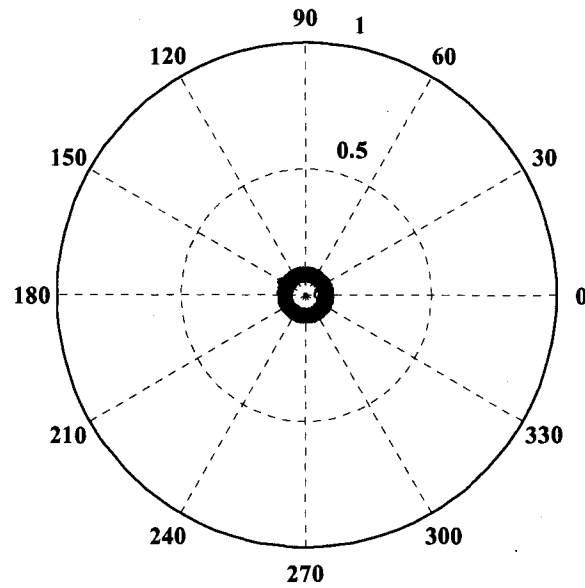


Figure A5.3:  $r$ - $\theta$  plot of electron drift orbit for  $\varepsilon = 100$  eV,  $r/a = 0.05$ ,  $\alpha = 85^\circ$ ,  $\theta = 0^\circ$  and  $\varphi = 0^\circ$  in the QHS configuration, integration time =  $10^{-4}$  sec.

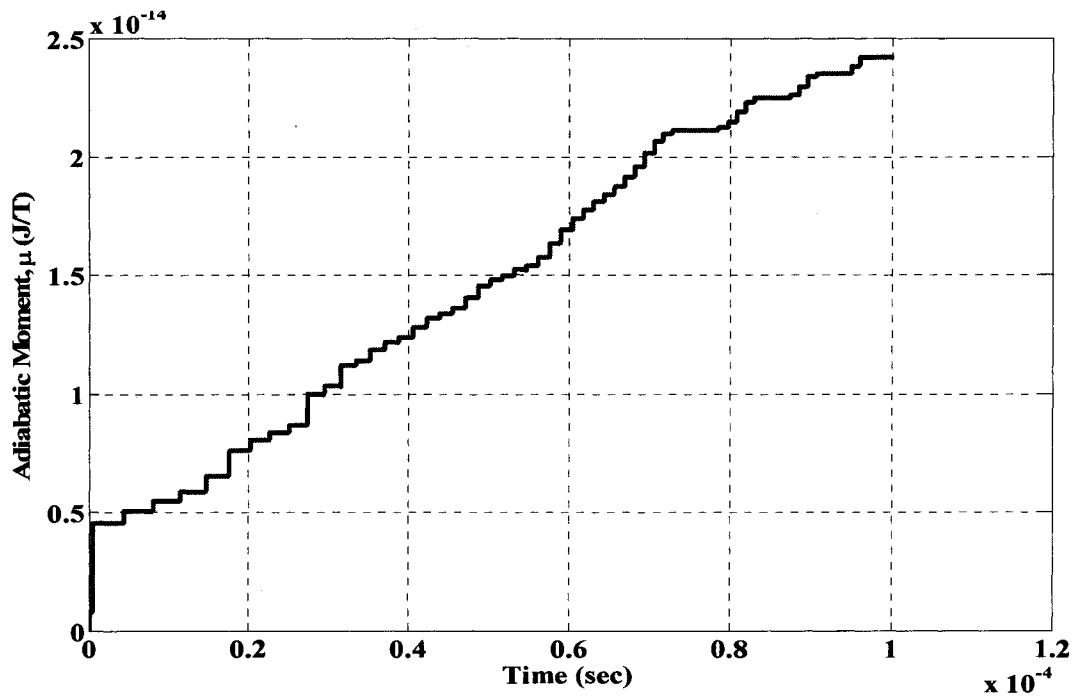


Figure A5.4: The time evolution for the magnetic moment for the electron shown in Figure 6.11

## A5.4 Program Listing

### A5.4.1 Function particle\_drift\_heating

```

Function[t_end_out,p_out,E_out,w_out,w_a_out]=particle_drift_heating(mode,heating,rovera,phi,theta,initialenergy,pitchangle,totaltime,noplot)
%#####
% PROGRAM Particle_Drift
%#####
close all;
%*****
% Constants
%*****
Bo      = 0.5;
r_over_a      = rovera;
electron_mass  = 9.1e-31; % electron mass in Kg
C_speed_of_light = 3e8;  % speed of light
electron_charge = 1.6e-19; % electron charge in Coloumbs
%*****
% Mode of Operation
%*****
if strcmpi(mode,'qhs') == 1
    a_average      = 0.113; % plasma average minor radius
    display('Now Calculating Drift Orbits for QHS Configuration');
elseif strcmpi(mode,'mirror') == 1
    a_average      = 0.1198; % plasma average minor radius
    display('Now Calculating Drift Orbits for Mirror Configuration');
elseif strcmpi(mode,'antimirror') == 1
    a_average      = 0.1198; % plasma average minor radius
    display('Now Calculating Drift Orbits for AntiMirror Configuration');
else
    display('You Entered Undefined Mode, modes are: QHS, Mirror and AntiMirror');
    return
end
%*****
% Calculating the initial conditions
%*****
Energy      = 1000*initialenergy*electron_charge; % Energy in Jouls
Pitch_angle = pitchangle; % Pitch angle in degrees
E_parrall = Energy*cos(Pitch_angle*pi/180)^2;
E_perp     = Energy*sin(Pitch_angle*pi/180)^2;
V_parallel = sqrt(2*E_parrall/electron_mass);

```

```

if strcmpi(mode,'qhs') == 1
    A = [1.05 0.0024 -0.02381 0.086768 -0.07433 0.0060676];
    iota = A(1)+A(2)*rovera+A(3)*rovera^2+
           A(4)*rovera^3+A(5)*rovera^4+A(6)*rovera^5;
    angle_phi = 0:2*pi/100:2*pi;
    angle_theta = iota*angle_phi;
    b41 = 0.14*r_over_a;
    db41dr = 0.14/a_average;
    B = Bo*(1-b41*cos(4*phi-theta));
    B2 = B^2;
    dBdr = -Bo*db41dr*cos(4*phi-theta);
    dBdtheta = -Bo*b41*sin(4*phi-theta);
    dBdphi = 4*Bo*b41*sin(4*phi-theta);
    for lm = 1:length(angle_phi)
        phi_new = angle_phi(lm);
        theta_new = angle_theta(lm);
        b41 = 0.14*r_over_a;
        db41dr = 0.14/a_average;
        B_magnetic = Bo*(1-b41*cos(4*phi_new-theta_new));
        Bmag2 = B_magnetic^2;
        dBmagdr = -Bo*db41dr*cos(4*phi_new-theta_new);
        dBmagdtheta = -Bo*b41*sin(4*phi_new-theta_new);
        dBmagdphi = 4*Bo*b41*sin(4*phi_new-theta_new);
        magnetic_field(lm) = B_magnetic;
    end
elseif strcmpi(mode,'mirror') == 1
    A = [1.0668 0.0077317
    -0.054029 0.24963 -0.30516 0.16543];
    iota =
    A(1)+A(2)*rovera+A(3)*rovera^2+A(4)*rovera^3+A(5)*rovera^4+A(6)*rovera^5;
    angle_phi = 0:2*pi/100:2*pi;
    angle_theta = iota*angle_phi;
    b41 = 0.14*r_over_a;
    b40 = 0.08;
    db41dr = 0.14/a_average;
    B = Bo*(1-b41*cos(4*phi-theta)+b40*cos(4*phi));
    B2 = B^2;
    dBdr = -Bo*db41dr*cos(4*phi-theta);
    dBdtheta = -Bo*b41*sin(4*phi-theta);
    dBdphi = 4*Bo*(b41*sin(4*phi-theta)-b40*sin(4*phi));
    for lm = 1:length(angle_phi)
        b41 = 0.14*r_over_a;
        b40 = 0.08;

```

```

        phi_new      = angle_phi(lm);
        theta_new    = angle_theta(lm);
        db41dr       = 0.14/a_average;
        B_magnetic   = Bo*(1-b41*cos(4*phi_new-
theta_new)+b40*cos(4*phi_new));
        Bmag2        = B_magnetic^2;
        dBmagdr      = -Bo*db41dr*cos(4*phi_new-theta_new);
        dBmagdtheta  = -Bo*b41*sin(4*phi_new-theta_new);
        dBmagdphi    = 4*Bo*(b41*sin(4*phi_new-theta_new)-
b40*sin(4*phi_new));
        magnetic_field(lm) = B_magnetic;
    end
elseif strcmpi(mode,'antimirror') == 1
    A    = [1.0304 0.0031904 -0.046077 0.11165 -0.10064 0.076335];
    iota =
A(1)+A(2)*rovera+A(3)*rovera^2+A(4)*rovera^3+A(5)*rovera^4+A(6)*rovera^5;
    angle_phi = 0:2*pi/100:2*pi;
    angle_theta = iota*angle_phi;
    b41        = 0.14*r_over_a;
    b40        = 0.08;
    db41dr     = 0.14/a_average;
    B          = Bo*(1-b41*cos(4*phi-theta)-b40*cos(4*phi));
    B2         = B^2;
    dBdr       = -Bo*db41dr*cos(4*phi-theta);
    dBdtheta   = -Bo*b41*sin(4*phi-theta);
    dBdphi     = 4*Bo*(b41*sin(4*phi-theta)+b40*sin(4*phi));

    for lm = 1:length(angle_phi)
        b41      = 0.14*r_over_a;
        b40      = 0.08;
        phi_new   = angle_phi(lm);
        theta_new = angle_theta(lm);
        db41dr    = 0.14/a_average;
        B_magnetic = Bo*(1-b41*cos(4*phi_new-theta_new)-b40*cos(4*phi_new));
        Bmag2     = B_magnetic^2;
        dBmagdr   = -Bo*db41dr*cos(4*phi_new-theta_new);
        dBmagdtheta = -Bo*b41*sin(4*phi_new-theta_new);
        dBmagdphi  = 4*Bo*(b41*sin(4*phi_new-theta_new)+b40*sin(4*phi_new));
        magnetic_field(lm) = B_magnetic;
    end
else
    display('You Entered Undefined Mode, modes are: QHS, Mirror and AntiMirror');
    return

```

```

end
mu      = E_perp/B;
muo     = E_perp/B;
mu_over_e = mu/electron_charge;
rho_parallel_o = V_parallel*electron_mass/(electron_charge*B);
y1o = rovera*a_average;
y2o = theta;
y3o = phi;
y4o = rho_parallel_o;
y5o = muo;
global_title = [mode,' E_t_o_t_a_l = ',num2str(initialenergy),' keV \phi = ',num2str(Pitch_angle),'^o'];
%*****
% Initial conditions and the ode solver
%*****
tspan = [0 totaltime];
y_initial = [y1o;y2o;y3o;y4o;y5o];
counter = 0;
options = odeset('Events',@loss_check_heating,'AbsTol',1e-9,'RelTol',1e-7,'refine',100);
[t,y] = ode45(@drift_heating,tspan,y_initial,options,mode,heating);
%*****
% Calculating the Probability and Crossing Times
%*****
phi_minimum      = -0.02767591503494;    % -4 cm from left at the center of the
Box Port
phi_maximum      = 0.02767591503494;    % 4 cm from right at the center of the
Box Port
phi_turns        = mod(y(:,3),2*pi);
phi_location     = find(phi_turns>phi_minimum & phi_turns<phi_maximum);
phi_value        = phi_turns(phi_location);
theta_value      = y(phi_location,2);
r_value          = y(phi_location,1);
t_value          = t(phi_location);
r_limit          = 0.1*a_average;
total_number_of_r_points = length(r_value);
r_location       = find(r_value<r_limit);
final_phi        = phi_value(r_location);
final_theta      = theta_value(r_location);
final_r          = r_value(r_location);
number_of_crossing = length(r_location);
crossing_probability = number_of_crossing/total_number_of_r_points;

```

```

Case_running = ['  Mode = 'mode,', E_i_n_i = 'num2str(initialenergy),' KeV, r/a =
',num2str(rovera),', phi = 'num2str(phi),', theta = 'num2str(theta),', pitch angle =
',num2str(pitchangle)];
%*****
% Calculating the Final Particle Energy
%*****
r_final = y(end,1);
theta_final = y(end,2);
phi_final = y(end,3);
rho_final = y(end,4);
mu_final = y(end,5);
rovera_final = r_final/a_average;
if strcmpi(mode,'qhs') == 1
    r_over_arovera_final = r_over_a;
    phi_new = phi_final;
    theta_new = theta_final;
    b41 = 0.14*r_over_a;
    db41dr = 0.14/a_average;
    B_final = Bo*(1-b41*cos(4*phi_new-theta_new));
    B2_f = B_final^2;
    dBdr_f = -Bo*db41dr*cos(4*phi_new-theta_new);
    dBdtheta_f = -Bo*b41*sin(4*phi_new-theta_new);
    dBdphi_f = 4*Bo*b41*sin(4*phi_new-theta_new);
elseif strcmpi(mode,'mirror') == 1
    r_over_arovera_final = r_over_a;
    phi_new = phi_final;
    theta_new = theta_final;
    b41 = 0.14*r_over_a;
    b40 = 0.08;
    db41dr = 0.14/a_average;
    B_final = Bo*(1-b41*cos(4*phi_new-theta)+b40*cos(4*phi_new));
    B2_f = B_final^2;
    dBdr_f = -Bo*db41dr*cos(4*phi_new-theta_new);
    dBdtheta_f = -Bo*b41*sin(4*phi_new-theta_new);
    dBdphi_f = 4*Bo*(b41*sin(4*phi_new-theta_new)-b40*sin(4*phi_new));
elseif strcmpi(mode,'antimirror') == 1
    r_over_arovera_final = r_over_a;
    phi_new = phi_final;
    theta_new = theta_final;
    b41 = 0.14*r_over_a;
    b40 = 0.08;
    db41dr = 0.14/a_average;
    B_final = Bo*(1-b41*cos(4*phi_new-theta)-b40*cos(4*phi_new));

```

```

B2_f      = B_final^2;
dBdr_f    = -Bo*db41dr*cos(4*phi_new-theta_new);
dBdtheta_f = -Bo*b41*sin(4*phi_new-theta_new);
dBdphi_f  = 4*Bo*(b41*sin(4*phi_new-theta_new)+b40*sin(4*phi_new));
else
    display('You Entered Undefined Mode, modes are: QHS, Mirror and AntiMirror');
    return
end

V_parallel_final = B_final*1.6E-19*rho_final/(9.1E-31);
E_parallel_final = 0.5*9.1E-31*V_parallel_final^2/1.6E-19;
E_perpendicular_final = y(end,5)*B_final/1.6E-19;
V_perpendicular_final = sqrt(2*E_perpendicular_final*1.6E-19/9.1E-31);
E_total_final = E_parallel_final+E_perpendicular_final;
final_pitch_angle = abs(atan(V_perpendicular_final/V_parallel_final)*180/pi);
%*****
% Calculating the Orbit Width
%*****
[maximum_r,maximum_r_indexes] = max(y(:,1));
maximum_r_over_a = maximum_r/a_average;
maximum_theta = y(maximum_r_indexes,2);
[minimum_r,minimum_r_indexes] = min(y(:,1));
minimum_r_over_a = minimum_r/a_average;
minimum_theta = y(minimum_r_indexes,2);
drift_orbit_width = maximum_r-minimum_r;
drift_orbit_width_in_units_of_r_over_a = drift_orbit_width/a_average;
t_end_out = t(end)
%*****
% Printing Out Results
%*****
if crossing_probability > 0
    heating_zone_indexes = find(phi_turns>phi_minimum & phi_turns<phi_maximum
    & y(:,1)<r_limit);
    indx_difference = diff(heating_zone_indexes);
    t_heating_zone = t(heating_zone_indexes);
    inner_indexes = find(indx_difference>1);
    if length(inner_indexes) == 0
        times = t_heating_zone;
        total_time = t_heating_zone(end)-t_heating_zone(1);
        time_fraction = total_time/t(end);
    fprintf(1,'\n=====
    fprintf(1, '%s ', Case_running);

```

```

fprintf(1,'\n=====
===== \n');
    fprintf(1,'\n 1- Total Time of particle following      = %8.4E Sec\n',t(end));
    fprintf(1,'\n 2- Total Time Particle stays in Resonance Zone      = %8.4E
Sec\n',total_time);
    fprintf(1,'\n 3- Fraction of Time Particle is in Resonance Zone = %8.4E
\n',time_fraction);
    fprintf(1,'\n 4- Resonance Zone Crossing Probability      = %8.4E
\n',crossing_probability);
    fprintf(1,'\n 5- Initial Particle Energy      = %8.4f eV
\n',1000*initialenergy);
    fprintf(1,'\n 6- Final Particle Energy      = %8.4f eV\n',E_total_final);
    fprintf(1,'\n 7- Initial Adiabatic Invariant      = %8.4E J/T\n',y(1,5));
    fprintf(1,'\n 8- Final Adiabatic Invariant      = %8.4E J/T\n',y(end,5));
    fprintf(1,'\n 9- Initial Pitch Angle      = %3.1f degree \n',pitchangle);
    fprintf(1,'\n 10- Final Pitch Angle      = %3.1f degree
\n',final_pitch_angle);
    fprintf(1,'\n 11- Orbit Width      = %5.4f m\n',drift_orbit_width);
    fprintf(1,'\n 12- Effective Orbit Width      = %5.4f
\n',drift_orbit_width_in_units_of_r_over_a);
fprintf(1,'\n=====
===== \n');

    fprintf(1,'\n');
    fprintf(1,'\n');
    else
        times      = t_heating_zone(inner_indexes);
        dt_initial  = t_heating_zone(inner_indexes(1))-t_heating_zone(1);
        for j=2:length(times)
            dt      = t_heating_zone(inner_indexes(j))-t_heating_zone(inner_indexes(j-
1)+1);
            dt      = dt_initial+dt;
        end
        dt_final    = t_heating_zone(end)-t_heating_zone(inner_indexes(end)+1);
        total_time   = dt+dt_final;
        time_fraction = total_time/t(end);

fprintf(1,'\n=====
===== \n');

    fprintf(1,'%s ',Case_running);
fprintf(1,'\n=====
===== \n');

    fprintf(1,'\n 1- Total Time of particle following      = %8.4E Sec\n',t(end));

```

```

        fprintf(1,'\n 2- Total Time Particle stays in Resonace Zone      = %8.4E
        Sec\n',total_time);
        fprintf(1,'\n 3- Fraction of Time Particle is in Resonance Zone = %8.4E
        \n',time_fraction);
        fprintf(1,'\n 4- Resonance Zone Crossing Probability          = %8.4E
        \n',crossing_probability);
        fprintf(1,'\n 5- Initial Particle Energy                    = %8.4f eV
        \n',1000*initialenergy);
        fprintf(1,'\n 6- Final Particle Energy                      = %8.4f eV\n',E_total_final);
        fprintf(1,'\n 7- Initial Adiapatic Invariant                = %8.4E J/T\n',y(1,5));
        fprintf(1,'\n 8- Final Adiapatic Invariant                  = %8.4E J/T\n',y(end,5));
        fprintf(1,'\n 9- Initial Pitch Angle                        = %3.1f degree \n',pitchangle);
        fprintf(1,'\n 10- Final Pitch Angle                                = %3.1f degree
        \n',final_pitch_angle);
        fprintf(1,'\n 11- Orbit Width                                    = %5.4f m\n',drift_orbit_width);
        fprintf(1,'\n 12- Effective Orbit Width                                = %5.4f
        \n',drift_orbit_width_in_units_of_r_over_a);

        fprintf(1,'\n=====
        ===== \n');

        fprintf(1,'\n');
        fprintf(1,'\n');
        end
    else
        time_fraction      = 0
        crossing_probability = 0
        fprintf(1,'\n=====
        ===== \n');

        fprintf(1,'%s ',Case_running);

        fprintf(1,'\n=====
        ===== \n');

        fprintf(1,'\n 1- Total Time of particle following      = %8.4E Sec\n',t(end));
        fprintf(1,'\n 2- Total Time Particle stays in Resonace Zone  = 0 Sec\n');
        fprintf(1,'\n 3- Fraction of Time Particle is in Resonance Zone = 0 \n');
        fprintf(1,'\n 4- Resonance Zone Crossing Probability          = %8.4E
        \n',crossing_probability);
        fprintf(1,'\n 5- Initial Particle Energy                    = %8.4f eV
        \n',1000*initialenergy);
        fprintf(1,'\n 6- Final Particle Energy                      = %8.4f eV\n',E_total_final);
        fprintf(1,'\n 7- Initial Adiapatic Invariant                = %8.4E J/T\n',y(1,5));
        fprintf(1,'\n 8- Final Adiapatic Invariant                  = %8.4E J/T\n',y(end,5));
        fprintf(1,'\n 9- Initial Pitch Angle                        = %3.1f degree \n',pitchangle);

```

```

fprintf(1,'\n 10- Final Pitch Angle                = %3.1f degree
\n',final_pitch_angle);
fprintf(1,'\n 11- Orbit Width                        = %5.4f m\n',drift_orbit_width);
fprintf(1,'\n 12- Effective Orbit Width                    = %5.4f
\n',drift_orbit_width_in_units_of_r_over_a);
fprintf(1,'\n=====
===== \n');

fprintf(1,'\n');
fprintf(1,'\n');
end
t_out = time_fraction;
p_out = crossing_probability;
E_out = E_total_final;
w_out = drift_orbit_width;
w_a_out = drift_orbit_width_in_units_of_r_over_a;
%*****
% Plotting the results
%*****
theta_last = 0:2*pi/100:2*pi;
r_last(1:length(theta_last)) = 1;
% Plotting the polar plot
if noplot == 0
    set(0,'defaultaxesfontsize',20,'defaultaxesfontname','times
roman','defaultaxesfontWeight','bold');
    % Plotting the polar plot
    figure(1)
    set(gcf,'DefaultLineLineWidth',1.5)
    rovera = y(:,1)/a_average;
    initial_rovera = y(1,1)/a_average;
    final_rovera = y(end,1)/a_average;
    polar(theta_last,r_last,'k')
    hold on
    polar(y(:,2),rovera,'r')
    polar(y(1,2),initial_rovera,'Ob')
    polar(y(end,2),final_rovera,'Ok')
    polar(maximum_theta,maximum_r_over_a,'Om')
    polar(minimum_theta,mininum_r_over_a,'Og')
    figure(2)
    set(gcf,'DefaultLineLineWidth',1.5)
    plot(t,y(:,5),'r','LineWidth',3)
    title(['\mu First Adiabatic Invariant Time Variation for ',global_title]);
    xlabel('Time (sec)');
    ylabel('Adiabatic Moment \mu (J/T)');

```

new

```

grid on

figure(3)
set(gcf,'DefaultLineLineWidth',1.5)
rovera = y(:,1)/a_average;
polar(theta_last,r_last,'k')
hold on
polar(y(:,3),rovera,'r')
polar(y(1,3),initial_rovera,'Ob')
polar(y(end,3),final_rovera,'Ok')
end
%#####
% End of the program RFHEATING
%#####

```

### A5.4.2 Function particle\_drift\_heating

```

function ydot = drif_heating(t,y,mode,heating)
%*****
% Constants
%*****
Bo      = 0.5;           % Magnetic Field on axis 0.5 Tesla.
g       = 1.44*Bo;       % Poloidal current outside flux surfaces  $g = R \cdot Bo$ 
e       = 1.6e-19;       % Electron Charge in Coloumb
m       = 9.1e-31;       % Electron mass in Kg
e_over_m = e/m;          % Electron charge to mass ratio
speed_of_light = 3e8;    % Speed of Light
one_over_g = 1/g;        % 1/g
if strcmpi(mode,'qhs') == 1
    a_average = 0.113; % plasma average minor radius
elseif strcmpi(mode,'mirror') == 1
    a_average = 0.1198; % plasma average minor radius
elseif strcmpi(mode,'antimirror') == 1
    a_average = 0.1164; % plasma average minor radius
else
    display('You Entered Undefined Mode, modes are: QHS, Mirror and AntiMirror');
    return
end
%*****
% Calculating the magnetic field
%*****
r      = y(1);
theta  = y(2);

```

```

phi      = y(3);
rho_parallel = y(4);
mu       = y(5);
mu_over_e = mu/e;          % First adiabatic invariant
r_over_a = y(1)/a_average;
one_over_Bor = 1/(Bo*y(1));
if strcmpi(mode,'qhs') == 1
    a_average = 0.113; % plasma average minor radius
    A = [1.05 0.0024 -0.02381 0.086768 -0.07433 0.0060676];
    iota =
A(1)+A(2)*r_over_a+A(3)*r_over_a^2+A(4)*r_over_a^3+A(5)*r_over_a^4+A(6)*r_ov
er_a^5;
    b41 = 0.14*r_over_a;
    db41dr = 0.14/a_average;
    B = Bo*(1-b41*cos(4*phi-theta));
    B2 = B^2;
    dBdr = -Bo*db41dr*cos(4*phi-theta);
    dBdtheta = -Bo*b41*sin(4*phi-theta);
    dBdphi = 4*Bo*b41*sin(4*phi-theta);
elseif strcmpi(mode,'mirror') == 1
    a_average = 0.1198; % plasma average minor radius
    A = [1.0668 0.0077317 -0.054029 0.24963 -0.30516 0.16543];
    iota =
A(1)+A(2)*r_over_a+A(3)*r_over_a^2+A(4)*r_over_a^3+A(5)*r_over_a^4+A(6)*r_ov
er_a^5;
    b41 = 0.14*r_over_a;
    b40 = 0.08;
    db41dr = 0.14/a_average;
    B = Bo*(1-b41*cos(4*phi-theta)+b40*cos(4*phi));
    B2 = B^2;
    dBdr = -Bo*db41dr*cos(4*phi-theta);
    dBdtheta = -Bo*b41*sin(4*phi-theta);
    dBdphi = 4*Bo*(b41*sin(4*phi-theta)-b40*sin(4*phi));
elseif strcmpi(mode,'antimirror') == 1
    a_average = 0.1264; % plasma average minor radius
    A = [1.0304 0.0031904 -0.046077 0.11165 -0.10064 0.076335];
    iota =
A(1)+A(2)*r_over_a+A(3)*r_over_a^2+A(4)*r_over_a^3+A(5)*r_over_a^4+A(6)*r_ov
er_a^5;
    b41 = 0.14*r_over_a;
    b40 = 0.08;
    db41dr = 0.14/a_average;
    B = Bo*(1-b41*cos(4*phi-theta)-b40*cos(4*phi));

```

```

B2    = B^2;
dBdr  = -Bo*db41dr*cos(4*phi-theta);
dBdtheta = -Bo*b41*sin(4*phi-theta);
dBdphi = 4*Bo*(b41*sin(4*phi-theta)+b40*sin(4*phi));

else
    display('You Entered Undefined Mode, modes are: QHS, Mirror and AntiMirror');
    return
end

%*****
% Calculating the Electric field
%*****
dpotentialdr = 0;
dpotentialdtheta = 0;
dpotentialdphi = 0;
%*****
% Defining the resonance zone
%*****
phi_minimum    = -0.02767591503494;    % -4 cm from left at the center of the Box
Port
phi_maximum    = 0.02767591503494;    % 4 cm from right at the center of the Box
Port
phi_turns      = mod(abs(y(3)),2*pi);
r_limit        = 0.1*a_average;
theta_minimum  = pi/2;                % -4 cm from left at the center of the Box Port
theta_maximum  = 3*pi/2;              % 4 cm from right at the center of the Box Port
theta_turns    = mod(abs(y(2)),2*pi);
%*****
% Setting the differential equations
%*****
iota_over_g    = iota/g;
B2_rho_e_over_m = e_over_m*B2*rho_parallel;
factor         = (mu_over_e+e_over_m*B*rho_parallel^2);
y1dot          = one_over_Bor*(-dpotentialdtheta-factor*dBdtheta);
y2dot          =
one_over_Bor*(dpotentialdr+factor*dBdr)+iota_over_g*B2_rho_e_over_m;
y3dot          = B2_rho_e_over_m/g;
y4dot          = -one_over_g*(dpotentialdphi+factor*dBdphi);
if heating == 1
    condition    = (phi_turns>phi_minimum & phi_turns<phi_maximum &
y(1)<r_limit);

```

```

%condition = (phi_turns>phi_minimum & phi_turns<phi_maximum &
y(1)<r_limit & theta_turns>theta_minimum & phi_turns<theta_maximum);
if (condition)
    if y(1) <= 0.01
        x = y(1);
        A0 = -6*x^2 + 0.21*x - 0.0054;
        A1 = -1E+07;
        A2 = 3E+06;
        A3 = -6E+08*x^2 + 8E+06*x - 117781;
        A4 = 7E+06*x^2 - 89650*x + 1446.5;
    else
        x = y(1);
        A0 = -22*x^2 + 0.97*x - 0.0114;
        A1 = -6E+10*x^2 + 3E+09*x - 3E+07;
        A2 = 3E+10*x^2 - 1E+09*x + 1E+07;
        A3 = -1E+09*x^2 + 4E+07*x - 388365;
        A4 = 1E+07*x^2 - 443643*x + 4502.4;
    end
    v_parallel = rho_parallel*B*e/m;
    v_perpendicular = sqrt(2*B*mu/m);
    pitch_angle = atan(v_perpendicular/v_parallel)*180/pi;
    Delta_power = 1.6e-
    19*(A0+A1*pitch_angle+A2*pitch_angle^2+A3*pitch_angle^3+A4*pitch_angle^4);
    dmudt = Delta_power/B;
    y5dot = dmudt;
else
    y5dot = 0;
end
elseif heating == 0
    y5dot = 0;
else
    return
end
ydot = [y1dot;y2dot;y3dot;y4dot;y5dot];
%*****
% End
%*****

```

### A5.4.3 Function loss\_check\_heating

```

function [value,isterminal,direction] = loss_check_heating(t,y,mode,heating)
%%%%%%%%%%%%%%%%%%%%%%%%%%%%%%%%%%%%%%%%%%%%%%%%%%%%%%%%%%%%%%%%%%%%%%%%%%%%%%
% Function loss_check_heating

```

```

%%%%%%%%%%%%%%%%%%%%%%%%%%%%%%%%%%%%%%%%%%%%%%%%%%%%%%%%%%%%%%%%%%%%%%%%
if strcmpi(mode,'qhs')== 1
    a_average = 0.113; % plasma average minor radius
elseif strcmpi(mode,'mirror')== 1
    a_average = 0.1198; % plasma average minor radius
elseif strcmpi(mode,'antimirror')== 1
    a_average = 0.1264; % plasma average minor radius
else
    display('You Entered Undefined Mode, modes are: QHS, Mirror and AntiMirror');
    return
end
r_over_a_loss = 0.8;
r = y(1);
r_over_a = r/a_average;
if r_over_a < r_over_a_loss
    value = 1;
else
    value = 0;
end
isterminal = 1;
direction = 0;

```

## Appendix 6

### Variation of Mod B along Field Line

#### A6.0 Introduction

The main factor determining the features of charged particle confinement in a non-axisymmetric toroidal magnetic device, such as torsatron, heliotron, stellarator is the character of the magnetic field. The adequate representation of the magnitude of the actual magnetic field requires expanding it in Fourier series. It is known that in stellarator devices, the behavior of the magnetic field strength along a field line can be represented adequately by Fourier-decomposition, in which a large number of harmonics with different toroidal (N) and poloidal (m) mode numbers should be taken into account. In this appendix, the variation of mod B along field line will be calculated for the three different magnetic configurations, QHS, Mirror and AntiMirror at different effective plasma radii,  $r/a$ .

#### A6.1 The HSX Magnetic Spectrum

The model magnetic fields were calculated based on a representation of the finite-size coil model. The spectrum is specified in Boozer co-ordinates as:

$$B = B_o \sum_{nm} b_{nm}(r) \cos(n\varphi - m\vartheta) \quad (\text{A6.1})$$

Where  $B_o = 0.5$  Tesla,  $b_{nm}(r)$  are the Fourier spectrum coefficients as a function of  $r$ ,  $n$  and  $m$  are the toroidal and poloidal mode numbers and  $\varphi$  and  $\vartheta$  are the toroidal and

poloidal angles. Figure A6.1 shows the magnetic field spectrum for the QHS configuration based on the above model. The magnitude of the largest 15  $b_{nm}$  components at  $r/a = 0.9$  are plotted as a function of radius. The choice of the number of components used to represent the spectrum was based on truncating any component that is less than 0.1% of the  $[0,0]$  component at  $r/a = 0.9$ . The mode numbers are defined as a pair  $[N,m]$  where  $N$  is the toroidal mode number and  $m$  is the poloidal mode number. The largest mode number for HSX is the  $[0,0]$ , which is the average magnetic field on the flux surface, as the figure shows, it increases from the axis out to the edge.

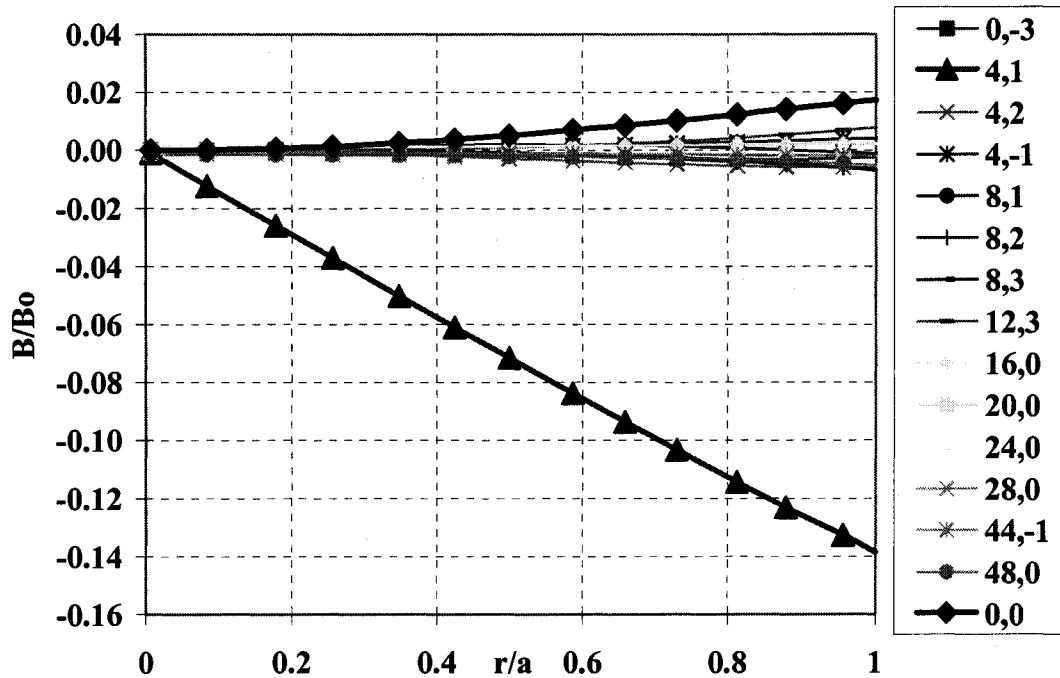


**Figure A6.1: The variation of QHS spectral components with minor radius.**

The value of the  $[0,0]$  mode number on axis was subtracted from all components, in order to plot them all on one scale. The second largest mode is the  $[4,1]$  which is the dominant mode contributing to the variation of the magnetic field on a flux surface. The principle

symmetry breaking components are the  $[48,0]$  term and the  $[4,2]$  mode. The first mode is due to the modular ripple since there are a total of 48 coils in the machine. The magnitude of the symmetry breaking terms in the spectrum for the finite size HSX coils is below 1% at the edge. The HSX differs from a conventional stellarator in that it lacks toroidal curvature. However, it is inefficient to break the quasi-helical symmetry by reintroducing toroidal curvature; the  $[0,1]$  component of the spectrum. Instead, the symmetry is broken with the excitation of a toroidal mirror term; the  $[4,0]$  component. Figure A6.2 shows the magnetic field spectrum for 10% Mirror configuration. The magnitude of the largest 21  $b_{nm}$  components at  $r/a = 0.9$  are plotted as a function of radius.

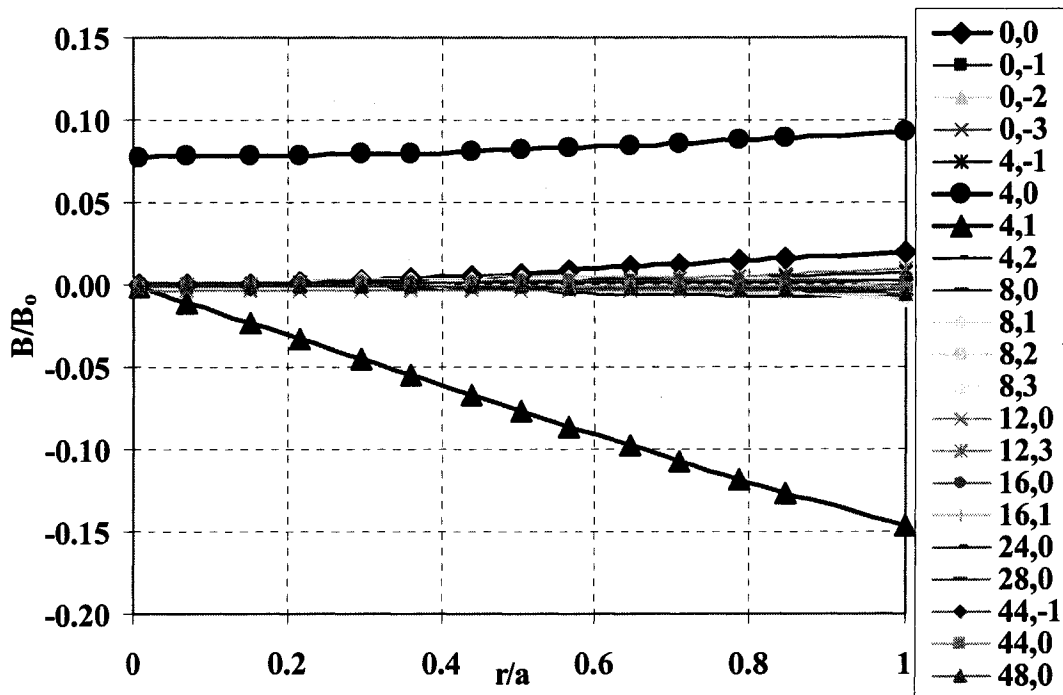


Figure A6.2: The variation of Mirror spectral components with minor radius.

The figure shows that the largest components are the [0,0], and [4,1] components as in the case of QHS, and a large [4,0] mode is excited, with only small changes in the other symmetry breaking components of the spectrum.

The QHS spectrum is approximated by:

$$\frac{B}{B_o} = 1 - |b_{41}(r)| \cos(4\phi - \mathcal{G}) \quad (\text{A6.2})$$

Where  $b_{41}$  is the N=4, m=1 mode. The Mirror configuration is approximated by:

$$\frac{B}{B_o} = 1 - |b_{41}(r)| \cos(4\phi - \mathcal{G}) + |b_{40}(r)| \cos(4\phi) \quad (\text{A6.3})$$

The AntiMirror is approximated by:

$$\frac{B}{B_o} = 1 - |b_{41}(r)| \cos(4\phi - \mathcal{G}) - |b_{40}(r)| \cos(4\phi) \quad (\text{A6.4})$$

Where,  $b_{40}$  is the symmetry breaking mirror component. The  $b_{40}$  component is added in the Mirror and subtracted in the AntiMirror configurations at box port C where the microwave antenna is located.

## A6.1 Mod B Variation Along Field Line

Figures A6.3 through A6.25 show the variation of the magnitude of the magnetic field along the field line for the three different magnetic configurations, QHS, Mirror and AntiMirror at different plasma effective radii. The effective plasma radius,  $r/a$ , is negative at the inboard side of the machine and positive at the outboard side.

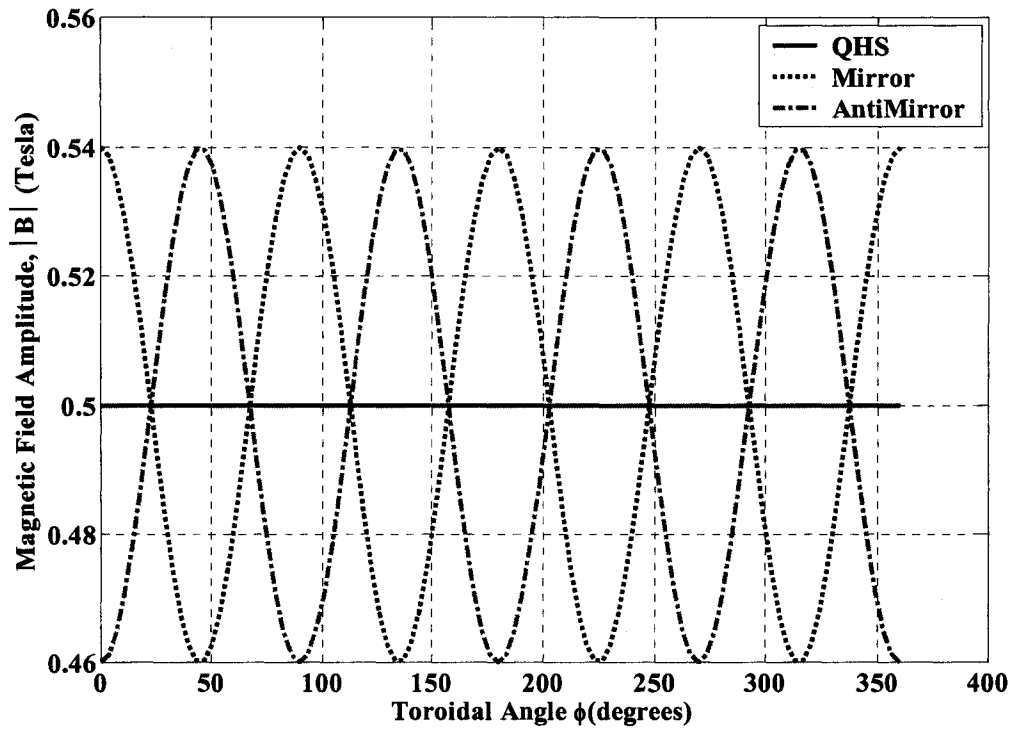


Figure A6.3: Variation of  $|B|$  along field line,  $r/a = 0$

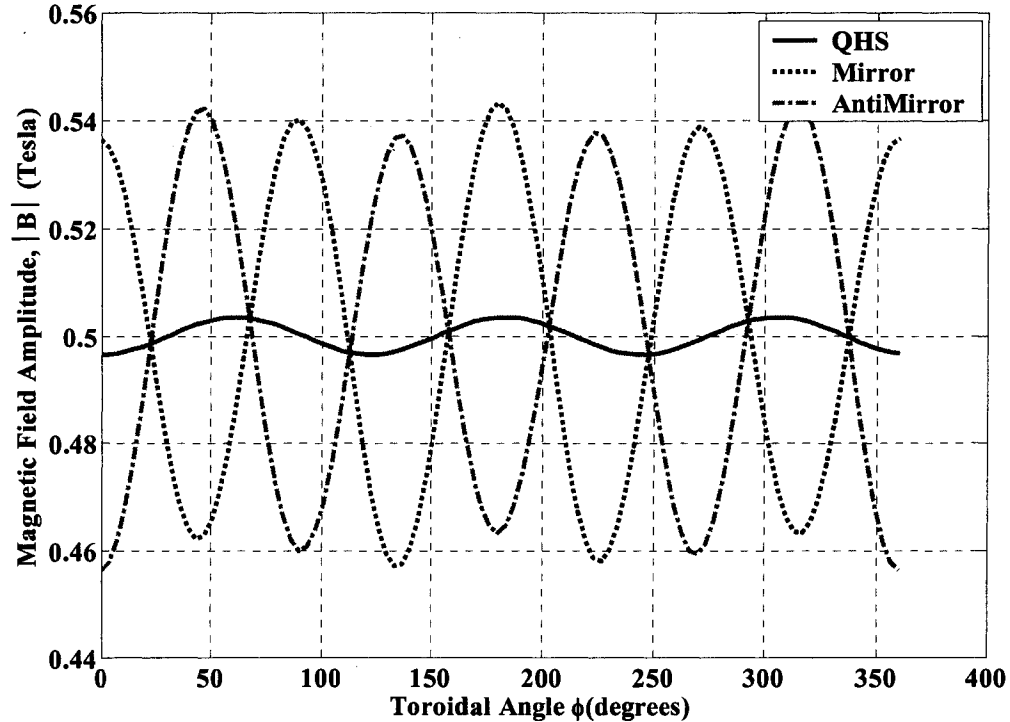


Figure A6.4: Variation of  $|B|$  along field line,  $r/a = 0.05$

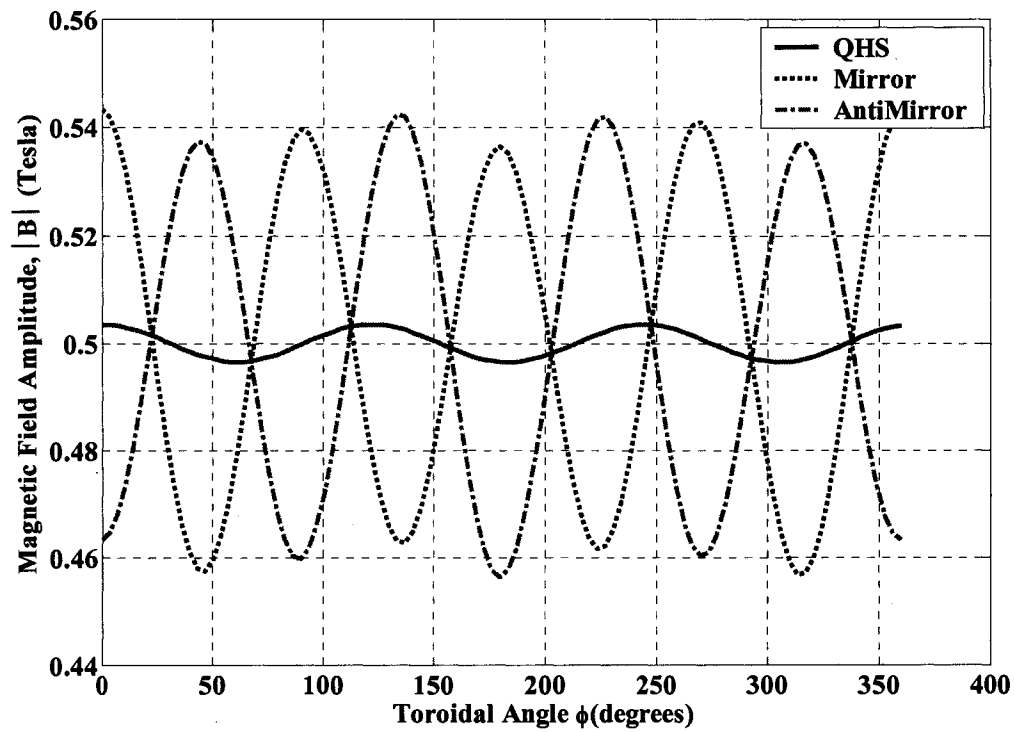


Figure A6.5: Variation of  $|B|$  along field line,  $r/a = -0.05$

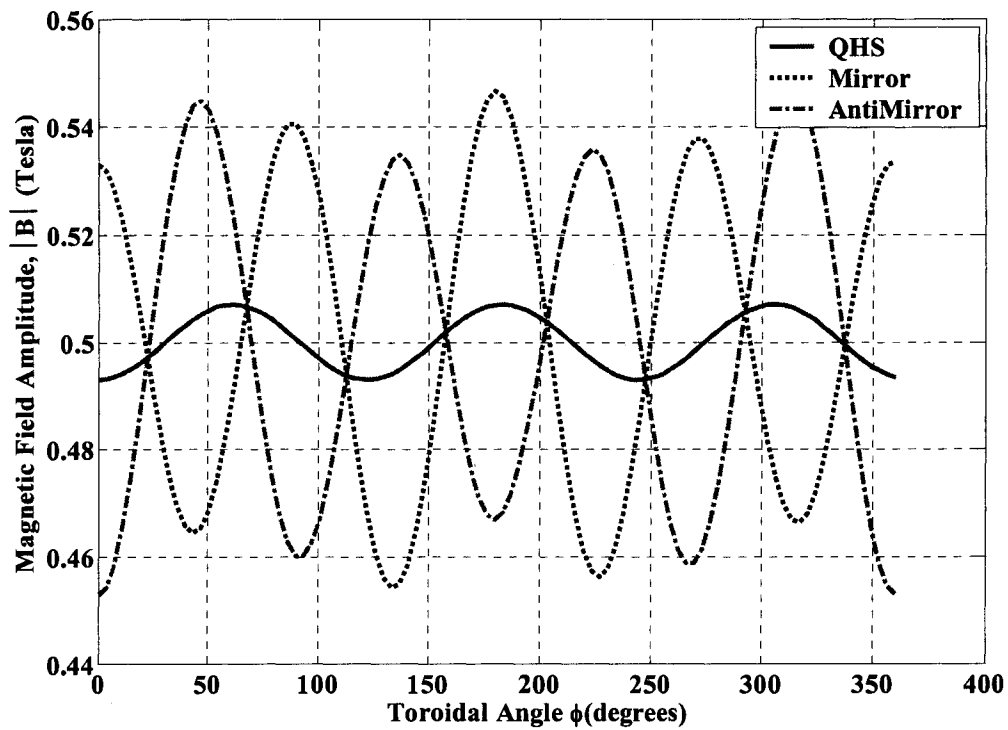


Figure A6.6: Variation of  $|B|$  along field line,  $r/a = 0.1$

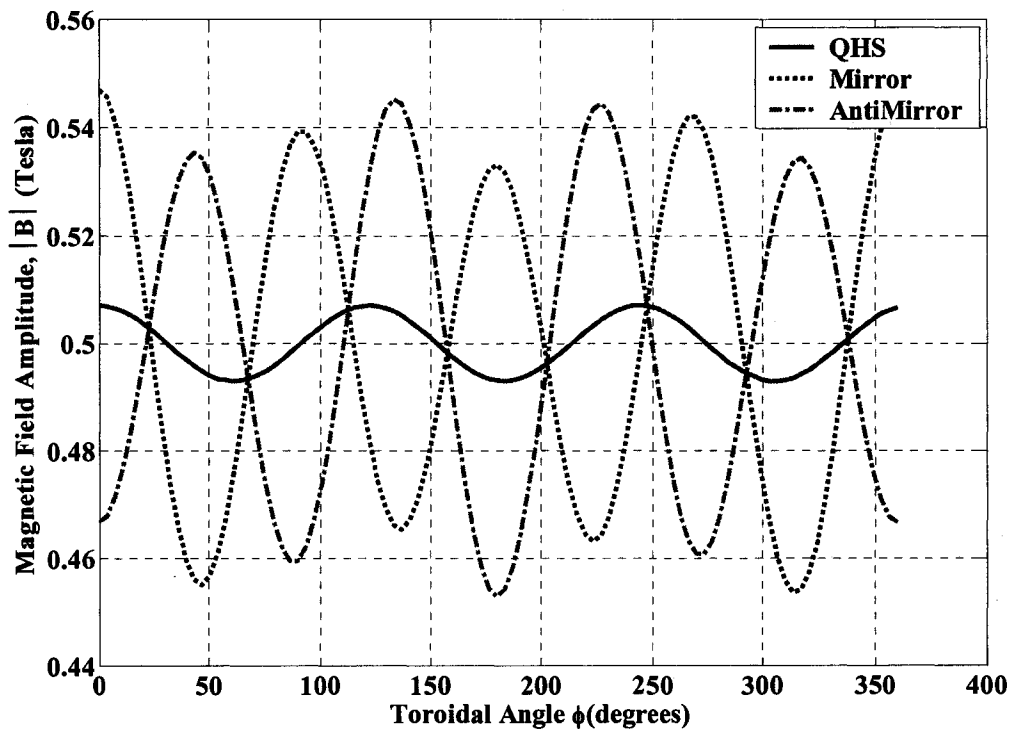


Figure A6.7: Variation of  $|B|$  along field line,  $r/a = -0.1$

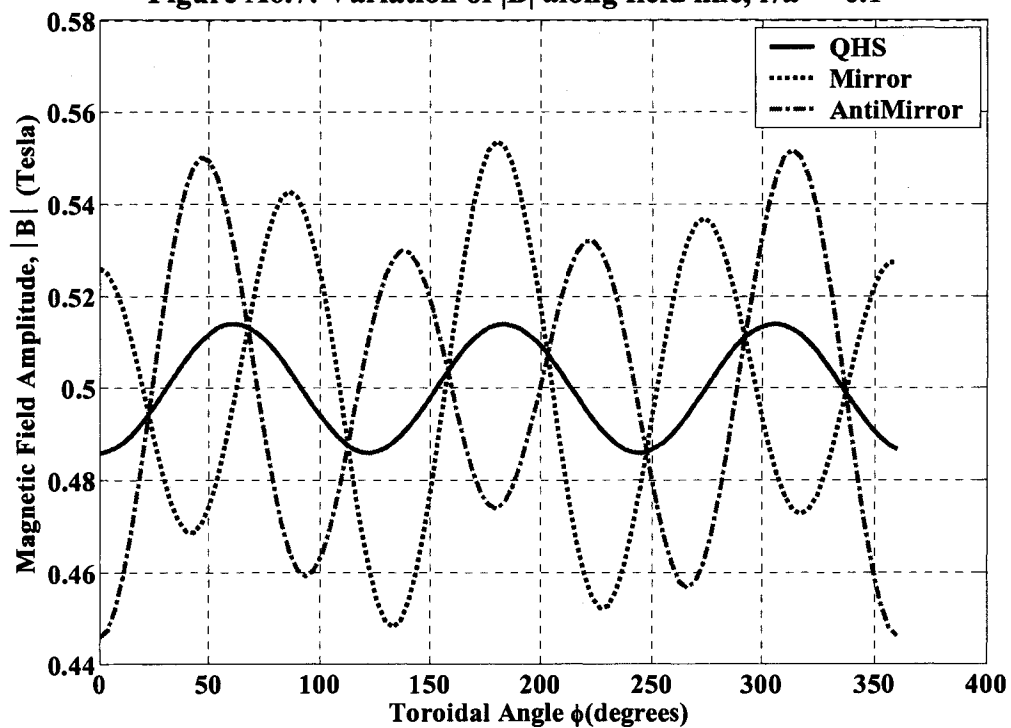


Figure A6.8: Variation of  $|B|$  along field line,  $r/a = 0.2$

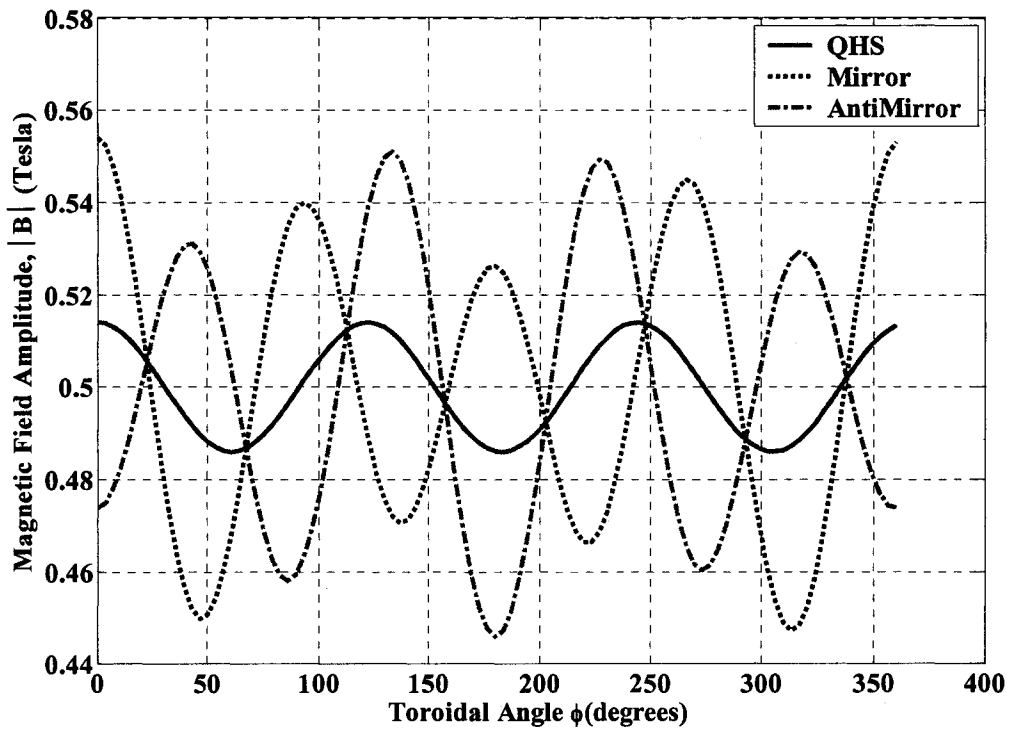


Figure A6.9: Variation of  $|B|$  along field line,  $r/a = -0.2$

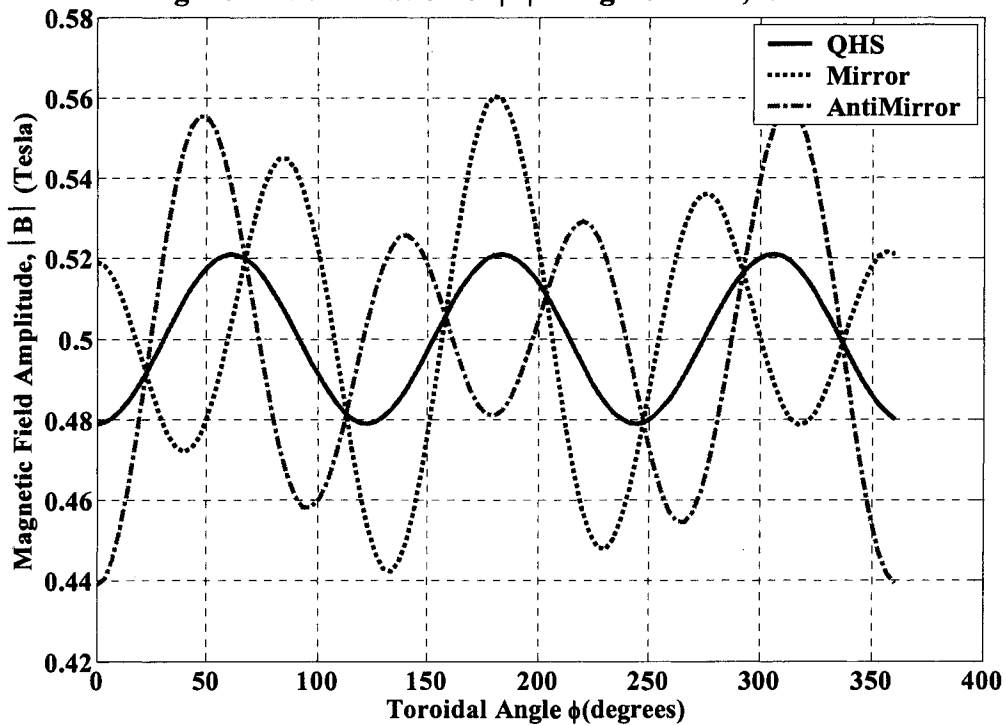


Figure A6.10: Variation of  $|B|$  along field line,  $r/a = 0.3$

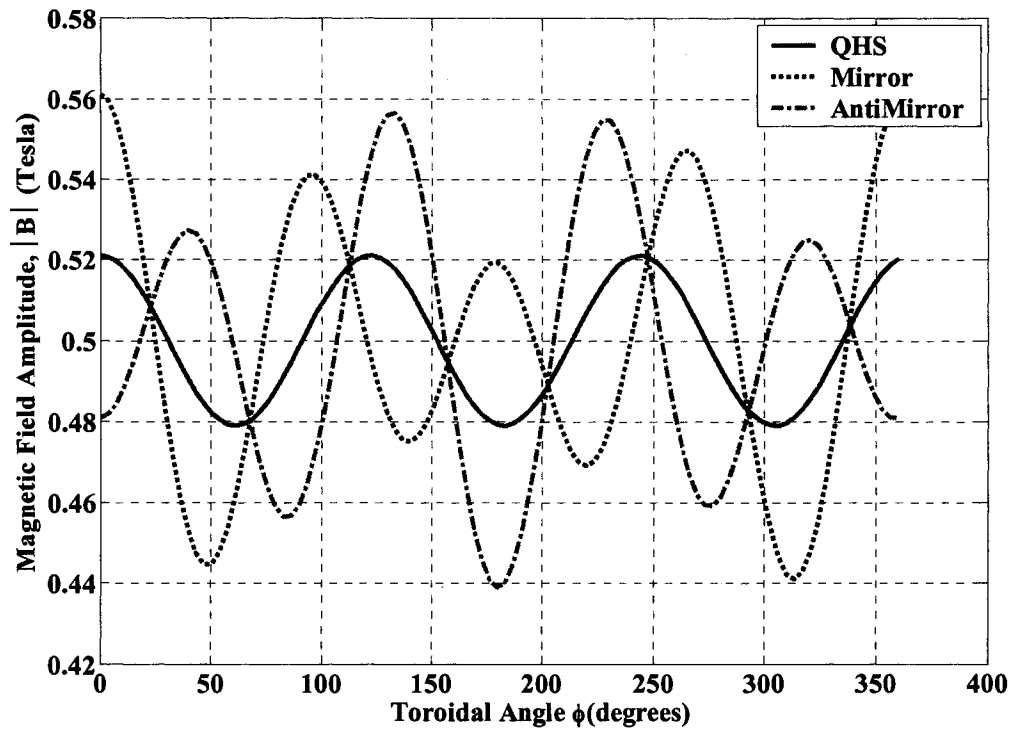


Figure A6.11: Variation of  $|B|$  along field line,  $r/a = -0.3$

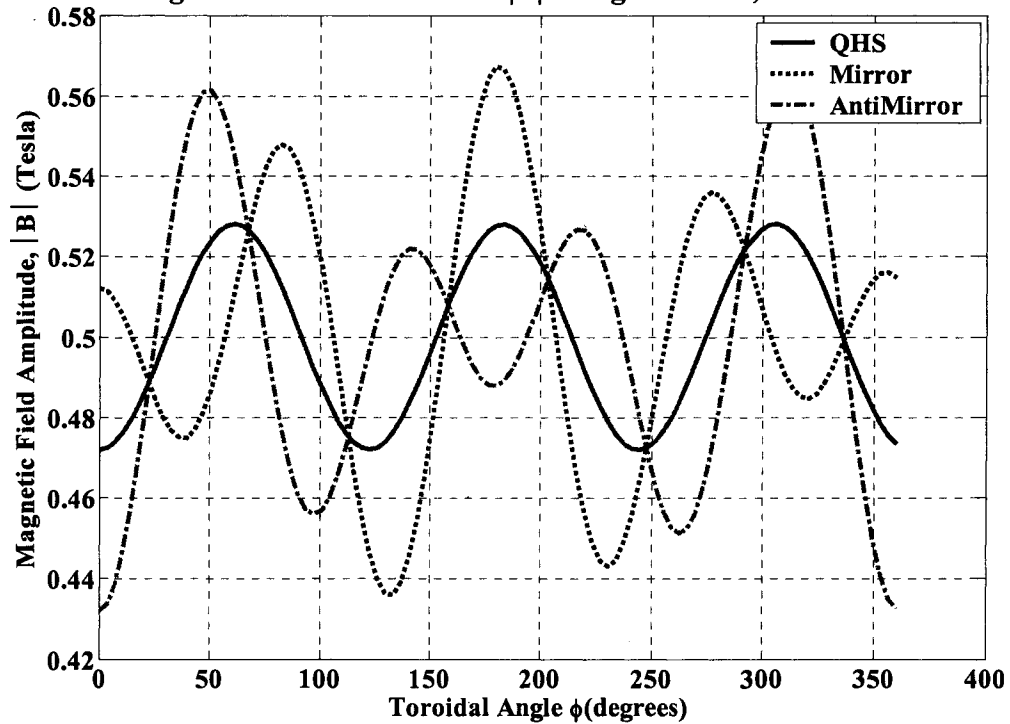


Figure A6.12: Variation of  $|B|$  along field line,  $r/a = 0.4$

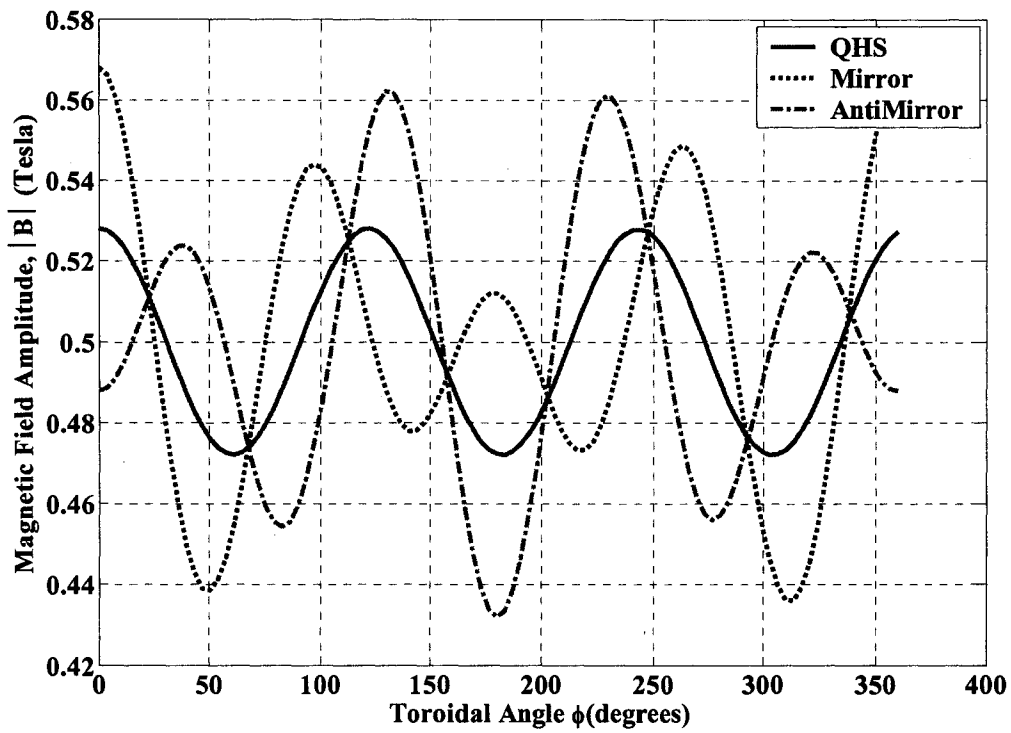


Figure A6.13: Variation of  $|B|$  along field line,  $r/a = -0.4$

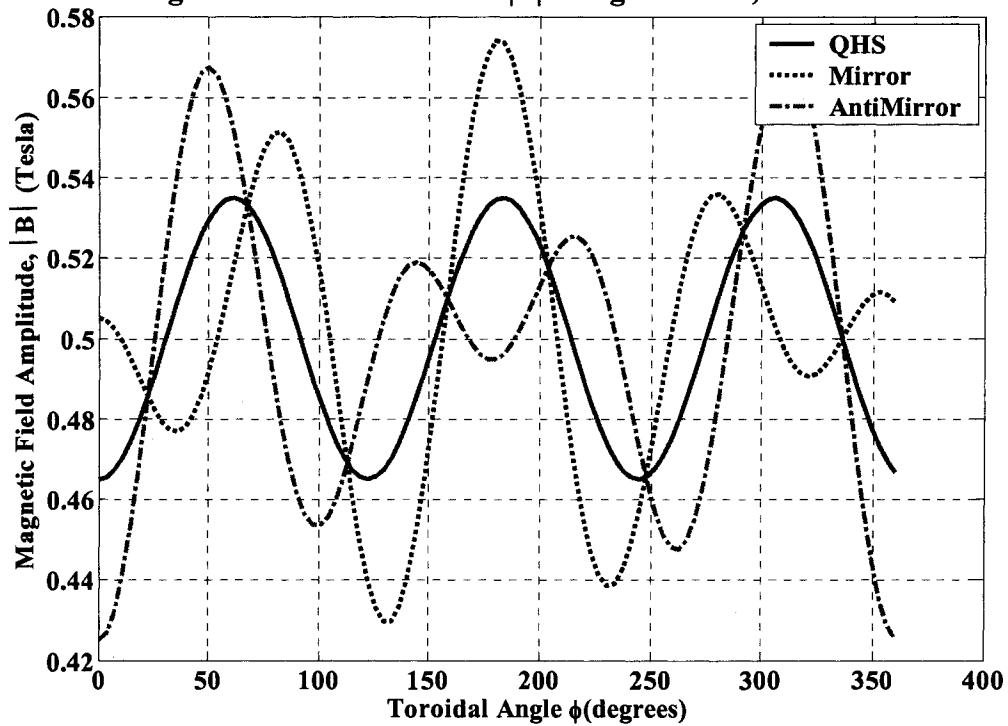


Figure A6.14: Variation of  $|B|$  along field line,  $r/a = 0.5$

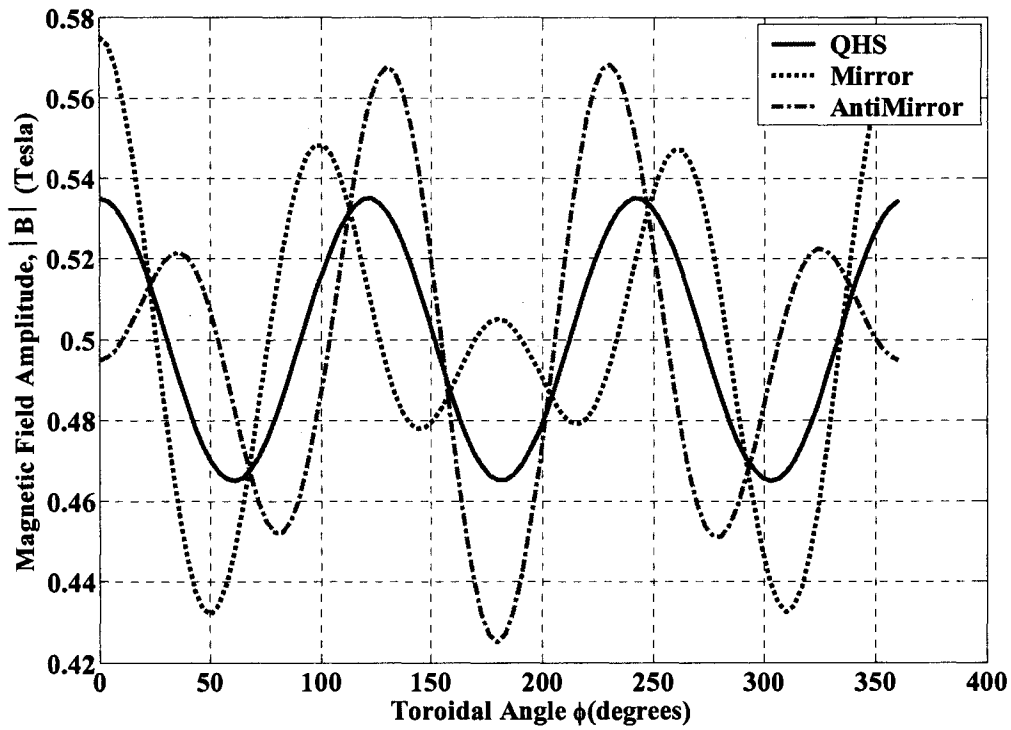


Figure A6.15: Variation of  $|B|$  along field line,  $r/a = -0.5$

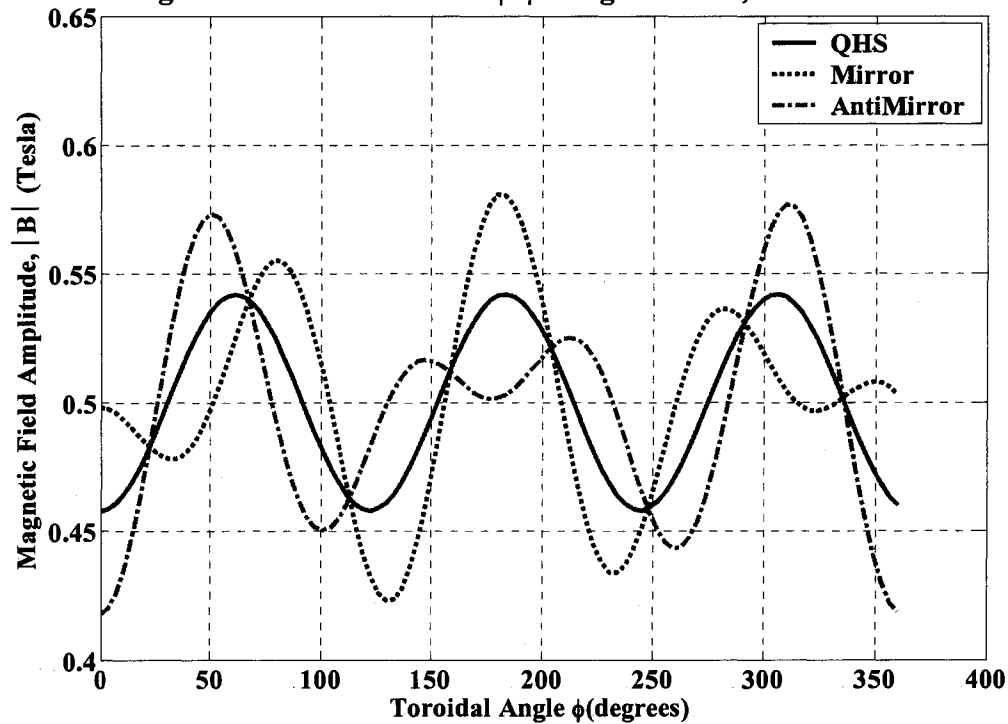


Figure A6.16: Variation of  $|B|$  along field line,  $r/a = 0.6$

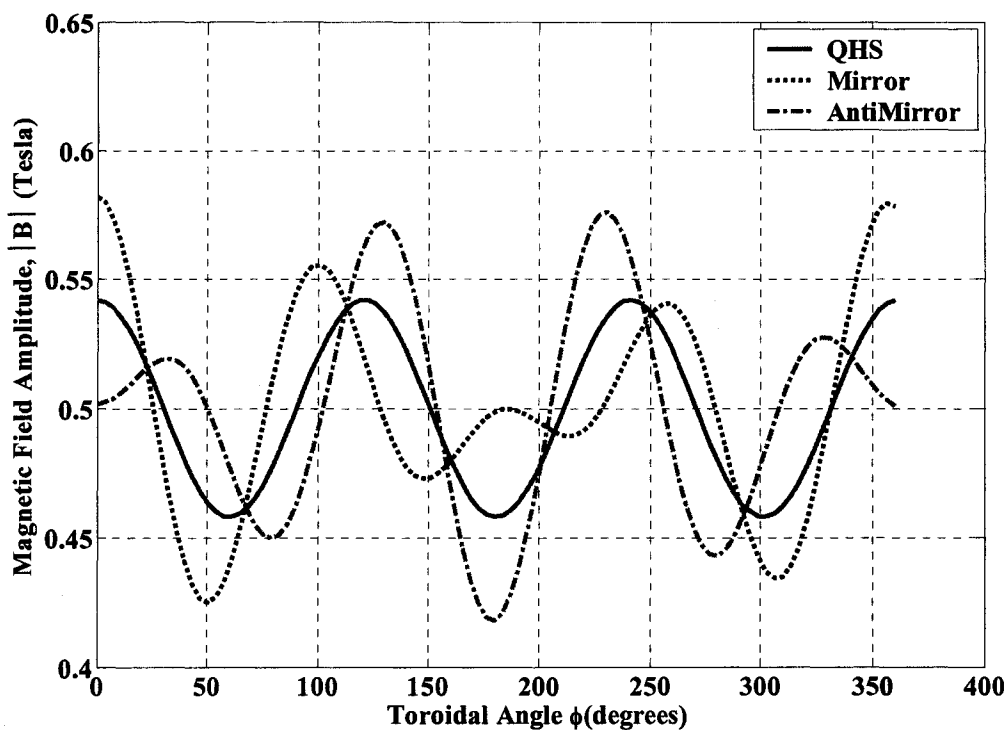


Figure A6.17: Variation of  $|B|$  along field line,  $r/a = -0.6$

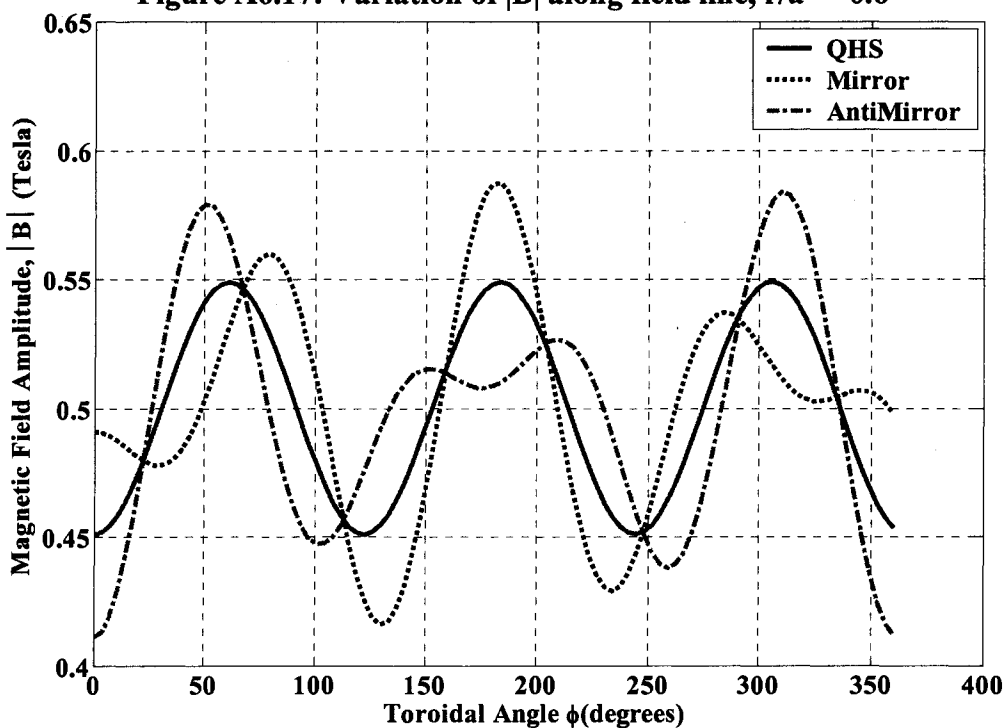


Figure A6.18: Variation of  $|B|$  along field line,  $r/a = 0.7$

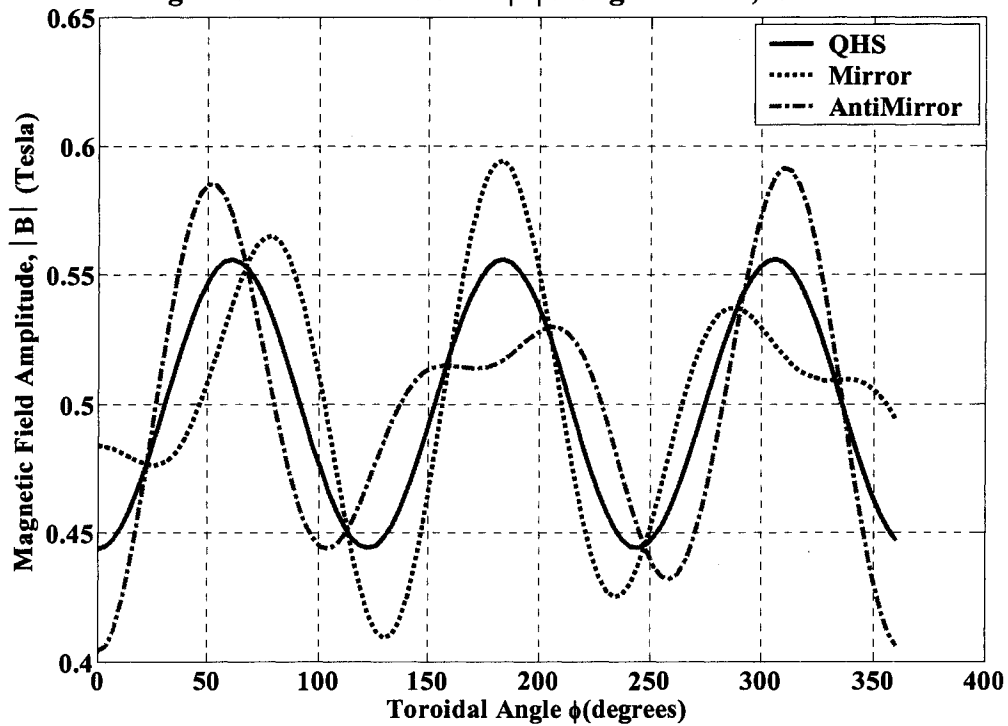
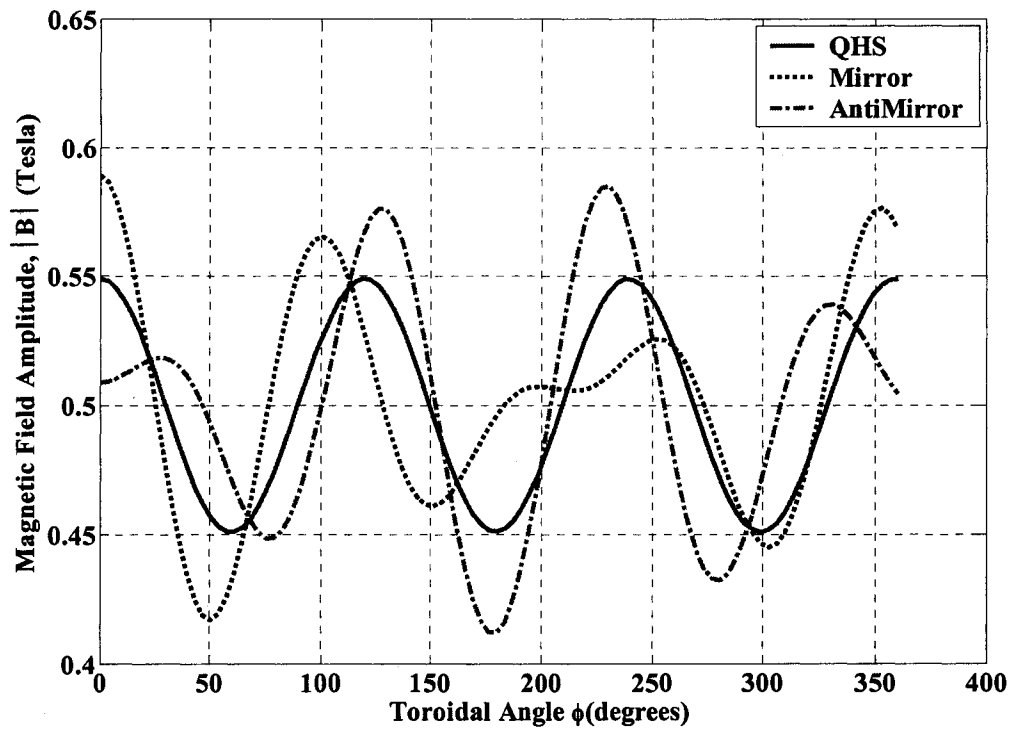


Figure A6.20: Variation of  $|B|$  along field line,  $r/a = 0.8$

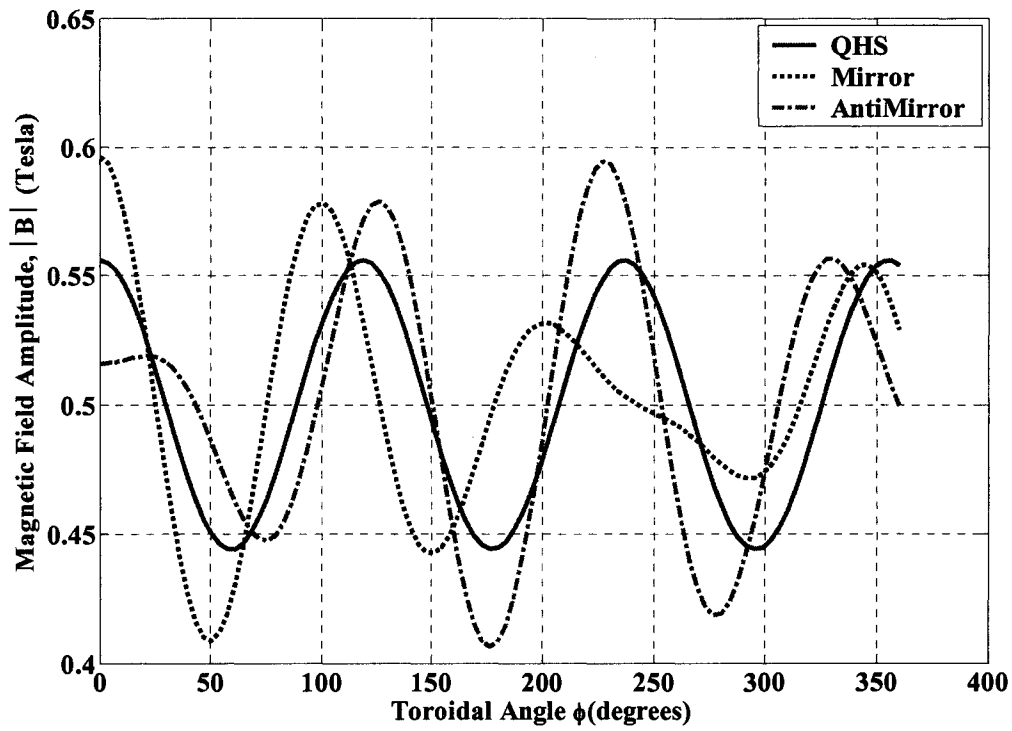


Figure A6.21: Variation of  $|B|$  along field line,  $r/a = -0.8$

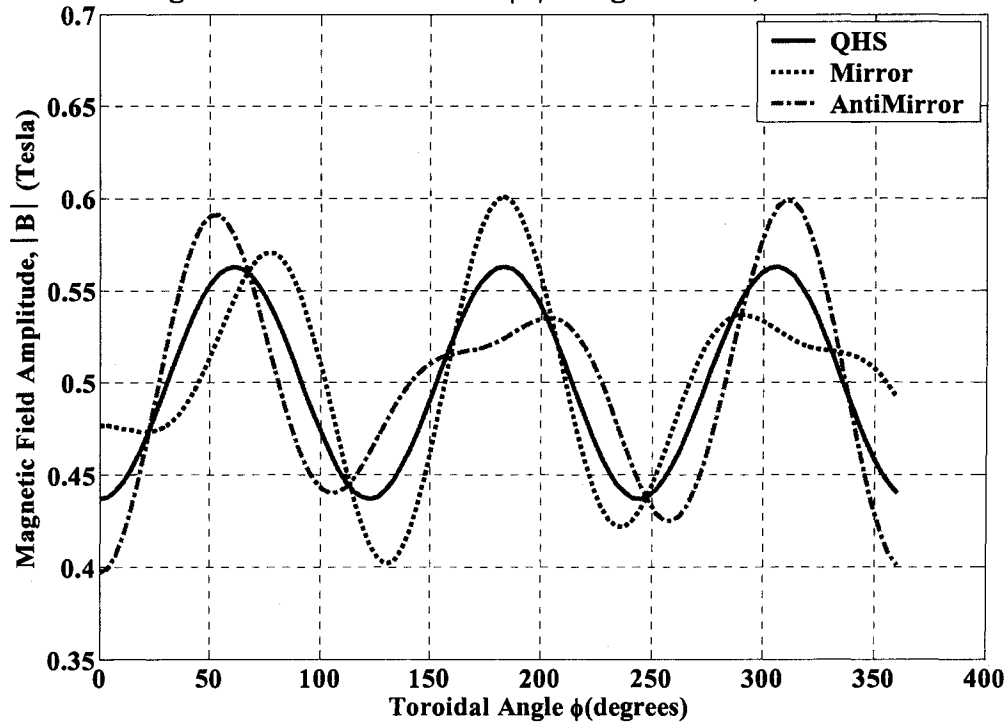


Figure A6.22: Variation of  $|B|$  along field line,  $r/a = 0.9$

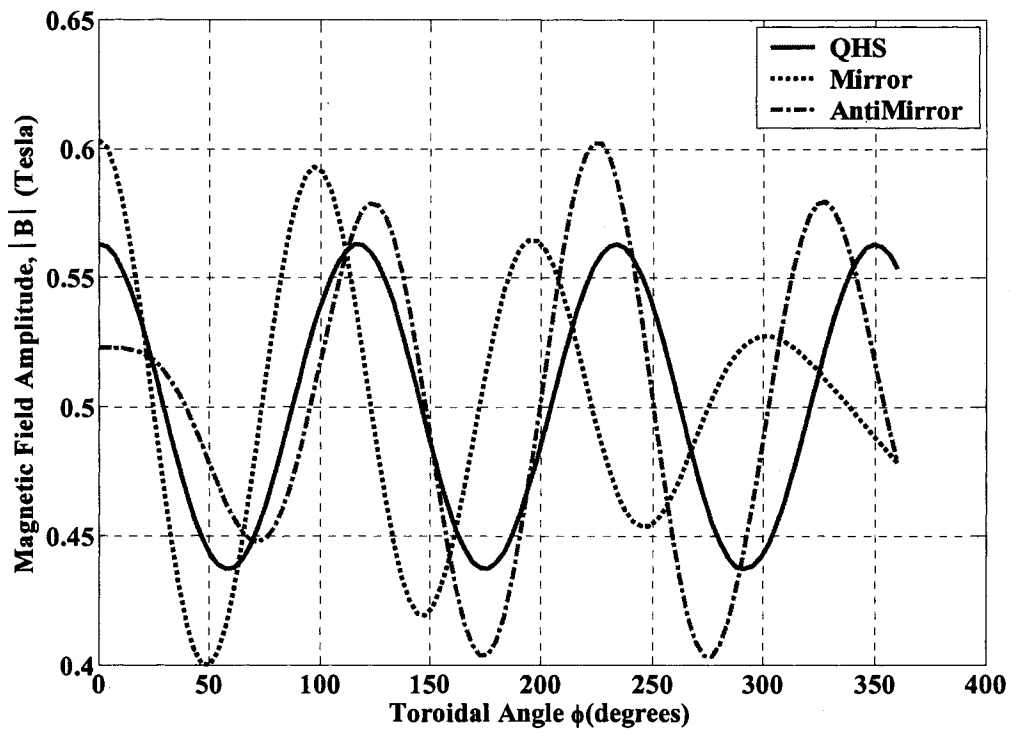


Figure A6.23: Variation of  $|B|$  along field line,  $r/a = -0.9$

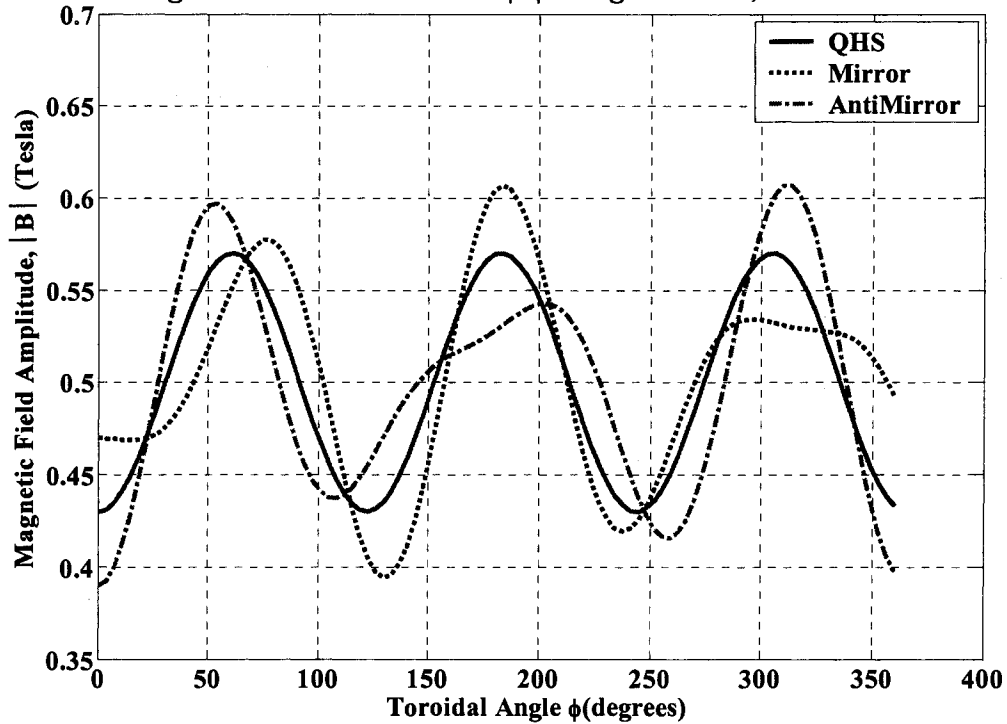


Figure A6.24: Variation of  $|B|$  along field line,  $r/a = 1$

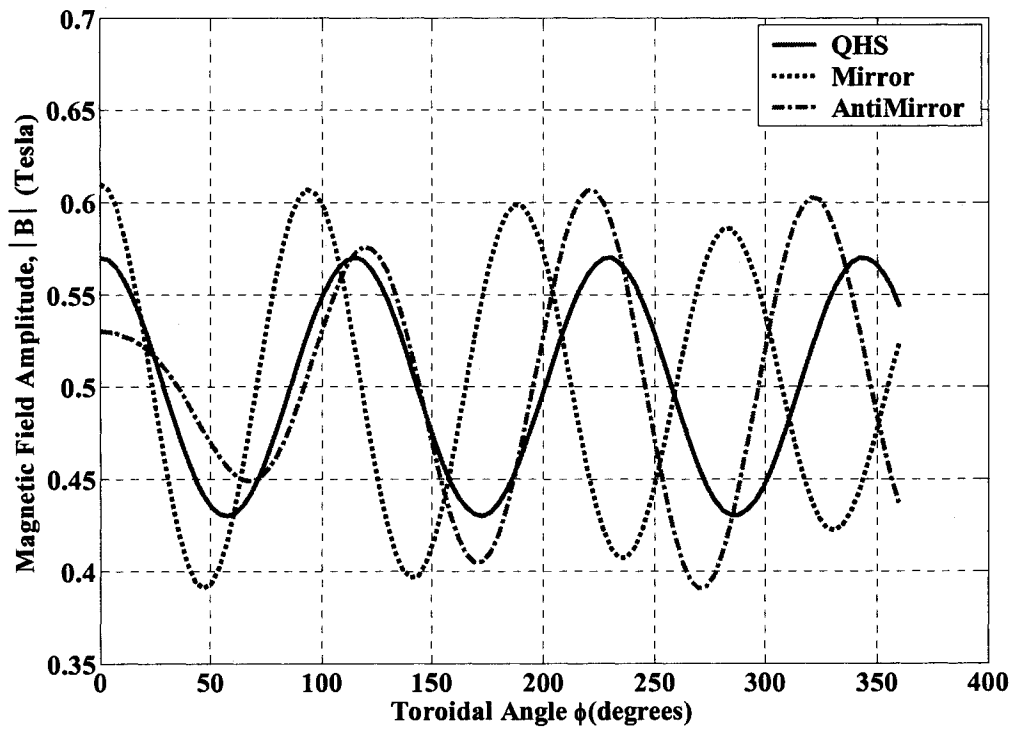


Figure A6.25: Variation of  $|B|$  along field line,  $r/a = -1$